Queen Mary, University of London

PhD Thesis

In Silico Modelling and Optimisation of Synthesised Apatite Coatings for Dental Implants

Author:
Lennox Ovando Vincent Carter

Supervisors:
Prof. Martin Dove
Dr. Maisoon Al-Jawad

Materials Research Institute, Centre for Condensed Matter and Materials Physics
School of Physics and Astronomy

May 2019

Statement of originality

I, LENNOX OVANDO VINCENT CARTER, confirm that the research included within this thesis is my own work or that where it has been carried out in collaboration with, or supported by others, that this is duly acknowledged below and my contribution indicated. Previously published material is also acknowledged below.

I attest that I have exercised reasonable care to ensure that the work is original, and does not to the best of my knowledge break any UK law, infringe any third party's copyright or other Intellectual Property Right, or contain any confidential material.

I accept that the College has the right to use plagiarism detection software to check the electronic version of the thesis.

I confirm that this thesis has not been previously submitted for the award of a degree by this or any other university.

.....

LENNOX OVANDO VINCENT CARTER

May 2019

QUEEN MARY, UNIVERSITY OF LONDON

Abstract

Centre for Condensed Matter and Materials Physics
School of Physics and Astronomy

Doctor of Philosophy in Physics

In Silico Modelling and Optimisation of Synthesised Apatite Coatings for Dental Implants

by Lennox Ovando Vincent Carter

In order to better understand the formation of ordered apatite coatings we have examined the surface energy and chemical effects on the morphology and optimal Ca/P values of nano-crystals synthesised through the precipitation method. This study was aimed at understanding and controlling mineral formation for use in the regenerative dentistry field. Titanium and hydroxyapatite substrate were submerged in a Ca^{2+} and PO_4^{3-} supersaturated solution and incubated separately at six different temperatures below 100 °C. The experiment was repeated using a solution that was buffered with bis-tris in order to maintain pH at 6 throughout the incubation. A range of morphologies were formed and catalogued. Compositional and structural analysis was carried out using standard characterisation techniques. We find that in general, increasing the surface roughness reduces the number of competing calcium phosphate morphologies found. However, there is an upper limit on how much the surface roughness can be increased. A apatite surface roughness between 0.212–0.360 μm can be used to form aligned rod-like nano crystals when incubated at 70 °C. Similar results were found on titanium surfaces that were pre-coated with apatite before incubation, indicating that these results could further be applied to implant coating techniques. Buffered samples encourage the formation of dicalcium phosphate over that of apatite at temperatures higher than solutions without bistris buffer. Where buffered samples showed evidence from 5–37 °C, but unbuffered samples only show indication at 5 °C only. Buffering also prevented the formation of any aligned rod-like apatite coatings. Thus buffered solutions were deemed unsuitable for further study.

Supersaturated solution incubated at temperatures 21 °C, and 70 °C, for 7 days were identified as yeilding aligned apatite. Coatings which were then characterised using SEM, EDX, FTIR and XRD. Images were then analysed via ImageJ which was used to quantify surface coverage achieved by coatings, and the size of morphological features. SEM shows interconnected crystals at day 6 which could indicate the formation of an amorphous epitaxial layer. Aligned crystals were formed by a successive layering of rod-like apatite nano-crystals.

Pair Distribution Function analysis and Atomistic modelling studies of synthesised apatite powders show that amorphous calcium phosphate plays a key role in the synthesis route. Amorphous calcium phosphate containing bond lengths consistent with apatite and DCPD were found in samples that were between 2–4 mins, after which only crystallised peaks could be found. The following 7 days showed a continual remodelling of bond lengths and bond formation. Furthermore, during the 7 days the bonds would transition between apatite-like and DCPD-like bond lengths in key regions. Bond length and bond angle analysis revealed that with an increase in time, there was an increase in the number of bond lengths and angle present in the data. This meant that there was an increase in the level of disorder even though there was clearly a presence of a crystalline phase throughout the 7 days incubation. This could suggest the presence of an amorphous phase throughout the 7 days.

Acknowledgements

I would like to thank my supervisors, Maisoon Al-Jawad and Martin Dove, for giving me the chance to work on such an interesting project. Also I would like to thank all the members of staff whom I gained support, Russel Bailey, Rory Willson, and Geoff Simpson. Finally, I would like to thank the students that shared ideas and methods. A special thanks is made to the developers of CRYSTAL MAKER, DLPOLY4, and GUDRUNx.

I would also like to thank the following conferences for accepting my work for both Oral and Poster presentations:

- Bioceramics 28, 18-21 Oct 2016–accepted for Oral presentation. Location: Omni Hotel, Charlotte, NC (USA).
- SurfCoat Korea 2017 International Conference, 29-31 Mar, 2017, Titled "Pair Distribution Function Analysis of Synthesised Fluorapatite/Francolite Implant Coatings for use in Regenerative Dentistry"–accepted for Oral presentation. Location: Songdo Convensia, Incheon–Korea.
- 28th European Society for Biomaterials (ESB) 2017, 4-8 Sept 2017, Titles "The effect of Bis-tris Buffer on the Synthesis of Apatite Coatings for Dental Implants". accepted for Poster presentation. Location: Athens–Greece.
- EUROMAT 2017,17-22 Sept 2017, Titled "Pair Distribution Function Analysis of Synthesised Fluorapatite Implant Coatings for use in Regenerative Dentistry" –accepted for Poster presentation. Location: Thessaloniki–Greece.
- Bioceramics 29, 25-27, Oct 2017, Titled "Pair Distribution Function Analysis of Synthesised Fluorapatite/Francolite Implant Coatings for use in Regenerative Dentistry"–accepted for Poster presentation. Location: Toulouse–France.

Contents

Abstract ii

Acknowledgements iv

Contents v

1 Literature review 1
- 1.1 Relevance to the greater world . . . 1
  - 1.1.1 Key aims . . . 1
  - 1.1.2 The stability dip and implant success . . . 1
  - 1.1.3 Contemporary solutions to secondary stability issue . . . 2
  - 1.1.4 Plasma spraying, the most commonly used industrial method . . . 3
  - 1.1.5 Interactions at the implant surface . . . 5
  - 1.1.6 The effect of nano structured materials on osteoblast-like cells . . . 8
  - 1.1.7 The effect of surface roughness on nucleation . . . 12
  - 1.1.8 Thesis Outline . . . 13

2 Calcium Phosphates - Structure, Phase transitions, and Morphology 15
- 2.1 Key aims . . . 15
- 2.2 Structure of calcium phosphates . . . 15
  - 2.2.1 Amorphous calcium phosphate a precursor phase . . . 15
  - 2.2.2 Apatites . . . 16
  - 2.2.3 The molecular structure of hydroxyapatite . . . 18
- 2.3 Phase transitions . . . 22
  - 2.3.1 Phase changes and pH . . . 24
  - 2.3.2 Transformation reactions to ACP in the presence of an aqueous phase . . . 24
  - 2.3.3 Kinetics of conversion of ACP to HAp . . . 26
- 2.4 Morphology . . . 27
- 2.5 Summary . . . 27

3 Methods - X-rays, Crystallography and Molecular Dynamics 29
- 3.1 Key aims . . . 29
- 3.2 Properties, production, detection and application of X-rays. . . . 29
  - 3.2.1 Electromagnetic radiation . . . 30
  - 3.2.2 The continuous spectrum . . . 30
  - 3.2.3 The characteristic spectrum . . . 32

3.2.4 Absorption . . . 34
3.2.5 Filters . . . 35
3.3 X-ray scattering and crystal structure . . . 36
3.3.1 Crystal's geometry and X-ray diffraction . . . 37
3.3.2 Lattices, unit cell, and atomic coordinates . . . 38
3.3.3 Bragg's law . . . 40
3.4 The diffraction experiment . . . 41
3.4.1 Key components . . . 44
3.4.1.1 Collimator . . . 44
3.4.2 Samples and containment . . . 44
3.4.3 Xray detectors . . . 45
3.4.4 Diffractometer resolution . . . 45
3.5 Rietveld Refinement . . . 46
3.5.1 Improving the goodness of fit for powder diffraction . . . 46
3.5.2 Least squares refinement . . . 48
3.5.3 Increasing the number of terms for fitting background . . . 49
3.5.4 Peak profile position, width and height . . . 49
3.5.5 Particle size broadening . . . 51
3.5.6 Sample displacement and transparency . . . 53
3.5.7 Asymmetric peak shape . . . 53
3.5.8 Lorentzian and Gaussian peak profiles . . . 53
3.5.8.1 Fourier transform and crystalline broadening . . . 53
3.5.8.2 Pseudo-Voigt profile . . . 54
3.5.9 Substitutions . . . 55
3.5.10 Preferred Crystallographic Orientation . . . 55
3.6 Distribution functions . . . 56
3.6.1 A history of atomic distribution functions and simulations . . . 56
3.6.2 Pair distribution function, pair correlation function, and higher correlation functions . . . 61
3.6.3 Radiation diffraction theory . . . 64
3.6.4 Normalisations . . . 66
3.7 Molecular dynamics . . . 66
3.7.1 Integration algorithms . . . 68
3.7.2 The molecular dynamics method . . . 69
3.7.3 Thermodynamic ensembles . . . 69
3.7.3.1 Microcanonical (NVE) ensemble . . . 69
3.7.3.2 Constant pressure (NPH) or constant stress (NSH) ensembles . . . 69
3.7.3.3 Constant temperature (NVT or NPT) ensemble . . . 70
3.7.4 Rigid bodies . . . 70
3.7.5 Ewald sum . . . 71

4 The Effect of Surface Roughness on the Formation of Bioactive Apatite Dental Implant Coatings 72
4.1 Key aims . . . 72
4.2 Introduction . . . 72
4.3 Materials and Methods . . . 74

4.3.1 Surface roughness analysis . . . 74
4.3.2 Preparation-substrates . . . 75
4.3.3 Mineralising solutions . . . 75
4.3.4 Powder collection - for structural and chemical characterisation . . . 76
4.3.5 Incubation–apatite coating synthesis method . . . 76
4.3.6 Spectroscopic and microscopic analysis . . . 77
4.3.7 Diffractometry . . . 78
4.3.8 Analysis and identification of morphologies . . . 78
4.3.9 Nuclear Magnetic Resonance . . . 78
4.3.10 Profilometry . . . 79
4.4 Results and Discussion . . . 79
4.4.1 Surface roughness . . . 79
4.4.2 Primary results - Surface morphologies . . . 80
4.4.3 Morphologies . . . 83
4.4.4 Powder analysis . . . 87
4.4.4.1 Derived from unbuffered solution . . . 87
4.4.4.2 Results derived from buffered solutions . . . 91
4.4.5 Pre-coated samples . . . 96
4.5 Discussion . . . 99
4.5.1 The effect of surface roughness on nucleation . . . 99
4.5.1.1 Flow conditions and temperature difference . . . 99
4.5.1.2 Particle size and surface topology . . . 100
4.5.1.3 Phase transitions and hydrothermal synthesis . . . 100
4.5.2 Competing equilibrium in buffered and non buffered systems . . . 101
4.5.3 nano-rod-slabs . . . 102
4.5.4 Morphology . . . 102
4.5.5 Compositional analysis . . . 103
4.5.6 Possible implications in other areas of study . . . 104
4.6 Summary . . . 105
4.6.1 Main findings . . . 106

5 Optimisation of Nano-engineered Apatite Implant coatings via Sequential Temporal Synthesis 108
5.1 Key aims . . . 108
5.2 Introduction . . . 108
5.3 Materials and Methods . . . 110
5.3.1 Incubation and crystal nucleation . . . 110
5.3.2 Spectroscopic analysis . . . 111
5.3.3 Powder X-ray diffraction and solid state NMR characterisation . . . 112
5.3.4 Surface coverage analysis . . . 112
5.3.4.1 Mineralisation coverage analysis . . . 112
5.4 Results . . . 113
5.4.0.1 Effect of temperature and substrate on aligned FAp growth 113
5.4.0.2 FAp formation as a function of time . . . 114
5.4.1 Synthesis pathway for samples produced at 21 °C . . . 122
5.5 Discussion . . . 130
5.5.1 Morphological analysis . . . 130

5.5.2 Compositional analysis . . . 132
5.5.3 Energy Dispersive X-ray Spectroscopy . . . 134
5.5.4 Cross-sectional analysis . . . 134
5.5.5 Fourier-Transform Infrared Spectroscopy . . . 135
5.5.6 Nuclear Magnetic Resonance Spectroscopy . . . 136
5.6 Summary . . . 137
5.6.1 Differences in synthesis model . . . 137
5.6.2 Main findings . . . 137

6 Pair Distribution Function Analysis of Synthesised Ordered Fluorapatite for Dental Application 140
6.1 Key aims . . . 140
6.2 introduction . . . 140
6.3 Experimental . . . 143
6.3.1 Cu-source powder X-ray diffraction . . . 143
6.3.1.1 Ag-source powder X-ray diffraction analysis . . . 143
6.3.2 Generation of Pair Distribution Function for seven day trials . . . 144
6.3.3 Synthesis of Amorphous Calcium Phosphate . . . 145
6.3.4 The potential model . . . 146
6.4 Results and Discussion . . . 148
6.4.1 Short range order analysis . . . 148
6.4.2 GULP models used to compare against PDF . . . 152
6.4.2.1 Analysis of Phase Transitions at Early Time Points . . . 156
6.4.3 Molecular dynamics model experimentation and development . . . 158
6.5 Summary . . . 162
6.5.1 Main findings . . . 162

7 Conclusions, Future work, applications and development of the field 164

8 Appendix 168
.1 Fitting . . . 168
.2 NRM deconvolution . . . 169
.2.1 Unbuffered NMR samples . . . 169
.2.2 Buffered NMR samples . . . 171
.2.3 NMR deconvolution 21°C . . . 173
.2.4 NMR deconvolution 70°C . . . 176
.2.5 NMR deconvolution 70°C between day 6 and 7 . . . 179
.3 Rietveld Refinement of cu-source data . . . 181
.3.1 Rietveld Refinement of unbuffered . . . 181
.3.2 Rietveld Refinement of buffered . . . 184
.3.3 XRD GSAS fitting 21°C . . . 187
.3.4 XRD GSAS fitting 70°C . . . 190

Bibliography 193

List of Figures **193**

List of Tables **202**

Chapter 1

Literature review

1.1 Relevance to the greater world

1.1.1 Key aims

To understand the problems to be solved (the stability dip), the top solutions used to address these problems and their short coming, and then to review the new solutions that are being developed on nano structured materials.

1.1.2 The stability dip and implant success

The use of implants to repair and replace damaged hard tissues is a growing field of research. Even though implants have a very high success rate, implant failures do still happen. In fact, most dental implant failures will occur within the first 2–4 weeks after implantation [1]. This is due to what is referred to as the "stability dip", which is the result of the decreasing primary (mechanical) stability and the increasing secondary (biological) stability with an increase in time [2]. In other words, a delay in the healing process is marked by the decreases in the total stability [1] of the implant during this 2–4 week period. Primary stability is an essential factor, since implant failure can occur due to the formation of a fibrous capsule around the implant [3, 4], which can result from the movement of the implant itself. Furthermore, secondary stability includes the formation of new woven and lamellar bone onto the implant surface, a process that can be prevented if there is too much micro-motion [5]. The secondary stability, being the result of the natural healing process, is subject to numerous variables. The speed

[1] Total stability is the combination of both the mechanical and biological stability. The transition between which is the point in the healing-phase where most implant failures occur

at which the osseointegration process occurs, the abundance and proliferation of bone forming cells that occur at the implant surface, the level of adhesion are among the most significant factors that contribute to the rate at which the secondary stability progresses. However, neither of these factors are under the direct control of the clinician.

1.1.3 Contemporary solutions to secondary stability issue

A number of methods have been employed to combat the issues related to secondary stability. Included are both subtractive and additive surface modification methods. Among the subtractive methods are grit-blasting [6–8], acid-etching [9–11], a combination of sand-blasting and acid etching [12–14] and machined surfaces[15, 16]. Whereas the additive method, such as plasma spraying [17] or precipitation, use the addition of materials to increase the surface roughness, but also to change the chemical interaction at the surface. These methods have been shown to increase osteoblastic differentiation[2], bone apposition[3] and osseointegration[4] within and around the implant [6, 18–20] with varying degrees of success.

The prevailing view point is that current implants experience a massive level success. An example of this is that dental implants made from grade 5 Ti-alloy with a machined surface have shown a survival rate of 96% over a 15 year period [21]. The tantalum based implants that mimic the micro structure of trabecular bone are able to achieve up to 80% bone ingrowth after 52 weeks [22, 23]. Sand-blasted and acid-etched surface implants that have also been coated with a hydroxylated layer have also been used. The hydroxylated layer provides its surface with hydrophilic qualities. Both the increased surface area and this hydrophilic property have been shown to enhances blood protein adsorption and fibrin network formation, which in turn, leads to faster secondary stability [24]. Other uncoated Ti implants show a high success rate of 97% [22, 23]. The former is a Ti implant that relies on a threaded pitch the permits the implant to be inserted four times faster than its contemporary. The later, uses a negatively charged Ti surface which attracts blood proteins and inactive platelets immediately after implantation.

As can be expected, these methods each have their own drawbacks. Machined surfaces have low resistance to removal torque and a reduced success in areas of low bone density. Osteoblastic cells (bone-forming cells) grow along the groves, which require a longer waiting time approximately 3–6 months of healing time as outlined by Branemark [25]. Sand-blasted and acid etched titanium (Ti) implants have a reduced fatigue

[2]The process whereby a relatively unspecialised cell acquires the specialised features of an osteoblast, a mesodermal or neural crest cell that gives rise to bone.

[3]This is growth of a cell wall by the deposition of new particles in layers on the wall

[4]This is the direct structural and functional connection between living bone and the surface of a load-bearing artificial implant

resistance. Owed to the fact that the process creates micro cracks, which act as focal points for load [11, 26]. Implants made chiefly of Ti are vulnerable to weak interfaces, caused by interfacial lines between the implant and the bone, and Ti ion release which can lead to a "host tissue response", whereby both of these cases can lead to implant rejection. Rough surfaces, obtained by Ti Plasma Spraying (TPS), explained in more detail shortly, and grit-blasted/acid-etched have shown torque-to-failure values significantly higher than implants with machined profiles [27, 28]. Moreover, TiO_2 layers have there own drawbacks. In the presence of an aqueous phase (e.g. blood) TiO_2 becomes thermodynamically unstable. This leads to the degradation of this protective layer and ultimately leads to the reduction in biocompatibility of the implant [29]. In the case of Ti-alloys, an acidic O_2 environment prevents the reformation of the oxide layer, leaving Ti-alloy based implants susceptible to galvanic behaviour and crevice corrosion [30]. Evidence suggested that the bone implant interface itself is weak [31]. Ti ions have been detected in the fibrous membranes encapsulating the implants, as well as in the synovial fluid, and in other studies this has been shown to cause aseptic loosening of orthopaedic implants [32]. both of these are indications that ion release in Ti implants may play a role in peri-implantitis.

Thus, given the number of issues related to contempoary methods it has been the focus to chemically and structurally engineer these coatings at the nano-topological scale in order to influence the early osseointegration at the implant surface. However, in the case of the precipitation methods, there are much less studies from which their shortcomings can be assessed as this technique is relatively novel.

1.1.4 Plasma spraying, the most commonly used industrial method

The most commonly used technique within industry today is the plasma-sprayed method, see Fig. 1.1. it has a well established history, having been used as a surface coating for orthopeadic and dental implants since the mid-1980s [33]. The plasma spraying method requires that the material, either hydroxyapatite (HAp) or Ti, that is to be deposited onto the surface of the implant, is fed into a plasma flame and directed at the surface. In the case of hydroyxapatite plasma spraying (HPS) the speed of the gas is 343.20 ms^{-1}, and a temperature ranging from 6,000–10,000 °C [34]. Which produces coatings of 40–54 μm that form on the surface [17]. In recent years, animal trial studies have shown greater advantage and affectiveness when using coated samples. Using rabbit femoral condyles [5], it has been demonstrated that the levels of osseointegration was greater on HA-coated samples than uncoated samples. Furthermore, bone maturation was more significant at the bone-implant interface [35].

[5] the rounded protuberance at the end of some bones, forming an articulation with another bone

In the case of the Ti plasma spraying method, the process is kept under vacuum conditions, at 0.1 Pa. After the Ti is injected into the torch, and the particles are projected onto the surface of the implant, they condense and fuse together [16] leaving behind a porous surface. It is these porous surfaces that have been shown to provide the most effective and fastest osseointegration on TPS surfaces that have a roughness of 50 to 400 μm, and the 3-dimensional (3D) topography increases the tensile strength at the bone-implant interface. One advantage the TPS has over HPS is that increasing the duration of plasma spraying, increases the coating thickness [36], in this way the desired effects are more controllable.

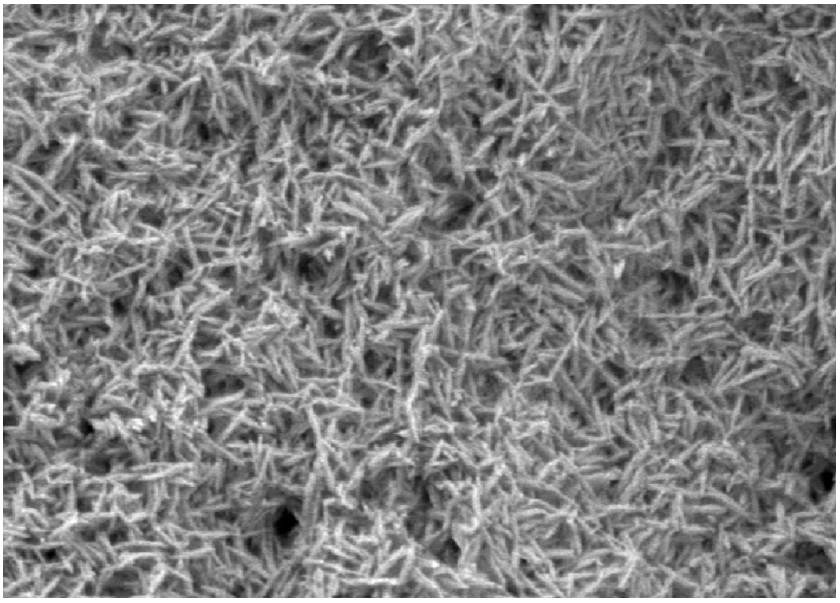

FIGURE 1.1: SEM image of plasma sprayed coatings. Showing rodlike apatite crystallites with a misaligned (or disordered micro-scale) orientation, taken from [37]

Just as with other methods, plasma spraying has many limitations. HAp coatings of low crystallinity dissolve faster in vivo [38], thus HPS coatings need to be relatively thick, which can lead to fractures within the coating or delamination from the substrate [39]. Plasma spraying cannot cover the entire porous surface because of the line of-sight nature of the process. Additionally, some implants are engineered to have a porous structure, a structure that permits bone ingrowth. However, "over-coating" using the plasma-spraying technique can block these pores [40]. Phases, both amorphous and non-bioactive Calcium Phosphate (CaP) phases [41] are also generated, possibly due to dehydroxylation of the HAp during the plasma spray process [42]. The high temperature, 6,000–10,000 °C, required for this process is not only expensive but also causes HAp to decompose [34]. Notably, natural bone is composed of crystalline HAp, thus the presence of amorphous phase HAp compromises the integrity of the bone-implant interface [43].

Amorphous phases also cause strong resorption, leading to mechanical and adhesive instability in the coating [44]. Mechanical tests show that failure of the bone-coating-implant interface consistently occurred within the bone for amorphous and poorly crystallised HAp coatings as a result of bioresorption [45]. However, in 1994 de Bruijin observed that bone seemed to be present on plasma-sprayed coatings with amorphous HAp as opposed to surfaces with highly crystalline HAp. Which would lead to the contrasting view that amorphous HAp coatings seem to be beneficial over highly crystalline coatings [46]. However, there is still not enough independently supportive evidence for these claims.

The development of a new method that is able to maintain the structural stability of the bone-implant interfact while at the same time being able to gain a greater control over the structure of the end product, and thus by extension, the host tissue responce.

1.1.5 Interactions at the implant surface

Over the last 30 years, Ti based implants have had a fair level of success when used as a dental or orthopaedic implant. This can be attributed to a number of reasons, including the innate quality of Ti to bond with Ca, and the effects of its oxide layer. To place Ti in its proper context, we know that bone is composed of 63% calcium (Ca), which has been shown to have a high affinity to the TiO_2 layer and penetrates deep into the implant surface [47, 48]. Because of this Ti implants success has been attributed to these strong bonds that are formed when in contact with bone.

Fig. 1.2 shows the ability for Ca atoms to penetrate deep into the implant surface, in doing so they form strong bonds at the implant-bone interface. Furthermore, the naturally forming TiO_2 layer both serves to prevent ion release [49, 50] and expresses antibacterial properties in the in vivo environment [51, 52]. Because of these factors and the high success-rate, osseointegrative implants are used worldwide. Just for reference, in the United States alone 100,000–300,000 dental implants are placed annually [53–56].

Even though current implants experience a high survival rate of over 97% in most cases, there are still demographics that are not able to access this technology. For example, those experiencing poor bone quality, the elderly, smokers [57], those on medications such as glucocoriticoids; and those experiencing periodotitis [58], all fall into this category.

As we have previously said, HAp coatings can be used to further enhance the biological response of the implant after implantation. Surfaces coated with synthetic HAp have a chemistry that is closely related to their biological counterparts, found in human tissue [59]. The improved surface chemistry has been shown to influence the adsorption of

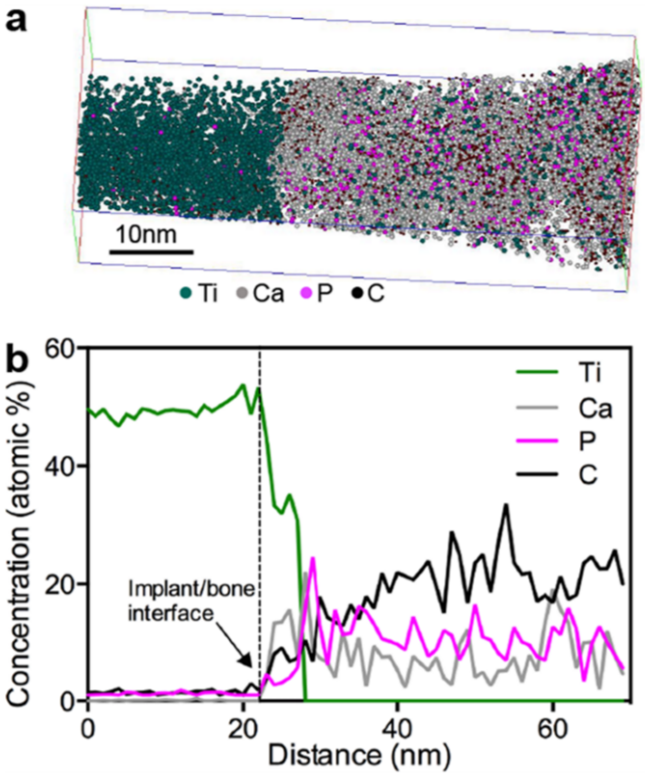

FIGURE 1.2: 3-dimensional reconstruction of the implant-tissue interface and 1D concentration profiles. (a) Atom probe microscopy image displaying the direct contact between Ca of the bone mineral and Ti of the coating surface. (b) 1D concentration profiles of Ti, Carbon (C), Calcium (Ca) and Phosphorus (P) from the coating and across the interface into the bone tissue, obtained from the reconstruction in (a), taken from [48].

non-collageneous proteins such as osteocalcin, osteonectin, silylated glycoproteins, and proteoglycans, which results in the eventual establishment of an osseoconductive union between the living tissue and the biomaterial. Finally, it has been shown that the accelerated bone formation during the initial stages of osseointegration result in an improved implant fixation following the healing process [60]. This could also be attributed to the CaP rich layer that is precipitated naturally on the implant in vivo through solid ion exchange [61]. D Buser and co workers showed that this CaP incorporated layer gradually develops into a biological equivalent of HAp that in turn will incorporate into the developing bone.

A quick search on google scholar will reveal that over the last 10 years, there has been a consistent increase in the number of articles that have a specific focus on apatite coatings, Fig. 1.3. This represents an increase of 140% from 2006 to 2016. Clearly we can see that not only is this an ever developing field, but also that this is a field of increasing interest within the academic arena.

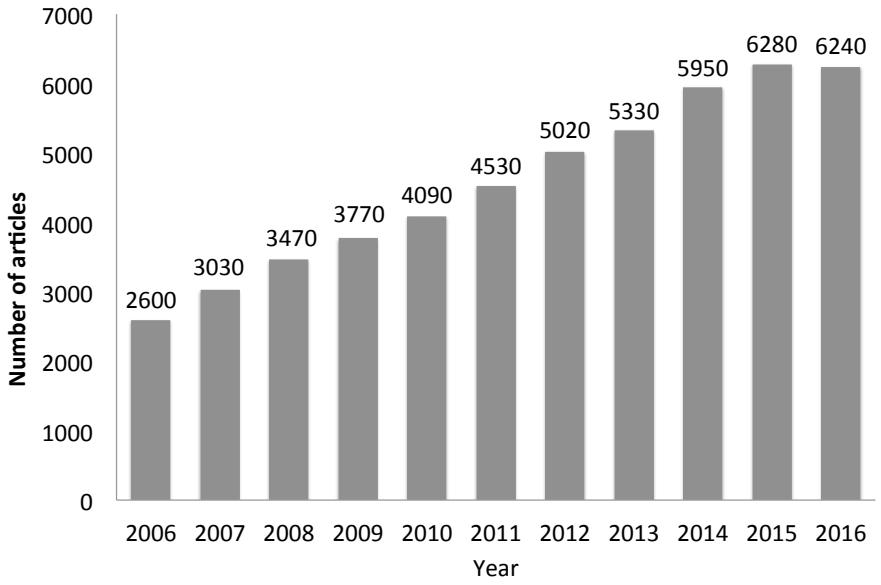

FIGURE 1.3: Increasing number of articles published on apatite coatings each year, for the last 10 years. Showing the increased interest and importance of that the scientific community have placed on this field.

Thus it can be seen that both non-coated, and HAp-coated Ti implants have many qualities that make them suitable candidates for implantation. However, there is evidence that even the TiO_2 layer has some drawbacks. Firstly, It has been shown that the interfacial tension between TiO_2 and aqueous phases (e.g. blood) is thermodynamically unstable. This effect can cause the degradation of the protective layer, which reduces the implants biocompatibility [62]. In the case of Ti-alloys, such as SS-Ti composites, acid/O_2 environments prevent the reformation of the oxide layer, leaving it susceptible to galvanic behaviour and crevice corrosion [63]. Depending on a person's diet, the intra oral environment may become more or less acidic, which can effect the success of the implant, and finally, Ti ions have also been detected in the fibrous membranes encapsulating implants, as well as in synovial fluid [64]. These particles are released from the orthopaedic implant and accumulate in tissues. This release is considered to cause aseptic loosening [6] of orthopaedic implants [65, 66].

These points highlight the fact that even with these successes, and the many years that this technology has been in use, that this technology is not without serious issues. An apatite-based coating with a more consistent deposition thickness could potentially prevent the loss of the TiO_2 layer and ultimately avoid the instance of ion release.

[6] Aseptic loosening is the failure of the bond between an implant and bone in the absence of infection

1.1.6 The effect of nano structured materials on osteoblast-like cells

Structures in the body are complex multi-levelled materials that contain macro, micro and nano-scale arrangements. Materials structured at the nano-scale have been shown to exhibit different properties than their macro-level counterparts. One example of this can be seen in a 2003, article where Kyung Mi Woo and co-workers [67] developed and studied the effects of nano fibrous scaffolds made from natural collagen. Scaffolds with nano fibrous pore walls showed four times more serum protein adhesion than those of solid collagen walls. Theses proteins mediate cell interactions, and selectively enhanced the protein adsorption of fibronectin and vitronectin, which lead to more than 1.7 times more osteoblastic cell attachment [68].

In another study, the proliferation[7] of bone forming cells on nano phase ceramics (of alumina, tintania, and HAp) where investigated. Even though less osteoblast colonies where observed after 4–6 days, there was significantly more osteoblast proliferation when compared to their non nano-structured forms between 3–5 days [67].

In 2003, Panjian and co-workers [41], coated titanium discs with apatite-coatings, which had composition and structure equivalent to that of bone mineral, as determined by Thin Film X-ray diffraction (TF-XRD), and Fourier Transform Infrared Spectroscopy (FTIR) analyses of the coatings after 3 days of incubation. They compared the level of bone ingrowth [8] within the trabecular bone [9] of a 14 year old patient Fig. 1.4 between Ti implants with and without nano-apatite coating. More osteoblast cells grew through the channels lined with nano-apatite surfaces Fig. 1.4(right) then in the channels lined with non-coated control Fig. 1.4(Left). These coatings were flake-like in morphology 100–200 nm long and 10–20 nm thick, as acertained by way of Transmission Electron Microscopy (TEM). Substantially more bone ingrowth was observed on implants coated with the nano apatite flakes than those without, after 8 weeks[69]. In another study, J. Liu found that aligned apatite surfaces with a width range of 25–100 nm, faired better than missaligned surfaces[70]. These rod-like crystals were aligned along the c-axis, similar to the typical structure found in dental enamel [71]. Structures like these have been used to yield promising results for cell growth.

Not only have researchers found that the use of nano-materials can elicit a biological response that is distinct from that of their macro-level versions[72], but they have also

[7] This is the process that results in an increase of the number of osteoblast cells , and is defined by the balance between cell divisions and cell loss through cell death or differentiation

[8] The term 'bone ingrowth' refers to bone formation within an irregular (beads, wire mesh, casting voids, cut grooves) surface of an implant

[9] Cancellous bone is made up of spongy, porous, bone tissue that is filled with red bone marrow. It is not as strong as cortical bone, which is found in the long bones, but it is very important for producing blood cells. It is found in the ends of long bones and in the bones of the pelvis, ribs, vertebrae, and skull.

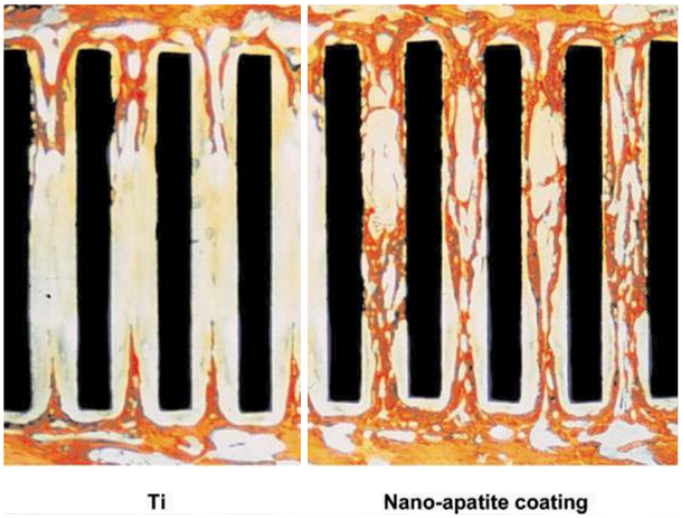

FIGURE 1.4: Histological examination of bone growth chamber implanted into the lateral metaphysis of the distal femur of dog for 8 weeks. Osteoblast cells (orange), Ti implant (black). Showing the improvement of bone ingrowth with the application of a nano-apatite coating. Taken from [41].

found that further difference can be found when these nano materials are structured differently from each other. We can consider the case where hydrothermally derived nano-apatite coatings were produced with two different structural orientations by J. Liu et all in 2011 [73], see Fig. 1.5.

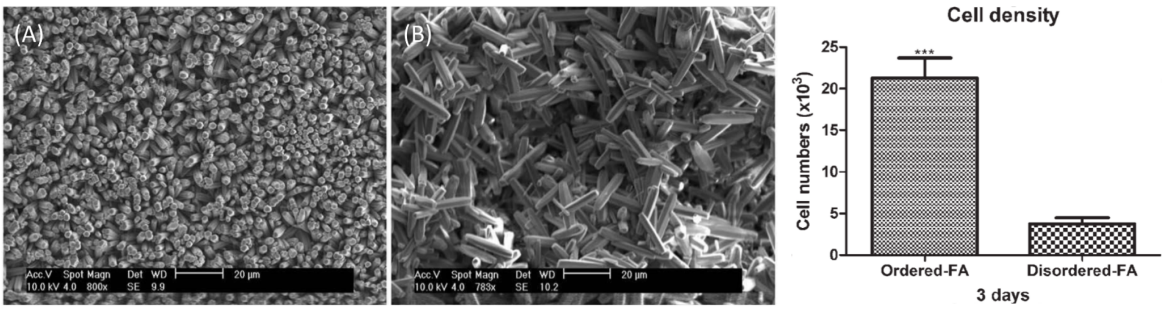

FIGURE 1.5: SEM of synthesised ordered (A) and disordered (B) FAp crystal surfaces. Cell density on ordered and disordered FAp surfaces (right). The attached cell numbers on the ordered FAp surfaces were significantly higher than that on the disordered surfaces (*** $p < 0.001$, see figure). Showing that the cell behaviour of the bone forming cells can be further enhanced by controlling the orientation of the crystals at the nano-scale. Taken from [73] In that paper ordered and disordered are the terms used in their research, but here we refer to this as aligned and misaligned to differentiate from crystalline structure.

They observed the effect of growing human Dental Pulp Stem Cells (DPSC) on these surfaces, and compared the difference between those cells that were grown on nano-rods aligned along their c-axis seen in Fig. 1.5(A), and misaligned nano-rods seen in Fig. 1.5

(B), which hold similar nano-structural qualities to that of coatings produced by the plasma spraying method, Fig. 1.1.

After 3 days of cell culture, Fig. 1.5 (right), it could be seen that the crystal orientation had a clear effect on the DCPD density, with a p-value <0.001. Where a $p<0.05$ signified the bench mark for statistical significance for this study.

It was also found that 20/84 focused pathway genes were either up or down regulated in cells cultured on aligned FAp. Cell adhesion molecules such as integrin alpha 7 and 8, integrin beta 3 and 4, and the vitronectin receptor-integrin alpha and key adhesion protein-fibronectin 1[10] were up-regulated[11] , [73]. In another study conducted in 2010, J. Lui and co-workers found that cells grown on etched stainless steel (SS) showed significantly higher numbers than on both ordered and disordered FAp surfaces after 3 days, Fig. 1.6 (light grey), they also found that FAp grown on etched SS and Ti surfaces had comparable crystal composition, alignment, size, shape, and structure. This is advantageous since SS is cheaper than Ti [74].

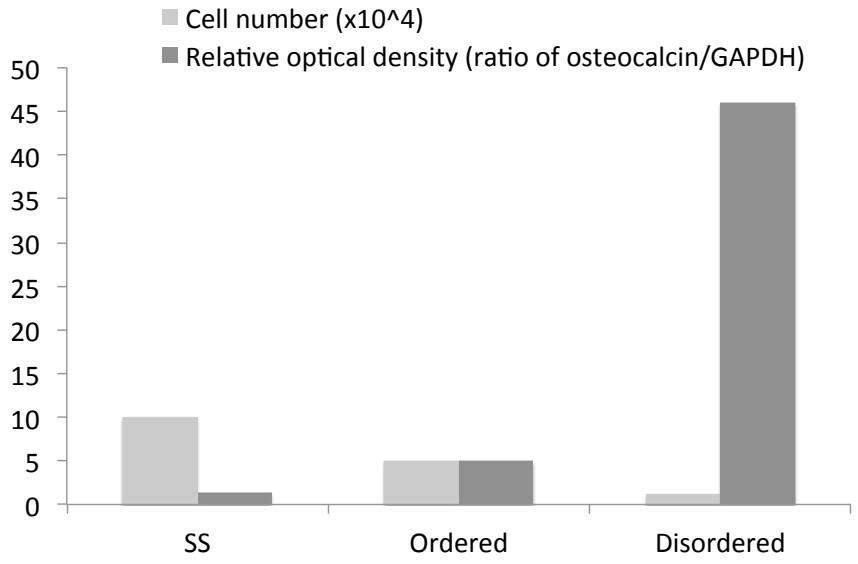

FIGURE 1.6: Cell density (light grey), on etched SS surfaces, and aligned and misaligned FAp surfaces. (SS and aligned, $p < 0.01$). Quantitative analysis of the optical band density of osteocalcin expression (dark grey), by the ratio of OCN/GAPDH using ImageJ program (NIH). Samples; stainless steel (SS), misaligned, aligned and control. Samples studied after 7 days of osseointegration for 7 weeks are accompanied by OI. Showing that Aligned nano-rods show a good trade off between the number of cells produced and the amount of osteocalcin produced when compared to non-coated and misaligned coatings. Adapted from [74].

[10]is a high-molecular weight (440kDa) glycoprotein of the extracellular matrix that binds to membrane-spanning receptor proteins called integrins and extracellular matrix components such as collagen, fibrin, and heparan sulfate proteoglycans

[11]the process which involves the increase of such components

Even though cell number/density were significantly greater on SS surfaces, it was also found that the initial adherence of a greater number of cells did not lead to earlier mineral formation at the cell-implant interface, Fig. 1.6 (dark grey). As a side note, we have more cell growth on SS than aligned, however we get less osteocalcin (OCN) expression after 7 days. The aligned structures have more cell growth than the misaligned, but the disordered have more OCN expression than misaligned. Let us remember that OCN is the non-collagenous protein that is secreted by osteoblasts during the bone forming process. Thus we can see that that the process of forming bone is more prevalent in misaligned surfaces, with aligned and non-coated surfaces following, in that order. In summary, it is the balance between high cell density and reasonable mineralisation is found within when using the aligned surfaces.[12]

That is to say that dental pulp stem cells (DPSC) that have grown on the surface have show three times more osteocalcin (OCN) expression when compared to uncoated surfaces, and 5 times greater cell density when compared to disordered surfaces [75]. Controversially, DPSC grown on uncoated stainless-steel surfaces were substantially greater than those grown on ordered surfaces, however, analysis of the focused pathway genes [13]. Showing that there was a reduction in OCN expression in these cells [74]. In other words, meaning that the level of bone forming activity was reduced by comparison. Thus the development of a biomimetic surface would be a trade off between high cell density and high OCN expression, and it is for this reason that aligned surfaces are chosen.

Even though the hydrothermal method has proven successful with regard to the level of cell growth and OCN expression, the high temperatures and pressures that are required for the implementation of this method makes it difficult to apply on an industrial scale. As can be seen by Fig. 1.7 we can see that even by 2013 [76] the hydrothermal method is only the third most popular area of research, preceded both by combination methods and the precipitation method, which stands as the prime area of research within the contemporary academic community.

So far, a precipitation method has not been developed that is able to match the aligned-apatite nano structure produced by the hydrothermal method. Furthermore, there is a lack of understanding of the fundamental physics that drive the mechanism behind such a synthesis route.

[12] Osteocalcin a noncollagenous protein hormone found in bone and dentin and is secreted solely by osteoblasts and thought to play a role in the body's metabolic regulation and is pro–osteoblastic, or bone-building, by nature.

[13] The expression of specific genes can be identified through the use of Polymerase Chain Reaction Arrays (PCR Arrays) and can also be customised to contain a panel of genes tailored to your specific research interests

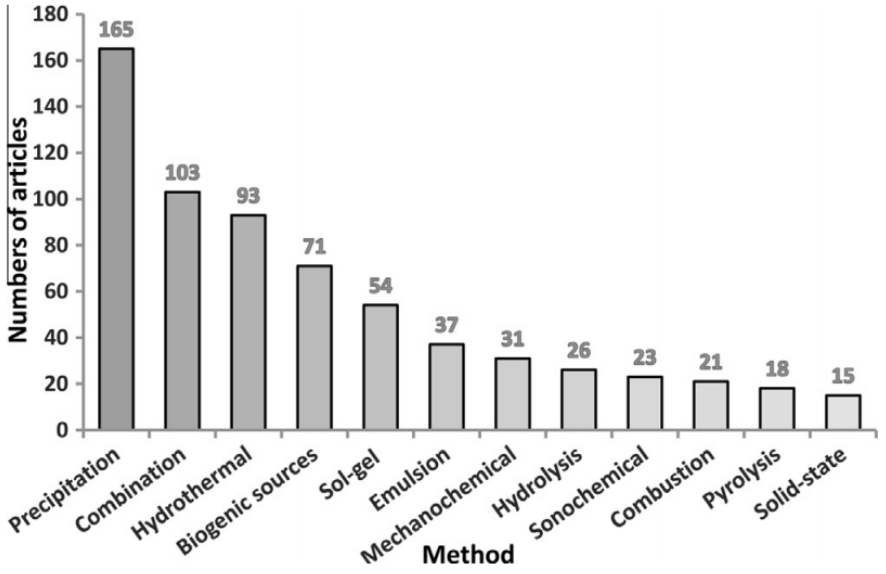

FIGURE 1.7: Articles released for different methods for apatite production. Out of all methods, the precipitation method is currently the most popular method for research. Typically owed to its low energy of production requirements when compared to its contemporaries. [76]

1.1.7 The effect of surface roughness on nucleation

In 2008, ZrO_2 nanofibers were used as a surface on which to grow Pt nanostructures [77]. When these ZrO_2 fibres had a smooth surface, both homogenious and hetrogenious nucleation was observed. This caused Pt nanofibres to be formed at the surface and free-standing Pt nanostars formed in solution. However, ZrO_2 nano fibres that had a rough surface caused hetrogenious nucleation to be favoured. This work demonstrated the significance of the surface roughness on the nucleation mechanism and the morphology of the resultant nano-structures.

In 2007 [78], C. Apricio et al were able to ascertain that not only was surface roughness was important but also surface chemistry. In an experiment in which titanium surfaces were first grit blasted, either by Al_2O_2 or SiC, and then thermodynamically treated, they found a marked difference in the nucleation. Surfaces that were grit blasted with Al_2O_2 saw an acceleration in the apatite formation, where as apatite formation was seen to be inhibited in that of SiC-grit blasted surface. This was considered to be caused by the increased concentration of Ca^{2+}-ions which was found in the concave part of the microfoughness that was created by the grit blasting method. They also started that the nucleation was aided by the lack of fluid mobility at these concave parts.

1.1.8 Thesis Outline

This thesis will be written for four demographics. As we have said, the most prominent method used commercially is Plasma Spraying, yet this method is riddled with problems. Furthermore, the most promising method used in the academic community, the hydrothermal method is too expensive for mass production. Thus, the first demographic will be that of the commercial world. Those who wish to learn about a new technique that can also be mass produced in a low energy manner with the potential of sharing the same bioactive properties that have been seen in the materials produced in the hydrothermal method. The second demographic consists of those who are not a part of the scientific field, here named the "un-initiated". In this case, this thesis has been written such that those who are not familiar with the most recent scientific advances and the background theory of the field can become better acquainted with the concepts contained here in. The academic field would define the third group in which we aim to speak to. For this band of merry men, focus will be given towards understanding the optimisation of the structure of the material at the nano scale and a deeper understanding of the energetics of the system that leads to the desired bioactive material. Finally, the fourth group this work is aimed at those members of my peer group. As this is an interdisciplinary project, there are many techniques that are not used by either discipline. That is to say that those techniques found in condensed matter physics, and those developed in dental materials science are often used independently of the other. This work focuses on how knowledge from both worlds can enhance the understanding of the other.

This thesis is split up into six chapters. **Chapter 1**, is composed of a literature review which introduced the over arching problem in the dental implantology field. Furthermore, explanation of key techniques that have been used commercially to address this issue and the current problems that it maintains. A brief overview of the advancements made by researchers was also included before discussing how an application of methods such as density functional theory, to better describe that changes between materials at the local level. **Chapter 2**, provides an overview of the background theory regarding the calcium phosphates. Here we show the transition pathway between phases, the defining differences between the structures and how the morphology can be a defining characteristic. Primarily, this chapter focuses on the chemistry that underpins this work. **Chapter 3**, focuses on the background theory of this work, which is based on the use of x-rays as an atomic probe for matter. A brief history of x-rays is given followed by Rietveld refinement and distribution function theory. Consequently, a brief example is given for how molecular dynamics methods have been used to develop apatite based

computer simulations and even that of the Posner's cluster, which is the accepted structure of amorphous calcium phosphate within the dental materials community. **Chapter 4**, focuses on how the surface roughness, solution chemistry, incubation temperature and material chemistry affects the formation of the nano-crystals that are formed. Here we find how the composition and morphology of the material changes based on the factors previously said. The main aim of this chapter was to see which specific temperature, surface and solution chemistry would lead us toward the development of a precipitated surface with similar material properties as those found in hydrothermal synthesis. After which, we could explore the science behind this in later chapters. **Chapter 5** explores the formation of aligned nano-rod crystals that have formed at 21 °C and 70 °C. The aim is to better understand the difference between the formation of the two, and to select one of these for further analysis. This section outlines the formation of coatings at both of these temperatures over a seven day trial. In this case, reading were taken every 24 hours. Analysis of the morphological changed along with the structural and compositional differences observed between days and also when comparing between the two temperatures. This section reveals that 70 °C showed greater promise than 21 °C for the formation of coatings that most closely resembled those that have the desired bioactive properties. **Chapter 6**, applies the use of the Pair Distribution Function method to analyses x-ray scattering data derived from the synthesised nano-material. Both methods, Ag-source x-ray analysis and synchrotron source x-ray analyses, such as Diamond, both revealed that there appears to be a continual reforming of the atoms at the nano scale throughout the seven days of incubation. This data was then compared to that of simulated apatite and amorphous calcium phosphate showed that the pair distribution function data for the simulated structures was entirely consistent with that of the experimentally derived nano-materials synthesised at 70 °C. Finally, **Chapter 7** outlines the future work that can be derived from this research base either directly on the main focus of the research 21°C and 70 °C samples in this work. Further to this, it will outline how this work has contributed to the field both academically and to the wider industrial work.

Chapter 2

Calcium Phosphates - Structure, Phase transitions, and Morphology

2.1 Key aims

To provide an understanding of the chemical theory that under pin the phase transition and system kinetics involved in the formation of these nano structured crystals.

2.2 Structure of calcium phosphates

Calcium phosphates occur as minerals, the most important of these being the apatites. Apatites for the mineral component of bones and teeth and as such have increasingly been used for biocompatible materials for bone replacement or for the coating of bone prosthesis. They all form white solids (unless doped with a coloured ion). Most are sparingly soluble in water, some are very insoluble, but all dissolve in acids. Each of the calcium phosphates have a defining space group and a unit cell, together with their composition. These factors help to distinguish the different crystal phases that can be formed.

2.2.1 Amorphous calcium phosphate a precursor phase

Electron microscopy of amorphous calcium phosphate (ACP) usually shows spherical particles with diameters in the range 200 – 1200 Å without structure, provided the

electron beam current is kept as low as practicable [79] The particles are small if they are prepared under conditions of high supersaturation and or pH. For a given pH, higher temperatures give larger particles [80]. It is possible that ACP has an apatite structure, but with a crystal size so small that it appears to be amorphous.

Amorphous phases are more soluble than their crystalline counterparts at equilibrium. ACP are made up of a random networks of bonds. Because its structure is fundamentally different from their crystalline counterparts (which are periodic in nature) they must enter phase transitions through dissolution. The process is therefore diffusion or surface-reaction controlled.

At neutral pH it has been observed in biological systems that transformation are achieved through stages. This starts with the aggregation of large numbers of A-CaP. Following this, a crystalline mass grows outward from the interior of the dissolving precursor. This mass slowly transforms into a calcium phosphate crystal phase known as Octacalcium Phosphate (OCP) and HAp (which are more stable minerals). One key problem with the study of amorphous phases is that it occur intermittently, and even if present in mature structures are readily dissolved during sample preparation [81].

2.2.2 Apatites

Apatites have the chemical focmula $Ca_{10}(PO_4)_6(X)_2$, where X can be F, OH, or Cl. Notably, X could also be a mixed state such as in the case of fluoro-hydroxyapatite or carbon in the form of C_3 The apatite structure is very tolerant of ionic substitutions, that is to say that Ca^{2+} ions can be partly or completely replaced by ions such as Ba^{2+}, Sr^{2+} , or Pb^{2+} ions, and PO_4^{3-} ions can be replaces be AsO_4^{3-} ions. However, none of which exist within my system. In general, apatites have a space group of $P6_3/m$, meaning that it has a 6-fold c-axis is perpendicular to a 3 a-axis at 120° to one another.

The $P6_3/m$ space group has three kinds of vertical symmetry elements, see Fig. 2.1, (1) six-fold axes passing through the corners of the unit cells marked by dashed lines in the figure. These symmetry elements are equivalent to a three-fold rotation axis with a superimposed two-fold screw axis; (2) 3-fold rotation axes passing through 2/3, 1/3, 0 and 1/3, 2/3, 0; and (3) two-fold screw axes passing through the midpoints of the cell edges and its centre. There are also mirror planes perpendicular to the c-axis at $z = 1/4$ and 3/4, and numerous centres of symmetry [82, 83], they form a hexagonal unit cell, which will be discussed shortly.

Coupled substitutions frequently occur in apatites. In these, one ion is replaced by another of the same sign, but different charge, and neutrality is maintained by substitutions

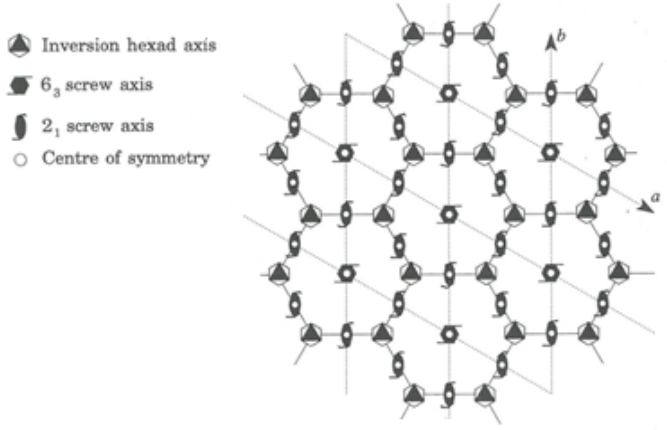

FIGURE 2.1: Vertical symmetry elements of the space group $P6_3/m$. The dashed lines indicate the apatite unit cells with the c-axis out of the plane of the diagram. There are also horizontal mirror planes at $z = \frac{1}{3}$ and $\frac{3}{4}$, and numerous centres of symmetry. [84]

of ions with dissimilar charged or vacancies elsewhere. The chemical variability that apatite posses is the feature of this material that can be exploited and tailored for various applications [85]. Apatite is considered the most thermodynamically stable phosphate phase and its calcium/phosphate (Ca/P) ratio is 1.67, when stoichiometric [86]. HAp has a "right hexagonal" prism unit cell of 18 ions, $Ca_{10}(PO_4)_6OH_2$ in composition. It has a space group of $P6_3/m$ with lattice parameters of $a = b = 9.432$ Å, $c = 6.881$ Å, $\alpha = \beta = 90°$, and $\gamma = 120°$. Even though apatite forms the mineral component of teeth (95–97 w%) [87] and bones (69 wt%), this apatite is not found in its stoichiometric form. In fact, apatite is found in the form of non-stoichiometric sodium-, magnesium- and most commonly carbonate-containing apatite. Typically, what is referred to as biological apatite refers to an apatite with carbonate substitutions.

Carbonated apatites, $Ca_{10-x}H_x(PO_4,CO_3)(OH)_{2-x}$, are typically, plate shaped, and thus have a high surface/volume ratio and forms sizes under the micron scale (see section on substitutions). The characteristic small size of Carbonated apatite CO_3-Ap crystallites is another reason why they are more soluble than chemically pure HAp [88, 89]. To further add to the difference between the apatite found in dental enamel and that of stoichiometric apatite, Synchrotron X-ray diffraction (S-XRD) studies in 1999 showed that powdered dental enamel had difference lattice parameters to its stoichiometric counterpart. In this case the lattice parameters for CO_3-Ap were found to be $a = b = 9.417 \pm 0.006$ Å, $c = 6.904 \pm 0.001$ Å [90], and in a more recent study conducted in 2012 these parameters were found to be $a = b = 9.473 \pm 0.009$ Å, $c = 6.881 \pm 0.004$ Å [91], showing a good level of consistency.

Synthetic 'organic' Hydroxyapatite, s-OHAp, is monoclinic with a space group of $P2_1/b$

[92] with lattice parameters $a = 9.4213 \pm 0.0008$, $b = 2a$, $c = 6.8814 \pm 0.0007$ Å, $\gamma = 120°$ [93]. When hydrothermally grown, OHAp has the typically expected space group of $P6_3/m$ with the hydroxyl oxygen atom at $z = 1/4$ [94]. FAp is also hexagonal with space group $P6_3/m$ and lattice parameters $a = 9.367 \pm 0.001$ and $c = 6.884 \pm 0.001$ Å [95] with one formula unit of per unit cell.

2.2.3 The molecular structure of hydroxyapatite

The molecular structure of apatite, determined in 1964 by Kay, Young and Posner [96]. Normally, the structure is considered by the arrangement of ions around the central column of hydroxyl ions, which extend along the c-axis of the crystal, Fig. 2.2. In the plane of the page, a single hydroxyl group would be surrounded by an equilateral triangle of calcium ions Ca(2). This is, in turn surrounded by a triangle of phosphate ions rotated by 60°. Finally, these triangles are enclosed by a hexagon of calcium ions Ca(1) [96]. Notably, the calcium's of the outer hexagon are shared between three adjacent similar hexagons, that is to say, that the crystal structure comprises of many such repeating hexagonal units.

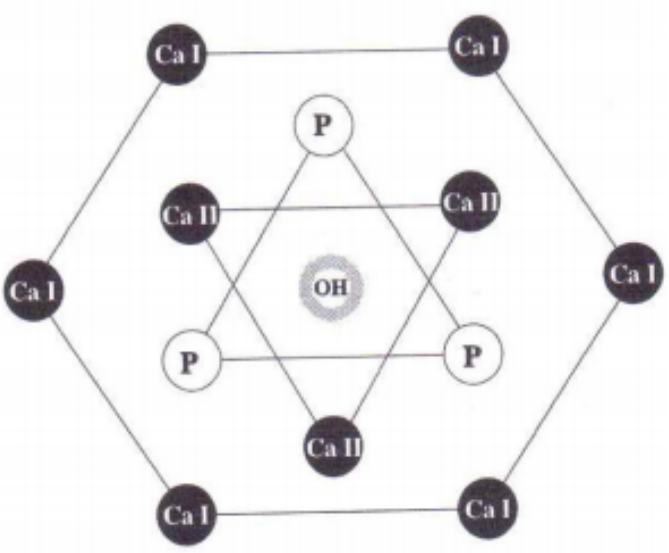

FIGURE 2.2: Depicting a view looking down the hydroxyl column of calcium hydroxyapatite. Here we see the arrangement of the Ca I, Ca II, the P atoms and the OH group which could be substituted by F, or Cl. [87].

In this way, we can visualise the entire crystals as a series of these hexagonal plates. Each stacked on top of each other, but each turned by 60°. Clearly, this means that the hydroxyls at the centre form a column at the centre of this structure as can be seen by Fig. 2.3. As previously mentioned, these hydroxyl ions are parallel to the direction of

the c-axis of the crystal. Fig. 2.3, also shows the relationship between the unit cell (a hexagonal unit cell, where $\alpha = \beta = 90°$, and $\gamma = 120°$), which is shown by the use of a parallelepiped. Furthermore, the stoichiometry, $Ca_{10}(PO_4)_6OH_2$ is made up of, four columnar calcium (Ca(2)), six screw axis calcium (Ca(1)), and six phosphates that are located around the hydroxyls. In practice many of the ions are shared with neighbouring cells to provide an average stoichiometry [87]

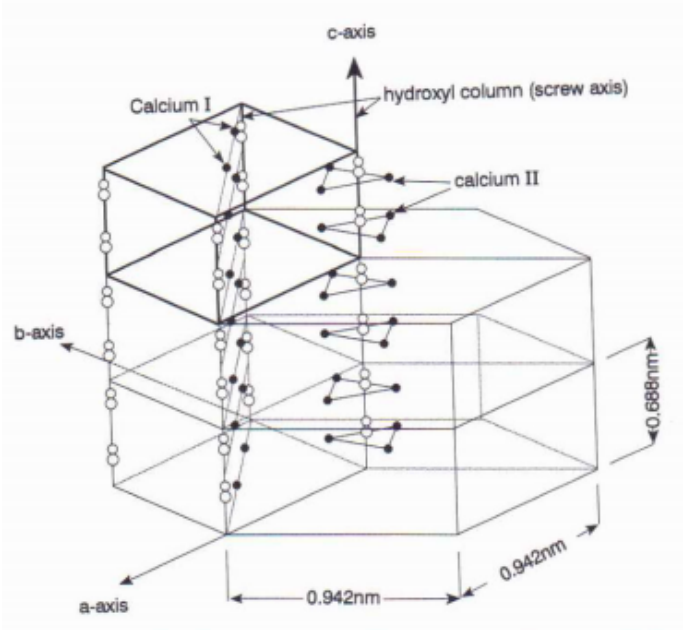

FIGURE 2.3: Diagram of the arrangement of calcium and hydroxyl ions in calcium hydroxyapatite. This schematic shows the relationship between the hexagonal cell described (in previous figure) and the hexagonal crystallographic unit cell, which is shown in heavier lines The hydroxyl column, calcium II triangles a, b, and c-axis directions are shown [87, 97].

Monocalcium phosphate monohydrate, MCPM, has a triclinic space group $P\bar{1}$ and unit cell $a = 5.6261 \pm 0.0005)$, $b = 11.889 \pm 0.002$, $c = 6.4731 \pm 0.0008$ Å, $\alpha = 98.633(6)$, $\beta = 118.262 \pm 0.006$ and $\gamma = 83.344 \pm 0.006°$ at 25°C with two formula units per unit cell [98] and structural determination has revealed the presence of ...$Ca(H_2PO_4)^+Ca(H_2PO_4)^+Ca(H_2PO_4)^+$... chains parallel to the c-axis that formed corrugated sheets in the (010) plane [98, 99]. These are similar to the sheets originally seen in DCPD formed by ...$CaHPO_4CaHPO_4CaHPO_4$... columns. Furthermore, layers of $H_2PO_4^-$ ions and water molecules lie between the sheets of chains [98].

Monocalcium phosphate anhydrous, MCPA has a space group $P\bar{1}$ and the unit cell parameters are $a = 7.5577 \pm 0.0005$, $b = 8.2531 \pm 0.0006$, $c = 5.5504 \pm 0.0003$ Å, $\alpha = 109.87 \pm 0.01$, $\beta = 93.68 \pm 0.01$ and $\gamma = 109.15 \pm 0.01°$ at 25 °C with two formula units per unit cell [100] has hydrogen bonded PO_4 groups in layers parallel to (010) and are joined together by hydrogen bonds on one side, and Ca^{2+} ions on the other

side. $H_2PO_4^-$ ions are held together into infinite chains by very strong, centred O–H–O hydrogen bonds.

Diacalcium phosphate dihydrate (also known as "Brushite"), DCPD, is monoclinic, space group Ia [101] with lattice parameters $a = 5.812 \pm 0.002$, $b = 15.180 \pm 0.003$, $c = 6.239 \pm 0.002$ Å and $\beta = 116°$ [102]. There are four formula units per unit cell with an asymmetric unit $CaHPO_4.2H_2O$, so that none of the five hydrogen atoms are related by symmetry. No evidence for disorder in the hydrogen atom positions and the acidic hydrogen atom was bond to an oxygen atom with a conspicuously long P–O bond (1.608 ± 0.006) compared with 1.506 ± 0.005 to 1.532 ± 0.005 Å for the other P–O bonds). The structure contains columns, parallel to the short diagonal of the (010) face of the unit cell, of alternating Ca^{2+} and HPO_4^{2-} ions. These columns are joined together to form corrugated sheets. The sheets have a composition of $CaHPO_4$, are normal to the b-axis, and are linked together by water molecules. Similar sheets are found in MCPM, $Ca(H_2PO_4)_2.H_2O$). In terms of the kinetics and crystal growth of DCPD, the growth is proportional to the concentration product $\left[Ca^{2+}\right]\left[HPO_4^{2-}\right]$ over a wide range of Ca/P ratios. This suggests a predominantly surface reaction controlled process. The rate is also proportional to the amount to be precipitated before equilibrium is reached.

The constant composition is a method used to study the crystallisation process at a constant super saturation. This is done by the use of a controlled addition of titrants to a crystalliser which maintains the pH. Constant composition studies have shown that crystal growth is pH dependent and is predominantly in two-dimensions. Constant composition kinetics have been used to show that, on DCPD seeds, lower pH and higher temperatures favour the growth of DCPD rather than OCP in the 60 to 80 °C range; at 70 °C the reaction order was two, but in contrast, at 80 °C, where the rate of DCPD growth was higher, it was four. DCPD grows on HAp seeds after an induction period with the same kinetics as determined earlier for the growth of pure DCPD. However in the systems in which CaPs are precipitated on HAp seeds;

1. The presence of F^- ions increase the quantity of the apatite phase.
2. Ethylidinediphosphonic acid encourages the formation of DCPD and crystal growth on sites already present on HAp seeds,
3. and finally, DCPD nucleates and grows on OCP seeds after a well-define induction periods at higher super-saturations.

The room temperature form of Diacalcium phosphate anhydrous (a.k.a. Monetite), DCPA, has a triclinic space group [103, 104] with lattice parameters $a = 6.910 \pm 0.001$, $b = 6.627 \pm 0.002$, $c = 6.998 \pm 0.002$ Å, $\alpha = 96.34 \pm 0.02$, $\beta = 103.82 \pm 0.02$ and

$\gamma = 88.34 \pm 0.03°$ [104]. There are four units per unit cell of DCPA. Double chains of ...$CaPO_4$ $CaPO_4$ $CaPO_4$..., extending along the a-axis, and are linked together in b-axis direction by Ca–O bonds to form distorted sheets of atoms approximately in the (001) plane. The centre of symmetry produces another sheet between this in the *c*-axis direction. Thus, the structure consists of a 3-dimensional, 3D network of phosphate tetrahedra held together by Ca^{2+} ions in their interstices. In the high temperature form, there are two crystallographically independent phosphate ions and three independent hydrogen atoms. One hydrogen atom is located on a centre of symmetry. In the low temperature for without a centre of symmetry, the hydrogen atoms that were in two-fold disorder become ordered, so that one of the two previously disordered sites become fully occupied and the other completely vacant, this changes the hydrogen bonding predominantly in the c-axis direction, which explains why it is the c-axis parameter that shows the greatest change through the phase transition. In terms of the characteristic external shape of an individual crystal, commonly referred to as the "habit", DCPA crystallises as triclinic (010) tablets elongated in the a-axis direction, but prismatic and rod habits also occur. Furthermore, the crystal are brittle with a "hacky fracture", without twinning.

Octacalcium Phosphate, OCP, is composed of an asymmetric unit $Ca_8H_2(PO_4)_6 5H_2O$, with two asymmetric units per unit cell. It also contains 'apatite' layers (about 1.1 nm thick) alternating with "hydrated" or "water" layers (about 0.8 nm thick) parallel to (100) are a conspicuous feature of the structure. The presence of the "apatite" layer explains the similarities of the lattice parameters with those of HAp ($a = 9.4176$ and $c = 6.8814$ Å). The "apatite" layer consists of alternating sheets of phosphate and Ca^{2+} ions; and the 'water' layer consists of more widely spaced phosphate and Ca^{2+} ions with a slightly variable number of water molecules between them. Six of the Ca^{2+} ions and one of the phosphate ions are in the "water" layer. The remaining tree phosphate ions lie at the junction of the "water" and "apatite" layers. The phosphate ion in the "water" layer and at the junction between the layers are protonated. The water layer causes a distinct difference between HAp and OCP XRD diffractogram data. This comes in the way of a (100) peak that is located at $2\theta = 4.7$ [105]. α-Tricalcium phosphate, α-TCP, crystallises in the monoclinic space group $P2_1/a$ with lattice parameters $a = 12.887 \pm 0.002$, $b = 27.280 \pm 0.004$, $c = 15.219 \pm 0.002$ Å and $\beta = 126.20 \pm 0.01°$ with 24 formula units per unit cell [106]. There is a prominent approximate sub-cell with a *b*-axis parameter of $b/3$ (9.09 Å) that contains 8 formula unit which corresponds to the unit cell reported earlier for α-$Ca_3(PO_4)_2$ [107]. β-Tricalcium phosphate, β-TCP, has the rhombohedral space group $R3c$ with unit cell $a = 10.439 \pm 0.001$), $c = 37.375 \pm 0.006$ Å (hexagonal setting) with 21 formula units per hexagonal unit cell [108]

2.3 Phase transitions

During the process of crystal growth chemical changes also occur. These compositional changes are accompanied by phase transitions and usually occur primarily by surface dissolution, which is then followed by the nucleation of the second phase. The evolution of intermediary phases is dictated by the solubility of the amorphous precursor and crystalline intermedary as well as the free energy (the energy of the system that can be converted into work) of their interconversions [109].

TABLE 2.1: Main calcium phosphate (CaP) salts. Taken from [76, 110]

Name	Ca/P
Monocalcium phosphate monohydrate	0.50
Monocalcium phosphate anhydrous	0.50
Diacalcium phosphate dihydrate (Brushite)	1.00
Diacalcium phosphate anhydrous (Monetite)	1.00
Octacalcium Phosphate	1.33
α-Tricalcium phosphate	1.50
β-Tricalcium phosphate	1.50
Amorphous calcium phosphate	1.20–2.20
Hydroxyapatite	1.67

To improve phase composition it is therefore important to develop new methods possessing precise control over the crystallographic and chemical structure of powder [76].

The process of enamel formation requires cells called ameloblasts which secretes amelogenin, a protein that plays a role in the formation of a well-organised prism pattern. Previous studies by Chen et al 2006 [111] have sought to grow similar structures without the aid of cells or enamel protein, instead these structures would be formed by direct crystal growth. By using the hydrothermal method Chen was able to produce closely packed FAp crystals which were aligned along the c-axis, similar to the enamel prism-like structure. In this study TEM and EDX analysis provided evidence of an amorphous particle phase formed at room temperature, however very few rod-like structures were found here. However, after autoclave for 5 mins the amorphous deposit is almost totally replaced by ball-like structures and more rod-like structures became apparent.

The hydrothermal method is a method that uses a chemical reaction in aqueous solution. The difference between this method and a simple wet chemical precipitation is that the ageing process of hydrothermally derived the crystals are conducted at high temperature and pressure, typically above boiling point of water and inside an autoclave or pressure vessel [76]. Typically the resulting apatite crystals formed are stoichiometric (Ca/P = 1.67) and form nano to micro size crystals. However, the limitation on this method for the purposes of industrial production come in the way of its processing requirements.

The elevated temperature and pressure dependence require expensive equipment. This makes the hydrothermal method more expensive than most other method of apatite synthesis. Phase diagrams show the thermodynamically stable phases and give an indication of the likely conditions required for synthesis. However, the actual phase that forms under any given condition is often dictated by kinetic, rather than thermodynamic considerations. The process of nucleation and growth of CaPs have been reviewed and it has been showed that the kinetic factors are of great importance in this system. Another complicating factor in the "solution-chemistry" of the CaPs, is the formation of calcium phosphate ion pairs, particularly $[CaHPO_4]^0$ and $[CaH_2PO_4]^+$. If these are not taken into account, the solubility product may appear to be dependent on the pH.

Note, the standard enthalpy ($\Delta_f H^0$), free energies of formation ($\Delta_f G^0$), entropies S^0 specific heats (c_p) and calculated solubility constants K_{sp}, for a number of CaPs at 25 °C are given in Table2.2.

TABLE 2.2: Standard thermodynamic quantities and calculated solubility product constants of caps at 298.15 K (25 °C)

Compound	$(\Delta_f H^0)$, kJ mol^{-1}	$(\Delta_f G^0)$, kJ mol^{-1}	S^0, J mol $^{-1}$K^{-1}	(c_p), J mol-$^{-1}$K^{-1}	K_{sp}
DCPA	−1814.39	−1681.18	111.38	110.04	1.83×10^{-7}
DCPD	−2403.58	−2154.58	189.45	197.07	2.59×10^{-7}
OCP	—	−12263	—	—	1.01×10^{-94}
β-TCP	−4120.8	−3884.7	236.0	227.82	2.07×10^{-33}
α-TCP	−4109.9	−3875.5	240.91	231.58	8.46×10^{-32}
HAp	−13477	−12677	780.7	769.9	6.62×10^{-126}
FAp	−13744	−12983	775.7	751.9	6.30×10^{-137}
H_2O	−285.830	−237.129	69.91	—	—
$Ca^{2+}_{(aq)}$	−542.83	−553.58	-53.1	—	—
$OH^-_{(aq)}$	−229.994	−157.244	−10.75	−148.5	—
PO_4^{3-} (aq)	−1277.4	−1018.7	-222	—	—
$F^-_{(aq)}$	−332.63	−278.79	−13.8	−106.7	—

$(\Delta_f H^0)$ and $(\Delta_f G^0)$ refer to formation from the elements and the assumption that these values for H+ ions are zero. The table includes data for the constituent ions of the various CaPs so it is possible to calculate their standard free energies of solution $(\Delta_s G^0)$ from the sum of the standard free energies of solution of the constituent ions minus the standard free energy of formation of the salt. K_{sp} is then given by $(\Delta_s G^0) = -RT \ln K_{\text{sp}}$, where R is the gas constant (8.314 JK^{-1}.mol^{-1}) and T the absolute temperature. As values of K_{sp}, calculated in this way depend on the difference between two numbers of nearly the same size, both determined from thermochemical experiments and subject to experimental error, it is better to use values of K_{sp} determined by chemical analyses of solutions in equilibrium with a pure salt, if these are available.

We can see in Fig. 2.4, that the formation of phases is dependent on both the concentration in solution and the pH. At the points where phases isotherms cross it can be expected that products can undergo a phase transition.

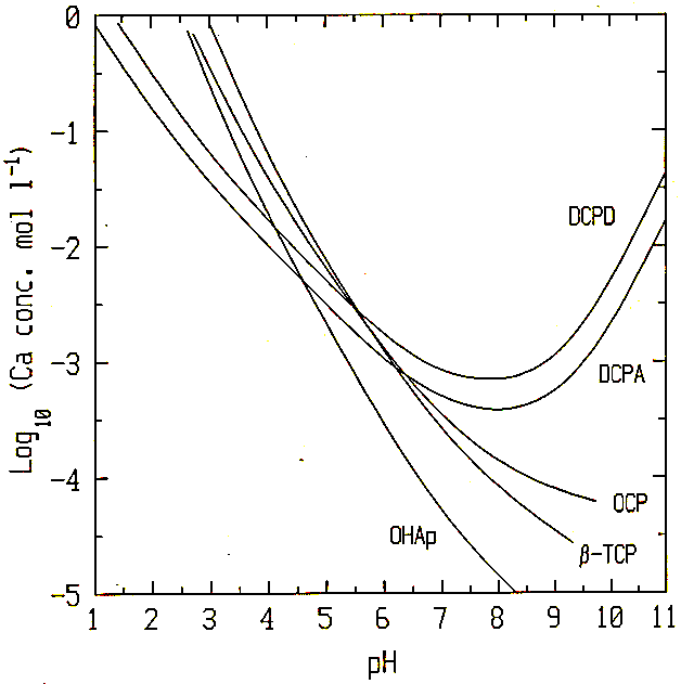

FIGURE 2.4: Solubility isotherms of CaP phases in a system $Ca(OH)^{2-}$ $H_3PO_4^-$ H_2O at 37 °C calculated with the program RAMESES. Showing the connection between pH of solution and the Ca concentration with that of phase transition between the calcium phosphate phases. Taken from [112].

2.3.1 Phase changes and pH

Crystalline phases change significantly with different pH. This is due to the fact that solubility's change with pH and thus the order of solubility's changes as pH is varied.

Brushite is the least soluble phase at pH values below 4 because HAp and OCP readily dissolve by protonation of the PO_4^{3-} ions in the crystal lattice. Above this pH, HA and OCP solubility's dramatically fall off, this means brushite becomes the most soluble at pH values above 5. Using the Ostwald-Lussac law we expect the phase sequence to follow brushite to OCP to HA [109].

2.3.2 Transformation reactions to ACP in the presence of an aqueous phase

As previously discussed, amorphous Calcium Phosphate, ACP is seen as a precursor phase in the formation of the other calcium phosphate phases. In water, the usual product after a few hours when ACP is in alkaline or slightly alkaline solutions is HAp. DCPD and OCP can also form ACP (in one case in the presence of Mg^{2+} ions). In one study [113], ACP matured at a constant pH of 7.4, the first formed crystals gave

an apatite XRD pattern with exceptionally large a-axis parameter (10.5 Å), but in the electron microscope, their appearance was closer to OCP than apatite, this suggested that the conversion proceeded via an OCP-like crystalline phase, followed by hydrolysis into apatite. The increased a-axis parameter has been explained by partially coherent x-ray scattering from inter-crystalline layers of OCP and OHAp. Solubility studies also indicated that an OCP-like maturation was an intermediate phase of the transformation. Moreover, investigations of hydrolysis, again at pH 7.4, in a solution "saturated" with ACP showed that conversion involved two processes:

1. Consumption of acid with the formation of an acidic intermediate with the solubility properties of OCP.
2. The intermediate is converted to an appetite with the consumption of base.

It also seemed that direct hydrolysis of ACP to HAp was possible. pH changes during the precipitation and transformation of ACP to crystalline phases has been explained by the initial formation of an amorphous phase ACP1, followed by the formation and growth of another amorphous phase, ACP2 [114, 115]. ACP is more stable when in solutions at high pH, ionic strength, rich in Ca^{2+} ions relative to HPO_4^{2-} ions, or low in initial supersaturation or temperature. It is also more stable in the presence of poly-l-glutamate, poly-acrylate, phosvitin, casein, large amounts of protein-polysaccharides [1], or on the addition of small amounts of Mg^{2+}, $P_2O_7^{4-}$, CO_3^{2-} or F^- ions. The presence of sufficient Mg^{2+} and/ or $P_2O_7^{4-}$ ions can increase the stability of some ACP samples so that they remain amorphous in hot solutions for many hours. The influence of pyrophosphate ions on the transformation has been investigated in detail, as well as chemical changes that take place during hydrolysis of ACP in the presence of CO_3^{2-} ions. The following are some of the findings of some of the factors that influence on the chemistry.

1. ACa, MgP can transform to DCPD at pH 7 if allowed to remain in the solution in which it was formed.
2. The addition of dentine phosphoprotein has no specific effect on the rate of transformation, but if it is added to the solution before ACP precipitates, apatite forms directly.

[1] Polyglutamic acid (PGA) is a polymer of the amino acid glutamic acid (GA). Gamma PGA (Poly-γ-glutamic acid, γ-PGA) - the form where the peptide bonds are between the amino group of GA and the carboxyl group at the end of the GA side chain); Poly-acrylate is a superabsorbent polymer has the ability to absorb as much as 100 to 1000 times its mass in water; phosvitin is commonly found in egg yokes and casein is a fmaily of phosophoproteins commonly found in mammalian milk; polysaccharides, or complex carbohydrates, represent the form that sugar takes when it is stored. Polysaccharides are the structural components of a cell. Moreover, polysaccharides and other sugars may function as markers for certain cellular recognition processes, including the intracellular movement of proteins.

3. There is an increase in the indication time for ACP transformations at 25 °C in the presence of Mg^{2+}, Sr^{2+}, Zn^{2+}, $P_2O_7^{4-}$ and $P_3O_{10}^{5-}$ ions, and combinations of these.

4. Synergistic effects were observed for combinations of Mg^{2+} or Sr^{2+} ions and $P_2O_7^{4-}$ and $P_3O_{10}^{5-}$ ions.

5. Heats of solution in phosphoric acid of ACP, previously heated at T up to 700 °C, have been reported. Calorimetric heat power measurements, pH and Ca^{2+} ion activity measurements as a function of time have been made in a study of the effect of Mg^{2+} ions on the precipitation of CaPs at 30 °C. The results could be understood if Mg^{2+} ions mainly inhibited the formation of ACP2 and the growth of OCP. Magnesium did not appear to be incorporated significantly in the solid phase or affect the solubilities. However, dehydration of Ca^{2+} and Mg^{2+} ions appeared to contribute significantly to changes in enthalpy during the precipitation process.

2.3.3 Kinetics of conversion of ACP to HAp

Where, the fraction of ACP that has been converted to HAp is given by, c, the time taken for conversion, t, the autocatalytic conversion constant, k_1 , and all other nucleating processes constant, k_2. In the case where $k_2 \gg k_1$ Then

$$\frac{dc}{dt} = k_1 + k_2 c, \tag{2.1}$$

has been shown to be the relationship of conversion. Notably, k_1, will depend on the number of seed crystals. In more detailed kinetic studies, it was found that k_2 decreases with increasing pH at constant temperature, and the activation energy for the conversion process was 16.4 kcal·mol^{-1} (68.7 kJ·mol^{-1}), showing that it was very temperature dependent.

The kinetics of the transformation have been studied in the presence of different magnesium concentrations. With a Mg/Ca molar ratio in the range 0.004 to 0.04, the induction period increased with increasing magnesium concentrations. If the Mg/Ca molar ratio exceeded 0.2, no conversion would take place. However, the rate constant for the first order transformation was independent of magnesium concentration. It was shown that Mg^{2+} ions affected the transformation by reducing the ACP solubility.

2.4 Morphology

As previously mentioned, the presence of soluble additives can affect the morphology of the crystal. This is because the rate of crystal growth is dependent upon surface processes that are highly sensitive to extraneous ions in the environment. Different faces have different structures; this is because each face exposes a different part to the underlying lattice to the external environment. Moreover, the quantity of kinks as well as the energy associated with surface attachment and ion incorporation also varies. In this way different morphologies arise. For example, faster growth along one axis alone gives rise to rod-like morphology; fast growth across 2 planes causes plate-like morphology; equal rates of growth causes cube-like (or octahedron) morphology. Due to empirical observations, referred to as the Ostwald-Lussac law of stages, it is known that the phase with the highest solubility is formed first. After this successive phases are produced in order of decreasing solubility. Thus, the solubility of the solubility of the expected phase/polymorph can be used to predict the order of deposition. The super-saturation level for the most stable polymorph is greater than the less stable crystal or amorphous phase. This is another reason we will expect the most stable polymorph to be the first to precipitate. To date, there are many different morphologies that have been catalogued by previous research: The irregular, formless, sphere (5 nm–200 μm), Sphere, microsphere, nanosphere, ball (10 nm–1000 μm), rod (length: 10 nm–150 μm, diameter: 3 nm–50 μm, aspect ratio: 2:1200), Plate (Length: 40 nm–50 μm, width: 20 nm–35 μm, thickness: 5 nm–3 μm), Self-assembled nano rods (Length: 200 nm–80 μm, width: 100 nm–50 μm), Dandelion (1–8 μm composed of organised nanorods of 80–500 nm diameter and 600 nm–5 μm length), leaf-flake (800 nm–10 μm composed of organised nanoplates of 20–100 nm thickness), flower (700 nm–60 μm composed of organised crystals of 20 nm–10 μm width and 180 nm–50 μm length), Porous microsphere (0.5–7 μm composed of pores of 20–150 nm), Dumbbell (2–3 μm composed of organised nanoparticles of 50 nm size), and Spherulite (Diameter: 28 μm composed of nano rods) [76, 116].

2.5 Summary

As we can see, the main issue in the implant world is the issue of the stability dip. Specifically enhancing the secondary stability such that the healing time can be further reduced. At present the main method for implant enhancement, plasma spraying has its own issues including delamination, and the generation of non-biocompatible by-products, to name a few. Thus the academic field have focused on developing an alternative and more controllable method based on wet chemical synthesis. Not only has it been seen that nano-structured material have a significant effect on osteoblastic cells, but also

that the way in which the nano-crystals that make up its structure are orientated can improve the density of the cells and the OCN expression and as a result the amount of bone formation, and specifically, those with rod-like nano crystals that are aligned along the c-axis show the best balance between cell growth and OCN expression.

For this reason, we aim to understand the formation process of the aligned rod-like nano crystal structures. Structural and compositional categorising methods can be sued to distinguish the various calcium phosphate structures (analysed by x-rays), and chemical differences (analysed by NMR, FTIR and EDX). Further from this, X-ray data can be used as the basis for further analysis through computational simulation of the molecular level. These methods will best help us to understand the changes that occur between the phases during the time of synthesis.

Chapter 3

Methods - X-rays, Crystallography and Molecular Dynamics

3.1 Key aims

To provide an understanding of the advantages and limitations of the main analytical method used in this research.

3.2 Properties, production, detection and application of X-rays.

The discovery of X-rays was first made by a German physicist by the name of Wilhelm Roentgen in 1895 [117]. At the time, their nature was still unknown, and because of this they were given the name "X" to reflect this. Even though these rays traveled in straight lines and affected photographs film in the same way as visible light, it was invisible and much more penetrating. X-rays could easily pass through the human body, wood and even thick pieces of metal to name a few. Because of this, X-rays were almost immediately utilised by none other than physicians and later by engineers who found it useful in the study of the internal structure of "opaque" objects. Points of fracture in a bone or the position of a crack in a metal casting could be located.

3.2.1 Electromagnetic radiation

As we know, X-rays and visible light share many of the same properties. This is because they are both types of electromagnetic radiation, only X-rays, have a much shorter wavelength. Typically, the unit that is commonly used to measure in the X-ray region is the angstrom (Å), equal to 10^{-10} m, and X-rays used in diffraction have wavelengths in the range of 0.5–2.5 Å. In contrast, the wavelength of light is of the order of 6,000 Å, thus it is clear to see that there is a dramatic difference in the amount of energy associated with each type of radiation.

Electromagnetic radiation, in this case X-rays, carry an associated X-ray. The rate of flow of energy through this area perpendicular to the direction of motion of the wave is called the intensity, I. Moreover, the average value of the intensity is proportional to the square of the amplitude of the wave. In the past, most X-ray measurements were carried out by counting the number of photons incident on a detector, or by measuring the degree of blackening of photographic film exposed to the X-ray beam. An accelerated charge radiates energy, and it is this acceleration, positive or negative, that can produce electromagnetic radiation (as we will explain in later section). In any case, the frequency of the radiation is the same as the frequency of the oscillator that produces it.

So far, we have described electromagnetic radiation in the classical sense. That is to say that we have described it as wave motion, but as we will touch on later, we can also describe this radiation at the quantum level. Here, electromagnetic radiation is considered to be a stream of particles called quanta or photons. Each photon has an associated defined amount of energy given by $h\nu$, where h is Planck's constant (6.63×10^{-34} Js), and ν, is the frequency of oscillation.

3.2.2 The continuous spectrum

In the case where an electrically charged particle of sufficient kinetic energy is decelerated rapidly, X-ray radiation is produced. Typically this is achieved in an X-ray tube which contains a source of electrons and two metal electrodes. The electrons are emitted from a heated filament and accelerated through a high potential difference (the voltage tube) towards an Ag anode (the target). Some tens of thousands of volts rapidly draws the electrons towards this anode which they strike with a very high velocity. At the point of impact, the electrons decelerate and some of their kinetic energy is converted in to electromagnetic energy. At this time, radiation is directed in all directions. If e is the charge on the electron (1.60×10^{-19} C) and V is the voltage across the electrodes, then

the energy of the electron on impact is,

$$KE = eV = \frac{1}{2}mv^2, \tag{3.1}$$

Where m is the mass of the electron (9.11×10^{-31} kg) and v its velocity in ms^{-1} just before impact. Notably, most of the kinetic energy that is converted upon impact is transformed into heat, with only less than 1% being converted into X-rays.

The X-rays that are emitted constitute a continuous spectrum, the bremsstrahlung (or breaking radiation). That is to say that the rays coming from the anode consist of a mixture of different wavelength, where by the variation of intensity with wavelength is found to depend on the tube voltage.

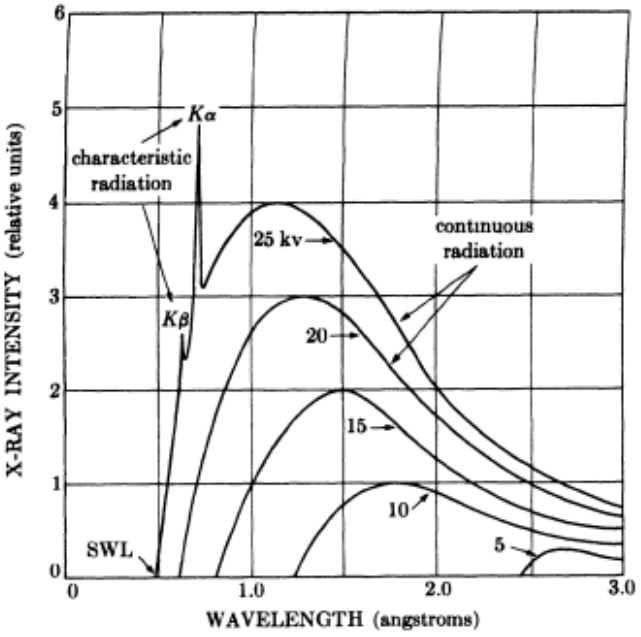

FIGURE 3.1: X-ray spectrum of molybdenum as a function of applied voltage (schematic). Line widths not to scale [118].

Not all of the X-rays will decelerate in the same way, however, some will stop in one impact, releasing all of their energy at once, while others are deflected in different directions by multiple atoms of the target. This causes them to lose their KE in successive interactions until all is spent. Clearly, those electrons that are stopped in one impact produce photons of maximum energy. Again, these electron transfer all of their energy into photon energy,

$$eV = h\nu_{\max} \tag{3.2}$$

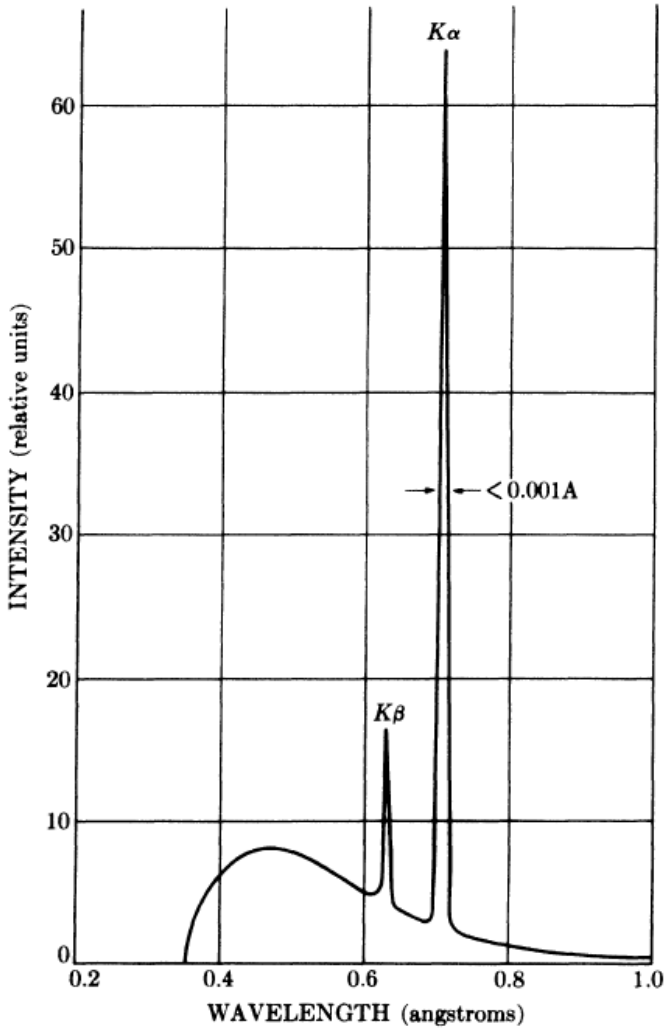

FIGURE 3.2: X-ray spectrum of molybdenum as a function of applied voltage (schematic). Spectrum of Mo at 35 kV (schematic). Line widths not to scale [118].

3.2.3 The characteristic spectrum

The characteristic X-ray lines were discovered by W.H. Bragg and summarised by H.G. Moseley. When the voltage of the X-ray tube is raised above a certain threshold value, dependent on the specific metal anode, sharp intensity maxima appear at certain wavelengths. These are said to be superimposed on the continuous spectrum. On the basis that they are both narrow, and that they are characteristic of the metal used for the anode, they are called characteristic lines. The characteristic lines, referred to as K, L, M etc correspond to transitions of the core electrons between orbitals with the principle quantum numbers 1,2, 3, ... When the two orbitals involved in the transition are adjacent (e.g. $2 \rightarrow 1$), the lines are called α, however, when the two orbitals are separated by another shell (e.g. $3 \rightarrow 1$), then the line is called β. It follows from this that since the transitions from β are greater than that for α,

$$\Delta E_\beta > \Delta E_\alpha, \tag{3.3}$$

and

$$\lambda_\beta < \lambda_\alpha \tag{3.4}$$

K lines have wavelengths of about 0.7 Å, the L lines about 5 Å, and the M lines longer still. These Kα_1, Kα_2, and K_β are approximately: Kα_1: 0.564 Å, Kα_2: 0.559 Å, Kβ: 0.497 Å.

The α_1 and α_2 components have wavelengths so close together that they are not always resolved as separate lines. These lines are shown on the upper most curve of Fig. 3.1.

The useful relationships between x-ray energy, wavelength and wave vector are based on, $E = hc/\lambda$, where c is the velocity of light:

$$E\,[\text{keV}] = \frac{12.3984}{\lambda}\,[\text{Å}] = 1.97327k\,[\text{Å}^{-1}] \tag{3.5}$$

$$\lambda\,[\text{Å}] = \frac{12.3984}{E}\,[\text{keV}] \tag{3.6}$$

Hence an X-ray tube operating at 30 keV will produce X-rays with wavelengths down to 0.413 Å. In our setup, we use a Silver (Ag) source as the material for the X-ray tube anode. This has Kα lines at 21.990 and 22.163 keV which corresponds to wavelengths 0.564 and 0.559 Å, respectively. At a synchrotron, a broad range of x-ray energies is generated up to of order 100 keV or more, depending on the operating energy of the synchrotron. Hence for both laboratory and synchrotron x-ray sources the energy is already appropriate for doing diffraction from atomic structures, so there is no need for the equivalent of the neutron moderator, although devices like wigglers and undulations can enhance the intensity dramatically in particular energy regions.

While the continuous spectrum, Fig.3.1, is a result of the rapid deceleration of the electrons at the target, it is in fact that atoms within the target material that cause the characteristic spectrum. In order to better understand this, we can consider an atom in which the nucleus is surrounded by electrons that find themselves in orbitals K, L, M... which in turn correspond to the principle quantum number $n = 1, 2, 3....$ Any electron that has sufficient KE will be able to knock an electron out of the K shell, here by leaving the atom in an excited, high energy state. It is in this situation that one of the

outer electrons are able to fall into the vacancy left in the K-shell while emitting energy in the form of an X-ray in the process. Notably, the K-shell vacancy may be filled by an electron from any one of the outer shells, thus giving rise to a series of K lines; Kα, and Kβ vacancies. Thus one atom of the target may be emitting Kα radiation while another adjacent to it may be emitting Kβ, see Fig. 3.3.

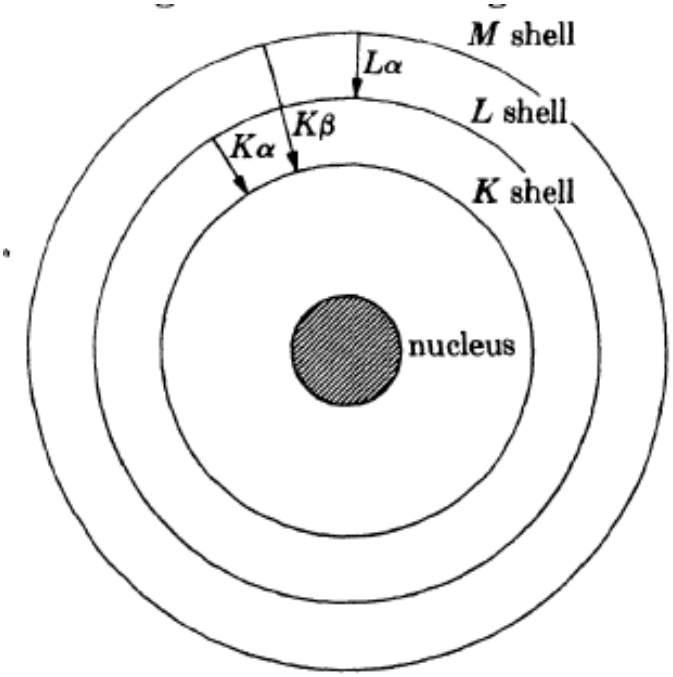

FIGURE 3.3: Electronic transitions in an atom (schematic) emission processes indicated by arrows [118]

.

3.2.4 Absorption

The interaction of X-rays with matter involves two processes. The first is transmission, and the second is absorbance. Early on, Röntgen established that the fractional decrease in the intensity, I, of an x-ray beam as it passes through any homogeneous substance is proportional to the distance traveled, x,

$$\frac{\mathrm{d}I}{\mathrm{d}x} = -I\mu, \tag{3.7}$$

$$\int \frac{1}{I}\mathrm{d}I = -\int \mu \mathrm{d}x, \tag{3.8}$$

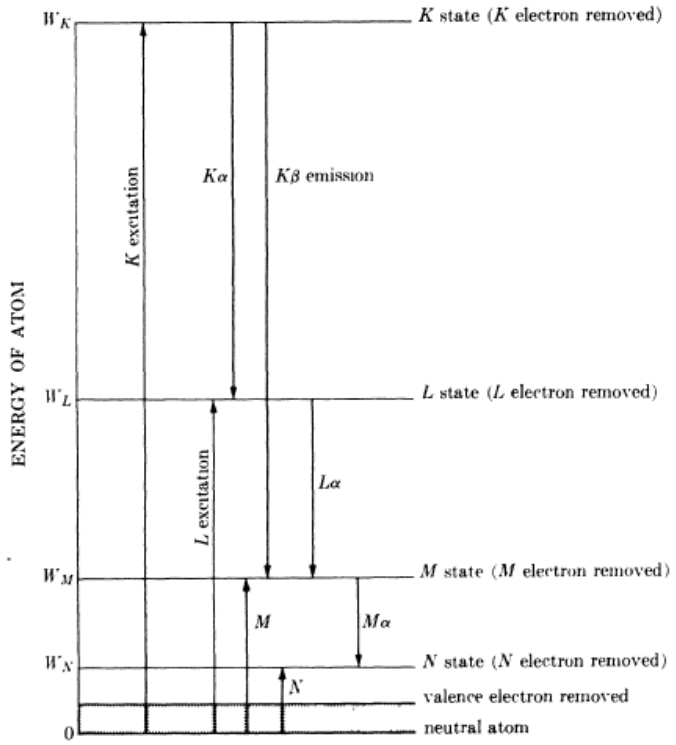

FIGURE 3.4: Atomic energy levels (schematic). Excitation and emission processes indicated by arrows. The insert at top shows the fine structure of the L state [118].

Where the proportionality constant, μ, is called the linear absorption coefficient and is dependent on the substance considered, the density of said substance, and the wavelength of the X-rays. Thus,

$$I = I_0 e^{-\mu x}, \tag{3.9}$$

Where the intensity of the incident beam, I_0, and the transmitted beam, I, having passed through a thickness x. Shows that the intensity of the X-ray bean decreases exponentially with the distance of the surface.

3.2.5 Filters

In many X-ray diffraction experiment, it is important that the beam used is as closely monochromatic as possible. However, in the case of a X-rays beam that has been produced as the results of operating an X-ray tube at a voltage above V_k contains strong Kα but also weak Kβ wavelengths specific to the target metal. Thus, in order to produce a beam that more closely resembles a monochromatic one, a filter can be used

to absorb the unwanted Kβ because there is an abrupt change between the absorption coefficient of it when compared to that of the Kα component, see Fig. 3.5,

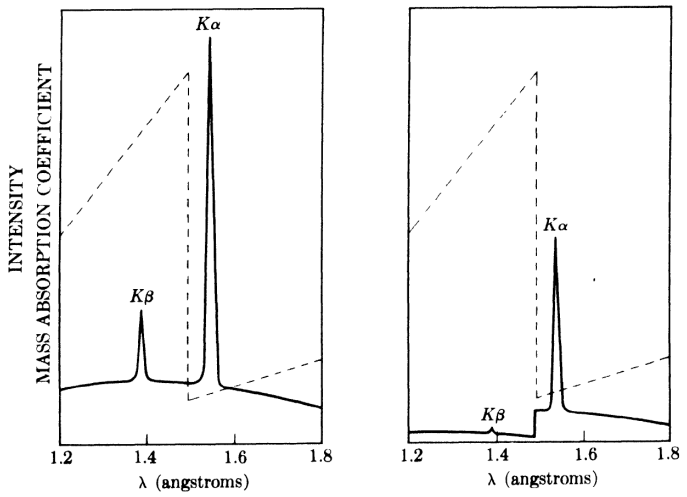

FIGURE 3.5: Comparison of the spectra of copper radiation (a) before and (b) after passage through a nickel filter (schematic). The dashed line is the mass absorbance coefficient of nickel.

[118].

The effect of the filter, again shown in Fig. 3.5, when an example of both a filtered and unfiltered beams derived from a coper target ($Z = 29$) are shown superimposed on a plot of the mass absorption coefficient of the nickel filter ($Z = 28$). The thicker the filter, the lower the ratio of intensities of Kα to Kβ in the transmitted beam. Even so, filtration is never perfect and so in practice there is a weakening of the Kα to about half its original value in an attempt to reduce that of Kβ.

3.3 X-ray scattering and crystal structure

As we know, an X-ray beam can be described as an electromagnetic wave characterised by an electric field whose strength varies sinusoidally with time at any point in the beam. Since an electric field exerts a force on a charged particle, such as an electron, the oscillating electric field of an x-ray beam will set any electron it encounters into oscillatory motion about its mean position. The acceleration and deceleration of these electrons causes the emission of an electromagnetic wave. As we have said before, in the case of an X-ray tube, X-rays are emitted due to the rapid deceleration of the electrons that strike their target (anode). It can also be said that an electron that has been set into oscillation by an x-ray beam is not only continuously accelerating and decelerating, but is also emitting an electromagnetic wave. Commonly, this is referred to as the "scattered" X-ray beam. Since electromagnetic waves have a wave particle duality, these beams can

be considered to be made up of quantised photon particles. This gives rise to the idea of inelastic and elastic scattering. In the first instance there is no conservation of the kinetic energy, KE, from the colliding "particles",

$$\Delta E \neq 0, \tag{3.10}$$

In this case, there is a loss of KE due to the vibration of the scattered body itself. This causes the dissipation of energy due to heat and sound. However, KE can also be lost due to the breaking of chemical bonds. One of the most famous examples of inelastic scattering is what is known as the Compton Effect, discovered by A. H. Compton in 1923. This effect occurs whenever X-rays encounter loosely bound or free electrons. The collision of the photon quanta and the electron causes a recoil of that electron and a scattering of the photon, where the energy of the photon is slightly less than before the impact. Notably, this effect is able to contribute to "noise" when crystal structure experiments are conducted.

In the case of elastic scattering, there is no loss in the kinetic energy of the colliding bodies, that is to say that the total energy is conserved,

$$\Delta E = 0 \tag{3.11}$$

Notably, it is elastic scattering that is used to characterise the crystal structure of materials. For x-rays, electrons are the principle scattering medium, which are in contrast to that of neutrons which are scattered by the nucleus.

3.3.1 Crystal's geometry and X-ray diffraction

Crystallography, the experimental science of determining the arrangement of atoms in the crystalline solid, is a very broad subject and its origins precedes even the discovery of x-rays. In 1611, the German polymath Johannes Kepler was the first to document the structure of crystals [119]. Kepler marvelled at the 6-fold symmetry (6-cornered) of the snow flake [120] and he suggested that the regular packing of water particles gave rise to the hexagonal symmetry of snowflake crystals. It was not until much later that this mathematical description was used to explain the geometric shapes of crystals in terms of packing of their constituent particles [121, 122]. Development of crystallography continued with Nicolas Steno in 1669, in his work "De Solido Intra Solidum", he observed for the first time the fundamental crystallographic Law of the Constancy of Interfacial Angles [123–126]. And by 1784, René Just Haüy mathematically proved that there

are only 7 distinct shapes, or classes of crystals [127–130], see Table 3.1 In general, a relationship can be generated by the symmetry of the crystal [131].

TABLE 3.1: The seven lattice types as defined by symmetry constraints [131].

Lattice	Defining symmetry	Constraints on lattice parameters
Triclinic	None	None
Monoclinic	One mirror plan or one 2-fold rotation axis	$\alpha = \gamma = 90°$
Orthorhombic	Each axis has either a mirror plane or 2-fold rotation axis or both	$\alpha = \beta = \gamma = 90°$
Hexagonal	One 6-fold rotation or -axis	a = b, $\alpha = \beta = 90°$, $\gamma = 120°$
Tetragonal	One 4-fold rotation or -axis	a = b, $\alpha = \beta = \gamma = 90°$
Trigonal	One 3-fold rotation or -axis	a = b, $\alpha = \beta = 90°$, $\gamma = 120°$
Rhombohedral	One 3-fold rotation or -axis	a = b = c, $\alpha = \beta = \gamma$? 90°
Cubic	4 intersections 3-fold rotation or -axis	a = b = c, $\alpha = \beta = \gamma = 90°$

Mathematical classification was carried out by August Bravais in 1849. Who established that there are 14 unique lattices in 3-dimentions (3D) crystalline systems [132]. Thus from here it was predicted that one could arrange lattices by the use of points in space, known as Bravais Lattices, and in 1890, 230 space groups were derived by Evgraf Fedorov, which was independently confirmed by Arthur Schoenflies. René Haüy's mathematical concepts were confirmed by Friedrich, Kipping and Von Laue, by passing a beam of X-rays through Sphalerite crystals. They observed distance diffraction patterns (ordered arrays of spots on a recording film). This experimental evidence provided the proof for the electromagnetic wave behaviour of X-rays, and also that crystals are composed of space lattices [133]. Essentially von Laue's team really showed the x-rays are waves, on the assumption that crystals are periodic. However, it was Bragg who interpreted this work in terms of Miller indices.

3.3.2 Lattices, unit cell, and atomic coordinates

Crystals are composed of an infinite array of points, a lattice. This can be considered to be a pattern which is commonly referred to as a motif, and repeats periodically in three dimensions by rotation, reflection and inversion. This motif can be a single atom, a group of atoms or ions or molecules arranged in a pattern periodic in 3D, then this material can be defined as a crystal [123]. Crystals differ in a fundamental way from gasses and liquids because the atomic, ionic or molecular arrangements in the latter do not poses the essential requirement of periodicity. The lattice is the starting point for a crystal, but associated with each lattice point is a region of space which contains the basis set of atoms. By convention we define this region of space as the quantity called the unit cell, which is a volume of parallelepiped shape bounded by lattice points on each of its eight vertices. By definition, the 'unit cell' pack together following the crystal lattice, and fill space completely. The edges of this parallelepiped has lengths a, b, c, and inter axis angles α, β, γ. The main feature of a lattice is that the environment of each lattice point should be identical. The basic crystal lattices of the seven crystal classes

as previously said are not the only possible crystal lattices. That is to say that the unit cell of a conventional lattice is not the smallest unit cell possible, and it encompasses more than one lattice point. These unit cells belong to the 14 Bravais lattices, Fig. 3.6.

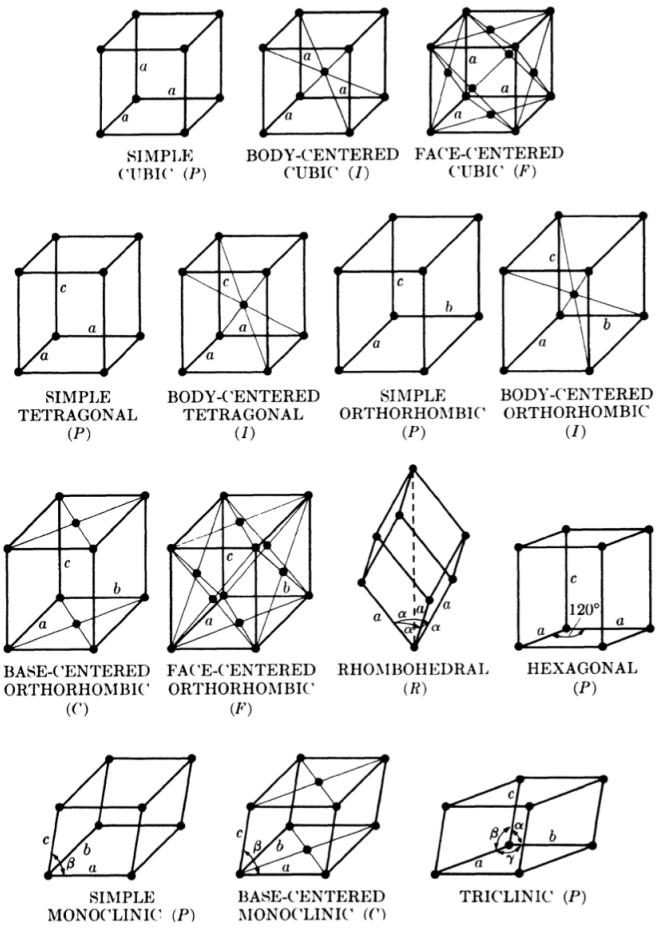

FIGURE 3.6: The conventional unit cells of the 14 Bravis lattices, with the lattice points represented by spheres. The primitive trigonal lattice is the same as the hexagonal lattice[118].

The orientation and inter-planar spacing of the lattice planes are defined in terms of the Miller indices h, k, l, a notation system introduced in 1839 by William Miller [134], which provide a key way to formally define what is known as the reciprocal lattice,

$$\mathbf{d}^*_{hkl} = h\mathbf{a}^* + k\mathbf{b}^* + l\mathbf{c}^*, \tag{3.12}$$

Where h, k, l , are the integers we met above, and which can take any value. The vectors $\mathbf{a}^*$, $\mathbf{b}^*$, $\mathbf{c}^*$ are the basis vectors of the new lattice, and $\mathbf{d}^*_{hkl}$ is called the reciprocal lattice vector. Usually the plane normal to $\mathbf{d}^*_{hkl}$ is represented by the notation (hkl), [131]. $d_{hkl} = 1/d^*_{hkl}$ is the distance between parallel planes and is used in Bragg's law to determine where diffraction peaks will be observed.

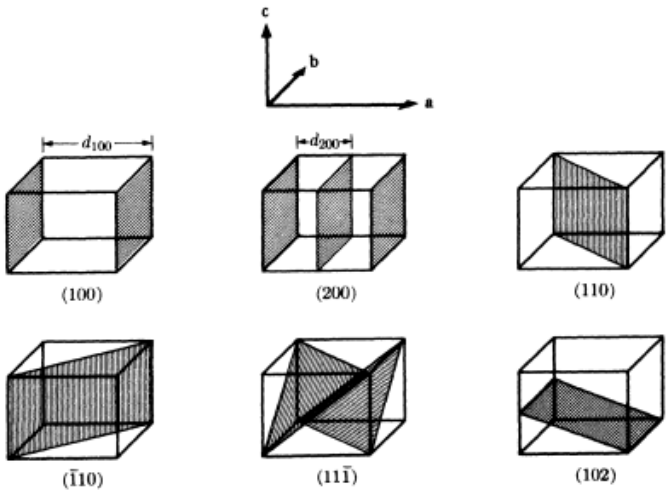

FIGURE 3.7: Miller indices of lattice planes. The distance d is the plane spacing [118].

3.3.3 Bragg's law

The structure of a material can be deduced when beams of radiation are scattered elastically with a coherent superposition of the waves. The representation of this process is encompassed in Bragg's law of diffraction, Fig. 3.8. Waves that are reflected from planes of atoms separated by a distance d, and the coherent superposition of the waves which occurs when the lengths of the paths taken by the components reflected from neighbouring plans differ by an integer number of wavelengths, $n\lambda$.

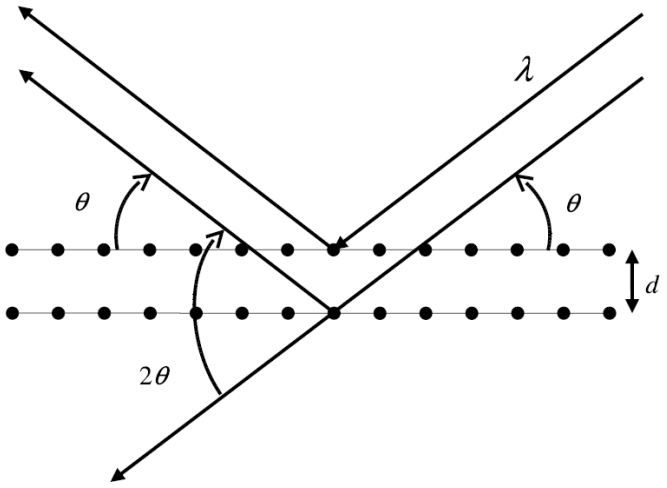

FIGURE 3.8: illustration of Bragg's law for crystal diffraction. A reflection will occur if $n\lambda = 2d\sin\theta$.

Thus it can be seen that planes with a given index hkl have a path difference that is one wavelength then,

$$\sin\theta_{hkl} = \frac{n\lambda}{2d_{hkl}} \tag{3.13}$$

which is otherwise known as Bragg's law. The important point to note is that Bragg's law is the relationship between the scattering angle θ, the Bragg angle, and the d-spacing [135, 136]. The wavelength of X-rays range from 0.01–100 Å, which is comparable to the range of the average distance between atoms in solids. Thus as we know from A-level physics a wave will be diffracted if it meets an aperture of comparable size. In this case the separtion between plane of atoms (or the electrons that surround the atoms and that are situated within a parallel lattice planes serves act in much the same way as a diffraction grating).

As previously said, a "scattered" beam is emitted, and it is these "scattered" waves that interfered constructively and destructively to produce the diffracted beam. Or in other words, the reciprocal lattice that is a projection of the "momentum" space. In fact, it was in 1919 that Hull established that each distinct crystalline structure has an attributable X-ray fingerprint. This unique pattern was derived from a procedure in which it was required that the crystalline material was analysed in powder form. The powder was exposed to a beam of monochromatic X-rays, and the diffraction pattern was captured on photographic film. Thus, from here, it could be seen that there were a number of distinct peaks that could be used to identify the particular crystal specimen in question [137].

3.4 The diffraction experiment

As we have touched on before, there are several principal components to a diffraction experiment:

1. A source of radiation;
2. An incident beam monochromator and collimator;
3. The sample being investigated;
4. A scattered beam collimator;
5. Radiation detector(s);
6. Data acquisition electronics to count the events seen in the detector;
7. Data analysis software, to convert the "raw" counts to useful differential cross section data.

in the case where the size of the grain is greater than the size of the beam; polychromatic (or Laue) method is used. However, in the case that the size of the grain is less than the size of the beam; monochromatic (or Bragg) method is used.

In this case our sample being a polycrystalline and having the length and width scales of the order of a few hundred nano-meters it can be seen that the approach we should use here would be to use monochromatic radiation.

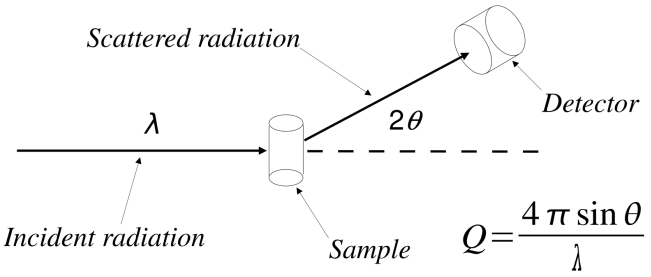

FIGURE 3.9: Primary layout of a neutron or X-ray diffractometer.

In Fig. 3.9, a beam of monochromatic radiation, wavelength, λ, impinges on the sample from the left, is scattered by that sample into scattering angle 2θ and then detected by the detector. The data are measured versus the variable $Q = 4\pi \sin\theta/\lambda$. The wavelength is normally selected either by means of a monochromator in the incident beam.

It is Q that determines the length scale that is probed by the diffraction experiment, with small Q corresponding to large distances and large Q corresponding to small distances. Any combination of θ and λ that gives the required Q values should in principle give equivalent data, although, as will be seen later, use of large scattering angles and long wavelengths with neutrons can in certain circumstances give rise to unwanted "recoil" effects that should be avoided if possible.

the simplicity of the underlying diffraction experiment belies many of the subtleties that are associated with it:

1. Any diffraction signal from a liquid of amorphous material is intrinsically weak and contains only diffuse scattering features.

2. It is impossible to produce a truly monochromatic beam. If this was achieved there would be no incident radiation flux with which to detect your already weak diffraction pattern! This means the diffraction pattern can only be measured with a finite resolution function. This problem is particularly serious with the neutron sources, which often have intrinsically much lower fluxes than x-rays sources. there is a highly non-linear relationship between the width of the allowed wavelengths

with get through the collimator and the final radiation fluxes on the sample. In other words, a change in resolution by a factor of 2 might affect the flux by a factor of 8.

3. Samples have to be contained (in this case a kapton capillary).

4. inevitably some of the radiation reaching the detector has not come from the sample. This is called background scattering which has to be removed from the radiation counts.

5. Because the signal from the sample is intrinsically weak, you are very dependent on the detector and its electronics to not introduce any spurious structure into the observed data. This structure might be caused by residual instabilities in the electronics themselves.

6. For a sample to scatter a measurable amount of radiation it also therefore has to reduce the affect of additional scattering to some extent. Thus, scattering due to samples and the container itself have to be taken into account.

7. Equally, if the sample scatters sufficiently to give a measurable signal, then some of that signal will come from multiple scattering events, namely those where the radiation is scattered twice or more before it leaves the sample. Since they mix up different scattering angles (and wavelengths if the scattering is inelastic) such events do not contribute a useful signal to the scattering pattern. Roughly speaking, is a sample scatters $x\%$ of the incident beam, then depending on the amount of radiation capture in the samples, the multiple scattering will be around $x\%$ of the primary scattering. Radiation capture occurs when the radiation is captured by an atom of the sample instead of being scattered by it.

8. As previously explained, x-ray particle interaction leads to electron recoil and the reduction of the x-ray energy. This process leads to distortions to the diffraction pattern that need to be corrected for.

9. Some materials may fluoresce in the X-ray beam, giving an additional sample dependent background. X-ray fluorescence (XRF) is the emission of characteristic "secondary" X-rays from a material that has been excited by bombarding with high energy x-rays (or gamma rays).

10. Stability in the incident beam. Stability within the sample itself the sample positioning, and stability in the detector electronics all effect the stability of the incident beam. This is because both x-ray and neutron measurements tend to occupy several hours of beam for each sample, so that if different samples are to be compared reliably, the parameters associated with the diffractometer itself

should not drift in the course of a measurement. In this way, the observed diffraction pattern differences do indeed arise from the two samples, and not from some systematic effect of the instrument on which they were measured.

11. Finally, in order to calculate useful quantities from the data related to the structure of the material in the sample, it is essential to put the scattered data onto some sort of absolute scattering cross section scale. This is typically measured in the units of electrons per atom per steradian (for x-rays).

3.4.1 Key components

3.4.1.1 Collimator

A device that produces a parallel beam of rays or radiation. It achieves this by using a limiting structure known as soller slits, Fig. 3.10, to narrow the beam. This is done either by selecting only those beams in which the direction of motion are most aligned (making collimated light more parrallel) or to cause the spatial cross-section to become smaller.

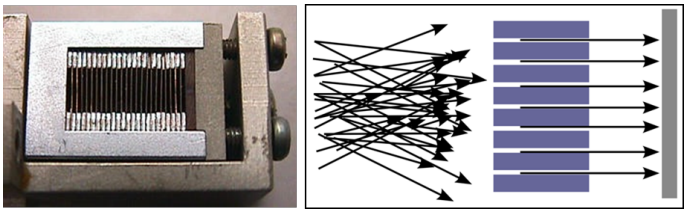

FIGURE 3.10: Sideways divergence of either the incident or scattered beam can be controlled using Soller slits (shown in the right-hand photograph above) inserted in the X-ray beam path. These consist of a set of fine parallel foils which prevent angular divergence of the beam out of the $\theta/2\theta$ plane. This gives a less asymmetric and narrower peak shape, especially at low scattering angles.

3.4.2 Samples and containment

Just as with neutrons, most materials to be investigated with x-rays require containment of some form or the other. Unless very high x-ray energies are involved, it is essential that the thickness of this containment is kept to an minimum. The normal rule of thumb is that the sample thickness, t, should be equal to the inverse of the attenuation coefficient: $t = 1/\mu$, although this can be difficult to realise when heavy elements are present.

In our experiment we use a polycabonate Kapton ($C_{22}H_{10}N_2O_5$) tube for containment. This is useful since it only contains low atomic weight elements, see Table 6.2.

TABLE 3.2: Atomic composition of kapton tube.

Symbol	Form Factor	Abundance	Q (e) (0)	Δ [Å^{-1}]
O	O	5.0	0.0	0.0
C	C	22.0	0.0	0.0
H	H	10.0	0.0	0.0
N	N	2.0	0.0	0.0

In other words the elements that form the greatest abundance within the material are Carbon (C) and Hydrogen (H), where both of these are weekly scattering. Thus, not only will the thickness be to an advantage, but also the inherent material properties itself

3.4.3 Xray detectors

In our setup we use an X'Celerator is a pixel area detector (PAD) which is composed of a 1D silicon strip detector for laboratory X-rays. In the 1D detector mode, all pixels in one column are added up to form a position-sensitive detector in one direction. Photons are counted by the detector at a high resolution. The advantage of this is that the detector can be brought closer to the sample, increasing the angular range to more than 28^o without compromising data quality.

3.4.4 Diffractometer resolution

The resolution of a pulsed neutron diffractometer is quite different in form to that from a fixed incident wavelength diffractometer with a monochromating crystal. The latter case was dealt comprehensively by Caglioti et al in 1958 [138] Theoretically, the Bragg diffraction peak from a crystalline material placed in the radiation beam would be infinitely narrow. This ideal situation can never be realised in practice because neither the scattering angle, nor the incident wavelength are precisely defined, leading to a spread in values of both. Indeed for neutrons, the crystal mosaic spread of a monochromating crystal is often made larger if possible to enhance the flux of radiation scattered by the crystal. This causes the beam on the sample to have an intrinsic divergence (spread in angles) and spread in wavelengths. However, for the monochromating crystal this spread in angles and spread in wavelengths are correlated, since all radiation particles reflected by the crystal must satisfy Bragg's law.

3.5 Rietveld Refinement

Rietveld refinement is a technique that was devised by Hugo Rietveld, and applied to the characterisation of crystalline materials. The neutron and X-ray diffraction of powder samples results in a pattern characterised by reflections (peaks in X-ray diffraction, XRD diffractograms) at certain positions. The height, width and position of these reflections can be used to determine many aspects of the material's structure. The Rietveld refinement uses what is commonly known as a "least squares" approach to refine a theoretical line profile until it matches the measured profile. The introduction of this technique was a significant step forward in the diffraction analysis of powder samples as, unlike other techniques of the time, it was able to deal reliably with strongly overlapping reflections. The method was first implemented in 1967 [139], and later it was reported in 1969 [140] for the monochromatic neutrons. Here the positions of the reflections were reported in terms of Bragg angle 2θ. Here we will describe the reflections with the same terminology, however, this technique is equally applied to alternative scales, namely X-ray energy or neutron time-of-flight. Another scale that can be used is the reciprocal space unit or momentum transfer, Q.

In this case, the scale is wavelength and technique independent but has been used rarely for powder diffraction when speaking from a historic sense. For our refinement, we use a General Structure Analysis System (GSAS) to conduct Rietveld Refinement. The GSAS package is written in FORTRAN which is a general purpose programming language that is especially suited to numeric computation and scientific computation. GSAS consists of a set of programs that are used in the process and analysis of both the single and powder diffraction data that is obtained from X-ray and neutron experiments. It is able to handle multiple sets of data simultaneously when analysing a given structural problem. Furthermore, it can handle powder diffraction data from a mixture of phases while refining the structural parameters for each phase. In our experiment, we analyse apatite crystals that have been precipitated onto either a HAp or Ti discs. For this reason, data was taken on a conventional Bragg-Brentano powder diffractometer using Cu Kα radiation, where Kα_1 = 1.540598 Å and Kα_2 = 1.544430 Å. These samples were also conducted in the flat plate geometry.

3.5.1 Improving the goodness of fit for powder diffraction

When performing a Rietveld refinement using GSAS, the main principle is to minimise a function Δ which analyses the differences between a calculated profile $y(calc)$ and the observed data $y(obs)$. Visually, this will be reflected in the difference curve $I_o - I_c$ in

such a way as to also reduce the difference between the theoretical and the observed data.

$$\Delta = \sum_i w_i \{y_i(obs) - y_i(calc)\}^2 \tag{3.14}$$

In order to measure the process of convergence it is useful to have several agreement indices. The first of these is weighted-profile R-factor, R_{wp}, which is related to the above function, and is defined as:

$$R_{wp} = \{\frac{\sum_i w_i \{y_i(obs) - y_i(calc)\}^2}{\{\sum_i w_i y_i(obs)^2\}}\}^{1/2} \tag{3.15}$$

$$= 1 - \frac{\sum_i y_i(calc)}{\sum_i y_i(obs)} \tag{3.16}$$

Here, y_i, which can also be thought of as the structure factor, can be found as $y_i(calc)$ and $y_i(obs)$, for calculated and observed data, respectively. As $y_i(calc) \rightarrow y_i(obs)$, $R \rightarrow 0$, thus any value near zero shows a goodness-of-fit.

The argument for removing the background contribution for $y(obs)$ is that the remaining provides a better estimate for the counts available. With the background included, one may find that they are fitting to the background rather than the peaks that hold the information about the structural parameters.

Another R-factor, known as the expected R-factor is a measure of data quality. it is calculated on the same basis as the weighted-profile one.

The expected R-factor is defined as:

$$R_{exp} = \{(N_o - N_P + N_C) / \sum_i w_i y_i(obs)^2\}^{1/2} \tag{3.17}$$

,

where N_o is the total number of observations, N_P, is the number of parameters refined, and N_C is the number of constraints used in the refinement. For structural refinement with powder diffraction data, the expression $(N_o - N_P + N_C)$ is dominated by the size of N_o [141].

The ratio between the two R-Factors gives the chi-squared values for the fit:

$$\chi^2 = (R_{wp}/R_{exp})^2 \tag{3.18}$$

which can also be expressed as,

$$\chi^2 = \sum \frac{(obs - exp)^2}{exp}, \tag{3.19}$$

where *obs* and *exp* are the values for the observed and expected data, respectively. We can see that in this case the value will always be positive, but as $obs \to exp$, $\chi^2 \to 1$. Where in this case, the closer it gets to one, the better the goodness of fit becomes. When refinement is applied, GSAS [1] will provide a difference curve that will provide the goodness of fit. This is achieved by calculating the difference between the intensity of the observed, I_o, and calculated, I_c diffractograms [142].

3.5.2 Least squares refinement

As said before, GSAS uses a least squares refinement method which is a standard approach in regression analysis to approximate solution of overdetermined systems, i.e. sets of equations where there are more equations than unknowns. 'least squares' means that the overall solution minimises the sum of the squares of the residuals made in the results of every single equation.

In general the expressions for the calculated values corresponding to the set of crystallographic observations are transcendental and thus the least squares minimisation function is nonlinear and the process is iterative. The minimisation function in GENLES can be made up of several components.

$$\Delta = f_k \sum \Delta_h. \tag{3.20}$$

The reduced χ^2 or "goodness-of-fit" is defined by the minimisation function as,

$$\chi^2 = \frac{\Delta}{N_{\text{obs}} - N_{\text{var}}}, \tag{3.21}$$

where, N_{obs}, is the total number of observations in all histograms and N_{var} is the number of variables in the least squares refinement [140]. Notably, each powder diffraction used in refinement occupies a separate histogram within GSAS and forms a separate contribution to the minimisation function. Where f_k is an adjustable weight factor.

[1] In GSAS, least squares refinement is performed by the program GENLES.

3.5.3 Increasing the number of terms for fitting background

Increasing the number of background coefficients helps to improve the fit. It gives more data points and allows for a greater mapping of the data to the background. The system accounts for the presence of the background by using what is referred to as a peak sample cut off. Anything below this is considered background and is not included in the fitting process. The system has a cut-off that is set to 1% of the peak height, however, one may want to reduce this further in order to improve the fit.

3.5.4 Peak profile position, width and height

The XRD peak position, can be effected by either the size or shape of the unit cell, or and overlap of concurrent phases that are present within the sample. In both of these cases, refining the lattice parameters will bring the refined peaks to a better position with respect to the recorded data. The contribution of each phase of the diffractogram, i.e. the amount of each that can be detected will also effect the goodness-of-fit and thus should be considered (refining the one that has a greater amount present over that of those that have a low amount). Peak width is a measure of the broadness of the peak. For example, at low angles a small value, say 0.05°, would indicate a sharp peak where as a large value, say 0.2° would indicate a broad peak. Peak maximum (peak height), denoted as $I_{\max}$, is fairly self-explanatory, however it should not be used as a measure of diffracted intensities. The peak intensity is actually given by the peak area, above the background,. The reason we can take this to be the peak intensity is because its represents the sum of all the diffracted X-ray photons (or neutrons) that have been detected regardless of peak shape.

Notably, the peak height can be effected by,

1. Fractional coordinates x, y, z of the atoms within the plane
2. Radial displacement from the origin,
3. Substitution of atoms or groups into the crystal structure
4. and, preferred orientation of the crystallites themselves.

These concepts will be outlined in more detail within the following sections. The peak width is also affected by multiple factors,

1. Mosaicity (the measure of the spread of crystal plane orientation)

2. Crystallite grain size,
3. Microstrain,
4. Thermal motion of atoms,
5. Background radiation
6. Kα_1, Kα_2... overlap
7. and, inherent spectral width

Where factors 1–3 are specimen based, 4–6 are physical phenomena based, and 7–8 are due to spectral reasons.

As previously stated, the process of improving the fit requires that the number of parameters are increased for the least squares refinement. The physical origin of these parameters will here be outlined.

In a continuous wave, CW, experiment, the strain broadening in real space is related to 2θ broadening from,

$$\frac{\Delta d}{d} = \Delta 2\theta \cot\theta = \text{constant}, \tag{3.22}$$

or

$$\Delta 2\theta = \left(\frac{\Delta d}{d}\right) \tan\theta, \tag{3.23}$$

where $\Delta 2\theta$ is in radians. Examination of the expression for Gaussian broadening,

$$\sigma^2 = u\tan^2\theta + v\tan\theta + w\frac{P}{\cos^2\theta}, \tag{3.24}$$

Indicates that the first term, $u\tan^2\theta$, contains a strain broadening component.

The Lorentzian component of a CW peak has the expression,

$$\gamma = \frac{x + x_s\cos\phi}{\cos\theta} + (Y + Y_e\cos\phi + \gamma_L d^2)tan\theta, \tag{3.25}$$

Where, x_s, is the sub-lattice anisotropic broadening, typically due to stacking faults, Y, represents the particle micro-strain, and, γ_L, is the empirical extension of the micro-strain anisotropy,

$$\gamma_\mathrm{L} = \gamma_{11}h^2 + \gamma_{22}k^2 + \gamma_{33}l^2 + 2\gamma_{12}hk + 2\gamma_{13}hl + 2\gamma_{23}kl, \tag{3.26}$$

Where γ_{11}, γ_{22}, γ_{33}, γ_{12}, γ_{13}, and γ_{23}, are variables. As we can see the strain term, γ, varies with $\tan\theta$. Again, any instrumental or spectral contribution can be subtracted to yield the strain components. This term is represented in cetideg and is already a full with half maximum. Generally, the strain (or micro-strain broadening) is caused when a material has residual stresses present, and some crystallites are compressed. This must be balanced by other crystallites that are stretched because $\sum F = ma = 0$. In turn, this leads to a range of lattice constants, and the spread between diffraction locations for the maximum and minimum lattice constants increases linearly with Q ($\Delta Q/Q$ or $\Delta d/d = \text{constant}$). Generally the strain, S, is represented as a percentage,

$$S = 100\% \frac{\pi}{18000} Y, \tag{3.27}$$

Where, $Y = \left[U - U_I\right]^{1/2}$, in this case, U, is the variable from the Cagoliti equation and U_I , accounts for the instrumental contribution. One way to conceptualise anisotropic peak broadening is to consider the case of a layered material. Consider the case where a material is made up of layers that are bonded by strong forces in the plane of the layer, but weak forces between layers. In the x direction layers can be pulled apart with some small effort, however, in the y direction (within the plane of the layer), strong bonding forces are resistant.

This means that the material can be compressed in the x-direction but rigid in the y direction. Which in turn causes the material to exhibit anisotropic strain. GSAS uses a modified strain expression, where the parallel and perpendicular anisotropic strain components can be calculated by,

$$S_\perp = 100\% \frac{\pi}{18000} (Y - Y_i), \tag{3.28}$$

and

$$S_\parallel = 100\% \frac{\pi}{18000} (Y + Y_e - Y_i), \tag{3.29}$$

3.5.5 Particle size broadening

As outlined before, particle size broadening is caused by the finite length of regularly spaced atoms. Mathematically, particle size broadening is obtained from,

$$\frac{\Delta d}{d^2} = \frac{\Delta 2\theta \cot\theta}{d} = \text{constant}, \tag{3.30}$$

from Bragg's law this becomes,

$$\frac{\Delta d}{d^2} = \frac{2\Delta 2\theta \cot\theta \sin\theta}{\lambda}, \tag{3.31}$$

where the broadening can then be expressed as,

$$\Delta 2\theta = \frac{\lambda \Delta / d}{2\cos\theta}. \tag{3.32}$$

so from here, we can take the first term in the expression for the Lorentzian broadening is of this form where,

$$x = \frac{\Delta}{d^2}, \tag{3.33}$$

and use this to describe the anisotropic particle size components which are given by,

$$P_{\perp} = \frac{18000k\lambda}{\pi x} \tag{3.34}$$

and

$$P_{\parallel} = \frac{18000k\lambda}{\pi(x + x_{\mathrm{e}})} \tag{3.35}$$

in centidegrees, where P is the particle size and, k is the Scherer constant in Å, where $k = 1$. The average stacking fault separation can be obtained from the sub-lattice anisotropic broadening, x_s, by,

$$P_S = \frac{18000k\lambda}{\pi x_s} \tag{3.36}$$

where the corresponding term in the Gaussian expression is obtained by converting from centidegrees to radians to give the expression,

$$P_S = \frac{18000k\lambda}{\pi\left[(8Ln2)P\right]'} \tag{3.37}$$

3.5.6 Sample displacement and transparency

In Bragg-Brentano geometry Samples are ideally placed exactly at the rotation axis and all diffraction occurs from the sample surface. In practice, neither is commonly true. Typically, peak centres are shifted by,

$$\Delta T^1 = \Delta T + S_S \cos\theta + T_S \sin 2\theta, \tag{3.38}$$

where the shift, S_S, caused by the radial distance from the origin, and the transparency coefficient, T_S. The sample displacement can also be represented by,

$$displacement = \frac{-\pi R S_S}{36000}, \tag{3.39}$$

and the effective sample absorption, μ_{eff}, can be determined from the sample transparency, T_S is given by,

$$\mu_{\text{eff}} = \frac{-9000}{\pi R T_s}, \tag{3.40}$$

where R is the diffraction radius. These correlations correspond very highly with zero correlation for 2θ, ZERO. Parallel-beam instruments (neutron or synchrotron) are very tolerant of displacement and transparency. In this case we, never refine the S_S or T_S, but do refine the ZERO, and for flat plate geometry, we never refine the ZERO.

3.5.7 Asymmetric peak shape

Peak asymmetry is related to the mirror plane (or lack of) that passes vertically through the peak maximum; if the left hand side (LHS) to this 'mirror line' is an identical reflection of the right hand side, RHS, the peak is said to be symmetric. Clearly, if the two sides are not, then the peak shape is said to be asymmetrical. Peak asymmetry is particularly noticeable with powder patterns collected from instruments on neutron spallation sources. X-ray peaks are usually asymmetric even after α_2 stripping. [2]

3.5.8 Lorentzian and Gaussian peak profiles

3.5.8.1 Fourier transform and crystalline broadening

The Fourier transform of an infinite array of regularly spaced objects (atoms in this case) is represented as an array of delta function. We know that the Fourier transform

[2] OnGSAS, peak asymmetry can be accounted for by using the peak asymmetry variable, (asym).

of a finite length array is broadened, thus the finite size of the crystals will broaden reflections. It is the crystallite broadening that can produce both Lorentzian or Gaussian peak shapes, where the former is the more common of the two. However, it is often the case that the broadening is caused by a combination of the two.

3.5.8.2 Pseudo-Voigt profile

The Voigt profile, named after Woldemar Voigt, is a line profile that results from the convolution of two broadening mechanisms. One of which alone would produce a Gaussian profile

$$Y(x) = G(x) = \frac{C_G^{1/2}}{H\sqrt{\pi}} \exp(-C_G x^2). \tag{3.41}$$

Usually, as a result of Doppler broadening in spectroscopy, where,

$$x = \frac{2\theta_i - 2\theta_k}{H_k}, \tag{3.42}$$

where x is essentially the Bragg angle of the i^{th} point in the powder diffraction pattern, with its origin in the position of the k^{th} peak divided by the full width half maximum (FWHM). $2\theta_i$, is the Bragg angle of the i^{th} point of the powder diffraction pattern; $2\theta_k$, is the calculated (or ideal) Bragg angle of the k^{th} Bragg reflection, $C_G = 4\ln(2)$, and $\frac{C_G^{1/2}}{H\sqrt{\pi}}$ is the normalisation factor for the Gauss function such that, $\int_{-\infty}^{\infty} G_{(x)} \mathrm{d}x = 1$.

The Caglioti formula,

$$H = (U\tan^2\theta + V\tan\theta + W)^{1/2}, \tag{3.43}$$

is the full with half maximum (FWHM) as a function of for Gauss, pseudo-Voigt function. U, V and W are free variables.[3] Notably, the Caglioti formula is used to describe the broadening change with a sum of the instrumental and sample broadening. The instrumental broadening is stored in the instrument object through a Caglioti like formula, whereas sample broadening is computed for each phase from crystallite size and macrostrain (plus other microstructural defect parameters) which are stored in the phase objects.

The other broadening mechanism produces a Lorentzian profile,

[3]For the reader who is interested in running their own refinement, one should note that the terms outlined here are given different labels from those given within the GSAS program. To avoid confusion, these will hear be included. The microstrain, Y ,from the sub-lattice anisotropic broadening is given as LY. Microstrain anisotropy variables are given as L_{11}, L_{22}, L_{33}, L_{12}, L_{13}, and L_{23}. Radial displacement S_s is called "Shift", and x from the anisotropic particle size expression is LX. Finally, from the Cagoliti equation, U, V, and W are represented as GU, GX, and GW.

$$Y(x) = L(x) = \frac{C_L^{1/2}}{H^1\sqrt{\pi}}(1 + C_L x^2)^{-1} \tag{3.44}$$

Where $C_{\mathrm{L}} = 4$, and $C_{\mathrm{L}}^{1/2}/(\sqrt{\pi})H^1$ is the normalised factor for the Lorentz function such that $\int_{-\infty}^{\infty} L(x)dx = 1$, and,

$$H^1 = \frac{U}{\cos\theta} + V\tan\theta, \tag{3.45}$$

is the FWHM as a function of for the Lorentz function, Again U, and V are free variables. Voigt profiles are common in many branches of spectroscopy and diffraction. Due to the computational expense of the convolution operation, where the Voigt profile is often approximated using a pseudo-voigt profile,

$$Y(x) = PV(x) = \frac{C^{1/2}}{H\sqrt{\pi}}\exp(-C_G x^2) + (1+\eta)\frac{C_L^{1/2}}{H\sqrt{\pi}}(1 + C_L x^2)^{-1}, \tag{3.46}$$

where $\eta = \eta_0 + \eta_{12}\theta + \eta_{22}\theta^2$, When $0 \leqslant \eta \leqslant 1$, is the pseudo-voigt function mixing parameter, i.e. the fractional contribution of the Gauss function into the linear combination of Gauss and Lorentz function, η_0, η_{12}, and η_{22} are free variables. In other words, this parameter shifts the profile more towards a pure Gaussian or pure Lorentzian when approaching 1 or 0, respectively.

3.5.9 Substitutions

As previously mentioned the peak height is effected by the position of the atoms within the plane. One of the greatest causes for this is the substitution of atoms, or compounds. For example, it is known that apatite formed in solution can be subject to carbonate substitutions. In this case the PO_4 is substituted for CO_3.

3.5.10 Preferred Crystallographic Orientation

Preferred orientation occurs in the case where the samples being studied consist of tens of thousands of grains, but the grains are not randomly oriented. Some phenomenon during crystallisation and growth processing, or sample preparation have caused the grains to have a preferred crystallographic direction normal to the surface of the sample. The main problem with preferred orientation is that it creates a systematic error in the observed diffraction peak intensities.

In the case of plate-like and needle-like particles, these particles tend to lie flat on the surface of a flat plate geometry X-ray diffraction experiment. This enhances the intensities of some Bragg reflection, while reducing others. GSAS has two different functions that can be used for preferred orientation. The first is the March and Dollase function, first used in 1986 [143] , the second is the spherical harmonics function, first implemented in GSAS by Von Dreele in 1997 [144]. The March-Dollase function (MDF), can be used both in the situation when needle and plate shaped crystals are present in the sample. The axial symmetry of both of these shapes can be corrected for preferred orientation using a single pole-density profile. However, in the case of the spherical harmonics function (SHF), GSAS uses the general axis equation as described by Bunge [144]. In this case, the preferred orientation correction depends more on the reflection, and on the sample orientation. When there is just one preferred orientation direction, it is better and safer to use the MDF, because even though the SHF will give a better fit, it can also loose the physical meaning due to the use of too many coefficients of the polynomial refinement. Based on previous studies, we expect some samples to show preferred orientation given the fact that crystals will align along the c-axis, forming pillars of rod-like FAp. For this reason, MDF shall be applied at these stages, to see if any affect has been made on the XRD pattern. Weight percent, as we can see, we are able to derive the particle size from knowing the value of x_s. We can also find out the weight percent by the value of the scale factors, $\mathrm{S_{ph}}$, where the weight percent,

$$w_p = \frac{S_{\mathrm{ph}} m_p}{\sum_{p=1}^{Np} S_{\mathrm{ph}} m_p} \times 100. \tag{3.47}$$

As can be seen, the weight percent is defined in terms of the phase fraction as applied only to reflection from the p^{th} phase, $\mathrm{S_{sh}}$, and the unit cell mass, m_p, for phase, p.

3.6 Distribution functions

3.6.1 A history of atomic distribution functions and simulations

In the past 50 to 100 years, the knowledge on materials has greatly improved the ability to determine the atomic structure of increasingly more complex materials. More recently, the field of biomedical engineering has begun to experience the same revolution by extension.

From 1998 to 2007, there was a greater interest in developing alternative methods for the analysis of crystalline materials. Traditionally, crystal structure refinement involved analysis of the Bragg peaks in a diffraction pattern which provided the average long range

atomic order [145]. Of course, this is a limitation in the sense that not all materials are exclusively crystalline, and thus these other materials are not open to investigation. Previously, researchers had outlined how other methods such as total scattering measurements, which were able to explore the local, instantaneous atomic structure of a material, glass or liquid [146, 147] could aid in this regard. This method, capitalises on the weak diffuse i.e. non-Bragg, scattering that arises from the non-crystalline structure present within the material under analysis. The variation in the density of the material, or in other words the local order can be represented by the pair distribution function (PDF), $g(r)$ [146]. This real (r) space function is derived as the results of taking the Fourier transform of the so-called structure factor, $F(Q)$, where Q is the change in the wave vector scattering experiment as previously defined. This means that the resolution of the peaks in the PDF is directly related to the largest value of Q in the diffraction experiment, $Q_{\max}$, which is proportional to the maximum scattering angle, and inversely proportional to the wavelength of the beam. To achieve the largest $Q_{\max}$, and the best resolution in the PDF, see Fig. 3.11, the wavelengths used in total scattering experiments tend to use the shortest wavelengths practicable, < 0.5 Å.

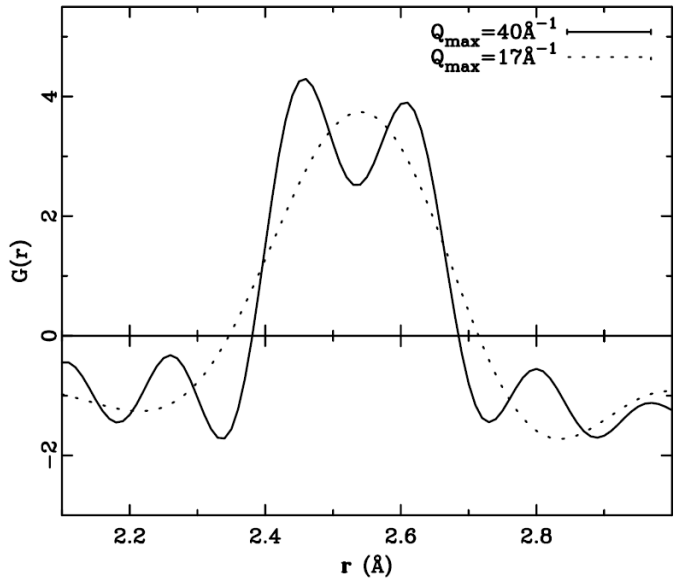

FIGURE 3.11: Example of the change in resolution with the change in Q, PDF around the nearest neighbour peaks of $ZnSe_{0.5}$ $Te_{0.5}$. The solid line corresponds to terminating at $Q_{max} = 40$ Å^{-1} clearly showing the two bond lengths Zn-Se and Zn-Te which differ by $\Delta r = 0.14$ Å. The dotted line shows the PDF obtained from the same data terminated at $Q_{\max} = 17$ Å^{-1}. In this case the peak split is smeared out, taken from [148].

Notably, radiation of this order can be found available at a reactor or pulsed neutron sources, such as ISIS in the UK, or at synchrotron x-ray sources, like Diamond, and also using laboratory sources such as an Ag-anode x-ray diffractometer. Reliable data was obtained for neutrons from what was then a new data analysis program, called

GUDRUN, and later GUDRUNx was a later version that was developed specifically for use in X-rays.

In 2011, Alan Soper and Emma Barney purchased an Ag-source x-ray diffractometer which was purpose built for ISIS users to obtain complimentary x-ray data for the materials they had investigated with neutrons. The system produced a mean Kα radiation wavelength of 0.5609Å, plus Kβ and the standard Bremsstrahlung radiation. With the maximum scattering angle near 156°, yielding a maximum Q of 21.9 Å^{-1}.

Experimental data derived from total scattering structure factors and radial distribution functions from neutron or x-ray scattering experiments have been used for structural analysis of various materials [149]. The structural models that can be derived from 'fitting' this data, typically through Reverse Monte Carlo Method, has found practical use in producing three-dimensional models for both liquid and amorphous structures without the requirement of interatomic simulations. In 2002, Thomas Proffen, et al, compared two simulated structures, both of which having the same lattice with one atoms per unit cell and the same concentration of vacancies. The distinguishing factor was the ordering in each, Fig. 3.12 [148].

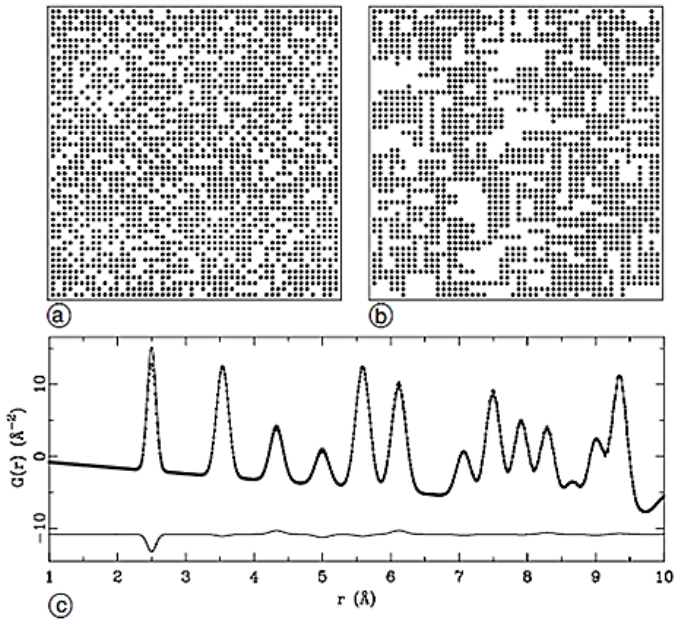

FIGURE 3.12: PDF comparison of the same material with different short range order, (a) shows a random distribution of vacancies and (b) preferred ordering in x and y directions. Panel (c) shows the corresponding PDFs for the random distribution (filled circles) and the short-range ordered distribution (solid line). The difference is shown below. Taken from [148].

As can be seen, Fig. 3.12(a) showed a random distribution, whereas Fig. 3.12(b) had chemical short range order (SRO), in this case vacancies arranged themselves along the

x- and y-direction. The PDF for both structures is shown in Fig. 3.12(c). What is important to note is that analysis of the Bragg scattering e.g. through Rietveld refinement would yield identical results for both structure. This is because the Bragg peak positions and intensities would be identical (i.e the average structure of both structures is the same, with the average occupancy being 70%). The two PDF data sets would also seem to show that there is no difference between the two structures. However, by observing the difference between the two, we can see that there is indeed some small difference in the short range order.

In 2003 [148], Thomas Proffen et al used the structure functions obtained from the $ZnSe_{1-x}Te_x$ [150] to generate corresponding PDFs. They were able to characterise the change in the bond lengths, as well as the formation and breaking of bonds when comparing the different compositions of $ZnSe_{1-x}Te_x$, see Fig. 3.13. They were also able to show that the PDF peaks broaden for intermediate compositions, and this in turn indicated that large static displacements were caused by strain in the alloys. Following on from this the PDF data of $ZnSe_{0.5}Te_{0.5}$, taken from work conducted by Peterson et al in 2001 [151], has also been compared to accepted interatomic potential models, such as the Kirkwood model [152], with a comparison between the PDF showing a mismatch of only 0.1–0.15 Å.

The local structures of doped magnets were studied in order to understand how the charge state affects the PDF [148]. Specifically the researchers wanted to understand the metal-to-insulator (MI) phase transition within the colossal magneto-resistant (CMR) magnetite $La_{1-x}Ca_xMnO_3$. In essence, the two phases can be considered as localised (insulating) and delocalised (metallic) phases. Again, different compositions of the material were analysed with neutron scattering experiments, and then subsequently Fourier transformed into PDF data. the PDF of each composition was compared to a resistivity vs. temperature analysis for the same compositions. They were able to show that the charges were able to localise upon heating, well before the MI transition temperature was reached. They also showed that in the lowest doped samples ($x = 0.12$) there was no evidence of an MI transition, however in the other two samples ($x = 0.21$, and $x = 0.25$) an MI transition could be observed, see Fig. 3.14

Following this, the PDF was carried out at on the $x = 0.25$ composition at two separate temperatures, $T = 20$ K and $T = 220$ K (at the MI transition). In this way, they were able to quantify the evolution of the phase separation as a function of temperature. By focusing on the range $1.7 < r < 3.2$ Å, a range that mainly describes the MnO_6 octahedra, they were able not only to show the difference between the localised and delocalised phases that were present at $T = 220$ K but also to extract the absolute

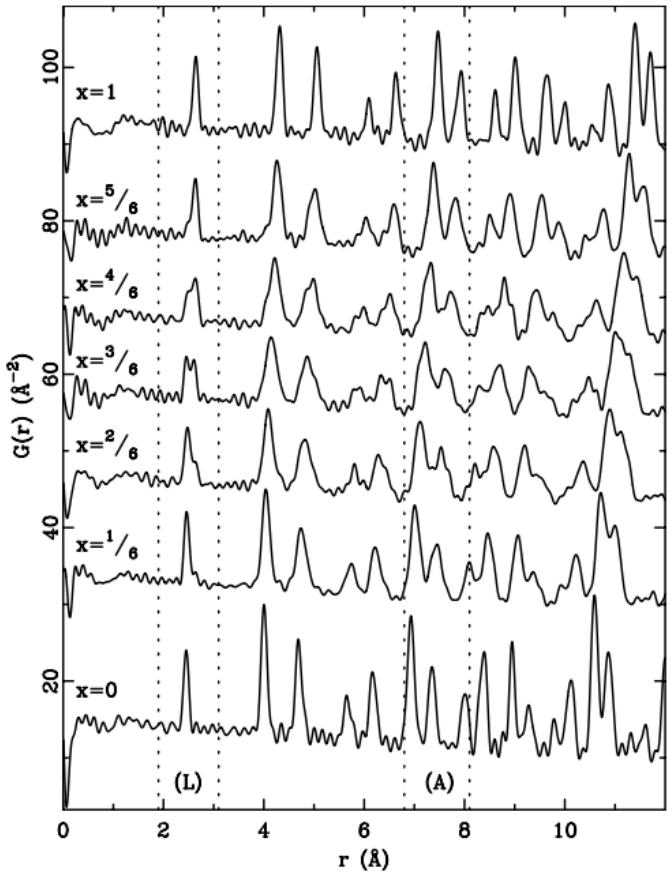

FIGURE 3.13: PDF, G(r), of $ZnSe_{1-x}Te_x$. Clearly showing two regions in which atom pair peaks show changes with a change in composition. Taken from [148].

proportions of Jahn-Teller and regular octahedra that were related to the localised and delocalised phases in the sample.

Thus we can see that a detailed analysis of the local structure of a material can yield a greater understanding of the properties exhibited on the macro-level, and it is through this technique that we aim to uncover the fundamental physical phenomena.

$G(r)$ will be defined later, but for now we can think of it as a histogram of all the interatomic distances. Within the community, there re a number of formalisms that are used to describe the same concepts. It can become confusing as some groups use the label G(r) and D(r) to mean the opposite to that of another group. These figures use the label G(r) to denote a function that we in our group would call D(r), which will be derived more formally later in this text.

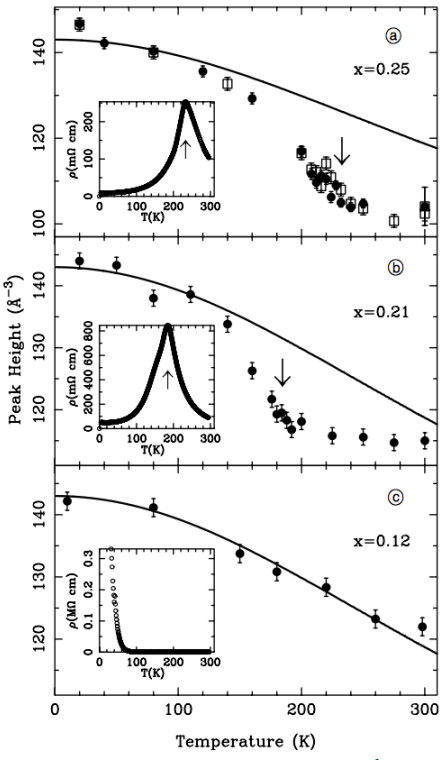

FIGURE 3.14: Normalized height PDF of $La_{1-x}Ca_xMnO_3$ at r = 2.75 Å vs. temperature for various conditions of x. (a) $x = 0.25$, (b) $x = 0.21$ and (c) $x = 0.12$. Insets show the resistivity vs. temperature for the same samples. The arrows indicate the MI transition temperature in both the insets an main panel. Taken from [148].

3.6.2 Pair distribution function, pair correlation function, and higher correlation functions

A sharp peak in the pair distribution function (PDF) will tell you at least three things. The first thing is the position of the peak will give the average bond length that exists between the two atoms, secondly, its width will indicate the temporal and spatial variations in the bond length (as said before, one source could be attributed to thermal motion of the atoms). Thirdly, the integral of the peak will tell you how many neighbours a single atom has.

To characterise the structure of a disordered material, the simplest function that can be conceived is the radial distribution function (RDF), also sometimes called the pair distribution function (PDF).

So what exactly is $g(\mathbf{r})$? Sometimes $g(\mathbf{r})$ is described as the probability of two atoms being separated by the distance r. We suppose the number density at some position in the material is $\mathbf{r}$ is $n(\mathbf{r})$, Fig. 3.15(a). The position of atom j is given by $\mathbf{R}_j$ in which case the local number density can be expressed as

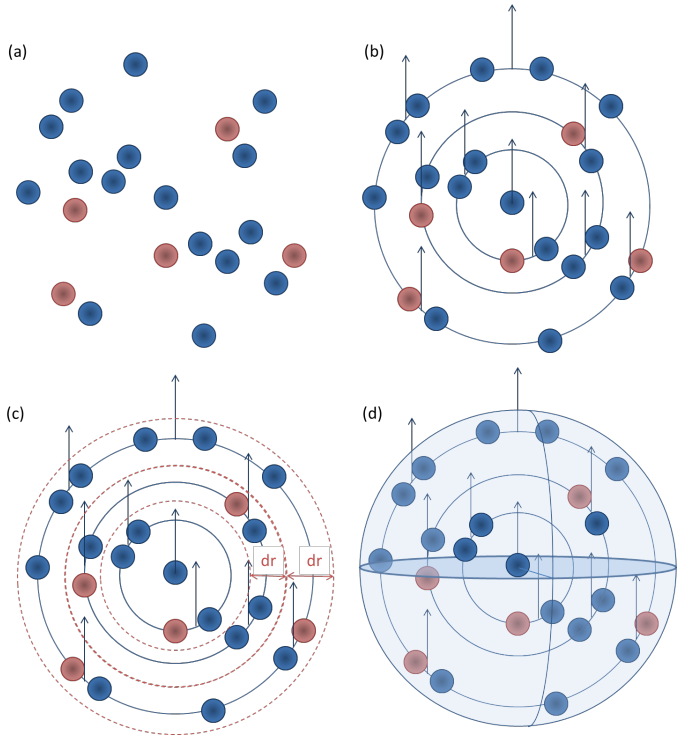

FIGURE 3.15: Graphic representation of (a) atoms within a material, (b) representing bonding pairs as existing on a circumference a distance r_i from the origin, each bonding pair is represented by a series of Dirac delta functions, (c) integration from $r = 0$ to $r = \infty$, (d) Spherical averaging for 3D modelling.

$$n(\mathbf{r}) = \frac{N}{V} = \sum_i \delta(\mathbf{r} - \mathbf{R}_j), \tag{3.48}$$

where the average is over the directions of $\mathbf{r}$.

If we roam around the material at the atomic level, and it is crystalline, we will see a regular fluctuation in the density caused by the repeated structure of the unit cell. However if it is a liquid or a glass there is no such regular order and all we will see is the random distribution of the atoms, except that there can be no atomic overlaps (unless the pressure is enormously high). This means that the centre of each atom is surrounded by a void caused by the repulsive interaction that takes over when atoms get too close to one another. Beyond that we would struggle to see very much because the arrangement of atoms would vary so much from place to place.

In order to learn more about how the atoms are arranged in the material we have to perform an autocorrelation on this density distribution:

$$G(\mathbf{r}) = \frac{1}{N}\int n(\mathbf{r}')n(\mathbf{r}'+\mathbf{r})\mathrm{d}\mathbf{r} = \frac{1}{N}\int \delta(\mathbf{r}' - \mathbf{R}_j)n(\mathbf{r}'+\mathbf{r})\mathrm{d}\mathbf{r} \tag{3.49}$$

where the last equality arises from substituting 3.48 into the middle term. It will be apparent that the terms with $j = i$ can be separated from those where $j \neq i$. Notably $\int_{-\infty}^{\infty} \delta(x-a)F(x)\mathrm{d}x = F(a)$, where in this case $r' = x$, and $a = r$. Hence we write

$$G(\mathbf{r}) = \frac{1}{N} \int n(\mathbf{r}' + \mathbf{R}_j) d\mathbf{r} \tag{3.50}$$

Let $\mathbf{r}' + \mathbf{R}_j = \mathbf{r}$, and use 3.48 again to form a description of a multi atom system.

$$G(\mathbf{r}) = \frac{1}{N} \int n(\mathbf{r}' - \mathbf{R}_i + \mathbf{R}_j) d\mathbf{r} \tag{3.51}$$

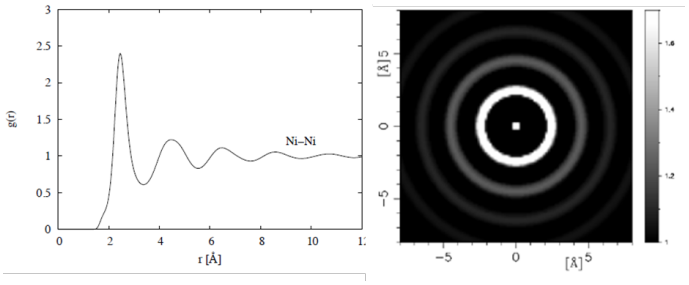

FIGURE 3.16: Example pair distribution function, $g(r)$, for supercooled liquid nickel shown in 1-dimensional (top) and 2-dimensional (bottom) representations. Derived from data shown in [153, 154].

As previously stated, we can represent the charge density of the atom (in this case the electron cloud) by delta functions Fig. 3.15(b). 3.51 describes the distribution of the atoms at a distance i and j from the origin, however we can include another $\delta(\mathbf{r})$ to describe the central atom.

$$G(\mathbf{r}) = \delta(\mathbf{r}) + \frac{1}{N} \int n(\mathbf{r}' - \mathbf{R}_i + \mathbf{R}_j) d\mathbf{r} = \delta(\mathbf{r}) + \rho g(\mathbf{r}) \tag{3.52}$$

where ρ is the average atomic number density (typically expressed in units of atoms per Å^{-3}). It can be seen therefore that $G(\mathbf{r})$ divides into two parts, a "self" part involving correlations of an atom with itself, and a "distinct" part involving correlations between distinct atoms. Equation 3.52 acts as the formal definition for $g(\mathbf{r})$. In effect you are sitting on an atom and counting all the atoms that you find at a given displacement, $\mathbf{r}$, from that atom, converting that number to a local density. This local density is then averaged over all the atoms in the system and compared with the density of atoms in the system as a whole. Therefore $g(\mathbf{r})$ is a convenient way of keeping track of how the local number density varies with respect to an atom on average and with respect to the average number density. The properties of the Dirac δ function are such that,

$$\int d(\mathbf{r})d\mathbf{r} = 1.0 \tag{3.53}$$

.

We can further describe $G(\mathbf{r})$ in terms of the fraction of the atoms, $c_\alpha = \rho_\alpha/\rho$, of atom type α. Where ρ_α is the number density of atoms of type α,

$$G(\mathbf{r}) = \sum_i c_i\delta(\mathbf{r}) + \rho\sum_{i,j}\delta_{i,j}c_ic_jg_{ij}(\mathbf{r}), \tag{3.54}$$

where the Kronecker δ_{ij} is needed in equation 3.54 to avoid double counting pairs of atoms of the same type. The atomic fractions are needed to take account of the different percentages of the different types of atom present.

3.6.3 Radiation diffraction theory

By consideration of the scattering amplitude $A(Q)$ one can describe the effect of the scattered wave that interacts with the charge density previously described by delta functions.

$$A(\mathbf{Q}) = \sum_i f_i(Q)e^{i\mathbf{Q}\cdot\mathbf{R}_i} \tag{3.55}$$

Where $f_i(Q)$, is the atomic scattering factor of the wave scattered by said charge density. We can use this to derive the structure factor, $F_i(\mathbf{Q})$, which is the scattering intensity per unit atom.

$$F(\mathbf{Q}) = \frac{1}{N} \mid A(\mathbf{Q}) \mid^2 = \sum_i f_i(\mathbf{Q})e^{i\mathbf{Q}\cdot\mathbf{R}_i}\sum_j f_j(\mathbf{Q})e^{i\mathbf{Q}\cdot\mathbf{R}_j} \tag{3.56}$$

given $\mid A(\mathbf{Q}) \mid^2 = A(\mathbf{Q})A^*(\mathbf{Q})$.

$$F(\mathbf{Q}) = \sum_i c_if_i^2(Q) + \sum_{ij} f_i(Q)f_j(Q)e^{i\mathbf{Q}\cdot(\mathbf{R}_i-\mathbf{R}_j)}\delta_{ij}\int c_ic_j\rho g_{ij}(\mathbf{r}), \tag{3.57}$$

From here we can define the dynamic scattering factor, $S(\mathbf{Q})$, as:

$$S(\mathbf{Q}) = \int \rho g_{ij}(\mathbf{r})e^{i\mathbf{Q}\cdot(\mathbf{R}_i-\mathbf{R}_j)}\mathrm{d}r, \tag{3.58}$$

Which accounts for the change in energy of X-rays and the phase difference between atoms. From here we can take an average $S_{ij}(Q) = \langle S_{ij}(\mathbf{Q}) \rangle$ and setting $r = \mathbf{R}_i - \mathbf{R}_j$ we can express the following:

$$S(\mathbf{Q}) = \int \rho g_{ij}(\mathbf{r}) \langle e^{i\mathbf{Q}\cdot\mathbf{r}} \rangle \mathrm{d}r, \tag{3.59}$$

$$\langle e^{i\mathbf{Q}\mathbf{r}} \rangle = \frac{\sin(Qr)}{Qr}, \tag{3.60}$$

Thus

$$\langle S(\mathbf{Q}) \rangle = 4\pi\rho \int r^2 g_{ij}(r) \frac{\sin(Qr)}{Qr} \tag{3.61}$$

Where $4\pi r^2$ is included to account for the spherical surface area of successive lamella, Fig. 3.15(c and d). A shell of large radius will contain a more uniform sample of atoms. Thus, at $r \to \infty$, $g_{ij}(\mathbf{r}) \to 1$, as the probability of finding an atom is high. We need to subtract this from the data, because it does no more than add a constant. Whereby a constant in a Fourier transform will give a delta function at $Q = 0$. Hence we can rewrite the corrected dynamic scattering factor, $i(Q)$ as:

$$i(Q) = 4\pi\rho \sum_{ij} f_i(Q) f_j(Q) c_i c_j \int r^2 (g_{ij}(r) - 1) \frac{\sin(Qr)}{Qr}, \tag{3.62}$$

Where we can define all real space terms as the differential correlation function, $D(\mathbf{r})$

$$D(r) = 4\pi\rho r \sum_{ij} f_i(Q) f_j(Q) c_i c_j (g_{ij}(r) - 1), \tag{3.63}$$

Thus from here we can see that $D(r)$ is the Fourier transform of $Qi(Q)$ such that:

$$Qi(Q) = \int D(r) \sin(Qr) dr, \tag{3.64}$$

and

$$D(r) = \int Qi(Q) \sin(Qr) dQ, \tag{3.65}$$

where an example is given in Fig. 3.16.

3.6.4 Normalisations

$G(r)$ is often normalised to remove the scaling arising from the species concentrations and scattering lengths [155], i.e.

$$G'(r) - 1 = G(r) \Big/ \Big(\sum_{i=1}^{n} c_i f_i(Q) \Big)^2, \tag{3.66}$$

which when rearranged, leads to

$$G'(r) = \Big(\sum_{i=1}^{n} c_i f_i(Q) \Big)^{-2} \sum_{i,j=1}^{n} c_i c_j f_i(Q) f_j(Q) g_{ij}(r). \tag{3.67}$$

This function now has the same limiting values as the $g_{ij}(r)$ from which it is composed:

$$G'(r < r') = 0, G'(r \to \infty) = 1$$

3.7 Molecular dynamics

In general, molecular dynamics (MD) is a computer simulation method that studies the physical movement of atoms and molecules. As the simulation runs, the atoms are permitted to interact for a fixed period of time, in this way a dynamic evolution of the system can be observed. Typically, the trajectories of the atoms and molecules are determined by numerically solving Newton's equations of motion for a system of interacting particles in which both the force and the potential energies between the particles are calculated using interatomic potentials. Originally, this method was developed within the field of theoretical physics in the 1950s [156–158] but is commonly used today within the fields of chemical physics, materials science and the modelling of biomolecules.

`DL_POLY` is a MD simulation package that has been developed by the CCP5 community at the Daresbury Laboratory since 1994 [159]. MD is a way of solving newtonian equations of motion for a collection of atoms that are run over a period of time separated by time steps. In the case of the replicated data (RD) strategy, it was chosen due to the fact that it offered the simplest approach to complex force fields. However, the first version using this method was only circulated in house, among collaborators for testing. Later in 1996, this package was released to the public as `DL_POLY_2`, written by T. Forester and W. Smith.

Today, this system has further developed in to two packages, `DL_POLY_Classic`, written by Bill Smith and Tim Forester, and `DL_POLY_4`, written by Ilian Todorov and Bill Smith. The distinction between the two lies in the fact that `DL_POLY_Classic` uses a RD strategy which works well for systems containing up to 30,000 atoms on up to 100 processors. `DL_POLY_4` is based on the Domain Decomposition (DD) strategy and is best suited for large simulations from 10^3 to 10^9 atoms on large processor counts. However, the packages are reasonably compatible so it is possible to scale up or down in order to move between them with little effort.

In 2006 [160], researchers at the University College London were able to use `DL_POLY` to simulate the uptake and distribution of carbonate groups into the hydroxyapatite lattice. Their research focused on the formation of both A-type and B-type substitutional defects. They were able to compare their results to various experimental techniques, such as x-ray diffraction, Fourier transform infra-red spectroscopy, electron paramagnetic resonance, electron-nuclear double resonance, nuclear magnetic resonance and neutron scattering. They were able to find that when a phosphate group was replaced by a carbonate group that it was also compensated by the substitution of sodium or potassium, and that B-type defects were energetically favourable ($\Delta H_{\mathrm{Na}} = -71$ kJ.mol^{-1}, $\Delta K_{\mathrm{K}} = -6$ kJ.mol^{-1}). However, over all they found that A-type defects in which two hydroxy groups are replaced by one carbonate group in the hydroxyl channel is the most stable defect structure.

As far back as 1987, it has been proposed that amorphous calcium phosphate (ACP) was the first calcium phosphate phase to nucleate from aqueous solution [161]. Even though the supersaturation of HAp in body fluids should permit direct nucleation, it has been found that this process is inhibited in vivo, permitting other calcium phosphates to precipitate before HAp [162], which in turn supported the potential for an ACP precursor phase.

Going further back still, in 1974 [163], Bettes, and Posner, identified that what was referred to as ACP could be characterised by spherical domains approximately 1 nm in size and a Ca/P ratio of 1.5 as well as a chemical formula of $Ca_9(PO_4)_6$, which would be referred to as Posner's clusters. Later studies suggested that the aggregation of these clusters formed the building units of HAp [164, 165]. More recently, in 2017 [166], Giulia Mancardi et al used an interatomic potential model developed by Ainsworth et al [167] to describe the intermolecular and interatomic actions of calcium-sodium-phosphate species in order to represent the Posner's cluster both in hydroxyapatite, C3 symmetry, and in water, see Fig. 3.17.

In their experiment, they were able to produce a range of different compositions of Posner's cluster by changing the composition of the starting solutions. From this they were

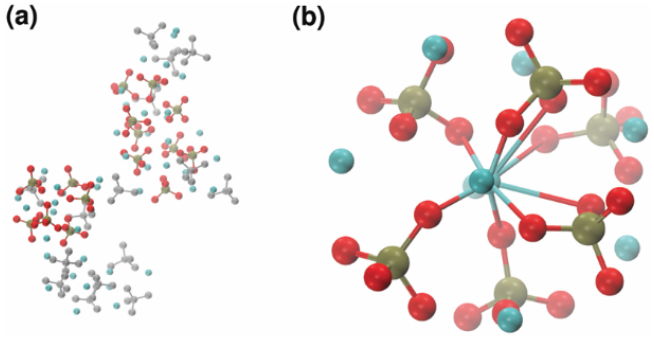

FIGURE 3.17: Molecular dynamics simulation of (a) aggregates after 5 ns: (b) detail of one of the Posner-like clusters formed with formula $Ca_9(PO_4)_6$. Colour key Ca: light blue, P: green, O: red, atoms not forming Posner's clusters: grey. Taken from [166].

able to use classical MD simulations (`DL_POLY_4`) to show the aggregation of Ca^{2+} and $PO_4{}^{3-}$ in solution. Under neutral conditions, Posner-like clusters deficient in calcium ions and composed of protonated phosphate groups formed spontaneously after a few ns. Thus their work was the first theoretical investigation that supported experimental findings that the structure of the Posner's cluster in solution, and confirmed the formation of the species in the early stages.

3.7.1 Integration algorithms

In a sense, molecular dynamics is a form of virtual reality which is focused on the atomic scale. It uses mathematical models to describe the forces between atoms during the simulation process. The configuration of the atoms changes over time providing the ability for the user to gain a sequence of snap shots of the system progression. Thus it is the positions, velocities and forces acting on the atoms from the previous time point that is used to direct the next stage. One example of using Newtonian mechanics, namely *force* = *mass* × *acceleration*. What should be noted is that in nature, this equation was integrated treating time as a continuum. However, in MD the snap shots are separated by the interval Δt known as the time step. This means that we need a method to generate the snapshot at time $t+\Delta t$ given that we have snapshots at times t, $t-\Delta t$, $t-2\Delta t$ etc. This means that not only does the method need to be resilient over many time-steps but also needs to satisfy time reversal. We can solve the first idea by expanding a spatial coordinate as a Taylor expansion in both the forward and backward direction in time.

3.7.2 The molecular dynamics method

Also known as the Verlet integration algorithm. This approach provides values for the velocities with a lower accuracy than for the positions. They are also always one step behind with the calculation of the velocity. Moreover, this algorithm updates the position without any reference to the velocity, which reduces the accuracy on the velocity as it is not propagated into the updated positions. One way to solve these issues is to use a refined version of this algorithm. The velocity Vertlet method is such a version. In this case, the system is able to generate more accurate velocities at the same time step.

3.7.3 Thermodynamic ensembles

3.7.3.1 Microcanonical (NVE) ensemble

The integration algorithm previously discussed updates the positions and velocities of the atoms in the system. As one might expect, the total energy of the system (potential plus kinetic) should be conserved, and that is exactly what we see. In a set-up in which the volume of the configuration has not been allowed to change, we refer to it as a constant-volume, constant-energy ensemble. This is given the abbreviation NVE to acknowledge that the number of particles is also conserved. In statistical mechanics, this ensemble is referred to as the micro-canonical ensemble.

3.7.3.2 Constant pressure (NPH) or constant stress (NSH) ensembles

In the case where one would want to permit the size and shape of the simulation to change, it is possible to treat the components of the edge vectors of the configuration, or the components of the strain tensor, as new dynamical variables. These variables can be coupled to the atomic variables by rescaling coordinates. The Hamiltonian (or Lagrangian) which contain both potential energy and kinetic energy terms (with the variables being coordinates and there time derivatives, i.e.velocities) are used to generate the equations of motions.

It was Rahmann and Parinello who were the first to successfully develop an approach for the case of having variable shape. They defined the three edge vectors of the sample configuration as $\mathbf{a}$, $\mathbf{b}$, and $\mathbf{c}$, and defined the square matrix, $\mathbf{h}$, as constructed from these three vectors arranged in columns. The volume V is given by $V = \det(\mathbf{h}) = \mathbf{a} \cdot (\mathbf{b} \times \mathbf{c})$. The position of the particle can be written by defining the column vector $\mathbf{s}_i$ with the fractional coordinates x_i, y_i and z_i such that the position of an atom is given as $\mathbf{r}_i =$

$\mathbf{h} \cdot \mathbf{s}_i = x_i\mathbf{a} + y_i\mathbf{b} + z_i\mathbf{c}$. The square of the distances between the two particles is also given as $r_{ij}^2 = \mathbf{s}_{ij}^{\mathrm{T}} \cdot (\mathbf{h}^{\mathrm{T}} \cdot \mathbf{h}) \cdot \mathbf{s}_{ij}$.

The Hamiltonian is given as

$$\mathcal{H} = \frac{1}{2}\sum_i m_i \dot{\mathbf{s}}_i^{\mathrm{T}} \cdot (\mathbf{h}^{\mathrm{T}} \cdot \mathbf{h}) \cdot \dot{\mathbf{s}}_i + \frac{1}{2}\sum_i E(\mathbf{s}_i, \mathbf{h}) + \frac{1}{2}M\mathrm{Tr}(\dot{\mathbf{h}}^{\mathrm{T}} \cdot \dot{\mathbf{h}}) + PV,$$

where the first, second and third terms describe the kinetic energy of the atom, the potential energy of the atom, and the effective kinetic energy of the cell. The pressure, P and the volume, V of the system presented in the fourth term. In essence, this expression allowed the cell vectors to vary, in doing so, allowing the shape of the box to change.

3.7.3.3 Constant temperature (NVT or NPT) ensemble

The ability to control temperature has been important even in the earliest days of MD simulations. This was achieved by starting with an initial set of velocities that were consistent with a given temperature. In the initial time steps this potential energy would be converted into kinetic energy, which would mean that the sample would heat up. At this stage the simulation would periodically rescale the velocities until the simulation temperature would oscillate around a mean value close to the intended temperature. After which the simulation would run in the NVE ensemble for any further analysis. However, this method is not suitable when the heat energy of the simulation needs to change continually to maintain a constant temperature. For this reason a number of recalling variants were proposed, and some of these variants have found there way into `DL_POLY`. Even though these methods enabled the MD simulation to operate around a chosen temperature, it was found that such methods do not obey the conservation law and do not correspond to any statistical mechanics ensemble. This was solved by a method developed by Nosé [168]. He introduced a new variable into the hamiltonian that scaled the momentum rather than the space.

3.7.4 Rigid bodies

In some cases, it has been useful to implement restrictions on the atoms. One of these restrictions is referred to as rigid bodies. In the normal case, atoms have 6 dynamic variables to describe their trajectories. Three for position, and three for momenta. In the case of rigid bodies, the set-up is extended to include orientational variables and the corresponding angular momentum variables. For example, a three-dimensional

rigid body requires three angular variable to describe its orientation. Notably, if you consider the moment around a sphere, we know that displacements in x, y, and z are not simple translated into rotations. A translation along x and then along y, is the same as a translation along y and then along x, but rotations about orthogonal axes do not commute. The common way to describe the orientations are the Euler angles. In this case the system is rotated by and angle, α, about the z axis, then rotated about an angle, β, about the x axis, and finally a rotation of, γ, about the z axis.

Sadly, MD simulations also have problems with Euler angles. If we consider polar angles with a rotation about x by an angle, θ, which is then followed by another rotation of ϕ about the original z axis. In the instance that $\theta = 0$ the angle ϕ becomes undefined. This means, that if θ and Φ are dynamic variables of the system, which they are, the system becomes unstable at $\theta = 0$. The solution is to use cartesian coordinates, the at subject to $x^2 + y^2 + z^2 = 1$. This generates a situation in which 2 independent variable are expanded to 3 with a constraint that avoids the instability problem when $\theta = 0$. Again, the same issue occurs with Euler angels when $\beta = 0$, and the solution is to invent new parameters analogous to the set (x, y, z). In which case we expect to have 4 new variables subject to the same quadrature constraints. These new variables are called the quaternions.

3.7.5 Ewald sum

MD simulations of the lattice can experience problems that arise in the Coulomb interactions. This can be due to issues in energy conversion caused by the turn on and off of interactions when the particles cross a pre-defined cut off. In the case of short-range interactions the cut-off is normally set such that atoms do not interact with copies in more than one configuration box. On the contrary, Coulomb interactions require interactions to distances $r = \infty$.

Contribution form the short-range is calculated in real space, whereas the contribution from that of the long-range contribution is computed via the use of a Fourier transform. Doing it this was allows for a higher accuracy to be achieved for long-range interaction. Furthermore, it progresses at a reasonable computing speed. Thus, it has been used as the standard method for dealing with long-range interactions in periodic systems. It should be noted that this method requires charge neutrality of the MD system to accurately calculate the total Coulombic interactions. A study of the truncation errors introduced in the energy and force calculations of disordered point-charge systems is provided by Kolafa and Perram [169].

Chapter 4

The Effect of Surface Roughness on the Formation of Bioactive Apatite Dental Implant Coatings

4.1 Key aims

- To find the best synthesis method for the production of aligned apatite coatings.
- Use a range of methods to analyse the
    1. Surface qualities (both chemical and roughness)
    2. Solution chemistry
    3. Temperature
- To see if the application of the organic BISTRIS buffer is able to promote the production of apatite over that of other crystal phases such as brushite or monetite.
- To compare this work with that previously found in literature before developing the field.

4.2 Introduction

The use of artificial dental prosthesis can be traced as far back as ancient Kemet 5,500 years ago [170]. However, it was not until 1940 when osseointegration (the direct structural and functional connection between living bone and the surface of a load bearing

artificial implant) was first observed by Bothe, Beaton and Davenport [171]. They implanted titanium in to animals and remarked at how it had the tendency to fuse with bone. Later, the concept that an implanted prosthesis had the capability to exist in harmony with the tissue without causing harm to the body would be first defined by the word biocompatibility in 1970 by CA Homsy [25]. However it would take almost two decades before this word emerged as a common term within the scientific literature. During this time advances in implantology would lead Branemark to use integrated titanium fixtures in the treatment of edentulousness, published in 1981 [172]. Albrektsson, having worked under Branemark published his thesis in 1979 on the subject of bone grafts, but he would later, in 1986, define the criteria for implant survival [173], which is dependent on the relationship between the following 6 factors:

1. Implant biocompatibility,
2. Macroscopic and microscopic nature of the implant surface,
3. The status of the implant bed in both a healthy (non-infected) and non-healthy,
4. The surgical technique used,
5. The undisturbed healing process of the subsequent prosthetic design, and
6. long-term loading phase.

From the late 1980s to 1990s [173–178], a stronger focus on understanding the reasons why dental implant failures occurred from such factors as apposition (the normal physiological formation of bone), and jaw bone resorption [1] were pursued. For instance, in 1987, S. D. Cook found that the use of hydroxyapatite-coated titanium implant improved not only integration rate but also strength, soon after hydroxyapatite-coated implants were used in animal testing [174], In 1989 M. S. Block used dogs as study subjects [174], and in the same year Lewandowski published investigations regarding structural failure [173]. Maistrelli in 1993 revealed that bone apposition was enhanced by the hydroxyapatite-coatings, in which apposition was approx. 72% higher when coated [176]. In 1994, Nancollas and Tucker showed that hydroxyapatite-coating failures can be classified as dissolution or resorption of the coating at the coating-titanium interface, which could lead to damaging effects with regard to the clinical use of the hydroxyapatite-coated implant [177]. Later in 1995 Takeshita made histological observations of 7 endosseous dental implants, and in 1996 Takeshita showed that hydroxyapatite-coated blade-form implants survived in the human mandible for 5 years showing 73.5% bone contact [178].

[1] Resorption - a process by which all or part of a bone structure is lost due to the activation of the body's innate capacity to remove mineralized tissue. For implantation this can lead to implant loosening and eventually failure

Since Ti implants have been studied longer than hydroxyapatite-coated Ti (HACTi) implants there exists a disparity in our understanding between the two. As recently as 1999, clinical studies for HACTi implants have a maximum study of 8 years, whereas titanium implants, had been studied over a 25 year period for screw implants alone [179]. This can be a problem as clinicians need to consider the possible failure of the coatings resulting from the coating-substrate interfacial structure; furthermore they need to be familiar with the materials characterisation in order to carry out effective clinical trials.

In 2003, Aebli used an in vivo comparison study between HACTi implant with titanium implants, and quantified the level of improvement that could be achieved with hydroxyapatite-coatings [180]. It was observed that HACTi implants, showed 139% higher biocompatibility and 48% higher osseointegration 2-4 weeks after implantation when compared to non-coated Ti (nCTi) implants. In 2011 Sukumaran described how for almost a decade from 1999 to 2007 implant surfaces had been developed based on the understanding that geometry and surface topography have a direct influence on the speed and strength of osseointegration [16].

It is clear that the lack of knowledge in apatite-coatings is a gap within the field of dental materials research. In this chapter, we will aim to develop a greater understanding of "apatite implant coatings" by understanding how different levels of surface roughness can effect the formation and structure of apatite at the nanoscale. Our aim is to find out how a variety of conditions including temperature, surface roughness and solution chemistry will affect the abundance of each species and the morphology at the nano scale.

We used HAp and Ti substrates to mimic the apatite coated and uncoated implant surfaces. The different temperatures were used to help to find the optimal temperature for the formation of the aligned rod-like apatite coating and to note the changes in the products due to the changes in the kinetics of the system.

4.3 Materials and Methods

4.3.1 Surface roughness analysis

Surface roughness were carried out using a BRUKER DEKTAKX stylus profilometer. Calibration was carried out using a Veeco SN96297 standard calibration sample with a step height accurate to 9.5 ± 1.0 Å. An average measurement of the peak and trough heights were taken and compared to the known value. 1000×1000 μm map scans were taken with both a 2.0 μm and 12.5 μm radius stylus for comparison. A duration of

10 seconds was selected with a map resolution of 20 μm/trace. The number of traces was set to 50, a 'Hills and Valleys' profile was selected. In the case of hydroxyapatite substrates, the force was determined by taking measurements at 1, 2 , and 3 mg, and then comparing the average step heights of each. These were found to be 0.70, 0.73, and 0.71 μm, respectively. Thus, 2 mg was chosen as it gave the greatest level of step height. The same settings were used on etched hydroxyapatite samples. while the stylus force of 4 mg was determined for the Ti substrates through trial, and subsequently ETi substrates.

4.3.2 Preparation-substrates

In this experiment, the surface topography and porosity of Ti and HAp substrates were varied via acid etching, respectively. This gave the experiment four different substrate surfaces (Ti, ETi, HAp and EHAp) on which to carry out apatite nucleation. 36 of the 20% porous pressed hydroxyapatite, HAp, substrates (from plasma Biotal Ltd, North Derbyshire, UK) were prepared before synthesis by etching with orthophosphoric acid 85% (specified, Fisher, Scientific UK Ltd, Leicestershire, UK) for 30 seconds. All discs were then rinsed with deionised water and dried with filter paper. Disposal of all acids was carried out using the lab safety protocols. In order to significantly etch the Ti substrates, a stronger acid was used. 36 of the commercially pure Ti (from Ti-TEK LTD, UK) were etched using a 1:1 ratio of hydrogen peroxide 50% GPR RECTAPUR (H_2O_2) (VWR International Ltd, Leicestershire, UK) and H_2SO_4 49-51% (Fluka Analytical®, Sigma-Aldrich®, St. Louis, MO) was used; by adding 10 ml H_2SO_4 very slowly to a beaker of H_2O_2 then left for 24 hours. Discs were subsequently removed, rinsed thoroughly with deionised water and dried using air and filter papers [181].

4.3.3 Mineralising solutions

Calibration of the pH meter was conducted at the beginning of the experiments using three serial standards of solutions of pH 4.01, 7.0 and of 10.01. A wet chemical precipitation solution was made by mixing 0.532 g HAp (sintering grade Capta Rl®powder, Plasma Biotal Ltd, North Derbyshire, UK) and 0.045 g sodium fluoride, NaF, into 500 ml of deionised water at 21°C. Powders were weighed using a DENVER INSTRUMENT SI-403, accurate to 0.001 g. The solution was magnetically stirred while nitric acid (69% AnalaR NORMAPUR, VWR international Ltd, Leicestershire, UK) was added drop wise via micropipette (p100 pipette adjusted to 50 μg) until a pH of 2.4 was reached. Once pH 2.4 was reached, ammonium hydroxide (28-30%, Sigma-Aldrich®, st. Louis, MO) was added drop wise until a pH 6 was reached.

Buffered solutions were also prepared by adding 7.3234 g of BisTris buffer [2] was added to 1000 ml double deionised water to make a 35mM solution. For this variation, BisTris buffer was added to the precipitating solution before NaOH. In this way the pH change attributed to the addition of the buffer could be better controlled. After BisTris buffer was added a pH of 5.54 was reached, after which NaOH was used to raise the pH up to 6.00. This solution was then added to the mineralisation solution at a ratio of 1:9 when incubating. In this way, BisTirs buffer was used to maintain the pH level near pH 6.00 to prevent the formation of unwanted CaPs that would more readily precipitate at lower pH values.

4.3.4 Powder collection - for structural and chemical characterisation

Powders were collected from solution since as the quantity that was precipitated on the surface of the substrates was to small to be used for NMR, FTIR and XRD analysis. This is because the quantity precipitated on the surface of the substrate was too small to be used with these techniques. A series of methods were trialled to determined the best approach to collect the largest quantity of material from each specimen vial for analysis. The first used filter paper, 150 mm (Fisherbrand, Fisher Scientific, UK). This method did not yield enough powder to be useful, as most powder became traped in the filter paper. the second utilised a syringe to remove the supernatant and then air dry for 1 week. This clearly had the problem of potentially allowing the solution to continue crystal maturation at a different temperature and concentration. The final method used a centrifuge set to 3000 rpm for 5 mins. Here all 3 repeats were mixed to maximise the powder quantity. Alternatively, in the case of solution analysis, 80 ml of solution was incubated at each temperature as opposed to 25 ml, allowing a greater amount of solution to be derived. 80ml solution produced 0.124 $\pm$ 0.001 g of powder, enough to fill an NMR rotor with a 14 μm inner volume. In the case of 25 ml, there was not enough powder produced to accurately measure by scales or analyse via NMR.

4.3.5 Incubation–apatite coating synthesis method

The precipitation solution was poured into 25ml vials containing either HAp, or Ti substrates of diameter 15mm in each case, 3 repeats were used. Following this the vials were sealed and then placed in a fridge set to temperature 5°C, 3 repeats for each substrate were incubated at room temperature with an average of 21°C, incubators (LTE Scientific LTD, Oldham, UK) set to temperatures 37°C, the final set were incubated

[2] BisTris Buffer is a buffering agent used in biochemistry. It is an organic tertiary amine with labile protons having a pKa of 6.46 at 25°C, and it is an effective buffer between pH 5.80 and 7.20

at 54°C, 70°C, 90°C using a water bath (Fisher®brand, Fisher Scientific UK Ltd, Leicestershire, UK) with 3 repeats for each substrate in each temperature. After 7 days samples were removed from incubators. It is believed from previous studies [71] that by this method apatite nano-crystals are formed through a precipitation process along with other possible phases of crystal growth and or compounds. Samples were rinsed with deionised water removing any excess crystals that did not form a strong bond with the surface, and then were air dried for 2 days. This precedure was repeated for the etched counterparts

4.3.6 Spectroscopic and microscopic analysis

For analysis via scanning electron microscopy (SEM), samples were coated with Gold-Palladium (Au/Pd) (AGAR AUTO SPUTTER COATING, Agar Scientific, Elektron Technology, UK Ltd, Essex, UK) for 30 seconds. This permitted spectroscopic analysis via Scanning electron microscopy, SEM (FEI Inspect F, Hillsboro, Oregon, USA), up to length scales of 80,000 ×. Here measurement of nano-crystal size and identifying whether rod-like morphology with a hexagonal group structure was formed (indicating the formation of apatite) lower magnifications 300 × were used to analyse levels of coverage which was quantified with further image analysis. Magnifications of 70 × was used to compare structures with larger morphologies which also had large areas of coverage.

Elemental analysis was carried out using energy dispersive x-ray (EDX) detector (Inca X-ACT, Oxford instruments, UK). EDX mapping was used and set to identify the presence of F, Ca, and P in order to identify the possible presence of apatite, and to determine the Ca/P ratio within the observed mineral morphologies.

Chemical analysis was carried out to check the validity of FAp production using Fourier transform infra-red (FTIR) (spectrum GX, Perkin Elmer®, Waltham, MA, USA). Here the infra-red window was cleaned using ethanol, and then a scan of the background was taken. After which the powder sample was placed over the IR window, covered with a metal disc, and then the sample was scanned. The program was set to take a sum of 10 scans, to analyse the samples between a wavenumber of 4000 cm^{-1} to 450 cm^{-1}, with respect to absorbance. Files were saved as ASCII format, and data was normalised to compare between different spectra, using Microsoft (MS) Excel.

4.3.7 Diffractometry

A flat plate geometry was employed to analyse the XRD spectra from the nano-crystals that were specifically precipitated on the surface of the substrates. Diffractometry was used to analyse the crystals that were precipitated on Ti and HAp disks from all incubation regimes. The (002) plane reflections were determined and identification of hexagonal structure using Rietveld refinement to identify the presence of apatite. A $\theta/2\theta$ arrangement was used to analyse Ti substrate samples. This was done to see if there was enough sample precipitated to be analysed by the grazing incidence method. Due to the unmeasurably small amount of synthesised mineral precipitate, grazing incidence was also used to acquire diffraction data, here the mineral precipitate did not need to be removed from the surface of the substrate instead the beam depth could be varied to prevent data collection that included that of the substrate itself.

The specimens were analysed using X-ray diffraction using a diffractometer (Bruker D2 Powder Diffractometer). Cu-source XRD, (Cu-XRD), Cu-K_α radiation ($\lambda = 1.54056$ Å) at 40 kV/40 mA was used. The diffraction pattern was taken in the 2θ range of 10° to 70° with a step size of 0.04°. The diffraction data were analysed by the Rietveld method [194] using the computer program GSAS [195] and used for phase analysis.

4.3.8 Analysis and identification of morphologies

Scans taken using SEM was used to search for morphologies at each of the incubation variants. Morphologies that have been found in previous scientific publications were identified and named to reflect the literature; new morphologies are given names based on the appearance, and used simply as a method for distinguishing one from other.

4.3.9 Nuclear Magnetic Resonance

^{19}F MAS NMR experiments performed on precipitated powders were performed using a Bruker 600 MHz (14.1 T) spectrometer. ^{19}F NMR data were collected at a Larmor frequency of 564.7 MHz under spinning conditions of 20.0 kHz in a 2.5 mm rotor. A low fluorine content probe was used, making background subtraction unnecessary. ^{19}F chemical shift scale was referenced using the -120 ppm peak of 1 M NaF aqueous solution. In each case, both for the unbuffered and buffered routes, each temperature had 3 repeats. As previously mentioned, the amount of powder required for each station was enough to fill a 14 μm inner NRM rotor volume.

4.3.10 Profilometry

Profilometry was used to characterise and distinguish the depth between samples. Different profilometry speeds were used to see if there was any 'skipping of the stylus' caused by the sampling rate. initially 10 seconds was used, which was later increased to 20 seconds to see if the depth of the surface features would increase. It was found that on etched-titanium samples, the average peak height was 0.455 ± 0.035 μm, and 0.496 ± 0.031 μm, respectively. Thus, it was determined that 20 seconds was a reasonable duration.

Comparing the non-etched titanium samples to that of the etched samples was also used to determine if the set-up was correct. the average step height was found to be 0.759 μm with a standard deviation of 0.034 μm for that of non-etched samples when scans were conducted using a 12.5 μm radius stylus. The fact that the peak height is greater in the non-etched samples over that of the etched samples is not true. Sampling of the same samples with a 2 μm stylus gave results that were more reasonable, see Table 4.1, thus, a stylus of 2 μm radius was used.

4.4 Results and Discussion

4.4.1 Surface roughness

The surface features of the four substrates were inspected using SEM, which can be seen below in Fig. 4.1. Qualitatively, there is a clear difference between the different surfaces, from HAp to EHAp, Fig. 4.1 (a) and (b), respectively, there appears to be an increase in the size of the surface features. That is to say that the porosity has increased after acid etching. Furthermore, following the etching procedure we can see that the grain boundaries have been revealed on ETi substrates, leaving crevices that are much larger than those seen on EHAp.

ImageJ analysis showed that on average these non-etched and etched HAp substrates had surfaces with gaps (pores) of 1.09 ± 0.01 and 1.64 ± 0.02 μm, respectively. In the case of Ti, non-etched surfaces showed no evidence of any crevices. In contrast, etched Ti surfaces had by far the greatest separation between surface features. Having an average gap size of 9.59 ± 0.01 μm in length.

The surface roughness of untreated HAp and Ti, as well as those subjected to etching are shown in Fig.4.2, Fig.4.3. These scans revealed that there is a statisticaly different level of surface roughness between samples. However, there is also a greater range in the

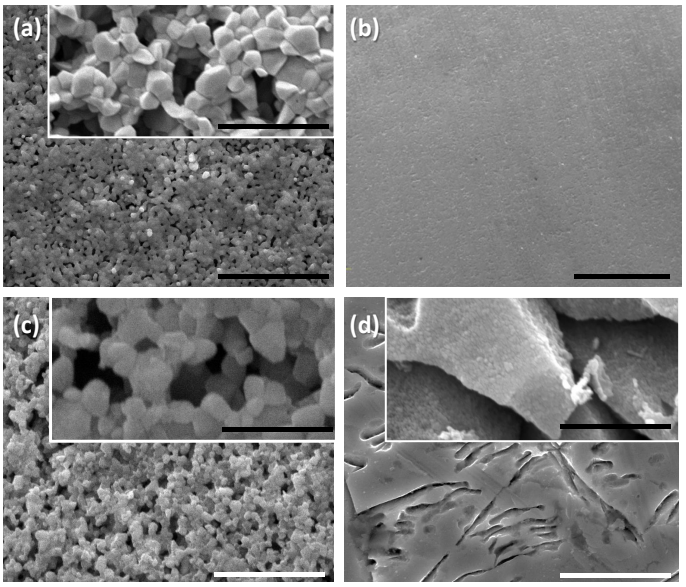

FIGURE 4.1: SEM of substrate surfaces, (a) HAp, (b) Ti, (c) etched-HAp, and (d) etched-Ti, before incubation. Inserts showing a higher magnification of the same material. Scale bars for (a), (c) and (d) were 10 μm, in both, the inserts were 2 μm. For (b) the scale bar is 3 μm.

TABLE 4.1: Profilometry scans performed of substrates.

Sample	Step Height (μm)	Standard Deviation (μm)
HAp	0.212	0.012
EHAp	0.360	0.018
Ti	0.635	0.032
ETi	0.802	0.042

step heights when moving from non-etched to etched samples. In the case of apatite, non-etched surfaces have a range of 3.239 $\pm$ 0.04 μm which changes to 6.867 $\pm$ 0.07 μm when etched. In the case of non-etced and etched Titanium the range changes from 6.444 $\pm$ 0.03 μm to 6.365 $\pm$ 0.01 μm.

4.4.2 Primary results - Surface morphologies

Fig. 4.4 and Fig. 4.5, show the typical morphological formations that occur under each regime, for unbuffered and buffered solutions, respectively. As can be seen, in most cases morphologies can be grouped in to three demographics, rod-like (i.e. Fig. 4.5 54°C HAp) , fan-like (i.e. Fig. 4.5 37°C ETi), and clump-like (i.e. Fig. 4.4 70°C Ti). In many cases, multiple morphologies are produced concurrently, and in the case of the buffered samples, slab-like structures can be found at 5 °C and 21 °C when incubated on Ti, however, these tend to be few in number.

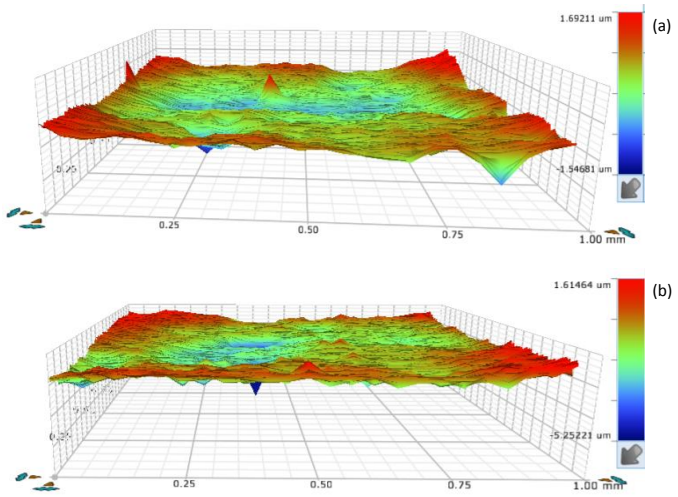

FIGURE 4.2: DECTAKX 1000 x 1000 μm map scans showing, (a) Ti, and (b) ETi surfaces. Positive and negative values indicate surface hight with respect to colour, red - elevated above mid point, blue - below base level.

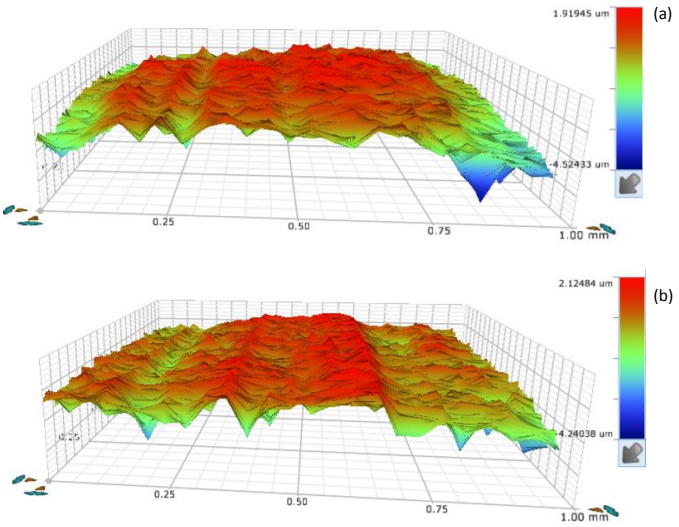

FIGURE 4.3: DECTAKX 1000 x 1000 μm map scans showing, (a) Ti, and (b) ETi surfaces. Positive and negative values indicate surface hight with respect to colour, red - elevated above mid point, blue - below base level. Distinct ridge seen could be a grain boundary, however, the DECTAKX optical resolution does not permit the indication of such surface features.

Where it may seem that the buffered samples create aligned surfaces at 54 °C, when incubated on ETi substrates, Fig. 4.5, the features are actually from nano-rod-slabs (NRS) Fig. 4.6 that are produced in such low abundance. As can be seen, NRS are micro scale slab-like structures that are composed on numerous nano crystals (typically rods but could also be fan shaped). Fig. 4.6(a) 5°C, is composed of fan-like crystals (Ca/P = 1.39) of length 201 – 498 nm that taper to the end, and spheres of diameter

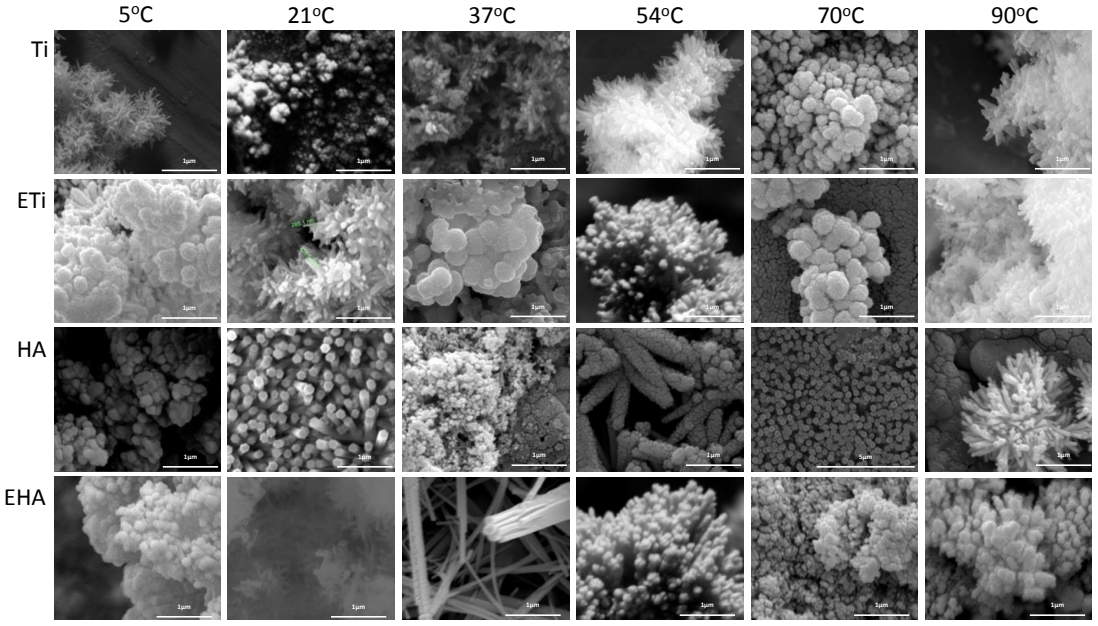

FIGURE 4.4: SEM images of typical precipitates formed of unbuffered samples, magnification $80,000\times$.

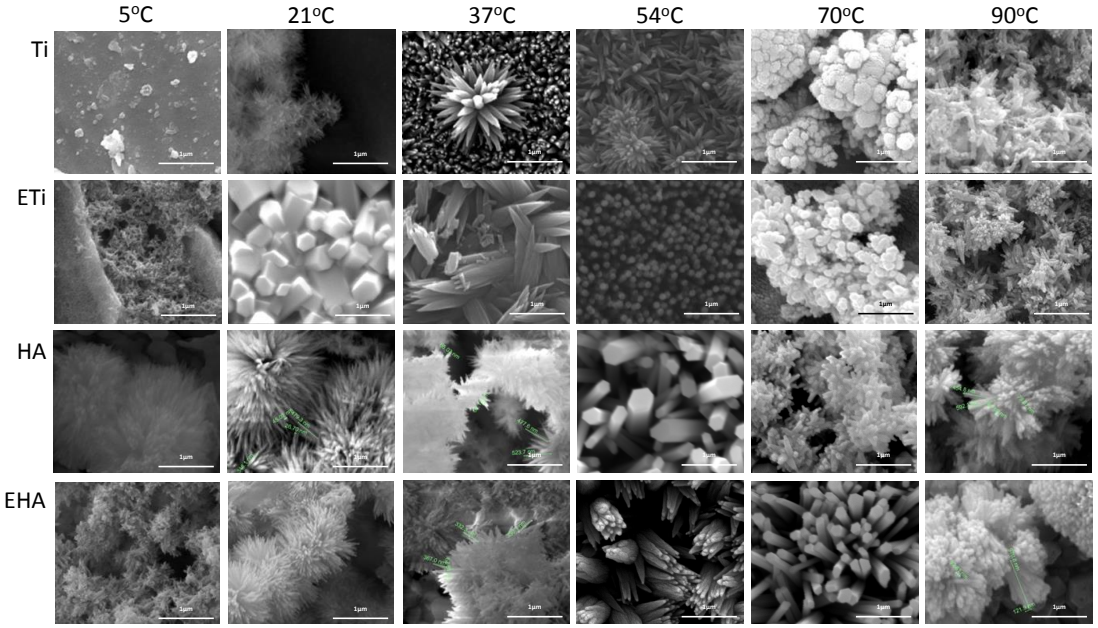

FIGURE 4.5: SEM images of typical precipitates formed of buffered samples, magnification $80,000\times$.

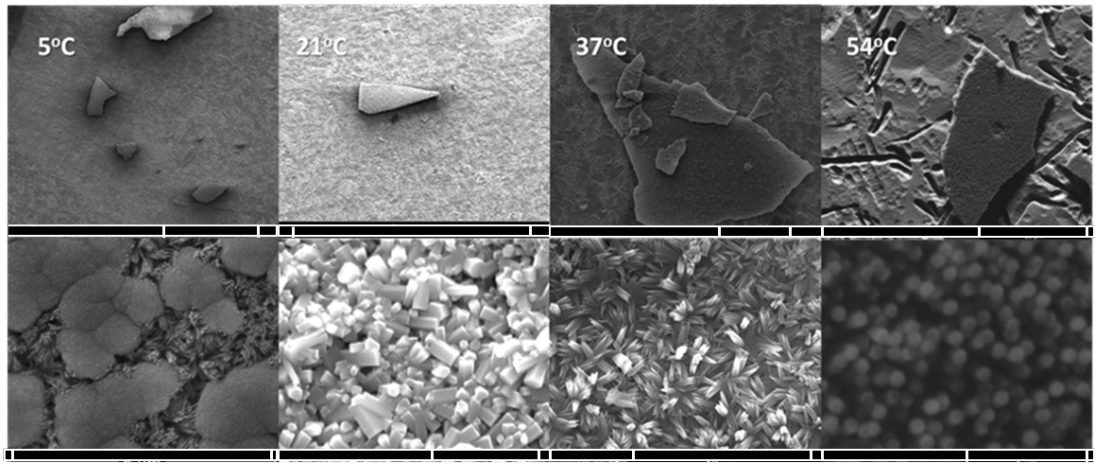

FIGURE 4.6: SEM comparison of NRS morphology formed on ETi in buffered solution and incubated at 5°C, 21°C, 37°C and 54°C. Images shown below are magnifications of pictures above. Scale bar (between internal white bars); top row: 100 μm, 1mm, 100 μm, 20 μm; bottom row: 5 μm, 1 μm, 10 μm, 1 μm.

353 – 1484 nm. These crystals were found on 17 NRS with a range of 8,968 – 308,791 nm in length. At the same temperature 18 diacalcium phosphate slabs (Ca/P = 0.99) were found to have a range of sizes from 69 – 131,885 nm in length. Fig. 4.6(b) 21 °C, here only 1 nano-rod-slab (NRS) of length 333 nm was found. However, this slab was composed of misaligned fluorapatite (FAp) crystals with a hexagonal cross-section, width: 203 – 605 nm, length: 145 – 1,657 nm. 37 °C, shows the formation of 11 distinguishable NRS with a length range of 10,492 – 88,381 nm. These are composed of fan-like nano crystals (Ca/P = 1.39) similar to those seen at 5 °C. The difference being that there is no sign of spherical structures and the length range is higher at 580 – 1,466 nm. It would appear that the nano fans at 37 °C, Fig. 4.6(c), align their *c*-axis closer to the surface of the substrate whereas nano fans at 5°C arrange their *c*-axis perpendicular to the substrate surface. Fig. 4.6(d) 54 °C, NRS (Ca/P = 1.47) found with a range of 28,209 – 250,289 nm composed of rods with a hexagonal width from 119 – 250,289 nm. The small numbers of NRS stresses the point that this is not a methods that is suitable for producing a coating and thus not a direction that this research would continue in.

4.4.3 Morphologies

Looking across all temperatures and all substrates morphologies were identified according to designations outlined in previous academic work [76, 116, 182]. Fig. 4.7, are given the following designations. (a) Slab-like, (b) Ball-like (porous cluster), (c) Self-assembled nano-rods, (d) formless, (e) Small Scale Nucleation, SSN, (f) Dandelion (porous cluster), (g) Ball-like, (h) Misaligned, (i) SSN-Longer Crystals, (j) Dandelion, (k) Clump-like, (l)

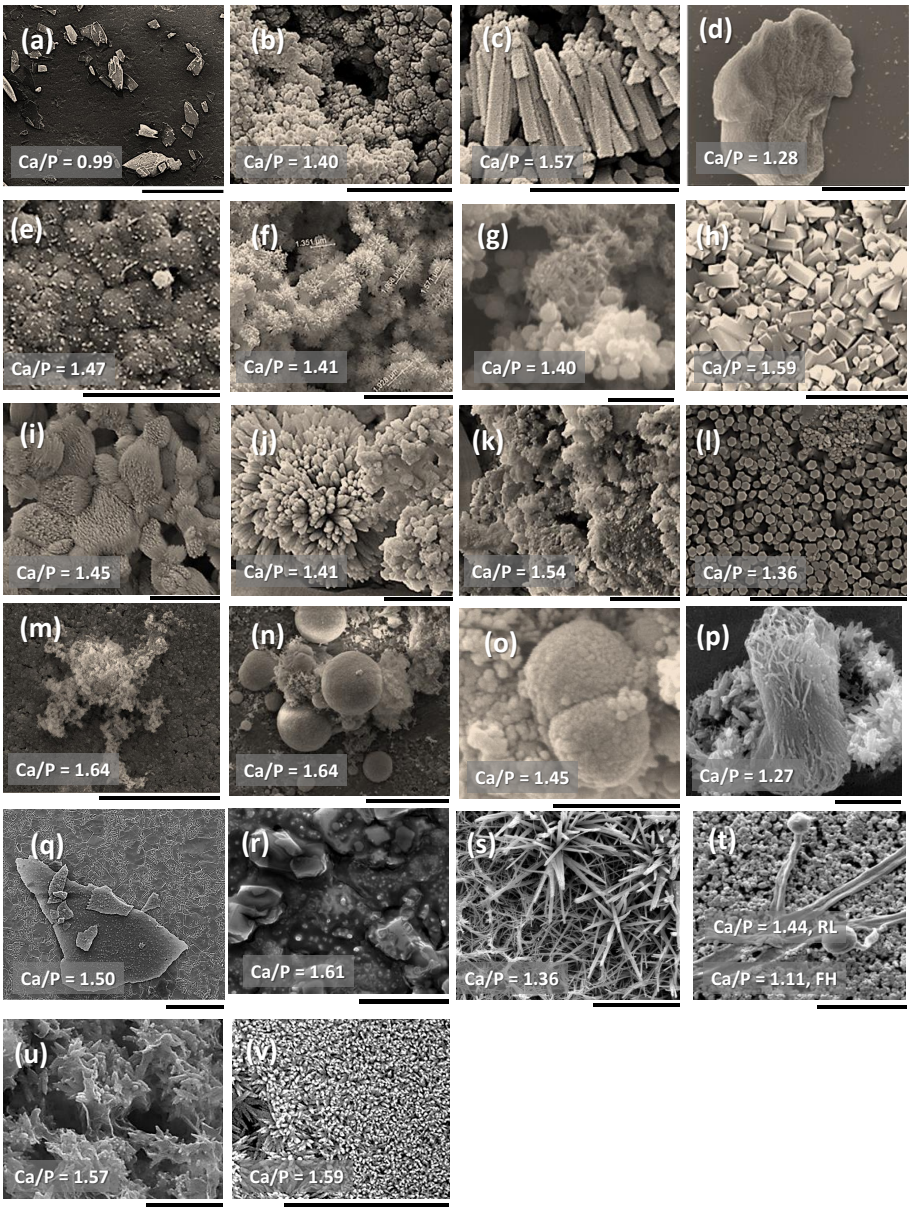

FIGURE 4.7: Catalogue of morphologies found to date, Scale bars as follows: (a) 300 μm; (b) 3 μm; (c) 2 μm; (d) 1 μm; (e) 2 μm; (f) 2 μm; (g) 1 μm; (h) 5 μm; (i) 1 μm; (j) 1 μm ; (k) 1 μm; (l) 5 μm; (m) 20 μm; (n) 100 μm; (o) 20 μm; (p) 1 μm; (q) 20 μm; (r) 1 μm; (s) 10 μm; (t) 10 μm; (u) 1 μm; (v) 5μm.

Aligned, (m) Crystal-Cluster, (n) Nano-rod-slab, (o) Lava, (p) Sweet-like, (q) Nano-rod-sphere, (r) Spherulite, (s) Fibre-Optic Cable, (t) Fungus-head-like, (u) Molten, (v) Ordered fan-like. Morphologies seen in Fig. 4.7 (a–o) have all been seen in previous work, where as (p–v) have been created and added to fully described to morphologies seen in this study. An average values of their Ca/P ratios were recorded using three repeats.

With regards to the size differences between the distinct groups, seen in Fig. 4.7. The

following measurements in were made using ImageJ. (a) the slab-like morphology, having a length range of 67.113 - 190.909 ± 0.001 μm, with an average length of 110.228 ± 0.001 μm. (b) ball-like (porous cluster), clusters of length 12.536 ± 0.001 μm and width 12.351 ± 0.001 μm were found, giving an aspect ratio of 1.02. These structures were composed of numerous nano scale balls ranging from 0.135 - 0.154 ± 0.001 μm. These clusters formed in an irregular manner, which yielded pores ranging from 0.675 - 53.344 ± 0.001 μm, with an average pore size of 11.522± 0.001 μm. (c) the self-assembled nano-rods had a width of 0.262 ± 0.001 μm, and a length of 1.265 ± 0.001 μm, giving an aspect ratio of 0.21. (d) the formless structure, has a width of 1.422 ± 0.001 μm and a length of 2.238 ± 0.001 μm, giving it an aspect ratio of 0.64. (e) the small scale nucleation shows very small crystallites that are forming on and apatite surface. Here the size range is from 0.045 - 0.088 ± 0.001 μm, with an average of 0.073 ± 0.001 μm. (f) the porous structure formed of dandelions created pores of size 0.217 - 0.897 ± 0.001 μm, with an average size of 0.535 ± 0.001 μm. (g) the ball-like structures had a diameter of 0.194 - 0.208 ± 0.001 μm. (h) the misaligned structure typically has a width range from 0.265 - 0.512 ± 0.001 μm, and a length range of 0.303 - 1.011 ± 0.001 μm. (i) SSN- Longer crystals with a cluster size of 0.394 - 0.902 ± 0.001 μm. (j) the dandelion structures having a diameter of 3.304 ± 0.001 μm. (k) the clump-like structures had a typical width of 34.176 ± 0.001 μm, and length of 110.118 ± 0.001 μm, giving it a typical aspect ratio of 3.22. (l) the aligned structures had rod-like crystals with a width range from 0.277 - 0.537 ± 0.001 μm. With an average of 0.416 ± 0.001 μm. (m) the crystal clusters have a typical width of 0.876 ± 0.001 μm and length of 1.385 ± 0.001 μm, giving it an aspect ratio of 0.63. (n) the nano-rod sphere, having a diameter range of 13.624 - 73.858 ± 0.001 μm. (o) the spherulite morphologies having a typical width of 16.764 ± 0.001 μm and length of 26.698 ± 0.001 μm, with an aspect ratio of 0.63, (p) the sweet-like structures with a width of 1.460 ± 0.001 μm and length of 3.281 ± 0.001 μm, giving it an aspect ratio of 0.44. (q) Nano-rod-slab, the biggest having a width of 189.827 ± 0.001 μm and length of 372.745 ± 0.001 μm, giving it an aspect ratio of 0.51. There were also a range of sizes with lengths going from 16.566 - 372.745 ± 0.001 μm with an average length of 74.93 ± 0.001 μm. (r) the molten morphology with cube like structures with an average size of 0.528 ± 0.001 μm. (s) fibre optic cable, with a width range of 0.686 - 5.680 ± 0.001 μm, the maximum width was 5.680 ± 0.001 μm which was composed of clusters of rods each around 1.491 ± 0.001 μm in width. The maximum length was 5.728 ± 0.001 μm. (t) the length of the root-like structure was hard to measure, and also varied greatly. The 'fungus heads' had a diameter range of 0.306 - 0.374 ± 0.001 μm. (u) the molten structures were formed in clusters that ranged in length from 12.668 - 178.928 ± 0.001 μm , with an average length of 89.263 ± 0.001 μm . The individual 'spikes' that emanated from the molten structure had a width range of 0.037 - 0.074 ± 0.001 μm , with an average of 0.058 ± 0.001 μm . (v) the ordered

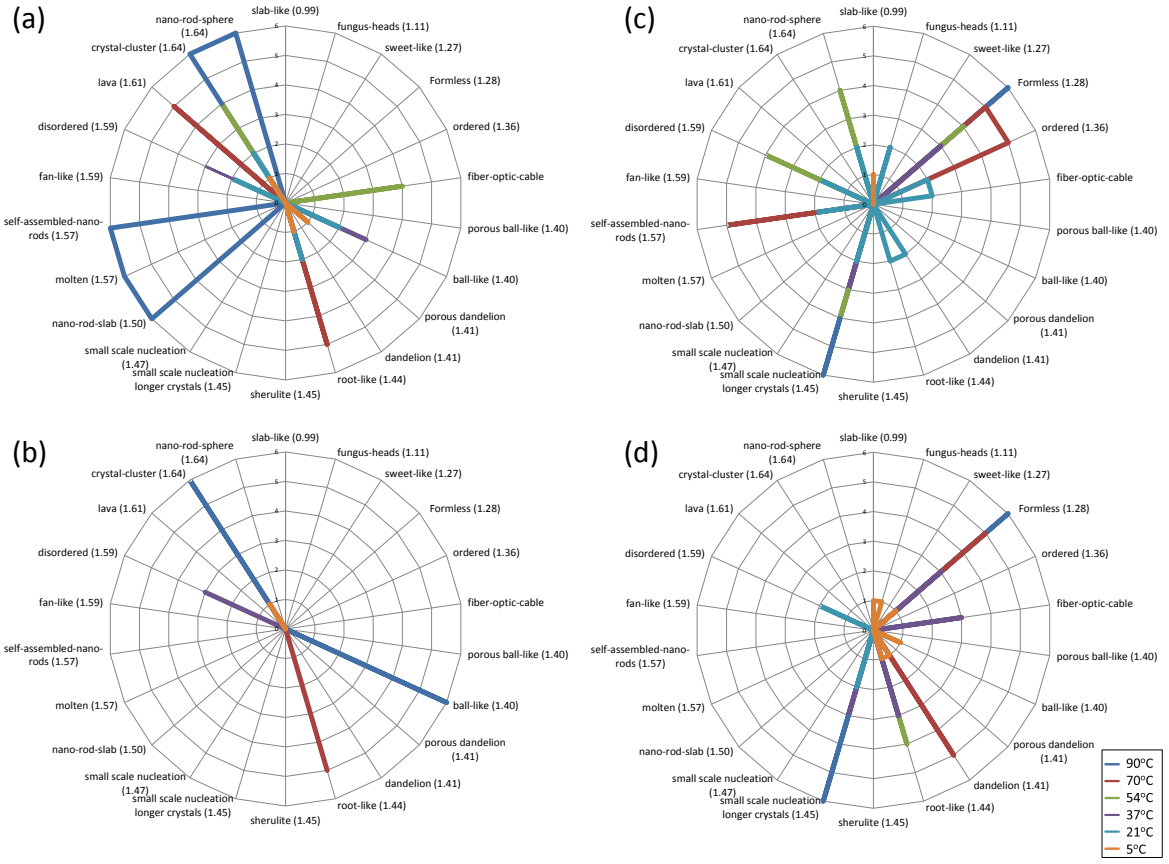

FIGURE 4.8: Morphologies found when incubated on (a) titanium, (b) etched-titanium, (c) HAp, (d) etched-HAp substrates while using unbuffered solution. NB: Connections between points are a function of the plotting software and do not represent a relationship between data points.

fan-like, having a width range of 0.125 - 0.228 $\pm$ 0.001 μm, and a length range of 0.882 - 1.317 $\pm$ 0.001 μm.

Morphologies were listed in ascending order with respect to their Ca/P ratios and their occurrence was represented in the form of spider diagrams for comparison. See Fig. 4.8, and later Fig. 4.12.

As can be seen in Fig. 4.8(a), there are two key Ca/P ranges in which over 80% of the CaP mineral structures were observed. The first range, from Ca/P = 1.36–1.44 encompasses 35% of all the CaPs found where as the second range, from Ca/P = 1.59 – 1.64, contains 47% of all the CaPs found on Ti surfaces. the region between 0.99 – 1.36 contains no evidence of CaPs at all. The three morphologies with similar Ca/P ratio are the self-assembled nano-rods, molten and the nano-rod-slabs, the first two having a Ca/P of 1.57 and the latter having 1.50. These have a striking similarity to the crystals found at the 70 °C samples when transitioning from day 6 and 7. In this study, it was found that misaligned surfaces appear to have interconnections, similar to the molten samples

found here, which then goes on to form nano rods aligned along the *c*-axis, similar to both self-assembled and the crystals formed at the surface of the nano-rods. When considering the mineral formed on ETi surfaces, Fig. 4.8(b), we can observe a 70.59% percentage decrease in the number of CaP morphologies formed. Again we observe a similar trend of having two optimal ranges, this time Ca/P ratio between 1.40 – 1.44 (containing 40% of the observed CaPs) and 1.59 – 1.64 (containing the other 60%), very similar to that of the ranges found on unetched Ti. All other regions show no evidence of any CaP morphologies. As can be seen, we can not find any aligned surfaces when precipitating directly onto Ti surfaces. For this reason we decided to use hydroxyapatite to see if that would fair better as a seeding surface.

Fig. 4.8(c), shows that 90% of all morphologies found on HAp substrates formed CaPs in three key Ca/P ranges, the first being between Ca/P ratio of 1.28 – 1.36 holding 33% of the distinct morphologies, the second being from 1.41 - 1.45 holding 29% of the distinct morphologies, and the third being from 1.57 - 1.64, which also held 29% of the distinct morphologies. The key finding here, is that at two temperatures, both 70°C and 21°C we were able to observe the formation of rodlike crystallites that aligned themselves along their c-axis.

Fig. 4.8(d), has a percentage decrease of 19.05% in the number of observable morphologies when compared to those formed on HAp. An optimal Ca/P range between 1.28–1.45 can be seen where 94% of all the morphologies observed can be found. There is no evidence for the formation of any CaPs between the ranges Ca/P 1.45–1.64, and there is no evidence of any aligned apatite being formed on EHAp surfaces at any temperature.

4.4.4 Powder analysis

4.4.4.1 Derived from unbuffered solution

TABLE 4.2: Rietveld refinement results for unbuffered samples incubated at the six temperatures. APS = average particle size.

Temp	ID	*a*	*b*	*c*	APS (Å)	w%	χ^2
5 °C	monetite	6.909251	6.637222	6.992045	1,462.72	100	3.017
21 °C	apatite	9.384204	9.384204	6.881904	213.97	35	1.648
37 °C	apatite	9.382361	9.382361	6.882343	180.98	29	1.255
54 °C	apatite	9.379956	9.379956	6.883296	283.31	31	1.681
70 °C	apatite	9.377765	9.377765	6.881796	281.33	51	1.966
90 °C	apatite	9.375393	9.375393	6.882684	252.39	75	1.494

Fig. 4.9(5°C), P=O (H–O) peaks found at 530, 572, and 648 cm^{-1} are due to acid phosphates; P–O-P asymmetric stretch peaks found at 773, 866, 979 cm^{-1}; P=O associated

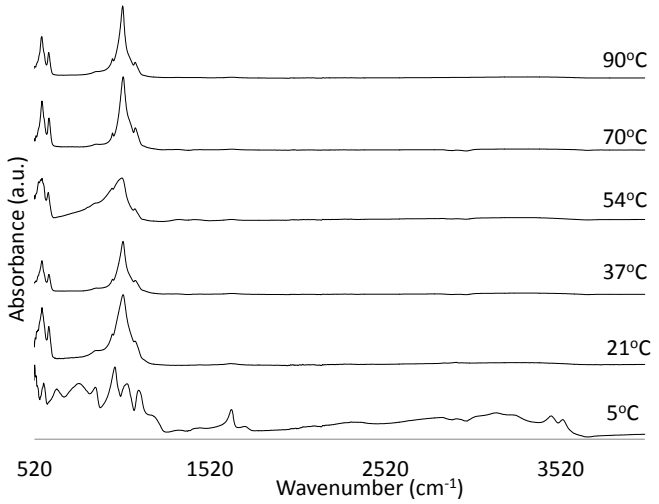

FIGURE 4.9: FTIR comparison of precipitate derived from unbuffered solution at different temperatures

TABLE 4.3: Deconvolution of NMR data performed by DMFIT. Showing percentage abundance of each chemical shift value identified for unbuffered samples derived at each temperature. Average ppm values are here given. Unidentified contaminant (UC).

ppm	Identification	5 °C	21 °C	37 °C	54 °C	70 °C	90 °C.
−89.11	UC	6.20	4.44	0.13	4.88	0.42	1.41
−95.74	CO_3	4.02	5.01	2.67	22.03	4.11	6.73
−103.20	FAp	28.68	23.88	22.62	53.25	21.73	26.97
−105.53	FHA	14.44	21.20	18.39	13.36	14.35	10.76
−109.13	CaF_2	46.65	45.47	56.19	6.48	59.40	54.13

stretch peaks found at 1048, 1115 and 1208 cm^{-1}; and finally H-O–H bending peaks found at 1640 cm^{-1}, these peaks are typical of Brushite [181, 183]. Fig. 4.9(21°C), PO_4^{3-} peaks are found at 563, 601, and 1093 cm^{-1}; CO_3^{2-} peaks are found at closer inspection at 1445 cm^{-1}. These peaks are typical of a apatite. Notably OH^- libration and OH^- stretch which would appear at 630, and 3603 cm^{-1}, respectively, are not seen in any of the peaks. This would indicate that HAp is not the form of apatite that is being formed, and may suggest that the OH^- group has been substituted with another group (likely F^-). Fig. 4.9 (37°C, 54°C, 70°C, 90°C) have peak values within 2σ when considering PO_4^{3-}, however peaks for CO_3^{2-} are 1437, 1432, 1460, and 1461 cm^{-1} for temperatures 37, 54, 70 and 90°C respectively. Given an error of 1, these are over 10 σ.

Data from Fig. 4.10 supports the claim that at 5°C monetite is formed. Whereas, at higher temperatures we see typical apatite XRD patterns. At 5°C we see (020) at 13.138 2θ, consistent with Brushite. This diffractogram also contains what could be a (002) peak at 26.441 2θ, and another peak at 40.077 2θ that could be a (310), both reminiscent of an apatite XRD pattern. From 21°C to 90°C, we can see that all diffractograms

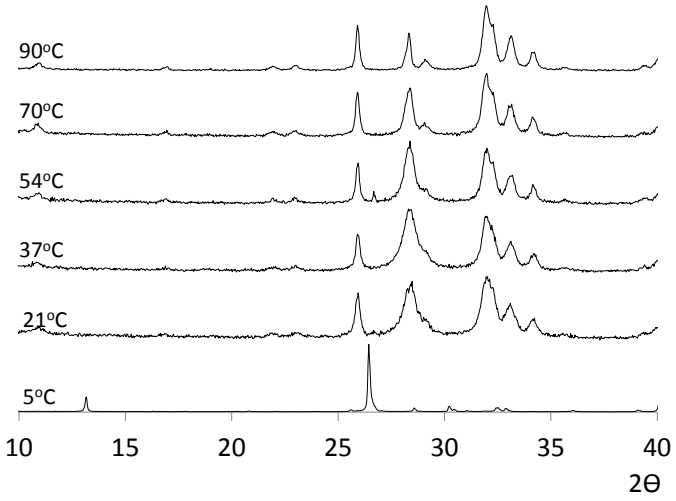

FIGURE 4.10: XRD comparison of precipitate derived from unbuffered solution at different temperatures

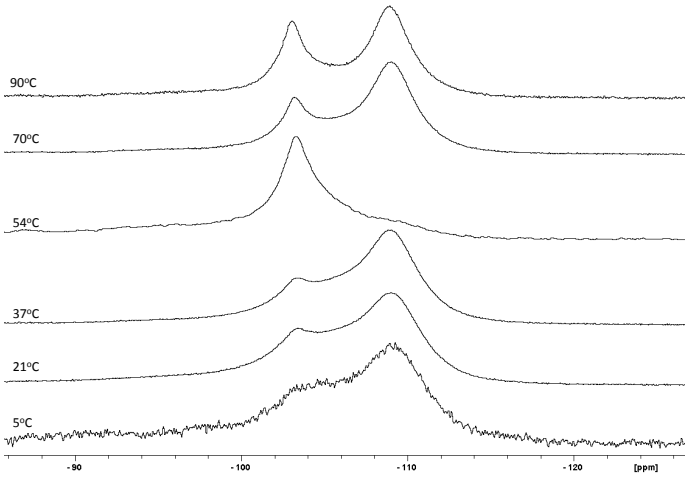

FIGURE 4.11: NMR analysis of precipitated CaP nano crystals formed via wet chemical method in unbuffered solution.

show evidence of apatite peaks. (002), (102), (210), (211), (300) and a (222) peak at approximately 25.939, 28.312, 29.081, 31.989, 33.158, and 47.029 2θ, respectively.

Rietveld refinement was applied to XRD patterns for the unbuffered 5 °C samples. After attempting various refinements with the expected DCPD, and later, combinations including apatite and CaF_2 we were not able to determine a reasonable fit with either. However, after closer inspection, the three main peaks found at 13.00 and 26.44 and 40.01 2θ, could represent the (031), (002) and (003) peaks of DCPA (monetite). Refinement with a standard crystal structure [104] of DCPA yielded a marked improvement of the fitting was achieved. Even so, the intensities of the (002) and (003) peaks were less than

half of that of the experimental XRD data. This was corrected using the March-Dollase preferred orientation function since we expected plate like structures to show a high degre of prefered orientation. The unit cell angles for 5 °C are $\alpha = 96.3315 \pm 0.005°$, $\beta = 103.8816 \pm 0.004°$, $\gamma = 88.3960 \pm 0.005°$ **w**hich is consistent with monetite. Refinement of all other temperatures revealed that these samples were composed of both CaF_2 and apatite as expected, see Table 4.2. The weight percent (w%) of CaF_2 is the antithesis of that of the apatite w% from temperatures 21 °C to 90 °C. The average particle size for temperatures 21 °C, 37 °C, 54 °C, 70 °C, and 90 °C, were 120.80, 96.09, 159.99, 240.77, and 132.76, respectively.

In the case of materials characterisation, XRD, FTIR, and NMR were again used. Unlike in Fig. 4.10, where we find the formation of monetite at 5 °C, in Fig. 4.14 we find the formation of DCPD not only in this temperature but also at 21 °C, identified by peak positions 11.65°, 21.0° and 23.4° 2θ. However, unlike at 21 °C, we can clearly see numerious peaks that are not related to DCPD at all, one at 26.0° 2θ is indicative of apatite, as has previously been stated. As temperatures are further increased past 37 °C, diffractograms maintained a standard apatite pattern, with peak positions similar to those found in Fig. 4.10.

With regard to the data derived from NMR analysis, Fig. 4.11, shows peak positions for nano-crystals mineralised at each of the 6 temperatures 5 °C, 21 °C, 37 °C, 54 °C, 70 °C, and 90 °C. It can be seen two major species can be found, the first being FAp at approximately -109 ppm and the second being CaF_2 having a peak at approximately -103 ppm. One major change we can see is that at 54 °C the FAp peak appears to have a very strong intensity, in contrast with all other temperatures, furthermore, there seems to be no evidence of a CaF_2 peak at this temperature. Using DMFIT the peaks were deconvoluted such that the percentage abundance could be derived, see Table 4.3. Here, we find that the NMR data is composed of at 5 peaks, with a 3rd peak identified as fluorohydroxyapatite, located at -105 ppm and having a range in percentage abundance from 10.76% – 21.20%. It also appears to favour lower temperatures given that the top three highest abundances are found at temperatures less than of equal to 37°C. The fourth and fifth peaks found at -89.11 ppm and -95.74 ppm, one of which was not identified (unidentified contaminant, UC), the other was clearly identified as a CO_3 peak. The unidentified contaminant had percentage abundances no greater than 6.20%, and its abundance did not go through dramatic changes when comparing the different temperatures. However, the CO_3 peak had a range that shifted between 2.67% – 22.03%, peaking at 54°C. The presence of both the fourth unknown peak found at -95.74 ppm and the fifth CO_3 peaks are required for a accurate fitting to occur.

Table 4.2, show that for unbuffered samples, 54 °C shows the highest level of apatite, including both FAp and fluor-hydroxyapatite (FHA), which again correlates with the increased presence of the carbonate group found at an average peak position of −95.74 ppm. There does not seem to be any trend with the increase in temperature when going from 5 °C to 90 °C as both ends of the temperature range have comparable percentage abundance of the species that have been identified. XRD fitting did not show any difference when using carbonated and non-carbonated forms of fluroapatite. However, when using carbonated forms we did find that the system would not fit CaF2 . For this reason fluroapatite was used for fitting with XRD.

It can be seen that there is a discrepancy between the percentage trends as determined by XRD and NMR. In Table 4.3, we can see that the temperature that yields the greatest abundance of FAp is that of 54°C, while those analysed by XRD showed that powers produced at 70°C and 90°C, having a w% of 51 and 75%, respectively. This could be due to the fact that CO_3 groups were not acounted for in the XRD systems. When attempting to include these groups, by considering a carbonated apatite crystal structure we were not able to achieve a decent fitting.

4.4.4.2 Results derived from buffered solutions

In this section, substrates that were incubated under buffered conditions will be differentiated by the use of a B. i.e., Ti, ETi, HAp, and EHAp become BTi, BETi, BHAp, BEHAp.

TABLE 4.4: Rietveld refinement results for buffered samples incubated at the six temperatures. APS = average particle size. DCPD and apatite samples were refined with space group Cc and $P6_3/m$, respectively.

Temp	ID	a	b	c	APS (Å)	w%	χ^2
5 °C	Apatite	9.389037	3.389037	6.887559	104.83	82	11.450
5 °C	DCPD	10.372854	15.245516	5.895811	85,534.66	18	11.450
21 °C	DCPD	10.244139	15.180429	5.810855	1,988.36	100	29.49
37 °C	Apatite	9.377233	9.377233	6.884718	1,031.66	73	2.758
54 °C	Apatite	9.382209	9.382209	6.883296	188.77	74	2.587
70 °C	Apatite	9.380061	9.380061	6.884997	325.85	64	1.587
90 °C	Apatite	9.375081	9.375081	6.883169	340.04	87	1.757

CaF_2 was found at temperatures 37 °C, 54 °C, 70 °C, and 90 °C, with a w% of 27, 26, 36, and 13%, respectively, see Table 4.4. It is conceivable that CaF_2 was also formed at 21 °C. However, when refinement was run with the addition of this phase, it was found that it became difficult to gain an good agreement between data and calculated XRD patterns.

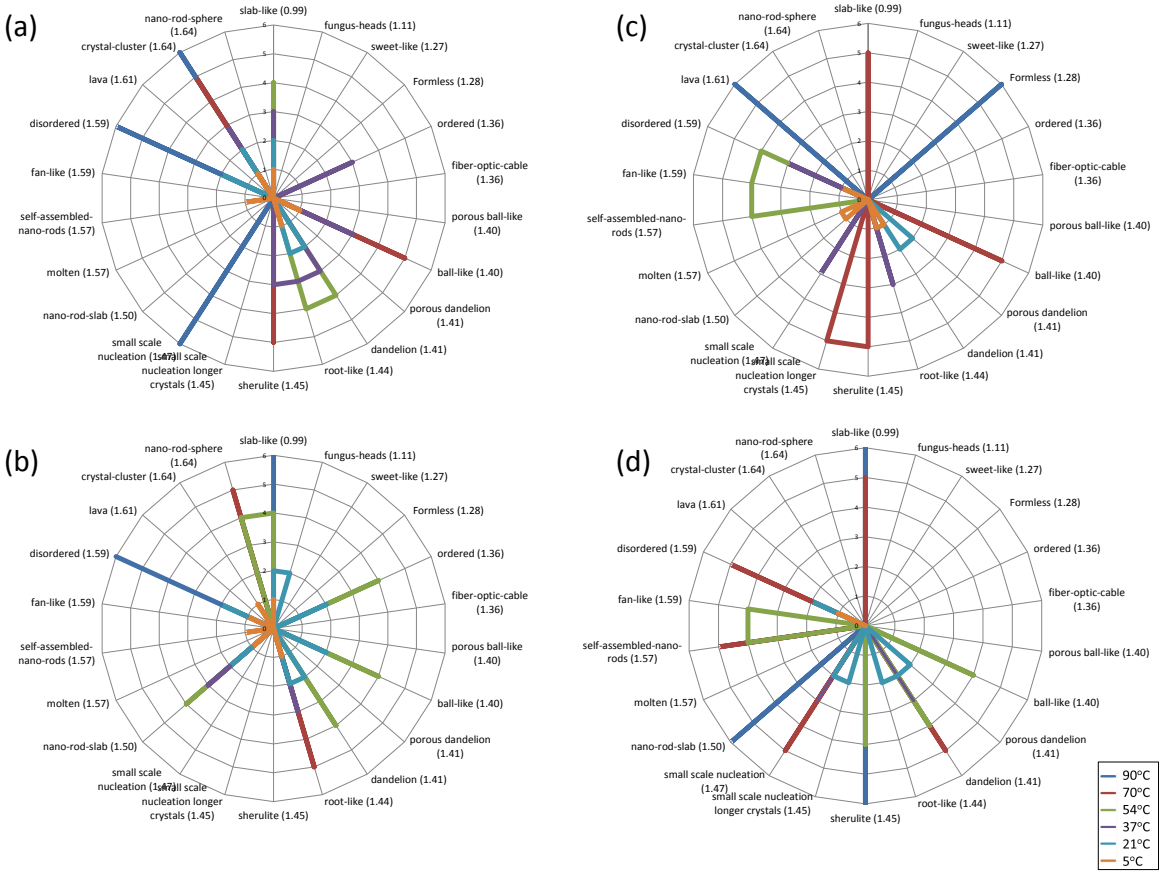

FIGURE 4.12: Morphologies found when incubated on (a) titanium, (b) etched-titanium, (c) HAp, (d) etched-HAp substrates while using buffered solution. NB: Connections between points are a function of the plotting software and do not represent a relationship between data points.

[ht]

TABLE 4.5: Deconvolution of NMR data performed by DMFIT. Showing percentage abundance of each chemical shift value identified for buffered samples derived at each temperature. Average ppm values are here given. Unidentified contaminant (UC).

ppm	Identification	5°C	21°C	37°C	54°C	70°C	90°C.
−88.93	UC	0.00	2.23	1.09	2.13	1.30	19.10
−96.27	CO_3	0.00	18.69	7.15	9.35	6.94	0.28
−103.12	FAp	0.00	47.17	19.94	26.59	23.72	14.05
−105.69	FHA	0.00	24.59	22.99	11.72	13.72	4.10
−109.05	CaF_2	0.00	7.33	48.84	50.22	54.33	62.47

Values from Rietveld fits based on the XRD patterns of the powders produced by buffered solutions are shown in Table 4.4. We can see that at 5 °C a mixture of DCPD and apatite was formed. Here, a standard DCPD structure was used with the Cc space group. This was because GSAS provided warning messages that the Ia space group was not a recognised command. For the refined samples produced at 5°C, α, β and γ where as follows, 90.0000°, 32.5867°, and 90°. For 21 °C samples, MD preferred orientation

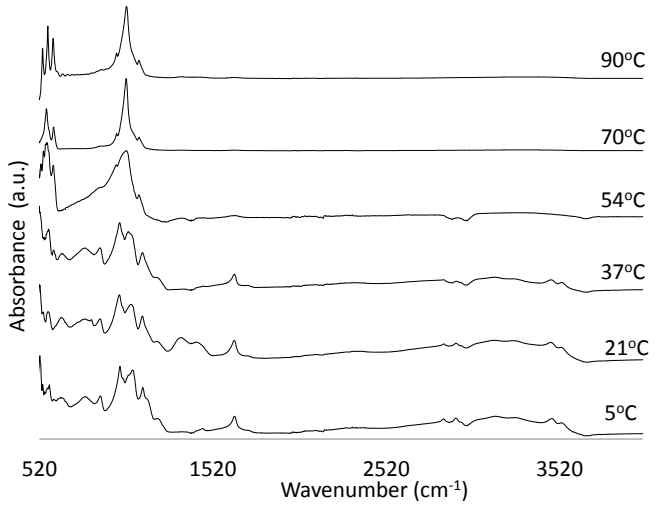

FIGURE 4.13: Comparison of FTIR spectra from precipitate derived from buffered solution at different temperatures.

refinement was required on the (020), (130), (121), and (002) peaks. Refinement with CaF_2 and apatite only served to reduce the agreement between the calculated and experimental data. Samples above 37 °C showed a mixture of CaF_2 and apatite. The CaF_2 produced at temperatures 37 °C, 54°C, 70°C and 90°C with values, 5.470835 ± 0.003878, 5.470839 ± 0.008281, 5.461548 ± 0.001972, and 5.456723 ± 0.002997 Å, respectively.

Fig. 4.12(a), There are two optimal Ca/P ranges, 1.40 – 1.45, and 1.59 – 1.64, found on Ti substrates when incubated under buffered solutions. This observation concurs with the trends found in unbuffered conditions. 68% of the occurrences are found a temperatures lower than 37 °C. There is no evidence of aligned surfaces, but we do find misaligned surfaces. It is known that misaligned surfaces can be progressed to aligned surfaces following an ageing stage. There are two distinct spaces where we have misaligned surfaces, the first is at 21 °C and the second is 90 °C. Interestingly there is a 39% increase in the number of occurrences of morphologies found on buffered Ti surfaces when compared to that of non buffered Ti.

Fig. 4.12(b), Again there are two optimal ranges for Ca/P, 1.40 to 1.44, and 1.50 to 1.64. 83% of all the morphologies formed on ETi were formed at temperatures lower than 54 °C. Curiously, the observations of the "morphological limitations" based on an increased surface topology do not hold true in the case of using a buffered solution. In fact, there is an expansion of the optimal Ca/P range when compared to Ti surfaces. Other comparisons between BTi and BETi are as follows; Slab-like structures tend to grow at higher temperatures on BETi when compared to BTi; disordered are sill seen at 90 °C, but no longer seen at 21 °C; and there is a 4% decrease in the number of morphologies formed on BETi when compared to BTi. Which again follows the normal

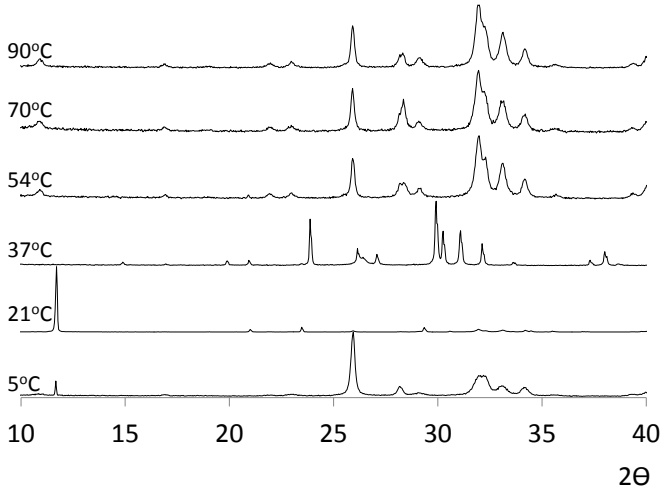

FIGURE 4.14: Comparison of XRD diffractograms from precipitate derived from buffered solution at different temperatures.

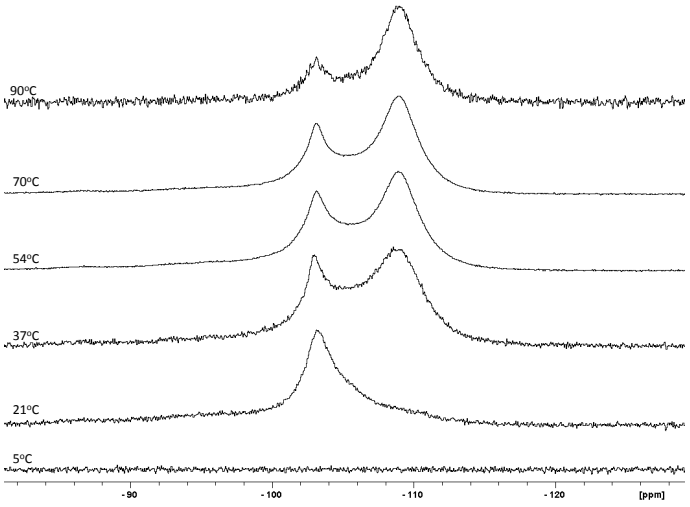

FIGURE 4.15: NMR analysis of precipitated CaP nano crystals formed via wet chemical method in buffered solution.

trend. Interestingly, we see for the first time, nano-rod-slabs, which occurs at every temperature from 5 °C to 54 °C. As shown in Fig. 4.6, a trend that is distinct from the buffered samples is that the misaligned coatings that have been found at 90 °C are one of 3 morphologies found at that temperature. Another way to put this is that 13% of all morphologies found on BETi surfaces are misaligned. adding to this, there are two morphologies found on BTi surfaces within the 90 °C range, which constitutes 9% of the total occurrences observed.

When considering disordered coatings that have been found at 90 °C found on BTi and BETi surfaces it can be seen that there are only 1 and 2 competing morphologies that

occur at that same temperature, respectively. Given that this represents only 9% and 13% of all the morphologies found on BTi and BETi it is fair to say that it may be easier to single out a morphology here than in the case of unbuffered samples.

Fig. 4.12(c), shows an optimal Ca/P ratio range from 1.40 to 1.61, for samples incubated with buffered solution, which encompass 89% of all the morphologies found on HA substrates when incubated under buffered conditions. Again, it can be seen that misaligned surfaces are found on BHAp surfaces. Specifically 5, 37, and 54°C. They key observations that the use of the buffer has limited the optimal range when comparing BHAp to HAp, but have increased the number of morphologies produced by 11%. Notably, there is no evidence of the formation of aligned surfaces. When we compare BHAp to BTi, we see a 24% decrease in the number of morphologies. This is in contrast with the our previous findings based on their unbuffered counterparts.

Fig. 4.12(d), BEHAp shows an optimal Ca/P range from 1.40 to 1.59. which is consistent with the overall trend, given that the optimal range of CaP occurrence reduces with an increase in surface roughness. 63% of all CaP occurrences are formed at temperatures less than 54 °C. Unexpectedly we see a 16% increase in the number of occurrences on BEHAp when compared to BHAp, a surface with lower surface topology.

The evidence shows that the surface material had an effect on the morphology and quantity. Ti consistently shows the formation of two optimal ranges, that are independent of the presence of a buffer. Furthermore, slab-like structures are also commonly formed under buffered conditions. On another note, one might tentatively suggest that if we want to minimise the morphological variety, we can use temperatures lower than or equal to 54°C, increase the surface roughness and use unbuffered solutions, which also lends towards the formation of aligned surfaces.

In the case of FTIR data analysis, Fig. 4.13, showed typical Brushite peaks; P=O (H-O) peaks at 522, 577, 648 cm^{-1}; P–O–P peaks 784, 872, and 984 cm^{-1}; P=O, 1060, 1116, and 1200 cm^{-1}; and H-O–H peak at 1646 cm^{-1}. Fig. 4.13 (b and c), also showed typical Brushite peaks which were consistent with literature to within 3 σ. Fig. 4.13 (d) Crystals formed at 54°C showed evidence of Brushite peaks. For example P=O (H-O) peaks at 530, 566, and 649 cm^{-1}; a lone P–O–P and H–O–H peaks at 876 and 1647 cm^{-1}, respectively. This data-set also showed evidence of apatite. Typical peaks of $PO_4{}^{3-}$ were found at 563, 599 and 1095 cm^{-1}, while CO_3^{2-} peak was found at 1432 cm^{-1}. OH^- libration and OH^- stretch, which would appear at 630, and 3603 cm^{-1}, respectively, are not seen in any of the peaks.

After using DMFIT to deconvolute the NMR spectra, see Table 4.5, it was found that samples precipitated at 5 °C did indeed have a mixture of apatite and DCPD. The addition of CaF_2 phase did not yield reasonable results with regards to fitting, as such, these phases were kept out of analysis at 5°C and 21 °C. At higher temperatures, a combination of CaF_2 and apatite refinements was required to achieve a successful fit. Table 4.5 shows the percentage abundance of apatite only, where the difference in abundance constitutes CaF_2. We can also see that the particles size for apatite crystals increases with an increase in temperature, with a rather large average particles size of 1,031.66 Å at 37 °C, and a particle size of 188.77 Å found at 54 °C, would again hint that this temperature may have some value due to the fact that this value falls close to the range of 25–100 nm required for bioactive coatings.

In Fig. 4.15, two peaks, approx. −103 ppm and −109 ppm, can clearly be seen. What is easily seen is that the -103 ppm peak 'FAp' peak reduces with an increase in temperature relative to the −109 ppm peak. For these buffered samples, the lower values of 21 °C is the temperature at which there seems to be a large abundance of apatite. This is in contrast to what we see in Fig. 4.11 where 54 °C qualitatively shows this feature.

Using DMFIT, Table 4.5, a deeper analysis revealed 5 chemical shift peaks at average values of −88.93, −96.27, −103.12, −105.69, −109.05 ppm, for an unidentified contaminant (UC), CO_3, FAp, FHA, and CaF_2, respectively. What can be seen is that even at the low temperatures of 5 °C and 21 °C, small amount of CaF_2 was indeed present, and the larger percentage abundance found at lower temperatures is consistent in both the Rietveld refinement and the DMFIT deconvolution. Generally, there is a reduction in the percentage abundance of FAp and FHA with an increase in temperature. Furthermore, there is a exchange of the dominance in abundance between UC and CO_3 over all temperatures.

4.4.5 Pre-coated samples

As mentioned in the introduction this work focuses on the development of the apatite synthesis method for implant coatings. Before we can carry out further research it was important to see if we could yield similar results when pre-coating Ti substrates with misaligned nano apatite crystals. The following incubations were held at 70°C as this seemed to be a temperature with promise.

In order to replicate the effects that were seen on the HAp substrate, Ti substrates were first coated with HAp. In this way, the surface on which the precipitation of FAp crystals would progress on would be of a similar chemistry and surface roughness. Below are the

results from a range of experiments that were designed to find a good starting point for the pre-coating of apatite onto Ti substrates.

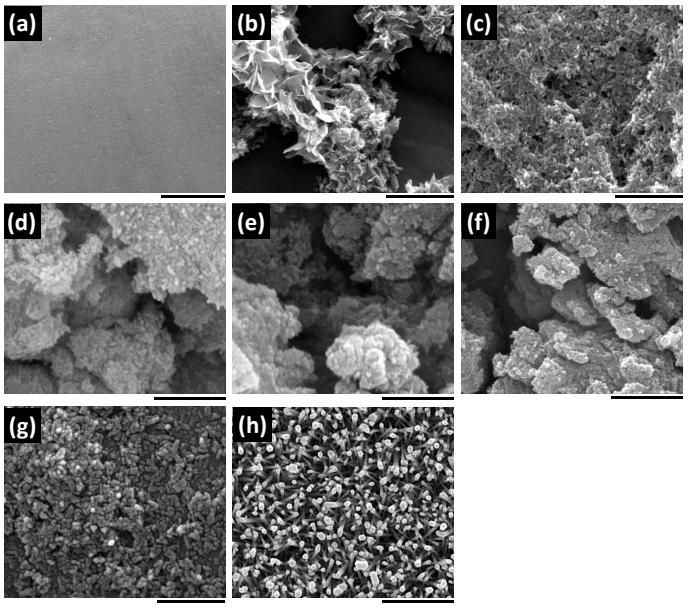

FIGURE 4.16: SEM images of pre-coated Ti samples before 7 day incubation. Scale bars for (a),(d), (e), and (g) are 1 μm; (b), (c), (f), and (h) are 2 μm.

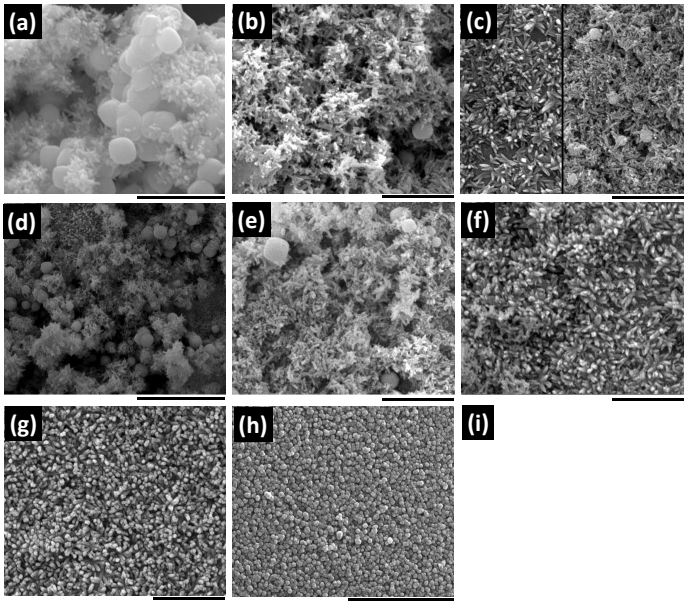

FIGURE 4.17: SEM images of pre-coated Ti samples after 7 day incubation. Scale bars for (a), (b), (c), (e), (f), and (g) are 2μm, (d) 5 μm, and (h) 3 μm.

In order to produce surfaces on Ti that resembled that of the non-etched HAp we made use of the natural ability of apatite to fuse with Ti. The regimes for the pre-coating of Ti samples shown in Fig. 4.16, are as follows. (a) non-coated Ti surface, samples (b–g) involved the submerging of Ti discs in a apatite-H_2O suspension. The normal concentration used for the seven day incubation was used for (b), where as in the case of (c) the concentration was doubled. (d–f) had a layer of this suspension painted onto

the surface of the disc. Each was given a different number of coatings, such that (d), (e) and (f) had 1, 2, and 3 layers, respectively. Each layer was allowed to dry over a two day period before the subsequent layer was applied. Again, these Ti samples used the normal concentration. Sample (g) was submerged over 2 weeks to see if a longer duration would provide a greater adherence to the surface. In Fig. 4.17, these same samples have been incubated following the standard seven day incubation method as previously described.

The average size of the ball-like and rod-like crystallites seen in Fig. 4.16 and Fig. 4.17, have been calculated via ImageJ. Fig. 4.16(a) shows the surface of the Ti substrate, and as such has no morphology to comment on. Fig. 4.16(b) reveals that the surface contained plate-like structures 452.2 ± 8.7 nm in length. These formed clusters on the surface of the Ti substrates. Fig. 4.16(c) showed rods of 238.1 ± 8.7 nm. It was not possible to a certain the width of these rods with the resolution of these SEM images. Fig. 4.16(d, e, and g) all produced clump-like morphologies. However, the ability to distinguish individual nano-crystals was not present. Fig. 4.16(g) produced nano-rods with a width of 59.7 ± 8.7 nm, and Fig. 4.16 Fig. 4.16(c–g) all produced conformations, which on the micro scale generated what is here referred to as a pseudo pore size (PPS). Scans found that the PPS for Fig. 4.16(a), (b), (c), (d), (e), (f), (g), and (h) were, 1.9167 ± 0.0009 μm, 1.1784 ± 0.0004 μm, 0.9083 ± 0.0004 μm, 1.7722 ± 0.0012 μm, 0.2016 ± 0.0009 μm, and 0.1230 ± 0.0009 μm, which are here given in μm to compare with HAp, EHAp and ETi substrates. Measurements of the PPS has been made by measuring the separation between the highest points in the surface. As can be seen, these values show a spread over the range set by the HAp and EHAp substrates which maintained values of 1.09 and 1.64 μm, respectively.

Following this, we can see that the different regimes played a strong role in the formation of further apatite on the pre-coated Ti during the seven day incubation. Fig. 4.17 shows the formation of ball-like structures in regimes (a–e). The diameter of which were found to be, 620.2 ± 6.9 nm, 545.5 ± 12.4 nm, 359.0 ± 12.5 nm, 660.2 ± 24.9 nm, 506.8 ± 12.5 nm, respectively. rod like structures could also be identified in all of these regimes. (L: 191.0 ± 6.9 nm), (L: 382.6 ± 12.4 nm), (L: 393.7, W: 102.8 ± 12.5 nm), (L: 315.6 ± 24.9 nm), (L: 311.8 ± 12.5 nm), in that same order. Regime (f) was the first to show the lack of any ball-like structures, only showing the presence of rod-like structures (W: 334.0, L: 110.3 ± 12.4 nm). Fig. 4.17(g) showed nano-crystals (L: 288.4, 92.1 ± 8.7 nm).

Thus, we can see that there are some similarities between the apatite substrates and the pre-coated Ti substrates, in the sense that an aligned apatite surface may be grown on both. Thus for reproducibility purposes we may continue to use the apatite substrates for future experiments.

4.5 Discussion

4.5.1 The effect of surface roughness on nucleation

4.5.1.1 Flow conditions and temperature difference

Previously, we outlined that the mechanism of crystal growth maybe considered as following a three stage process, starting from supersaturation, which is followed by crystal nucleation, and eventually crystal growth [184]. The two main factors that affect the location of initial precipitate formation on the surface are, the flow conditions present and the available overall temperature difference at the solute-substrate boundary. In the case where supersaturation is present at the solute-substrate interface, precipitation is likely to occur at the surface of said substrate. However, if supersaturation is away from the surface, crystals will form in the bulk of the solution and then will later migrate towards the surface. In some cases, fluid turbulence can bring crystals to regions where the concentration of the solute falls below the saturation concentration for the local temperature. In this case, crystals may re-dissolve before they have the chance to become deposited on the surface. In 1997, Jie Weng and co-workers investigated the nucleation and growth of apatite on the surface of plasma-sprayed hydroxyapatite coatings [185]. In their experiment, they formed a surface with an R_a of 3.3–4.0 μm by sandblasting an alloy with Al_2O_3 powder. Following this, the surfaces were plasma sprayed to form an amorphous-crystalline coating with a 4:6 ratio, respectively. They found that after a few hours the layer that formed was composed of calcium deficient apatite. It was poorly crystallised and contained carbonate and magnesium. They also found that nucleation occurred within the pores and cracks first, where the higher supersaturation was maintained. They found that the dissolution of the amorphous phases that were produced as part of the incubation were important for the formation of apatite on the surface of recessed regions, pores and along cracks.

As has been mentioned, in both Fig. 4.8 and Fig. 4.12, we observe that when transitioning from a lower to higher surface roughness there is a reduction in the number of morphology types. This could be indicative that many crystallites formed require a greater fluid flow in order to form at the surface.

Crystal formation is typically aided by the presence of suitable nuclei that may come in the form of impurities within the suspension or on the sites on the substrate surface itself. The growth of crystals, following the formation of a stable nuclei within a supersaturated region is dependent on the surface energy effect. The morphology of the crystal is altered based on the minimum surface energy requirement, sequential adsorption (in which layer upon layer forms on the crystal surface), and diffusion (in which the crystal growth

is affected by the concentration difference between the bulk solution and the crystal surface) [184].

4.5.1.2 Particle size and surface topology

If an artificial implant is to bond to living bone, it is essential that a bioactive layer is formed on its surface [186]. In this case, apatite is used as the bonding interface. In 2008, Xiaobo Chen et al, found that pretreated Ti surfaces were able to form apatite coatings on the surface [78]. In this study, Ti surfaces with a surface roughness of 0.20 ± 0.08 μm, 0.60 ± 0.12 μm, 1.00 ± 0.18 μm, and 1.20 ± 0.15 μm were used as the starting substrates. A surface roughness of 0.6 μm led to the fastest apatite formation on the metal surface.

The distinct difference between their method and ours is that they used simulated body fluid (SBF) with an ion concentration close to that of blood plasma as the mineralising solution. They found that untreated Ti surfaces of R_a 0.6 μm formed tiny ball-like particulates that did not change obviously until 7–14 days of incubation within the SBF solution. In a similar way, our untreated Ti surfaces produced ball-like crystallites that persisted until day 7. They also found that the surface defects (grooves) on the samples with an R_a of 0.6 μm had widths of 3 μm, which corresponded to size of the apatite particles of spherulite morphology that were also about 3 μm. They asserted that the greater rate of formation on these surfaces was due to the ability of the particles being absorbed onto the surface due to the similarity in size. In This study, we found that the particle size of the apatite precipitated, as found by Rietveld refinement, Table 4.4 and Table 4.2, were a factor of 20 times smaller than than the gap size of the surface features seen on the substrates. monetite and brushite crystallites were found to be a factor of 10 smaller than that of the substrates. In this case, it would seem that the gap size (or width) of the surface features did not closely match that of the size of the crystallites that are formed.

4.5.1.3 Phase transitions and hydrothermal synthesis

The morphology of apatite crystallites have been found to form needle-like (rod-like) form when synthesised under hydrothermal conditions [187]. In this research, Seiji Ban and Jiro Hasegawa grew apatite on to commercially pure Ti plates. For the mineralisation solution they used an electrolyte containing calcium and phosphate ions. forty five conditions were used using twelve different electrolyte temperatures from 90–200 °C, five different current densities 5.0–25.0 mA/cm^3 and current loading times, 10 -120 min, where the later two were conducted at three different temperatures 100 °C, 150 °C and 200 °C. Finally, the longitudinal length of one side of the apatite was measured using

field emission-type scanning electron microscopy photographs. The solution was maintained at a pH of 7.0 using 50 mM tris(hydroxymethyl)-aminomethane and hydrochloric acid. They found that the size of the crystals increased with electrolyte temperature. Furthermore, increasing the time of incubation from 10 min to 90 min revealed a transition from plate-like crystallites to a rod-like morphology with their orientation aligned along the c-axis. Similarly, increasing the temperature from 100 °C to 200 °C caused a similar transition from plate- to rod-like. However, in this case the alignment of these rods was more disorganised. In general, the longitudinal length of the hexagonal crystals increased with an increase in temperature, where as, the aspect ratio decreased with the same temperatures.

As we know, the formation of a solid crystal nucleus leads to a Gibbs free energy change which is dependent on the solid-liquid interface area and energy. In the case of a heterogeneous nucleation, one in which the solid is forms on the surface of a substrate or an impurity within the solution, as previously outlined. At any temperature below the melting temperature there is a driving force for solidification. The Gibbs free energy of transfer from a supersaturated to a saturated solution at the interface is the driving force for crystallisation, also expressed as the relative supersaturation. Notably, the contribution of interfacial energy results in a kinetic barrier for the phase transformation. The different levels of surface roughness provided by the different substrates in this experiment are expected to drive the occurrence of heterogeneous nucleation. The nucleation points will decrease the energy required to form a nucleus [81, 188]. Different morphologies might arrise due to the localised changes arising from the different solution-substrate surface roughness. That is to say that the small changes in ionic concentration and pH can shift the energy balance from from one morphology to another.

4.5.2 Competing equilibrium in buffered and non buffered systems

The advantage of using the buffered solutions was that it maintained the pH throughout the seven day period. In this way, we were able to maintain the pH at the interface and keep the solution in a dynamic state without disrupting the growth of the crystallites. As we can see, this method resulted in very different nucleation routes. Given that these closed systems are conducted at distinct but constant temperatures we will note that a dynamic equilibrium will have been set up in each regime. Super-saturation is based on the fact that a sparingly soluble compound, in this case apatite, will partially dissolve. An equilibrium between the ions in solution and the undissolved solid is set up. Typically, the solubility products are used to determine if the system is not saturated, super-saturated, or not saturated at all. This is done, by comparing the magnitudes of the concentration of the ions in the solution with that of the solubility product. However,

even in the non-buffered case, the addition of nitric acid and ammonium hydroxide will also create their own equilibrium within the solution. Strong acids and strong bases completely ionise in water, while on the contrary, weak acids and bases only partially ionise in water. In this case an equilibrium is set up. However, even in the case of strong acids and bases, they require a proton acceptor, or donor in order to ionise. Here, an equilibrium is set up between the conjugate pairs that are formed in this process, and there is also a competing equilibrium between all of the different calcium phosphates that could be formed, most notably between the hydroxyapatite, which is here used as a starting material and that of fluorapatite which is the desired end product. Notably, the former has a solubility product that is 10^{11} times greater than that of the latter. Thus, it would take a lower concentration of ions to precipitate fluorapatite than it would for hydroxyapatite. That being said, certain areas of the solution will have at times greater concentrations of ions than others which could lead to the presence multiple phases (due to concentration differences) and substitutions being formed. For the buffered solutions, the situation is further complicated by adding another equilibrium into the solution. In other words, the equilibrium between the weak acid and one of its salts in which the buffer is made. Thus the equilibrium should maintain the pH level at the value at which the solution was prepared.

4.5.3 nano-rod-slabs

As previously said, Fig. 4.6, shows some interesting trends in terms of nano-crystal alignment and temperature. With the exception of 54 °C, SEM analysis qualitatively shows that the c-axis of these crystals tends towards a more parallel arrangement when moving from 5 °C to 37 °C. This would suggest that the level of alignment has decreased with an increasing temperature. If the spheres are also apatite crystals, we may infer that crystals at the 5 °C are less mature and would require a maturation stage.

4.5.4 Morphology

We can see that slab-like structures are a common feature on the morphological index as it occurs in 54% of all samples analysed. We can also see that NRS form concurrently with the slab-like structures at the same temperatures, which may suggest that these slab-like structures are independently growing phases that follow different routes. We have qualitatively noted that with increasing temperature, crystals become more aligned, Fig. 4.6(a) It can also be seen that at 5 °C, ball-like structures are still present. This may suggest that apatite crystals are still forming. Strangely, crystal alignment seems

to follow a trend of becoming more aligned with an increasing temperature, with the exception of those formed at 54 °C.

The analysis of the mineral that formed on the HAp substrate show an increase of 23.53% in the number of observable morphologies when compared to those formed on Ti. In any one temperature, there are a number of morphologies that are produced concurrently. In Fig. 4.8(c), it can be seen that there is no optimal range of Ca/P when formed on HAp. However, this substrate is the only one to have produced ordered structures both at 21°C and 70°C. Again a repeat of the trend seen in Fig. 4.8 where by there is a reduction in the number of CaPs found on surfaces with a greater level of topology can be here seen. In fact, the limitation on the types of morphologies that have been produced has extended to include ordered coatings. This could be advantageous given that the number of morphologies produced at 21 °C have reduced from 9 to 2 moving from HAp to EHAp, that is to say that there may be some optimal surface roughness between the non-etched-HAp ($R_a = 0.212 \pm 0.012$ μm) and the etched-HAp ($R_a = 0.360 \pm 0.018$ μm) that both maintains the aligned surfaces produced, while at the same time reducing the number of competing morphologies formed. Notably, there are only 3 distinct morphologies formed concurrently with the aligned apatite when the solution is incubated at 70 °C on HAp substrates.

One observation is that even though the solution was mixed to Ca/P = 1.67, there are in fact a range of Ca/P values formed on inspection of the crystals. This could suggest that there are multiple mechanisms in place for the formation of the various morphologies here seen. Given that both the number of CaPs found reduces as well as a reduction in the spread of the Ca/P range we can surmise that an increase in surface topology limits the number of morphologies that can be produced on both Ti and HAp substrates.

4.5.5 Compositional analysis

The composition of the powders precipitated under buffered and unbuffered conditions clearly show some distinct differences. It is clear from XRD and FTIR that dicalcium phosphate, DCP, (either in a hydrated or dehydrated form) is limited to lower temperatures, where DCP is found at 5 °C in unbuffered samples, Fig. 4.9 and 4.10, but can be found both at 5 °C and 21 °C for their buffered counterparts, Fig. 4.14. However, adding to this there are clear differences in the percentage abundance as seen through NMR analysis, discussed later.

For the unbuffered system, FTIR, XRD and NMR are consistent. FTIR and XRD both confirm the presence of DCP only at 5 °C and Rietveld refinement and deconvolution using DMFIT yield similar percentage abundance for the apatite and CaF_2 samples.

However, this is not the case when we inspect the results from buffered solutions. FTIR data shows that DCP should be found at all temperatures up to 37 °C, however, XRD analysis shows no evidence what so ever for DCP at any temperature above 21 °C. Adding to this, NMR analysis shows that at 21 °C, the powders have a percentage abundance of 47.17% and 24.59% for FAp and FHA. When comparing this to the results found from XRD analysis we can see no evidence for apatite, in fact, it would appear that this temperature exclusively produces DCP when using this technique. It should be expected, that with such a large abundance of apatite in the system, as seen by NMR, we should be able to see a contribution to the XRD diffractograms.

It should be clearly noted that each set of data presented was only accepted when there were a repeat of 3 experiments for each temperature, which allowed for a greater level of consistency with each analytical technique. Thus, this could be due to the nature of the solution itself. It is possible that the chemical route may yield slightly different results on different days and that any phase transition, which would occur over a few nano seconds could indeed happen. Moreover, the increased complexity of the buffered solutions, owing to the equilibrium phenomena present could results in a less predictable and repeatable solution.

It appears that 54 °C shows an optimal temperature for the formation of nano particles with a large percentage abundance of apatite. However, as we can clearly see from Fig. 4.8, there is no evidence for aligned rod-like nano-crystals that cover the surface when observing the SEM of samples incubated at 54 °C.

4.5.6 Possible implications in other areas of study

The trend seen in the NRS hints at a much larger story with regards to the coating of aligned rod-like mineral on the surface. As can be seen in Fig 4.6, we can see that with an increasing temperature we gain a greater level of crystal alignment at 5 °C and 54 °C. The fact that these were conducted at different temperatures suggests that there may have been a lack of energy needed for further continuation of the growth progression. That being said, these NRS are found in buffered solutions only, and there is no evidence for the formation of aligned rod-like crystals on any of the surfaces incubated under these conditions.

A lot of information is packed into Fig. 4.8 and Fig. 4.12 . The changes in Ca/P ratio, and by extension the distinct morphologies is observed within a particular surface but can also be compared across the four surfaces here analysed. Furthermore, greater information can be found when looking at the buffered samples. However, in this work, we will draw out only the information that is relevant to us. As we have mentioned, in

general there is at least two main features that can be seen as consistent trends. The first is that there are optimal regions of Ca/P ratios, and that the locations of these ratios have a dependence on the R_a of the material as well as the surface chemistry. The second is that when increasing the R_a, we see a limitation on the number of morphologies that are expressed onto the surface, and the Ca/P ratio-region also reduced in most cases. If it is true that the formation of CaP phases at the surface could be driven by the concentration of ions that are present there, and that the gap size of the surface feature effects the amount of ions that are present at a local point. Then one might expect that with a greater gap size you would have a greater variety of chemical compositions that could be formed and potentially could give rise to a greater number of phases. However, this is not the case.

4.6 Summary

There are a number of key findings that has come from this study. The first is that increasing the surface roughness in both titanium and hydroxyapatite substrates limits the number of distinct morphologies that are formed. As we know, SEM analysis of the surface has revealed that the average size of the voids in the x-y plane ranges from 1.09 to 1.64 μm on average. Given that the only surface that showed any evidence of the formation of aligned rod-like apatite coatings was on the apatite substrates, and that pre-coating titanium substrates with apatite has proven successful in replicating similar results, it stands to reason that we next need to focus on finding the optimal surface roughness that lies between 1.09 to 1.64 μm. The aim would be to isolate the rod-like structures, free from any other undesired morphological types.

The second point is that only 21 °C and 70 °C show evidence of aligned apatite surfaces, and only when an unbuffered solution was used. These show two optimal temperatures for the growth of apatite nano-structures that have the potential for use as a biomimetic coating material. This solution produces at least four phases, two of which are the standard products; apatite, and CaF_2. While DCPA and DCPD are also produced, typically at the lower temperatures of 5 °C and 21 °C. For this study, neither DCPD or DCPA are of interest and as such these temperatures provide to small an abundance for further study.

Buffered samples provided no evidence of aligned structures, in fact they served to encourage the formation of DCPD and DCPA at higher temperatures, increasing even up to 37 °C. For these reasons, further study into the effects of BISTRIS buffer will not be continued. NMR shows that 54 °C is the only temperature in which the apatite chemical shift peak is dominant over the CaF_2 peak. In all other cases the reverse is

true. Even so, the lack of aligned apatite coatings found at this temperature suggests that further study into samples incubated at 54 °C would not be a direction to pursue at this time.

Following from this, 21 °C and 70 °C prove to be the most interesting temperatures for future study, and development of this process.

4.6.1 Main findings

We found that:

- After caring out experiments under 48 different conditions, 24 for unbuffered samples and 24 for buffered samples we found 22 distinct morphologies. These morphologies fit into one of three subgroups, plate-like, Rod-like and formless.
- Out of the 22 morphologies found, 7 of these were previously not seen before in the literature. Including an interesting morphology, the nano-rod-slab, which shows evidence of being composed of individual nano rods.
- From 5°C to 54°C we can see a increasing level of alignment on the nano-rod-slabs, with the samples at 5°C showing evidence of ball-like structures along side the misaligned nano-rods. This would hint to the effect of temperature on the level of alignment and development of the crystals. However, since only 4 to 5 of these micro sized morphologies could be found at best these were not considered for further research.
- Each regime yielded at lest 2 different types of morphologies concurrently. This would suggest that there are multiple mechanisms for crystal growth that are in competition with each other. For example, aligned rod-like structures found at 70°C were also accompanied by dandelion-like morphologies, formless, and self-assembled nano rods. All of which were undesirable end products.
- After grouping the morphologies according to their Ca/P ratio it was found that ranges of morphologies were formed according to the surface chemistry. For unbuffered samples these ranges were reduced when the surface roughness increased on both surfaces. However, in the case of the buffered samples there was no over arching trend observable.
- Surface roughness also limited the number of morphologies, and as such could be used to select out the morphologies that were not desirable.

- Only two regimes showed evidence of aligned rod-like apatite coatings, 21°C, and 70°C.
- FTIR, XRD, and Rietveld refinement all confirmed the presence of monetite at 5°C, where all other temperatures were a mixture of apatite and CaF_2. NMR experiments and deconvolution provided a greater level of detail by revealing that there are in fact 5 distinct chemical environments, two of which belong to FAp and FHA, and another two belonging to CO_3. Indicating that the solution contained some amount of dissolved carbonates.
- NMR deconvolution also showed that 54°C showed the greatest reduction in CaF_2, favouring the production of FAp, and FHA. However, given that there was no evidence of aligned rod-like apatite at these surfaces in any of the methods this is not a direction I intend to peruse.

Hence in the next section we will focus on the synthesis pathway for the development of aligned rod-like apatite coatings incubated at 21°C, and 70°C.

Chapter 5

Optimisation of Nano-engineered Apatite Implant coatings via Sequential Temporal Synthesis

5.1 Key aims

- To gain an understanding of the stages of development of the synthesis pathway of the aligned samples produced at 21°C and 70°C.
- Use both visual, structurally and compositional analysis to characterise the changes every 24 hours during the 7 day synthesis period.

5.2 Introduction

As previously mentioned in chapter 1, apatite coatings were first used to coat implants in the 1980. Notably, the method of application was through a process know as Plasma spraying, which is now the most commonly used method for implant surface coatings. As previously said, this method produces disorganised layer of apatite crystals with poor crystallinity. The industrial method has circumvented the fact that as crystallinity reduces the crystals dissolve quicker by increasing the thickness of the coating layer, typically around 300 μm [190]. However, this in turn has its drawbacks, the level of thickness required caused fractures and delamination at the bone-implant-interface, and can block porous implants [69]. These limitations can cause micro-motion (leading to fibrous encapsulation)[24, 191] and inhibit bone ingrowth respectively. Some contemporary implants are not Ti based but in fact a composite of vitrified carbon coated with

tantalum. This is done to produce a porous structure that permits bone ingrowth. However, its porous structure would be limited by the use of plasma spraying techniques. The high pressures required causes the decomposition of HAp and cause the generation of amorphous HAp along with non-biocompatable CaP phases. Both of which reduce the biocompatability of the coating. Machined surfaces are subject to a low removal torque [21], and has a reduced success in areas of low bone density[192].

As yet, a detailed understanding of an apatite crystal growth mechanism is not fully understood. Thus, the goal of this research is to gain an understanding of the growth conditions such as substrate topography, chemistry and temperature that affect the synthesis of apatite coating growth. Furthermore, these conditions will then be tailored to optimise the morphology, organisation, coverage and chemistry, thus enhancing the biomimetic properties of the implant. This research aims to develop technology that has the potential to be cheaper than current method, while at the same time maintaining the structural integrity of the implant while at the same time opening up access to demographics that are currently deemed high risk.

Traditional methods, such as Rietveld refinement, used to analyse of crystal structure has the clear limitation of only yielding information based on long range order (LRO). Thus, any two versions of the same material with different short range order cannot be distinguished with the Rietveld method, and the early stages of nucleation, and crystal growth cannot be detected. The pair distribution function (PDF) is primarily used for powder diffraction. Unlike Rietveld refinement, PDF contains information about both the long range order, for the distance range $r > 5$ Å, (derived from Bragg scattering) and the short to mid range order, in the distance range $r < 5$ Å, (derived from diffuse scattering) [193]. Notably, the PDF method was originally applied to the study of liquids and amorphous materials but can also be applied to disordered crystalline materials. Thus the advantage of this approach is that it can be applied to the complete range of materials from non-crystalline materials to crystals with varying degrees of disorder on various length scales. PDF has been used to study the local disorder in crystalline materials. Determining the atomic arrangements holds the key to understanding and possibly predicting properties of materials.

Our method synthesises crystals at the nano-scale that maintaining a size that is more advantageous for porous implants. Furthermore, due to its chemical synthesis it is able to better coat the implant than plasma spraying which is limited by line of sight application[69]. Even within the academic world the previous methods for the synthesis of aligned surfaces relies a technique called the hydrothermal method. Due to this methods reliance on high pressure and temperature equipment, the hydrothermal method would be difficult to industrialise.

Within the previous chapter different temperatures and surfaces were used to explore their effects on crystal growth. This was primarily done with the aim of finding a surface that produced aligned rod-like apatite nano crystals. Which was achieved at 21 °C and 70 °C. In this chapter, the mechanism of crystal growth will be evaluated for samples synthesised at 21 °C and 70 °C. The aim of this chapter with to optimise these coatings in order to fulfil the implant criteria outlined in chapter 1. This being densely packed rod-like apatite crystals that are aligned along their c-axis. Having a width of 25 - 100 nm, and a hexagonal crystal group (i.e. apatite).

5.3 Materials and Methods

Preparation-substrates and solution

In this experiment, 1 × 15 mm discs of commercially pure Ti (from Ti-TEK LTD, UK) was used to approximate the surface of an uncoated Ti implant. 20 % porous Hydroxyapatite, HAp, 1 × 15 mm discs (from plasma Biotal Ltd, North Derbyshire, UK), was used to approximate the surface chemistry and roughness of HAp coated implants. In this way, the effect of surface characteristics could be analysed. In order to remove any unwanted contaminants that may have been present, the discs were rinsed thoroughly with deionised water, and dried using air and filter paper. Following this, a supersaturated solution containing F^-, $PO_4{}^{3-}$, Ca^{2+} and OH^- was made, by mixing mixing 0.532 g HAp (sintering grade Captal ®R powder, Plasma Biotal Ltd, North Derbyshire, UK) and 0.045 g sodium fluoride, NaF (weighed using a DENVER INSTRUMENT SI-403, accurate to 0.001 g), into 500 ml of deionised water at 21°C. pH meter calibration was conducted at the beginning of the experiments using three serial standards of solutions of pH 4.01, 7.0 and of 10.01. After calibration, the solution was magnetically stirred continuously throughout the experiment. Nitric acid (69% AnalaR NORMAPUR, VWR international Ltd, Leicestershire, UK) was added drop wise via micropipette (p100 pipette adjusted to 50 μg) until a pH of 2.4 was reached, and the solute had completely dissolved. In order to allow the precipitated fluorapatite nanocrystals, ammonium hydroxide (28–30%, Sigma-Aldrich®, st. Louis, MO) was added drop wise to raise the pH until a pH value of 6.0 was reached. This process produces what will be referred to as the mineralisation solution.

5.3.1 Incubation and crystal nucleation

In order to achieve a nano layered coating of FAp crystals on to the surface of the substrates the mineralisation solution was poured into 25 ml vials containing one disc of

either HAp or Ti. For each substrate three repeats were used to check the reproducibility of the experiment. Following this, the vials were sealed and incubated 21°C (at average room temperature) or 70°C, using a water bath (Fisher®brand, Fisher Scientific UK Ltd, Leicestershire, UK). After seven days, samples were removed from incubators, rinsed with deionised water, and then were air dried for 2 days. It was important to see the changes in the precipitated material throughout the seven day period. For this study, seven samples of the same substrate, either HAp or Ti, were incubated at the same time. Every 24 hours, one substrate was removed, air dried and the pH of the solution was recorded at that time point. The precipitated powder was then isolated from the solution using a centrifuge that was set to 3000 rpm and run for 5 mins.

5.3.2 Spectroscopic analysis

For analysis via SEM, samples were coated with Gold-Palladium (Au/Pd) (AGAR AUTO SPUTTER COATING, Agar Scientific, Elektron Technology, UK Ltd, Essex, UK) for 30 seconds. This permitted spectroscopic analysis via Scanning electron microscopy, SEM (FEI Inspect F, Hillsboro, Oregon, USA), up to length scales of 80,000×. Here measurement of nano-crystal size and identifying whether rod-like morphology with a hexagonal group structure was formed (indicating the formation of apatite) lower magnifications 300× were used to analyse levels of coverage which was quantified with further image analysis. Magnifications of 70× was used to compare structures with larger morphologies which also had large areas of coverage. The level of surface coverage was assessed through use of ImageJ (and image processing program developed by the National institutes of Health, USA). Elemental analysis was carried out using EDX detector (Inca X-ACT, Oxford instruments, UK). EDX mapping was used and set to identify the presence of F, and Ca/P ratio in order to identify the possible presence of apatite. The standard error of the mean (SEOM) was analysed for each of the 10 SEM images for one of the three experimental repeats. These values were then calculated for each of the 3 repeats and compared. The sample size was considered 95.0% acceptable since the values of the SEOM were within 2× SEOM for each samples.

Fourier transform infrared (FTIR) analysis was conduced using the FTIR Spectrum GX (PerkinElmer, Waltham, MA, USA). The Infrared window was cleaned using ethanol, then the background was scanned. The powder sample was placed over the infrared window to cover it with a metal cover and the sample was scanned. The program was set to take the average of ten scans, to analyse the samples at a wavenumber of 4000 cm^{-1} to 450 cm^{-1} in respect to % of transmittance and files were saved as ASCII format. Data was normalised and plotted on excel for data comparison.

5.3.3 Powder X-ray diffraction and solid state NMR characterisation

The specimens were analysed using X-ray diffraction using a diffractometer (Bruker D2 Powder Diffractometer). Cu-source XRD, Cu-K_α radiation ($\lambda = 1.54056$ Å) at 40 kV/40 mA was used. The diffraction pattern was taken in the 2θ range of 10° to 70° with a step size of 0.04°. The diffraction data were analysed by the Rietveld method [194] using the computer program GSAS [195] and used for phase analysis.

^{19}F magic spinning (MAS) nuclear magnetic resonance (NMR) spectra where obtained on a 600 MHz Bruker Avance NMR spectrometer (14.1 Tesla), operating at 564.7 MHz, and using a low fluorine background probe. The chemical shift reference was 1 M NaF solution with the signal at -120 ppm. Prepared samples were packed into a 2.5 mm zirconia rotor and spun at the magic angle to remove anisotropy effects. The ^{19}F MAS-NMR spectra of the samples were recorded at spinning frequencies 21 kHz. Phase and baseline corrections were carried out using the TopSpin software while measurements were deconvoluted using the DMFIT software package [196]. Using DMFIT, peak width was fixed in to the same values for each spectra for the purposes of comparison.

5.3.4 Surface coverage analysis

5.3.4.1 Mineralisation coverage analysis

In order to analyse surface coverage it was necessary to develop a new method which utilised EDX, SEM and ImageJ analysis. SEM images were taken of the substrate surfaces after incubation. A magnification of 70× was used as a standard for coverage analysis of at the mm range. Images were then analysed using ImageJ. Here a histogram of different pixel values was used to identify covered and non-covered regions. Pixels with a value below 230 were considered to be black and thus a non-covered area. White pixels were considered to be mineralised crystal. EDX mapping was used, this allowed identification of F with in the coatings. This would distinguish the coating from the substrates since none of the substrates used contained F. Before analysis of incubated samples, a Ti control was used to identify the level of noise inherent in EDX the scan. Commercially pure Ti was used and scans were repeated 3 times. Ti, P, Ca, F were analysed with 5 frames. A signal of 100% Ti, and 0% P, Ca and F would be expected if there was no noise. Thus any pixels that appeared or did not appear where expected would be considered noise and would be accounted for in future scans. It was found that, Ti, P, F, and Ca had noise percentage of 20%, 4%, 6% and 6%, respectively. The Ca/P ratio uncertainty incurred due to measurement was found to be 0.01.

5.4 Results

5.4.0.1 Effect of temperature and substrate on aligned FAp growth

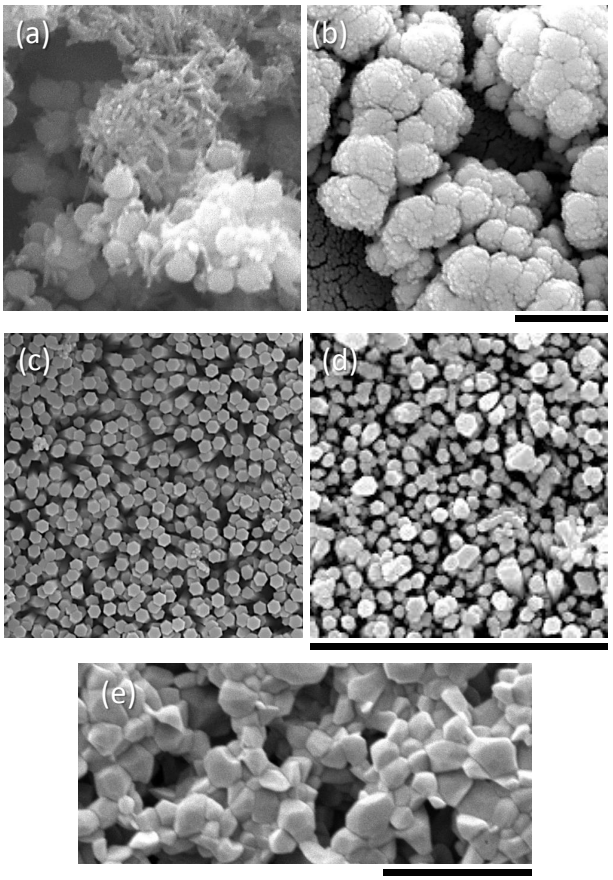

FIGURE 5.1: SEM showing the surface morphology of mineral that has been precipitated on Ti surfaces at (a) 21 °C, and (b) 70 °C, scale 1 μm. SEM of ordered apatite on HA surfaces. Incubated at , (c) 21 °C, showing a regular hexagonal cross-section with width range from 276–341 nm, and (d) 70 °C, showing an irregular hexagonal cross-section, scale 6.6 μm. (e) Uncoated 20% porous HAp substrate

Fig. 5.1 (a) and (b), shows the typical morphology that was found on Ti surfaces when the mineralising solution was incubated at 21 °C and 70 °C, respectively. Here, it can be seen that neither one of these temperatures yield the desired aligned rod-like morphology. That is to say, a morphology that has been shown previously to enhance the cell behaviour of bone forming cells. In contrast to this, aligned rod-like surfaces can be found when the substrate is changed from Ti to HAp while keeping the temperatures the same, see Fig. 5.1 (c) and (d). The level of surface coverage of the aligned rod-like structures formed on HAp substrates were performed using ImageJ. For the two temperatures 21 °C and 70 °C, incubated on HAp substrates, the coverage was found to be 9.167 ± 0.004 % and 70.083 ± 0.004 %, respectively.

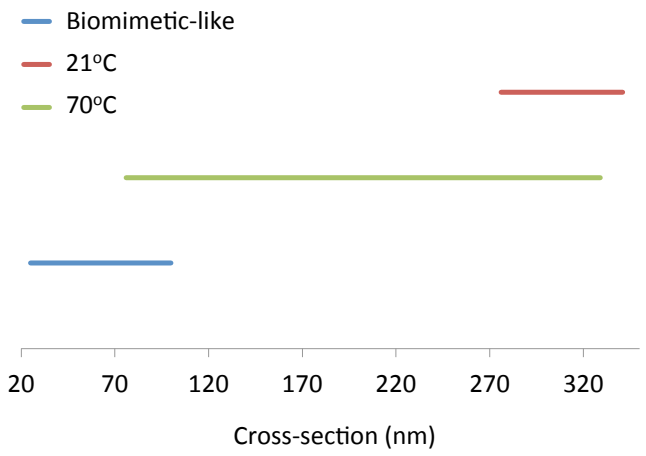

FIGURE 5.2: ImageJ analyse of 21°C and 70°C compared with desired biomineral dimensions. As can be seen, there are a range of cross-sectional sizes in crystals formed at 70^oC where as the range in cross-section is much smaller in those formed at 21°C.

Upon inspection of the coatings through SEM, we can visually see two major difference between these two ordered coatings. The first being that there are at least two cross-sectional sizes at 70 °C where as the range of size at 21 °C appear more uniform. The second of these is that the morphology of the crystal-cross-section are found to be regular-hexagonal at 21 °C but irregular-hexagonal at 70 °C.

The diameter of nano-crystal cross-section, see Fig. 5.2, was quantified with ImageJ. Crystals formed at incubation temperatures 21 °C and 70 °C had width ranges of 276–341 ± 1 nm, and 76–329 ± 1 nm. Only those found at 70 °C fall within the size range of 25–100 nm required for the bioactive properties previously discussed in Liu in 2011 [70]. Nano-coatings produced at 21 °C, fell far outside the required size range. Thus given the larger surface coverage of 70% and the ability to produce crystals within the bioactive range, also defined by Liu. Thus, further study was on samples produced at 70 °C were favoured over those made at 21 °C.

5.4.0.2 FAp formation as a function of time

The following represents the average value for peaks found over all the seven days. All data was normalised for comparatison.

Typical apatite peaks can be seen at each day in Fig.5.3. Visually, no obvious difference can be seen when inspecting XRD diffractograms from each time point, thus Rietveld analysis was employed in order to quantify the changes.

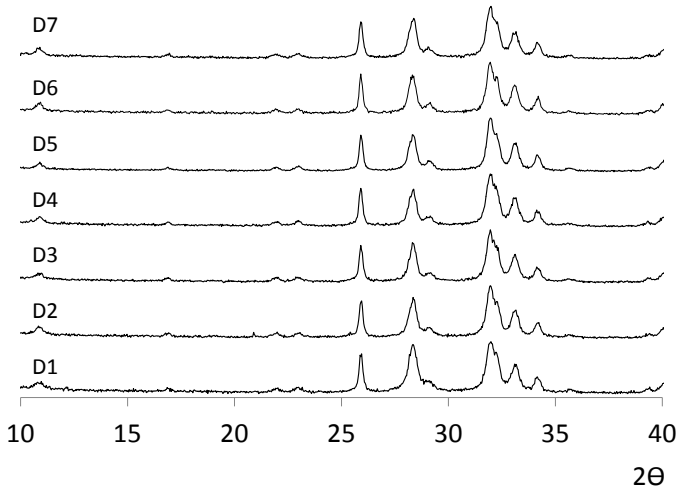

FIGURE 5.3: XRD of powders formed at 24 hour time points over seven days and incubated at 70°C.

TABLE 5.1: Rietveld refinement results for samples incubated at 70 °C, and refined against FAp unit cell. $a = b$, and $\alpha = \beta = 90°$, $\gamma = 120°$ for all values, indicating a hexagonal unit cell. APS = average particle size.

Day	a (Å)	c (Å)	APS (Å)	w%	χ^2
1	9.380070	6.885523	175.99	64	1.281
2	9.379970	6.882502	252.70	55	1.191
3	9.379666	6.883554	246.33	54	1.234
4	9.373875	6.879460	232.76	55	1.302
5	9.376419	6.881545	281.63	54	1.211
6	9.380467	6.883300	252.63	92	1.924
7	9.379660	6.882743	222.64	69	1.655

Table 5.1 show the results from the Reitveld refinement of the XRD patterns shown in Fig. 5.3. An example of refinement can be seen in Fig. 1 of the appendix. CaF_2 was also found with an average $a = 5.4679 \pm 0.0003$ Å. The average particle size which was derived from the XRD by way of Scherrer's equation was used for both apatite, shown in Table 5.1, and CaF_2. For CaF_2 the particle size was found to be 236.83, 203.14, 211.65, 237.59, 215.02, 197.78, and 146.40 ± 0.07 Å, for days 1, 2, 3, 4, 5, 6 and 7, respectively. The weight percent was also found to be 36%, 45%, 46%, 45%, 46%, 8% and 30% ± 2%, in that same order.

In order to reconcile the results of the XRD with that of the NMR results I ran refinements including CO_3FAp. On days 6 and 7 CO_3FAp was found to have percentage abundance of 0.04 w%. It was not possible to find an appreciable influence by that of CO_3FAp, thus this phase was disregarded for XRD refinement.

The data in Fig. 5.4 show the that day 1, to day 6 , look identical whilst day 7, shows

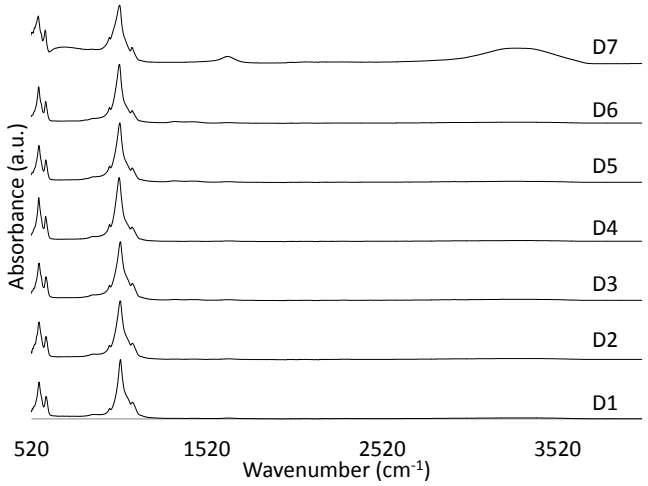

FIGURE 5.4: FTIR of powders formed at 24 hour time points over seven days and incubated at 70°C.

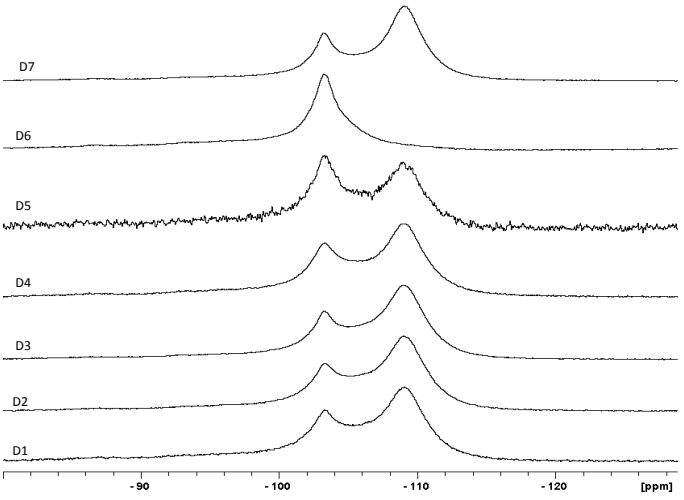

FIGURE 5.5: NMR of powders formed at 24 hour time points over seven days and incubated at 70°C.

some additional broader peaks. Each spectrum maintains a typical apatite pattern [197] with PO_3^{2-} peaks were found at 562.1, 601.9, 1088.5 cm^{-1}, the lack of a OH^- libration peak around 613.1, and a broad OH^- stretch band that peaks around 3574.0 cm^{-1} suggests a very low hydroxyl content, or that the formation of FAp was favoured over HAp on precipitation for days 1 to 6. However, this is less certain in day 7 where we can see a broad peak ranging from 3000–3665 cm^{-1}. CO_3^{2-} bands were observed at 872.6, 1431.3, and 1456.3 cm^{-1}. With the exception of the 872.6 cm^{-1} CO_3^{2-} bands which had a 5.2 σ, all other values were within 3.5σ when compared to literature. This indicates we can be confident that the result is 99.98% consistent.

^{19}F MAS NMR spectra, Fig. 5.5, clearly show the change in precipitate composition

between apatite and calcium fluoride over the seven days. What can be seen is that at days 1 to 4 the height of the −109 ppm (CaF_2) peak is greater than that of the −103 ppm (FAp) peak. On day 5 we begin to see that the −109 ppm peak is lower than that of the −103 ppm peak and on day 6 this peak has become unobservable. Using DMFIT, see Table 5.2, we were able to deconvolute these spectra further. Peaks at −87.70 ppm and −95.74 ppm could both indicate the presence of a carbonate group [198, 199]. However, a value of −87.70 ppm could also be ascribed to CaF_2 [111]. Given that we are not able to fully distinguish which of these are responsible for this value, it would not be wise to provide an identification for this peak. For this reason we have referred to this peak as an unknown contaminant (UC) in Table 5.2. Further to this, a fourth peak at 105 ppm was necessary for accurate fitting to the NMR data. Table 5.2 also shows an agreement with the Rietveld refinement data. In both cases we can see an increase in the apatite phases and a decrease in the CaF_2 on day 6.

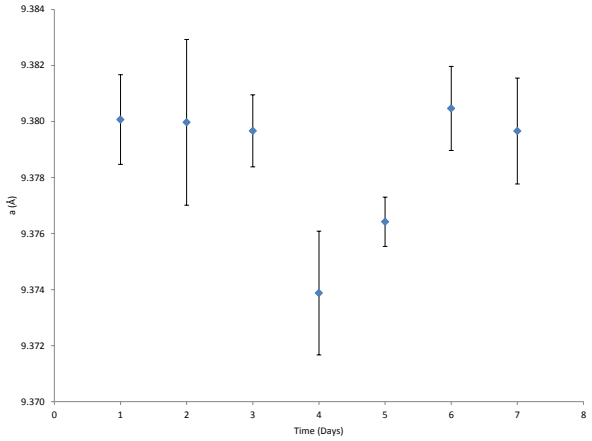

FIGURE 5.6: a-axis unit cell parameter plotted against time.

Fig. 5.6, For the FAp samples, the progression of the synthesis from days 1 to 7, the a-axis there is no statistical significance between time points throughout the seven days. Based on the work of Yajie Gao [200], we know that an increasing percentage of F^- ion substitution within FHA leads to a reduction of the a axis. Thus, this could imply that the amount of F^- ions being substitute remains constant throughout the synthesis process. If we consider both the contribution from FHA and FAp we can see that DMFIT analysis, Table 5.2 agrees with this result.

Qualitative SEM image analysis appear that organisation and size are not constant throughout the seven day crystallisation process. Fig. 5.7, from days 1-5, the precipitated crystals formed on the surface have more than one orientation with respect to the c-axis. The hexagonal face of some rod-like crystals face towards us where as in some cases it is the crystal face parallel to the c-axis that faces are directed toward us. Finally, in other

TABLE 5.2: Deconvolution of NMR data performed by DMFIT. Showing percentage abundance of each chemical shift value identified at 70°C. Average ppm values are here given. An unknown contaminant (UC) has been included for completeness. Uncertainty on ppm, $\sigma = \pm 0.03$.

ppm	Identification	D1	D2	D3	D4	D5	D6	D7
−87.70	UC	1.77	0.49	1.63	1.05	1.54	10.61	0.79
−95.77	CO_3	8.52	5.35	2.14	7.77	9.01	15.71	4.13
−103.35	FAp	24.13	23.55	24.88	26.72	42.96	24.15	27.98
−106.03	FHA	19.20	20.31	18.75	17.06	3.88	49.35	5.90
−109.12	CaF_2	46.37	50.31	52.61	47.40	42.60	0.00	61.19

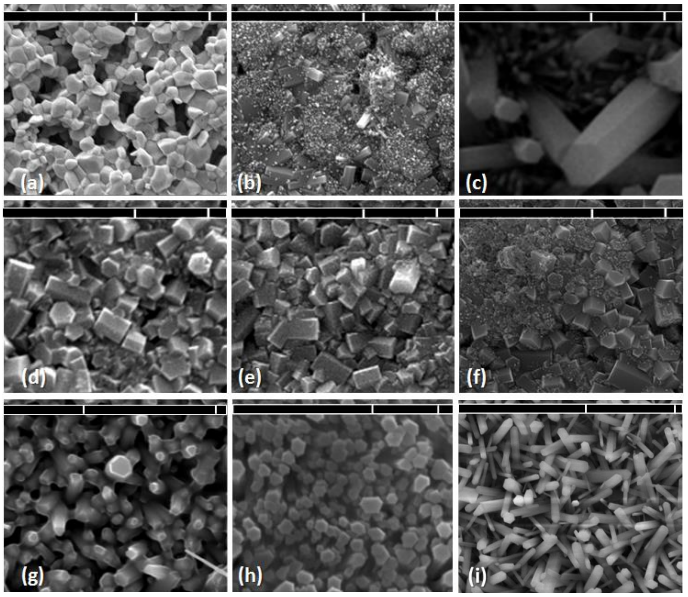

FIGURE 5.7: SEM of 20% HA substrate incubated at 70°C for seven days. Days 0 to 5 (a) to (f) scale bar: 2 μ m, day 6 (g) and 7 (h) and 8 (i) have scale bars 10 μm and 1 μm respectively.

cases it can be seen that there are some crystals that are oriented at some raised angle from the surface. It is for this reason that we refer to this state as being missaligned, where as the crystals seen at day 7 are clearly all aligned along the c-aixs of the rod-like crystals.

Fig. 5.7 (a) day 0, shows HAp substrate with 20% porosity. Measurements of the surface gaps on HAp substrates showed a of length 0.49–0.90 μm, and width 0.24–0.74 μm, as determined by ImageJ analysis of SEM samples. Fig. 5.7 (b) Day 1, rod-like crystals with a small aspect ratio are deposited within the first day. On day 2, Fig. 5.7, there appears to be crystals of two distinct size ranges. Both small (a few nano meters in length) and large (in the range of hundreds of nanometers) crystals coexist at this time point and persists until day 6. At day 3, Fig. 5.7 (d), rod-like crystals return but with a smaller aspect ratio, this time we gain small scale nucleation around these rods;

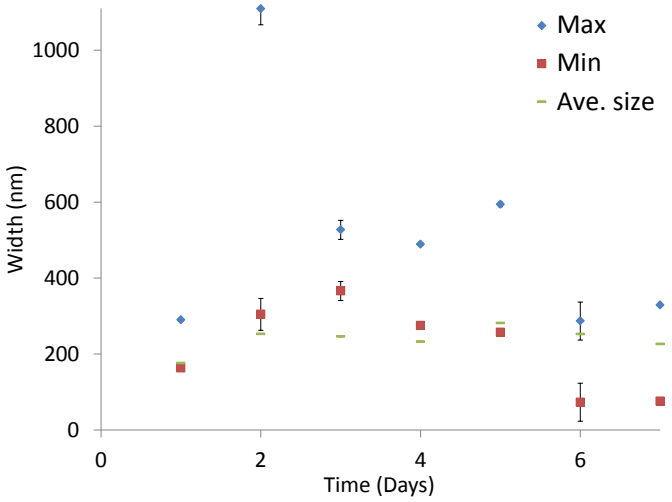

FIGURE 5.8: Analysis of hexagonal crystal width, measured from furthest most corners. The width range is as follows: day 1 (290–163 nm), day 2 (1,109–305 nm), day 3 (527–366 nm), day 4 (489–275 nm), day 5 (594–257 nm), day 6 (287–73 nm), and day 7 (329–76 nm). Average crystal s size (Ave.size) derived from Rietveld refinement, an uncertaintly of 0.69 was calculated.

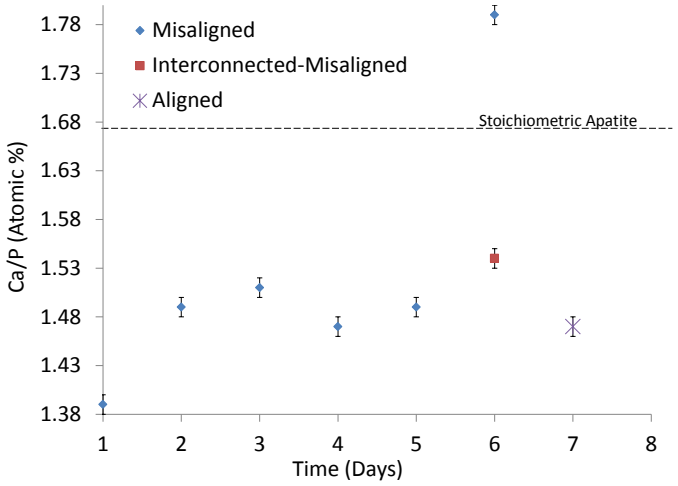

FIGURE 5.9: EDX analysis from atomic %, Ca/P ratio of disordered crystals incubated over seven days. Calculated uncertainty of 0.01 is not visible on figure. Interconnected misslaligined, see Fig. 5.7(g)

this feature seems to reduce when we enter into day 4, Fig. 5.7 (e), but returns again in day 5, Fig. 5.7 (f). At day 6, Fig. 5.7 (g), we observe connected structures that appear as if they have formed as one single object. It can be seen that even though crystals are connected, they maintain a hexagonal cross-sections. The size appears to have reduced considerably and we begin to see some level of alignment between the nano-crystals. Finally, on day 7, Fig. 5.7 (h), aligned apatite is formed. It can be seen that the interconnections between nano-crystals has disappeared. In fact, here we notice

clearly defined boundaries. Adding to this, we also notice that the interstices appear reduced relative to those found at day 6. Here crystals become more closely packed. Day 8, Fig. 5.7(i), illustrates how further incubation time leads the crystals to fall out of alignment. Thus we can see that between days 6 and 7 show the most promise for an optimal time point.

A more quantitative analysis of morphological changes was conducted using ImageJ. Measurements of the cross-sectional area of the rod-like crystals, see Fig. 5.8. From day 1 to day 2, with a range of (163.0–290.0 nm) and (305.0 – 1,109.0 nm), respectively; there is a massive increase in the cross-sectional width of the biggest crystals but only a small rise in the smallest. Crystal cross section has an overall reduction in size on day 3 (366–527 nm), which is maintained throughout day 4 (275.0 – 489.0 nm) and day 5 (257.0 – 594.0 nm). Again, there is another reduction in crystal size when going from day 5 to day 6 having a range of (73.0 – 287.0 nm) which is maintained until the end of day 7 where a range of 76.0 – 329.0 nm is observed. What can be seen is that the maximum crystal cross-section (MACC) seen on day 1 falls within the margin of error for the minimum crystals cross-section (MICC), which also encompasess the MICC of day 1. These crystals could indicate the same crystals that persist throughout the first three days. We see this pattern again when considering the MACC on day 6, here the MICC of day 4 and 5 together with the MACC of day 7 all fall within the margin of error for that of day 6. It could be possible that in both of these cases, this is an indication of a layering effect. Crystals that start precipitating at day 1 increase in size quickly within the first day, following this the size remains fairly constant until day 3 where they maintain a stable size. After this, crystals continue to grow in size until day 5, where they are over run by smaller crystals that initially start to grow in day 4. Crystals that grow from day 4 to 7 are able to completely cover the larger crystals that were previously seen.

EDX analysis was used to characterise the calcium/ phosphate (Ca/P) ratio within the synthesised coatings. Fig. 5.9 Ca/P ratios observed at day 1, 2, 3, 4, 5, 6 and 7, were 1.39, 1.49, 1.51, 1.49, 1.79, and 1.47 respectively. Interconnected misaligned crystals found at day 6 were 1.54 and other hexagonal disordered , those predominantly found at days 1 to 5, were 1.60. On day 6, distinction is made between interconnected misaligned crystals and 'regular' misaligned crystals (those that are not interconnected) that are also observed at this time point. the Former Ca/P being 1.54 the latter 1.79.

Fig. 5.10(a) day 4, with clump-like structures existing on top of the misaligned rod-like crystals; Fig. 5.10(b) day 5, small crystals growing within the interstices of the misaligned rod-like crystals; and Fig. 5.10(c) day 6, smaller crystals appear to have completely grown over the larger misaligned crystals.

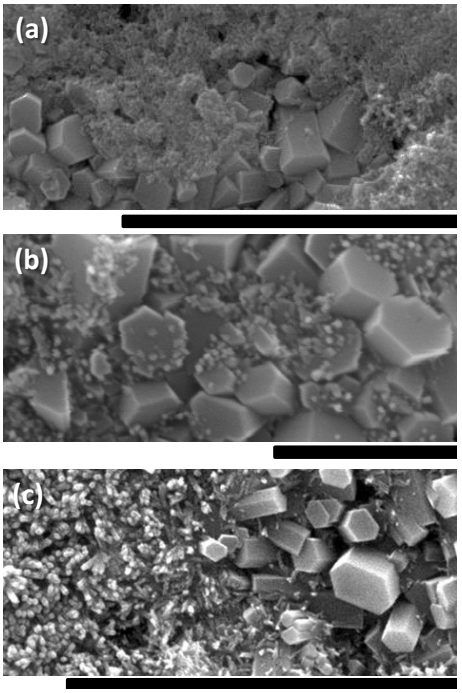

FIGURE 5.10: SEM of nano crystals grown on 20% porous HAp. (a) day 4, (b) day 5, and (c) day 6. Scale, 4μ m, 2μ m and 5μ m, respectively.

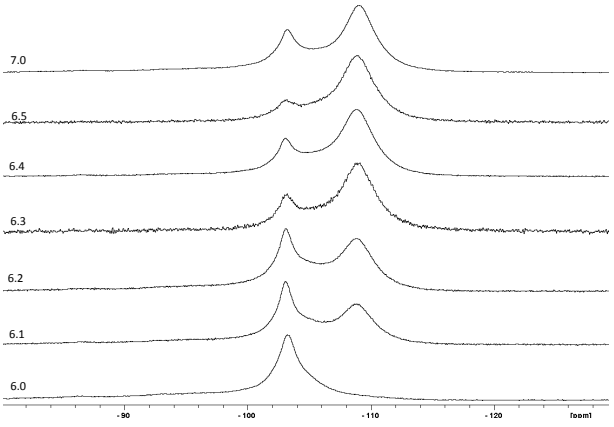

FIGURE 5.11: ^{19}F MAS NMR of time points between day 6 and 7 with 70°C samples.

We wanted to better understand the exact point of optimal apatite formation. As we have seen before, the optimal point for apatite abundance has been day 6 for samples that have been incubated at 70 °C, but at the same time showing the desired nano conformation only at day 7.

Is there some middle ground that can be achieved through a consideration of the time point between day 6 and 7? From Fig. 5.5, we can see that there is a gradual shift from a CaF_2 dominance to a apatite dominant one from day 1 to day 6. However, after day 6 there seems to be a quick change back to a CaF_2 dominance. It was important to

TABLE 5.3: Deconvolution of NMR data performed by DMFIT. Showing percentage abundance of each chemical shift value identified for 5 time points 6.1, 6.2, 6.3, 6.4, 6.5, between day 6 and 7 at 70°C. Average ppm values are here given. An unknown contaminant (UC) has been included for completeness. Uncertainty on ppm, $\sigma = \pm 0.03$.

ppm	Identification	6.1	6.2	6.3	6.4	6.5
−86.25	UC	0.55	1.38	1.14	0.85	2.41
−94.94	CO_3	7.27	13.26	1.53	4.23	3.16
−103.10	FAp	21.72	26.19	12.10	16.52	12.29
−105.12	FHA	30.35	17.77	20.03	16.31	10.81
−108.93	CaF_2	40.12	41.40	65.21	62.08	71.33

know the exact time point of optimal apatite dominance for the better refinement of the experimental method. Fig. 5.11, shows the data from five time points (6.1 – 6.5) between day 6 and 7, separated by 4 hour intervals. It can clearly be seen that after day 6, there is a gradual decline in the abundance of apatite with respect to CaF_2. See also Table5.3, here we find that there is a general trend in which the abundance rises from 40.12 to 71.33 %, where as the collective FAp and FHA declines from 52.07 to 23.10 % in the same time. Thus, we can see that day 6 is actually the optimal time point for the formation of apatite.

5.4.1 Synthesis pathway for samples produced at 21 °C

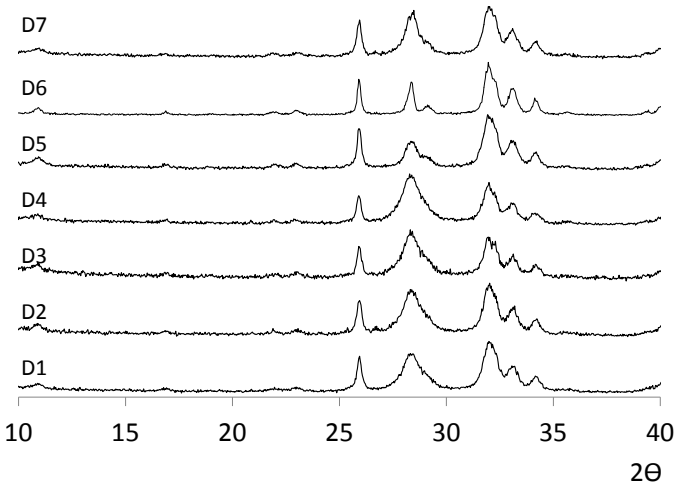

FIGURE 5.12: XRD of powders formed at 24 hour time points over seven days and incubated at 21°C.

Fig. 5.12 shows XRD diffractograms obtained from the same samples incubated at 21 °C. These peaks maintain a typical apatite peak at all time points. As we will see later, SEM images do show that plate like calcium-phosphates are formed throughout the seven days, however, the abundance is so low that they do not contribute to the XRD

TABLE 5.4: Rietveld refinement results for samples incubated at 21 °C, and refined against FAp unit cell. $a = b$, and $\alpha = \beta = 90°$, $\gamma = 120°$ for all values, indicating a hexagonal unit cell. APS = average particle size.

Day	a (Å)	c (Å)	APS (Å)	w%	χ^2
1	9.380467	6.87905	157.84	56	3.758
2	9.379193	6.877777	165.13	74	1.399
3	9.380605	6.878235	218.47	23	1.375
4	9.380362	6.879804	200.52	16	1.581
5	9.349455	6.856674	162.97	55	1.469
6	9.387437	6.885197	198.40	40	2.854
7	9.384204	6.881904	213.97	35	1.648

pattern here. What can be seen in this figure is that there is a change in the relative peak height (intensities) of various peaks. When considering only the (002) and (102) peaks we can see that 1–4 the (002) peak is of a lower intensity, relative to that of the (102) peak. This relationship shifts, where on days 5 and 6 it is the (102) peak that has a greater peak intensity. Finally, on day 7, we return to the original pattern as seen in the first 4 days. As we know, the peak height is effected by the position of the atoms within the plane. Which could be indicative of substitutional effects of groups such as the carbonate group or the various amounts of OH^- that was found within those samples incubated at 70 °C. It can also be seen that the width of the peaks also change throughout the samples. This could be due to the changes with the crystallite size or an overlap with CaF_2 that have previously been found to have formed as a by-product of the crystallite formation at 70 °C.

Rietveld refinement, Table 5.4, has confirmed the presence of apatite along with a certain percentage of CaF_2 with an average particle size of 236.83, 623.48, 90.99, 82.36, 106.37, 61.89, and 120.80 Åfor days 1, 2, 3, 4, 5, 6, and 7, respectively. Various apatite forms were used to see whether there was any significant difference between the goodness-of-fit. Standard crystallographic files for HAp, FAp, and FHA were interchanged and were refined against the data either separately, or along side CaF_2. It was found that the samples in which FHA and CaF_2 were used as the crystallographic standards showed the best fit both, visually, and in terms of χ^2. For this reason, FHA was used as the apatite form for further refinement. This would also be consistent with the NMR results that was found when analysing the 70 °C samples.

Data for FTIR data collected from samples incubated at 21 °C are shown in Fig. 5.13. Just as we saw with the samples incubated at 70 °C, the spectra shows a typical apatite pattern. On average, PO_3^{2-} peaks were found at 563.7, 604.0, 1091.2 cm^{-1}, and the lack of a OH^- libration peak around 613.1 suggests a lack of the OH^- group. A broad OH^- stretch band that has an average onset from 2987.0 – 3660.8 cm^{-1}. From days 1 – 5,

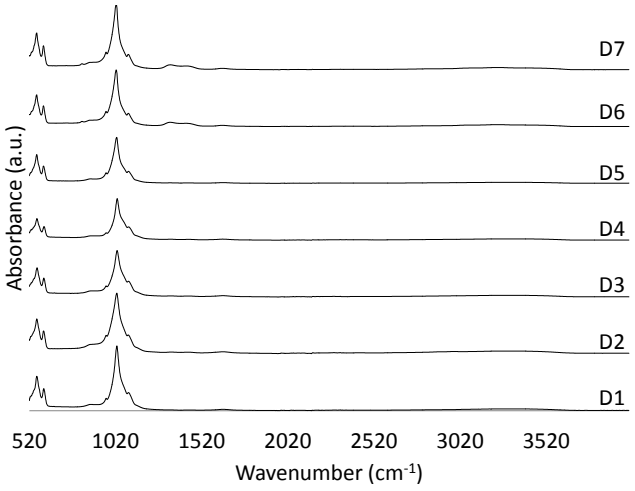

FIGURE 5.13: FTIR of powders formed at 24 hour time points over seven days and incubated at 21 °C.

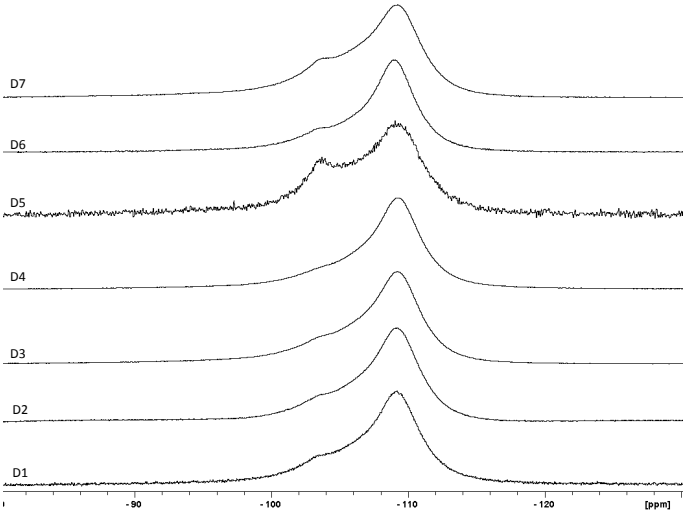

FIGURE 5.14: NMR of powders formed at 24 hour time points over seven days and incubated at 21 °C.

this broad band is less obvious than other peaks, having an intensity of around 1.33% of the total intensity. Notably, in some parts, the background has been recorded to be 4.00% of the total, and as such these peaks provide little evidence towards the presence of an OH^- group. On day 6, the peak intensity rises to around 3.43%, suggesting that there may be some incorporation of OH^- at later stages of formation. There did not seem to be a consistent shift in the peak positions through out all the separate days and not even within an individual day, thus this was not considered to be a contributing factor to the uncertainty seen in the signal onset. The final possibility in this case is that their may be a very low hydroyxyl content within the samples. Previously we have mentioned the same reasoning for that of samples produced at 70 °C.

A signal onset at 865.7 cm^{-1} was consistently found in all data sets. This proved to have an agreement of 1.2σ and is indicative of the presence of CO_3^{2-} bands. Again, like its 70 °C counterpart this suggests the formation of B-type carbonate apatite. Other peaks could be found in the region of 1430, and 1460 cm^{-1} however, these were not consistent and also had intensities around 1.40% which was near indistinguishable from the local background reading of 1.11 cm^{-1}. These peaks were discounted from further analysis. All other peaks had a value less than 3.8σ which indicates a confidence that the result are at least 99.98% consistent.

Based on the solid state NMR analysis, Fig. 5.14, we would expect that unlike its 70 °C counterpart, the samples produced at 21 °C do not have a single time point in which a majority of the samples is apatite. This is because at all time points, the CaF_2 peak, seen around −109.00 ppm is always the more dominant of the two. peaks. Apart from day 5, which shows a clear peak at −106.98 ppm, all time points show only a shoulder at this position. Peak deconvolution, conducted with DMFIT revealed that an average of 63.30% was found for the percentage abundance of CaF_2, with a maximum abundance of 70.78% on the second day. It would appear that the abundance is reducing with an increase in time given that from day 4 to 5 the abundance drops by 15.64%, and this appears to be constant at day 7 with a similar value of 51.91.

TABLE 5.5: Deconvolution of 21 °C NMR data performed by DMFIT. Showing percentage abundance of each chemical shift value identified. An unknown contaminant (UC) has been included for completeness. Average ppm values are here given.

ppm	ID	D1	D2	D3	D4	D5	D6	D7
−91.24	UC	0.00	0.00	0.00	0.00	0.00	0.54	1.71
−97.55	CO_3	0.00	0.00	0.00	0.00	1.62	1.29	2.24
−103.63	FAp	15.59	13.11	14.79	15.66	25.06	15.35	22.43
−106.90	FHA	16.45	16.11	17.60	15.76	20.37	15.00	21.71
−109.31	CaF_2	67.97	70.78	67.61	68.59	52.95	67.82	51.91

As before, an attempt to fit peaks at −86.00 ppm and −95.00 ppm were also tried. It was found that in most cases, these peaks did not exist. In other cases such as those at higher time points, dat 5 and day 7 for example it was found that the carbonate group added some small contribution to the over all composition at 1.62 and 2.24%, respectively. Whereas, in the case of the unknown contaminant, UC, it was found that a peak at −94.29 ppm contributed to 1.71% of the composition in powders found on the seventh day of incubation.

Analysis of the *a*-axis of the FHA unit cell reveals that there is a significant change between the different days. By comparing the uncertainty derived from Rietveld refinement we can see that the a values found on days 2 – 4 could be considered the same value. Days 6 and 7 also could be considered to be the same value. However, these

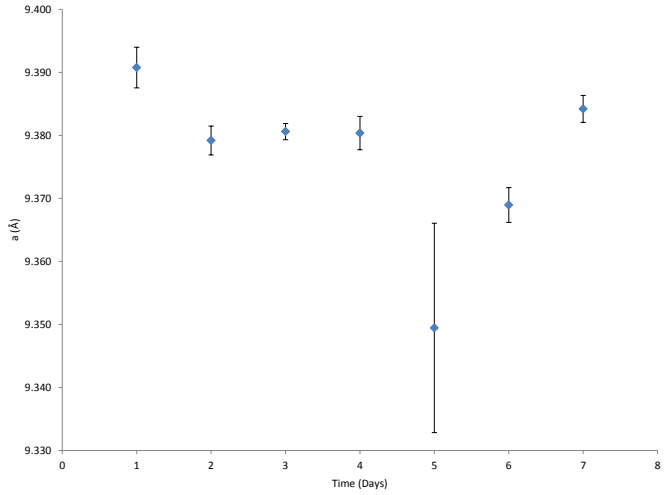

FIGURE 5.15: a axis unit cell parameter plotted against time for samples incubated at 21°C.

data points fall into a different group than those previously mentioned. Day 1, serves to form a third group, where as the value found on day 5 has a much bigger error than others seen here. It is also an outlier and will not be considered. Here, it would appear that there is a reduction in the size of the unit cell from day 1 to 2. This could be due to the substitution of F^- ions for the OH^- ions, from here on there is a gradual lengthening in the a-axis over the 7 days which would be consistent with the gradual incorporation of more OH^- ions throughout the synthesis period. However, the results from the DMFIT deconvolution would appear to tell a different story. In fact, it is the F^- ions that appears to have a greater incorporation over time. Strangely, on day 5 we do see a massive increase in the presence of FAp, having a 9.4% increase in the percentage abundance. This could explain the massive reduction in the a-axis value seen from Rietveld refinement. However, if this is the case why do we not see an equally large reduction when we observe the a-axis value of day 7. It too had an abundance of FAp that was in fact greater than the first 4 days, thus it would be expected that a similar effect should be observed.

Clearly, the synthesis route for samples produced at 21 °C follows a path different to that of those produced at 70 °C. Instead of forming rod-like structures on day 1, ball-like structures, 1,561.40 nm in diameter, are first formed. These structures completely cover the porous apatite substrate covering as can be seen by Fig. 5.16 (b), and Fig. 5.17. By day 2, Fig. 5.16(c), we begin to see the formation of disorganised clump-like ranorods that appear to be an out growth of the previously mentioned ball-like structures. Notably, the ball-like structures have also reduced in size to 519.00 nm. Perhaps suggesting that material from the ball-like structures have been consumed by the rod-like structures during their formation on day 2. On day 3, Fig. 5.16(d), we see that the

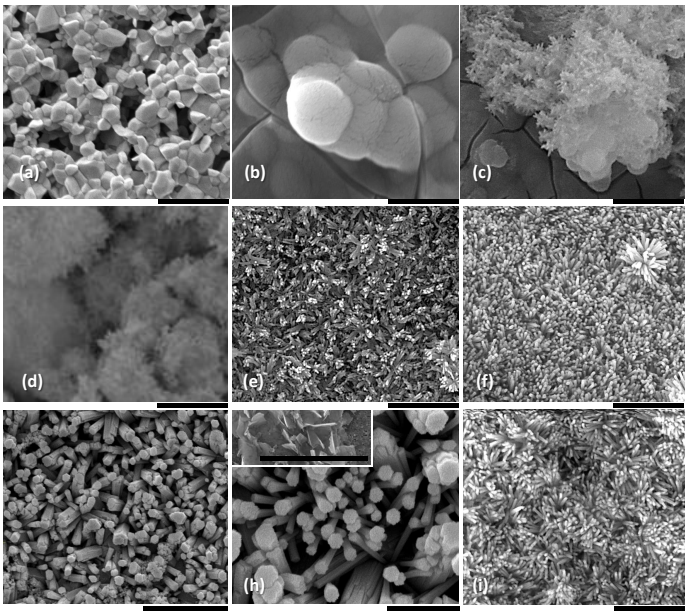

FIGURE 5.16: SEM of mineral formed on HAp substrates at 24 hour time points over seven days and incubated at 21°C. Days 0 to 6 (a) to (f) scale bar: 2 μ m, day 6 (g) scale bar 5 μm, day 7 (h) has Scale bar of 1 μm (insert 40 μm) and day 8 (i) has a scale bars of 2 μm.

disorganised rod-like structures have become the dominant structure that can be seen with SEM. Their orientation seems to follow that of the previous surface contours of the ball-like structures. By day 4, Fig. 5.16(e), it would appear that the 3-dimensional nature observed in day 3 has been lost. In this case, the rod-like structures still maintain a disordered orientation but these crystals appear to have formed a fairly '2-dimensional surface'. By day 5, Fig. 5.16(f), these crystals began to organise them selves into aligned rod-like crystals. Day 6, Fig. 5.16(g) shows a return back to a disorganised nano-rod state. As can be seen, Fig. 5.16(h), crystals formed at day 7 shows aligned rod-like crystallites however in some sections the formation of plate-like crystal have been found, reminiscent of DCPD and DCPA. These crystals were so rarely found, and also did not appear to contribute to any of the previous characterisation methods, chiefly XRD that we may ignore these structures. One similarity between the synthesis route here with the one observed at 70 °C is that on day 8, Fig. 5.16(i), these rod-like crystals return to a misaligned morphology. Again, this shows that the 7 day time point is an optimal time point for the growth of these ordered structures. In comparison, this same process took over 5 days to occur in those crystals formed at 70 °C, but only required three days when incubated at a temperature of 21 °C. Furthermore, it would appear that these initial crystals began with an initial cross-section that is much smaller than their higher temperature counterparts. The poor resolution experienced on days 2 and 3 prevented any image analysis of the cross-section. Instead, only the crystal length could be here analysed to be 305.00 and 545.00 nm, respectively. Following on from

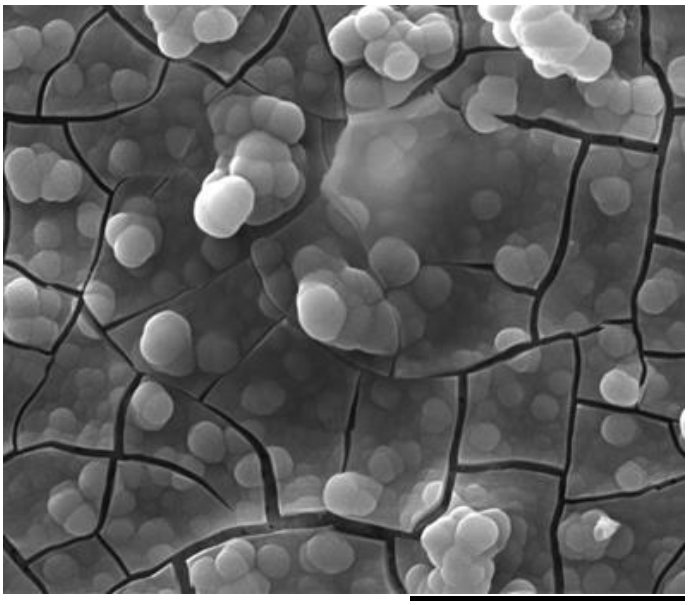

FIGURE 5.17: SEM of mineral formed on HAp substrates on day 1 and incubated at 21°C, as seen in Fig. 5.16. Scale bar 10 μm.

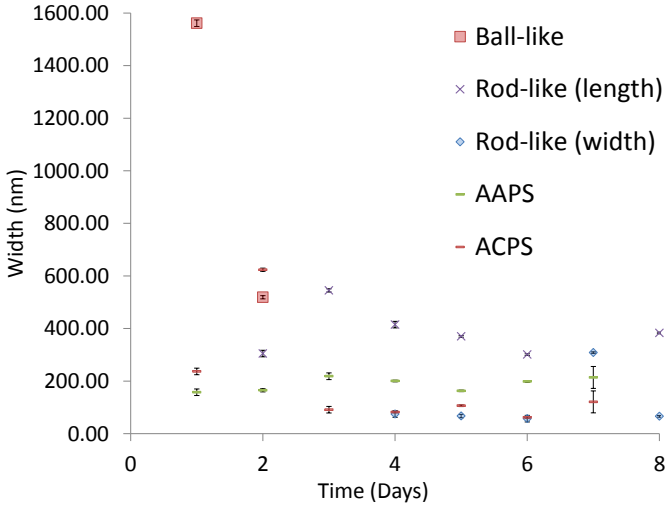

FIGURE 5.18: Size analysis of morphologies seen at 24 hour time points over seven days and incubated at 21°C. Average apatite particle size (AAPS) and average CaF_2 particle size (ACPS).

this the cross-sections (width, W) and length (L) could be measured for days 4, 5, 6, 7, and 8, to be (W:74.80; L:415.00 nm), (W:67.10; L:370.00 nm), (W: 355–710 nm), (W: 182–1495 nm), and (W:66.00; L:383.00 nm), respectively. As can be seen, there is a large discrepancy in the cross-section observed on day 7 crystallites. This is likely due to the level of resolution that could be achieved due to a higher magnification. Crystals observed on day 7 were taken at a magnification of $20,000\times$, where as on other days the best magnification that could be achieved was $80,000\times$.

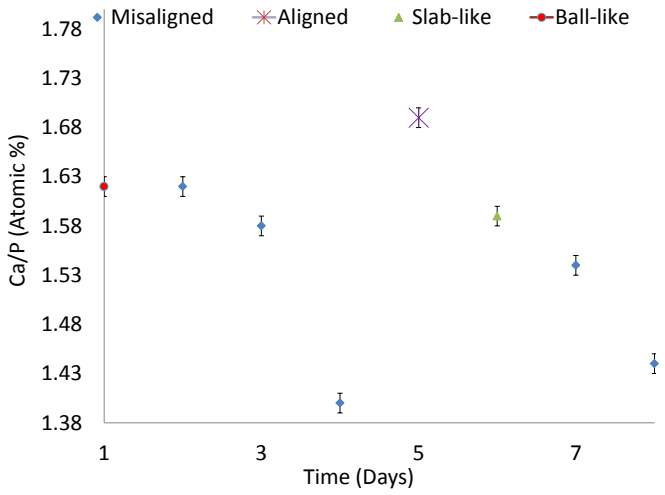

FIGURE 5.19: EDX, Ca/P ratios of powders formed at 24 hour time points over seven days and incubated at 21°C. $\sigma = 0.01$

Fig. 5.18, shows the analysis of images seen in Fig. 5.16 using ImageJ analysis. The level of uncertainty was limited by the size of each pixel within each SEM image. These errors were included in Fig. 5.18. However, since it is not clear they will here be stated. For days 1, 2, 3, 4, 5, 6, 7, and 8, the uncertainty was calculated to be 12.44, 6.22. 12.51, 3.12, 3.14, 12.48 and 3.13 nm, respectively. For the insert, seen in Fig. 5.16 ((h), the error was calculated to be 41.65 nm.

Considering the average apatite particle size (AAPS) derived from Rietveld refinement, we can see that there should be small apatite crystals 157.84 Å in size on day 1. These crystals were not seen on SEM, however this may be due to the massive difference in the size of the ball-like structures when compared to the AAPS, which is two orders of magnitude smaller. That is to say that it is conceivable that these micro spheres are composed of apatite nano-crystals. In both cases, either with the apatite crystallite width or the AAPS we can see that there is a gradual increase in the size over the first 7 days. Length, however, seems to have the opposite effect, showing a gradual decrease over the duration of synthesis. The only exceptions to this are the 8^{th} day, in which the width decreases and the length increases. In the case of the average CaF_2 particle size (ACPS), we can see their average size on day 1 is also one order of magnitude smaller than the ImageJ derived ball-like structures. Furthermore, even though there is a similar size. Uncertainty ascribed to the ACPS and the ball-like crystallites on day 2 can not be considered the same point. These two observations of the size discrepancies at day 1 and 2 calls into question, whether or not these ball-like crystallites are in fact CaF_2 as we first assumed. Following on from this, we can see that from day 3 to 7, the size of the CaF_2 becomes small enough to be comparable with that of the widths of the rod-like apatite crystals. As we have previously seen in both the Rietveld refinement, Table 5.4,

and the DMFIT data derived from NMR, Table 5.2, we expect that the composition of these powders to lean more towards that of CaF_2 in most cases. However, based on the SEM, we can not see much evidence for the presence of CaF_2. It is possible that these ball-like crystals are so small that these CaF_2 crystals are not easy to find within the SEM images. It is also possible that the CaF_2 that is being picked up in both that XRD and the NMR patterns are actually existing within a sub-surface layer, over which the apatite crystals have grown.

Unlike the samples formed at 70 °C, where the Ca/P ratio values suggest that the material formed is closer to that of calcium deficient apatite, than those formed at 21 °C, Fig. 5.19. Here, we can see a more restricted spread of Ca/P values from 1.40 to 1.69, with 63% of the readings falling between 1.54 and 1.62 which would appear to have reached values closer to stoichiometric apatite.

5.5 Discussion

5.5.1 Morphological analysis

Throughout Fig. 5.7(a-f), we can see the formation of both small and large rod-like crystals. In the later stages it appears that the smaller rod-like crystals form at the boundaries between the larger crystals. With the finding of interconnected crystals, seen in Fig. 5.7(g) we can see that crystals have become interconnected, though at the same time they maintain a hexagonal cross-section. These interconnections have a curved appearance and also it seem that the hexagonal cross-section of the nano-crystals do not have a strongly defined boundary, almost as though the crystals them selves were with covered with a new layer or the crystals them selves melt. There are 3 main explanations for this observation,

1. Compositional changes that cause a transient amorphous phase during phase transition,
2. The formation of amorphous deposits leading to an independently occurring crystal phase, and
3. Surface dissolution that indicates the growth of the crystal has reached its limit.

It could be argued that there is no evidence for the formation of amorphous calcium phosphates (ACPs). The key reason for this is that the morphology of ACP typically takes on a particulate form. These particulates have diameters in the range of 200–1200

Å and maintain no definite structure [201]. However, we know that SEM evidence alone is not sufficient to indicate the presence of amorphous ACP, and traditional methods such as Rietveld Refinement would not have the ability to distinguish ACP from its crystalline counterparts.

ACPs are considered thermodynamically unstable compounds and unless stored in dry conditions or doped by stabilisers, spontaneously they could transform to crystalline calcium orthophosphates, mainly to calcium apatite's [201]. Notably, during the two day air drying stage of our material preparation there is a possibility for the ACP to undergo a transformation to a more crystalline CaP. Un-substituted ACPs are unstable in aqueous solutions and even when stored dry they tend to transform into calcium deficient hydroxyapatite (CDHA), [202]. If this were indeed the case, we would expect that there would be no evidence of the amorphous phase.

Another indication that these structures are not the result of independent amorphous deposit formation is provided by the lack of evidence of any ball-like crystalline structures. The method of crystal formation appears to follow a different pathway to the one, which was observed by Chen in 2006 [203]. Within this paper Liu observed rod-like structures surrounded by ball-like structures with SEM. Upon inspection with TEM it was found that the ball-like structures were a shell made of many small crystals aligned in different orientations, where as the rods were composed of many small crystals aligned parallel to each other. TEM also revealed that they had a typical apatite structure, however, the ball-like structures contained relatively more fluoride than their rod-like counterparts. However, as previously stated, there are fundamental differences between the processing method used to produce the ordered apatite surface when comparing Chen's method to ours, see following.

However, it is conceivable that ACP could form as a part of our synthesis pathway. It is well known that during the process of crystal growth compositional changes do occur. These compositional changes are referred to as phase transitions and usually occur primarily by surface dissolution, which is then followed by the nucleation of the second phase. We know that low temperature ACPs are often encountered as a transient precursor phase during precipitation of another CaP-phase in aqueous systems. Usually, an ACP is the first phase precipitated from supersaturated solutions prepared by rapid mixing of solutions containing ions of calcium and orthophosphates. The higher the super saturation the better. Thus, it can be expected that amorphous CaP-phases to be present [202]. The evolution of intermediary phases are dictated by the solubility of the amorphous precursor and crystalline intermediated as well as the free energy of their inter-conversions [109].

ACP has been suggested as the precursor in a similar method for the production of ordered apatite coatings. In 2006 [203], Chen proposed a mechanism for the synthesis method of ordered nano-rod-like apatite coatings with a hexagonal cross-section. It should be noted that this method maintained some differences from the one presented in this report based given that Chen's method used a Stainless-steel substrate whereas ours used 20% porous-HA, furthermore, it used a hydrothermal method rather than just a wet chemical precipitation method.

Finally the case for surface dissolution caused by the growth of crystals reaching their limit. Chen also stated that the growth of the crystal would reach its limit due to the depletion of Ca^{+2} precursors which lead the crystal bundle to fuse together. At this point, small sharp branch ends with high surface energy will dissolve and tend to fill the kink and steps of the bundle structure to form a well defined hexagonal crystal due to the Ostwald ripening process. The observations seen at this stage could be reminiscent of surface dissolution due to the depletion of Ca^{+2} ions in solution [203]

The principal indications of this finding are that there seems to be some epitaxial growth occurring throughout the seven days. This may be preceded by the formation of what could be another phase either by phase transition or primary deposition.

5.5.2 Compositional analysis

Each of the calcium phosphates have an indicative Ca/P ratio that can be used to identify them. When CaP-slats are formed at low temperature it is common to find other CaP-salts that form as impurities alongside the specific CaPs that we are trying to produce, in this case FAp. Monocalcium phosphate monohydrate (MCPM), and monocalcium phosphate anhydrous have Ca/P = 0.50; diacalcium phosphate dihydrate (DCPD, Brushite) and diacalcium phosphate anhydrous (DCPA, Monetite) have Ca/P = 1.00; Octacalcium phosphate (OCP) has Ca/P = 1.33; α–tricalcium phosphate (α–TCP) and β–tricalcium phosphate (β–TCP) have Ca/P = 1.50; amorphous calcium phosphate (ACP) has the range 1.20–2.20, and hydroxyapatite (HA) has Ca/P = 1.67 [109, 204].

It is known that OCP typically maintains a rod-like morphology [205] similar to that found in Fig. 5.7. However, we can conclusively discount this CaP-phase based on three key points, 1. The presence of F^- ions, 2. The lack of (200) peak in XRD diffractogram, 3. Ca/P ratio. The most obvious indication that OCP is not present is given in the fact that OCP has a value that is lower than the lowest measured Ca/P value of 1.39. Though it could still be argued that some impurity could effect the Ca/P ratio enough to produce a value as high as 1.39. Structurally OCP has "apatite" layers (about 1.1

nm thick) alternating with "hydrated layers" (about 0.8 nm thick) parallel to (100) are a conspicuous feature of the structure. From XRD, OCP and HAp can be distinguished by this hydrated layer that is denoted by a (200) peak which is located at 9.343 Å, [206, 207]. However, we can see no evidence of this peak within our XRD.

Our solution contains F^- ions, which previously, have been reported to act as an inhibitor to the formation of OCP in the c-axis [206]. In 2001, Mayumi Iijima studied the effects of both CO_3 and F^- ions in solution while forming OCP. Mayumi found that both CO_3 and F^- ions limit the groth of OCP in the c-axis, however the presence of CO_3 generated rectangular shape crystals. In contrast, F^- did induce the formation of flake like crystals. Notably, at pH $<$ 6.5, the effect of F^- ions on the growth in the c-axis was quite small, however it was found that its inhibitory ability was increased at pH $>$ 6.8. Mayumi then considered the affect of concentration. The concentration of F^- ions in solution was varied between 0.1 and 1.0 ppm. Without F^- ions, the OCP formed ribbon-like crystals, but when a low concentration of F^- was added the crystals formed became tape-like with a large length to width ratio, further increases in the F^- ion concentration showed a progressive decrease in size, eventually becoming wisker-like in morphology [208]. Conversely, when a concentration of 2.0 ppm was used, rod-like apatite crystals were formed, and at 10.0 ppm these crystals gained an increase in size. Thus, the increasing concentration of F^- reduces the size of OPC while increasing the size of apatite. However, we can rule out OCP given that the typical ^{19}F MAS NMR peak of 70.3 ppm was not found when powders were analysed.

Clearly, MCPM and MCPA have Ca/P ratios far below the lowest values thus these can be discounted easily. However, both α and β–tricalcium phosphate fall within the range. It can be seen from the XRD diffractogram, in Fig. 5.3., that there is no evidence to suggest that either of these salts are present. Among other distinct peaks, we would expect strong (031), (132), and (290) peaks at 12 Å, 23 Å, and 34 Å, respectively when considering α–TCP. For β–TCP, we would expect (110), (210) and (220) peaks at 17 Å, 31 Å, and 34.5 Å, respectively [206]. Given that we do not see evidence of these peaks we can conclude that both α–TCP and β–TCP are not present.

DCPD has a Ca/P much lower than any of the crystallites found; it also forms a plate-like morphology [209], which is distinctly different from the rod-like morphology we have seen in Fig. 5.7., thus we can discount DCPD. As we know, the typical Ca/P ratio of DCPA like DCPD is 1.00, much lower than the measured values of our crystallites. Thus one might conclude that DCPA could not possibly be present within the samples. However, previous reports by Philip James in 2013, show that materials composed of HAp/DCPA mixtures (72.0% DCPA) not only show rod-like morphology, but also have a Ca/P ratio = 1.40 [210], thus it could be conceivable that DCPA was formed and a

HA/DCPA mixture could explain the low Ca/P values seen in Fig. 5.9. By comparing the spectra of DCPA to our XRD diffractogram we can see distinct difference. We would expect peaks (001), (002), and (120) at positions 13 Å, 26.5 Å, and 30 Å, respectively [206], thus we can also discount DCPA as a possible CaP-phase.

Apatite has various forms from other than the stoichiometric from which we can select. Calcium deficient apatite (or non-stoichometric apatite) has a Ca/P range from 1.50 to 1.66 [211], and calcium rich apatite have Ca/P ranges from 1.63 to 1.75 (Elliot, 1994). Given that we have already identified the apatite structure to be present through Rietveld analysis we can expect this phase to be present. Based on the Ca/P values we know that this is not stoichiometric apatite, however, we can expect that the nano-crystals formed at a times $\neq$ day 6 are calcium deficient apatite. Notably, since we have observed a value of 1.79 at day 6 we can also expect that another phase is present. Again, this value is higher than the range for calcium rich apatite, and in fact, the only CaP-phase that has a range that encompasses 1.78 is amorphous calcium phosphate (ACP). This supports the claim that the structures seen at day 6 are ACP.

5.5.3 Energy Dispersive X-ray Spectroscopy

Monetite is known to be found at Ca/P = 1.00 [76, 110], however, if the monetite exists in combination with other phases then EDX may not be the best way to ascertain its presence. In a study conducted by Philip J. T. Reardon his team that samples containing 72.0 % monetite and 28.0 % apatite yielded Ca/P ratio values 1.4 [212]. As is commonly known, apatite at a Ca/P ratio of 1.67 is deemed Stoichiometric apatite. EDX analysis reveals that most of the crystals throughout the 7 days have Ca/P values between 1.38 and 1.53. At day 3, there is evidence of a similar disordered morphology with different Ca/P values, the first 1.51, the second 1.60 (closer to stoichiometric apatite).

5.5.4 Cross-sectional analysis

With regard to the cross-sections presented in Fig. 5.8., we can see that there are three distinct size ranges throughout the 7 day period. What was not expected is that from day 2 to day 3 there is a 52% decrease in maximum size and from day 5 to 6 there is a 52% decrease in maximum size. Due to Ostwald ripening, it is expected that crystals size would increase as crystal growth progressed, further smaller crystals would be sacrificed at the expense of larger crystals. Thus we would expect the crystal cross-section range to reduce and found at higher values at time progressed. It would seem that this is indeed the case within a layer but not from layer to layer. One explanation for this

would be that we are not actually looking at the same layer of crystals, but actually are observing successive crystal growth at each of these time points.

It would appear that the rate of crystals growth decreases as time progresses, see Fig. 5.8. Within each layer crystals size does increases from day to day. When the crystals of one layer finish, the crystals of another layer begin again from a smaller nucleus. It is possible that the growth first layer of crystals is stopped because the lack of Ca^{+2} ions in solution, however, if this is true why then is it possible to grow new crystals?

As we know, the termination of the crystal growth can happen for numerous reasons:

1. If the supersaturation level falls to the equilibrium level defined by the solubility product,
2. the accumulation of a large number of surface defect that can not be assimilated into the bulk structure, and
3. the crystal surface becomes blocked by the overgrowth of a more soluble secondary phase.

The last of which can occur even if the solution remains supersaturated to the first mineral since the surface phase has reached equilibrium [109]. Thus, it is more realistic to believe that both crystal sizes are growing at the same time. However, crystal growth of the lower layer will be inhibited due to being covered by the crystals of the smaller size. This may also explain why we see a greater amount of order in the later time points. With less space to grow the crystals are pushed together into a greater alignment. Furthermore, at these later stages the lack of Ca^{+2} ions in solution will prevent the crystal from growing to large sizes in such a short space of time.

5.5.5 Fourier-Transform Infrared Spectroscopy

With regards to the broad peak seen in Fig. 5.4, with a range of 3000–3665 cm^{-1}, this is likely to be a carbonate-water bridging vibration which is recorded to have a range from 2900–2850 cm^{-1} [213] rather than a OH^- stretch bands. The $CO_3{}^{2-}$ observed at 872.6, 1431.3, and 1456.3 cm^{-1} in all time point, suggesting that substitution was about the c-axis channel and the formation of B-type carbonate apatite was formed [198]. The FTIR spectrum of samples day 1-6 have an absent OH^- libration and stretch mode, see Fig. 5.4. Weak or absent IR bands have been seen in $NaCO_3$Aps have been shown in previous work [214–216]. As has previously been shown IR observations should not be taken as a reliable indication of a low OH^- ion content in the unit cell. Another example worth

noting is the presence of the apatitic OH^- group within bone mineral [217–220], As far back as 1995 there has been some discrepancy between the sensitivity of FTIR and even ^1H MAS NMR spectroscopy [217] in its ability to identify any evidence of the presence of OH^- ions. C. K. Loong and coworkers [218], could not observe any vibrations due to OH^- libration or stretch when using inelastic neutron scattering. However, contrary to this, a high-energy transfer inelastic neutron scattering spectroscopy study conducted by MG Taylor et al in 2003, has identified both the OH^- libration and stretching modes [219]. Again, in 2003, G Cho, Y Wu and JL Ackerman conducted a 2D solid-state NMR experiment which revealed that bone mineral contains as much as 20% of the OH^- ions expected in stoichiometric HAp [220]. Again, the evidence for the limitation of FTIR has been seen in 2004 [216]. RM Wilson et al found a high content of OH^- ions through determination of the O(H) occupancy which was derived from Rietveld refinement and the ^1H NMR spectroscopy. Notably, they were unable to find OH^- libration modes and only very weak OH^- stretch, much like our results. In light of this knowledge, we know that the lack of OH^- peaks in FTIR spectra do not suggest the absence or low abundance of these ions. Furthermore, the ^{19}F MAS NMR results, Table 5.2, suggest that there is a substantial amount of FHA that is being produced along side the FAp. As we can see, day 6 has the greatest amount of CO_3, and also we see a complete loss of the CaF_2 peak. This is a drastic change given that the average value for all other days is 49.53%. Thus it can be said that the increase in CO_3 incorporation favours the formation of FAp over CaF_2. It should also be noted that in 1967 and 1968 LeGeros et al, found that both sodium containing and sodium free CO_3Aps showed a weak OH^- libration mode at 633 cm^{-1} and an absent OH^- stretch when there was more than 2.5 wt% and 11.0 wt% CO_3 by composition, respectively [214, 221].

5.5.6 Nuclear Magnetic Resonance Spectroscopy

With regard to NMR results, shown in Fig. 5.5, It would appear that between days 4, 5 and 6 there is some mechanism that causes a reduction in CaF_2. What was unexpected is that on day 7 the -109 ppm peak returns again which indicates that day 6 would be the optimal time point for the formation of FAp in the absence of CaF_2.

Previous work by Yajie Gao et al [200] found that hydroxyfluorapatite (FHA) had a peak value of -105 ppm when studied on ^{19}F MAS NMR. Their experiment had some significant difference to ours. First of all, to avoid carbonate concentration the reaction was kept in the inert N_2 atmosphere for 3 hours. Extra ammonium fluoride (Sigma-Aldrich) was added to the solution for the FHA precipitation, the aqueous solutions were prepared in atmosphere without further purification. Our FTIR suggests that we have lost our OH group, however, there research is based on the fact that the OH groups

are still present and actually contributing to the chemical shift value. And finally, there samples were heat treated at 300 °C, 750 °C, and 900 °C, where as the samples presented here in this work are incubated at 21 °C, and 70 °C, thus the mechanism will be different.

5.6 Summary

5.6.1 Differences in synthesis model

The first stage of Chen's method involved the formation of amorphous deposits, which then formed hollow balls. Finally well-defined crystals were formed after an autoclaving process. Given that rod-like crystals will have a tenancy to aggregate together due to Van Der Waals forces, it is expected that these rods will form bundles by aligning themselves along the c-axis. This stage is consistent with Fig. 5.7.(h) in which we can qualitatively see a greater level of alignment than those in Fig. 5.7.(g).

It could be possible that the interconnections between the crystals is caused by the formation of an amorphous CaP-salt which in tern leads to the formation of new apatite crystals at later stages of the process. It was expected that ball-like crystals would form the basis of our synthesis pathway given the similarity in the initial solution chemistry. One reason for the difference maybe that our surface was not only 20% porous but also was composed on HAp, but also the structure of the substrate "HAp" and the precipitated coating "FAp" both have a hexagonal unit cell. For the former, this meant that there were a greater number of nucleation sites and thus a lower energy was required to initiate nucleation, where as for the later we can expect epitaxial growth to play a role in the initial formation. Both of these may provide an explanation as to why it is acceptable for the ball-like structure phase to have been by passed.

5.6.2 Main findings

We found that:

- Levels of coverage for the two temperatures, 21 °C and 70 °C, incubated on HAp substrates, the coverage was found to be 9.167 ± 0.004 % and 70.083 ± 0.004 %, respectively.
- Incubation temperatures 21 °C and 70 °C had width ranges of 276–341 $\pm$ 1 nm, and 76–329 $\pm$ 1 nm. Only those found at 70 °C fall within the size range of 25–100 nm required for the bioactive properties.

- For samples incubated at 70 °C.

    1. Both Rietveld refinements of XRD data and deconvolution of NMR data show a rise in the formation of apatite on day 6 when considering percentage abundance.
    2. Again, NMR reveals the same 5 key peaks representing Ca_2F, FHA, FAp, CO_3, and an unidentified contaminant that could also fit the range for CO_3. Day 6 shows the least amount of Ca_2F.
    3. Both visually using SEM, and through use of Scherrer's law, we were able to compare the changes in crystal size. From day 0 - 5 there appears to be an increase in size, with a sharp drop on day 6. The size at day seven is fairly similar to that of those at day 6 along with a greater level of alignment than previously seen.
    4. further SEM analysis revealed that smaller crystals grow at the interstices of the larger crystals, forming a secondary layer that grew on top of the previous one. This is supported by the size analysis that showed two groups of crystal size that both grew at different rates.
    5. Ca/P ratio analysis would indicate that the apatite formed was in the carbonated apatite range.
    6. NMR data collected from 5 time points separated by 2 hrs between day 6 and 7 showed that the optimal time point for the formation of apatite was indeed day 6. Following this the percentage of Ca_2F increased back to the dominant position.

- For samples incubated at 21 °C, there are some distinct differences to that of 70 °C.

    1. SEM analysis reveals a different pathway to that of 70 °C. Here, the crystals go through a ball-like, and clump-like phase before forming the first rod-like structures. The crystals maintained a misaligned arrangement until day 7, before becoming misaligned on day 8 again. Proving that day 7 was the optimal time point. No evidence of a layering process.
    2. 21 °C shows only one day in wich the rod-like crystals maintained alignment, whereas those formed at 70 °C showed two days of alignment. It also takes 21 °C samples 2 days before the formation of any rod-like crystals but then quickly moves though the misaligned phases in the next 3 days, where it took those formed at 70 °C five days to achieve alignment.
    3. Both XRD and NMR analysis show that over 50% of the powders produced at 21 °C were composed of Ca_2F. NMR shows that thee is no evidence for

carbonate groups until day 5. From day 5 to day 7 the percentage abundance changes from 1.62% to 2.24%.

4. Size analysis both by SEM and Rietveld refinement shows a general tend of increasing crystal size with increasing time. Supporting the claim that this synthesis route does not require a layering process.
5. Ca/P ratio analysis supports the observation that thee is not much carbonates present. Ca/P ratios are found at higher values, being much closer to that of stoichiometric apatite than those formed at 70 °C.

Hence in the next section we will focus on using a combination of the Pair Distribution Function and Molecular Dynamics to understand the structural changes at the short range, and the kinetic effects at short time scales, of the order of pico seconds.

Chapter 6

Pair Distribution Function Analysis of Synthesised Ordered Fluorapatite for Dental Application

6.1 Key aims

- To apply Molecular Dynamics to the research of the implant coating synthesis procedure in order to derive some understanding of the system kinetics at time scales of pico seconds.
- Use the Pair Distribution Function to reveal whether or not this system undergoes an amorphous phase.
- Use the Pair Distribution Function method to characterise the changes in the crystal structure at lenght scales less than 5 Å.
- Develop a Molecular Dynamics system that closely represents the real world chemical synthesis pathway.

6.2 introduction

As early as 1965, Prof. E. D. Eanes, Dr. I. H. Gillessen and Prof. A. S. Posner wrote a paper called the "Intermediate States in the Precipitation of Hydroxyapatite". In this work, they found that they were able to show the transition of amorphous calcium

phosphate into hydroxyapatite over a 5 hour period. The full experiment, took over 28 hours, used X-ray diffraction to characterise an amorphous-like pattern, and was compared to a crystalline form that was precipitated at a much later time point [222]. Shortly after this, in 1968, A. Bienenstock and A. Posner used calculations to determine how the X-ray diffraction pattern would vary for hydroxyapatite crystallites [223]. At this time, scientists had provided chemical and kinetic evidence to show that amorphous calcium phosphate and apatite could be separated into two distinct phases. Furthermore, diffraction results would further support this conclusion [222]. However, it was suggested that amorphous material is not a separate phase, but was actually caused by the formation of hydroxyapatite crystallites that were so small that they would cause an amorphous-like pattern. Bienenstock made comparisons between crystallites with one unit cell, three unit cell parallelograms formed in the plane perpendicular to the hexagonal axis, two such parallelograms stacked along the hexagonal axis, and finally five unit cells stacked along the hexagonal axis. They found that as the number of unit cells used to define the calculated crystallites reduced, the diffraction pattern did in fact broaden to an amorphous-like pattern. This would seem to support the contention that the amorphous-like diffractograms are indeed the result of small crystallite size. However, when compared to X-ray diffraction data showing the transition from amorphous calcium phosphate to hydroxyapatite two discrepancies could be seen. The first was that the maximum peak height of the amorphous data was approximately $1/3^{rd}$ the height of its crystalline counterpart. The second was the amorphous patten showed a maximum at 29° 2θ, however, all of the calculated curves showed a maximum in the region of 32° 2θ. Thus it was determined that there was no possibility that the scattering pattern from the noncrystalline calcium phosphate could have been attributed to an array of small hydroxyapatite crystallites.

In 1975, 10 years after the initial discovery of amorphous calcium phosphate, Posner teamed up with Foster Betts. In their work, entitled "Synthetic Amorphous Calcium Phosphate and Its Relation to Bone Mineral Structure" the application of the reduced Pair Distribution Function (PDF) to both ACP and HAp. They found that the first two peaks in the PDF for ACP and HAp were very similar which they attributed to the similar composition of the two phases. However, when approaching higher r values, the PDF peaks decreased rapidly, which in contrast to the crystalline HAp remained strong due to the existence of its long range order[224]. This marked the beginning of a time in which the bond distribution analysis of amorphous materials could be used to advance the knowledge of complex materials in the medical arena.

To date, the early time points of synthesised bioactive apatite implant coatings have not been analysed with short range order analysis < 5 Å. The Pair Distribution Function has been used to characterise amorphous phases from X-ray and Neutron diffraction

data [225], notably with regards to work on silica glass [226, 227]. Being able to extract information of the short range order. The mechanism by which amorphous calcium phosphate, transitions into the apatite phase is still some what of a mystery. Thus, the use of this method will aid in the development of a better understanding of the synthesis pathway.

One of the main advantages of the Ag-source X-ray method is the ability to use in house equipment. This means the individual is able to gain access to the equipment on a more regular basis, and as such is able to experiment more with the experimental design, while at the same time allowing time for the natural development of the experiment as a whole. A large number of the previous experiments are heavily dependent on the use of neutron spallation sources to which the experimentalist may not be able to gain access in the time that is required for their experiment. Moreover, if something should go wrong, there is no chance to improve things.

The correlated displacements of different atom types within the structure are effected by temperature and time. That is to say that as time progresses, the location of atoms relative to each other changes. Likewise, as temperature increases, the energy that each atom has will also increase, alowing for a greater range of movement and even the breaking of bonds due to the ataining energy above that of the activation energy. We know that even subtle analysis derived from atomistic models can provide an insight into how the physical phenomena leads to the materials behaviour throughout the synthesis process [228]. Thus, we aimed to apply the same concept to gain an understanding of the process that causes the formation of a greater abundance of apatite relative to CaF_2 specifically we aim to focus on the sixth day of the 70°C synthesis route. Furthermore, we may be able to gain an understanding of the phase transition form amorphous calcium phosphate to the apatite phases in the early stages of crystal formation.

The other method that is used was molecular dynamics via a program called DLPOLY. The advantage of using molecular dynamics simulations is that they use semi-empirical models to represent forces between the atoms, which in turn allow the atoms to move classically under these forces. That is to say that the behaviour of large systems of atoms can be modelled with a reasonable level of accuracy, as long as the interatomic forces adequately represent the true forces between atoms. Radiation damage has successfully been investigated in minerals using molecular dynamics, [229–231]. In addition, it has been demonstrated that apatites can be accurately simulated using classical dynamics with empirical inter-atomic potentials [232–234], as well as also found use in studying the transport properties of water molecules that are confined between HAp surfaces [235], as well as computational investigations of the interaction of collagen with HAp [236] among other things.

In this chapter, we aim to use PDFfit2 [1] on XRD data to derive information for a starting point for Molecular Dynamics (MD) simulations. Then we aim to use MD to give us a better understanding of the development of the amorphous calcium phosphate and the potential transition into its crystalline counterparts.

6.3 Experimental

6.3.1 Cu-source powder X-ray diffraction

The specimens were analysed using X-ray diffraction using a diffractometer (Bruker D2 Powder Diffractometer). Cu-source XRD, Cu-K_α radiation ($\lambda = 1.54056$ Å) at 40 kV/40 mA was used. The diffraction pattern was taken in the 2θ range of 10° to 70° with a step size of 0.04°. The diffraction data were analysed by the Rietveld method [194] using the computer program GSAS [195] and used for phase analysis.

6.3.1.1 Ag-source powder X-ray diffraction analysis

Before Ag-source ($\lambda = 0.56088$ Å) XRD scans were performed on the samples, a background and of the empty kapton tube were taken. In the case of the empty kapton tube care was taken to ensure that the long axis of the tube was aligned at 90° to the path of the X-ray beam. Calibration was performed using a goniometer and a microscope, which was able to view 3 mm of the tube. 0.04 rad soller slits were selected along with a 20 mm mask. The anti scatter slit was set to $\frac{1}{2}$, with 0.04 rad soller slits and a PASS or 1^o. The power of the potential with in the diode valve was set such that V = 45 kV and I = 40 mA. Calibration was complete when the tube was central in the cross-hairs. five separate 4.4 hr XRD runs were taken back to back for both background and the empty capillary measurements. The powders produced at each of the 24 hr time points (during the 7 day trial) were collected and tightly packed into a kapton tube. The tube specifications were of length 30 ± 1 mm, inner diameter of 10.033 ±0.013 mm, and a wall thickness of 0.508 ± 0.006 mm. Care was taken to ensure that 20 mm of the tube length was exposed to the x-ray beam. five 4.4 hr XRD scans were taken for each of the time points using the same method described above.

[1] PDFfit2 is a program as well as a library for real-space refinement of crystal structures. It is capable of fitting a theoretical three-dimentional (3D) structure to atomic pair distribution function data and is ideal for nano-scale investigation

6.3.2 Generation of Pair Distribution Function for seven day trials

Total x-ray scattering data of seven day trial studies were collected for 21°C and 70°C were collected on an in house PANanalytical (X'Pert PRO, Powder diffractometer, Almelo, Netherlands) (40 keV, $\lambda = 0.56088$ Å) generated from a silver source, using a rhodium (Rh) filter. The PDF was obtained by Fourier transformation of $Qi(Q)$ truncated at $Q_{\max} = 23$–24 Å^{-1}. The composition used in the normalisation of each experimental structure function was $Ca(PO_4)_3F$, based on the NMR and XRD results from previous experiments. A material density of 3.202 gm/cm^3 based on theoretical data. Samples were tightly packed in a kapton capillary tube, with an inner radii of 0.5 mm and an outer diameter of 0.55 mm, its length 20 mm. The density of the tube was 1.41 gm/cm^3 and a container tweak factor[2] of 0.5 was used. Which was then mounted on a rotating axis within a θ/θ geometry set-up. To reduce statistical error five separate scans were taken at four hours each, thus analysis of each 24 hr time point would take seven working days, along with two more days to run a set of five scans both for the background and empty kapton capillary tube. Background subtraction and R-space fitting were performed as part of the GUDRUNx package.

For samples produced at 70 °C, the optimal setting for GUDRUNx was found to be the following; Q-range 0.65–20.00 $\pm$ 0.05 Å^{-1} to reduce the presence of termination ripples, $r_{\max} = 50$ Å, with an r-step of 0.03 Å. A tweak factor of of 1.5 was calculated from $\rho_{\text{Theory}}/\rho_{\text{Observed}}$ but 0.5 was found to satisfy the condition that $S(Q \to \infty) \to 0$ by calibration. A top hat[3] width of 2.3 Å^{-1}, chosen to be greater than $3/r_{\min}$. A broadening width in r-space of 0.05 Å and a broadening power of 0.00 Å was found to reduce noise peaks to expectable standards. An $r_{\min}$ of 1.35 was used to exclude any noise peaks less than the smallest distance for a bonding pair of atoms. These values were found to be slightly different when the calibration was conducted for the samples that were synthesised at 21 °C. In this case, $r_{\min}$ was set to 1.50 Å, and the tweak factor was set to 4.859. It was also found that the best resolution of the signal was given when $Q_{\max}$ was set to 23 Å^{-1}.

Noise peaks were identified due to the presence of peaks at r $<$ 1 Å as this would indicate bond lengths shorter then the size of an atom. Application of Lorch parameters were used to smooth the function. After this the r-range was limited to a minimum of 1.35 Å. Below this point we do not expect any characteristic peaks. This value was decided upon after varying Q(max) between 15–22 Å $^{-1}$. Calibration was satisfied when $G(r < r^o) = -(\sum_i c_i f_i(\mathbf{Q}))^2 \ - 1$, and $G(r \to \infty) = 0$ since $g(r \to \infty) = 1$.

[2]The "tweak factor" and can be thought of as the inverse of the packing fraction.

[3]the data analysis may not have proceeded perfectly, the structure factor is on some kind of Q dependent background. This needs to be removed prior to Fourier transform. The background is generated by convolution of the data with the top hat function

Values were also checked in reciprocal space. Both S(**Q**) and I(Q) were expected to have a based line that lies between [-1,1]. If either tended to infinity at high Q further calibration was required. The TF was further reduced, along with the application of a Top Hat Function, THF, (which should be $< \frac{3}{r_{(min)}}$). S(**Q**) and I(Q) satisfied this condition when the settings for were as follows: top hat (2.30), TF (1.50), and broadening in r-space (0.05 Å). The following settings were applied to all following time points to ensure consistency. At each time point care was taken to ensure that the conditions for $G(r < r^o)$ and $\frac{\sin(\mathbf{Qr})}{\mathbf{Qr}}$ were satisfied.

6.3.3 Synthesis of Amorphous Calcium Phosphate

The synthesis method for the formation of amorphous calcium phosphate was modified from one proposed by Hayek and Stadlmann [237], which was later modified by Eanes et al in 1965 [222]. This method required the use of a freeze drying method, which avoided changes in the solid during the drying of the slurry. Samples were prepared for freeze drying first by removing the supernatant, and then replacing it with deionised water. In this way, the samples were rinsed of any remaining ions that remained in the solution, this preventing the continuation of crystal growth. Following this, samples were centrifuged at 2000 rpm for 5 mins. The deionised water was poured away leaving only the powder. Liquid nitrogen was then poured into a polystyrene container, which was in turn placed into a vacuum desiccator. An Edwards 8 E2M8 Rotary Vane Dual Stage Mechanical Vacuum Pump was used to reach an ultimate pressure of 10^{-3} mbar in order to produce a solid nitrogen slush mixture with liquid nitrogen [238]. After 30 mins the pressure was released and the tube holding the sample was then submerged into the slush nitrogen. The tube was then held in the slush for 5 mins until the sample was frozen solid. Using this method, freezing was uniform throughout the material as opposed to a quick freezing at the surface and the much slower freezing at deeper levels of the powder [239]. The samples was then stored in a liquid nitrogen dry storage container before being transported to the freeze drying apparatus. In order to ensure that the freeze drying method did not encourage the formation of new contaminant materials, day 6 and 7 samples were subjected to this method for comparison with previous results. Following this, 5 time points were taken between 0 to 14 mins of incubation.

6.3.4 The potential model

The General Lattice Utility Program, GULP [240] [4], was used to generate a phonon information from interatomic potential models, a core-shell model [5] using Buckingham potentials,

$$U(r_{ij}) = A\exp\left(-\frac{r_{ij}}{\rho}\right) - \frac{C}{r_{ij}^6}, \tag{6.1}$$

where A, ρ, and C are constants. The two terms on the right-hand side constitute an repulsive and attractive potential. Here used for the interaction of two atoms that are interacting but are not directly bonded as a function of the interatomic distance r. Three-body potential of 1.686 keV rad^{-2}, where a Three-body potential is defined as,

$$U = \frac{1}{2}k(\theta - \theta_0)^2, \tag{6.2}$$

where k is the spring constant of the bond in question, θ_0 is the expected angle between the atoms, and θ is the observed angle. [6]

and a spring potential,

$$U = \frac{1}{2}\alpha x^2, \tag{6.3}$$

where $\alpha = 89.34$ keVÅ^{-2} and x is the distance to the centre of the cell. This potential information is accompanied by the information of the species charges and crystallographic structural information [241]. GULP derived Pair Distribution Functions were compared to that of GUDRUNx data to ensure that the potential model was able to construct a reasonable distribution that could reflect experimentally observed data.

All molecular dynamics simulations were carried out using DLPOLY version 4.8. The potential model used for molecular dynamics study has previously been used successfully both for static calculations of apatites [242] as well as dynamic in silico models [232, 234,

[4] GULP is a program for performing a variety of types of simulation on materials using boundary conditions of 0-D (molecules and clusters), 1-D (polymers), 2-D (surfaces, slabs and grain boundaries), or 3-D (periodic solids). The focus of the code is on analytical solutions, through the use of lattice dynamics, where possible, rather than on molecular dynamics. A variety of force fields can be used within GULP spanning the shell model for ionic materials, molecular mechanics for organic systems, the embedded atom model for metals and the reactive REBO potential for hydrocarbons.

[5] Where an atom is described by a core, which holds all the mass, and a shell, which holds the charge

[6] Three-body potential represents the repulsion between bond pairs, or even occasionally lone pairs. Hence, the form chosen is usually a harmonic one that penalises deviation from the expected angle for the coordination environment

243]. The model uses the ion-shell model and a semi-empirical potentials to represent the forces between ions.

The potentials employed are: the Coulomb potential for interaction between charged species; the Morse potential for the covalent bonds in phosphate and hydroxide ions; the Buckingham potential, which incorporates a Born-Mayer repulsion term and a Van der Waals attraction term between ions; and three-body harmonic angle terms to maintain covalent bond angles. The relevant parameters are reproduced in Table 6.1. In all of the simulations, a real space cut off range of 7 Å was used both for the Ewald sum and for the short-range potentials.

TABLE 6.1: Parameters for the inter-atomic potentials used in this study. Note, O_po has been used to differentiate oxygen that is found as part of the phosphate group from those O that are found else where in the apatite lattice.

Ions	A(eV)	ρ (Å)	C(eVÅ^6)
Buskingham parameters			
O–O	712.36	0.066	25.8
O–F	9.451×10^6	0.163	0.0
O–Ca	521.46	0.379	0.0
F–F	91.19	0.055	0.0
F–Ca	10433.9	0.242	0.0
Ca–O	521.46	0.379	0.0
P–O	983.45	0.326	0.0

Ions	Charge		
	Core	shell	k (eVÅ^{-2})
O	0.587		
O		−1.632	
O	0.587		
O	−1.632		
F	−1.0		
Ca	2.000		
P	4.342		
O_po	0.587		
O_po		−1.632	
O_po	−4.207		
Ca	2.000		

Lennard Jones parameters		
Ions	ϵ	σ
O–O	0.00673678	3.166
O–H	0.00000	0.00000
H–H	0.00000	0.00000

Ions	θ_0	k (eV rad^{-2})
Three-body parameters		
O–P–O	109.47	1.32626

6.4 Results and Discussion

6.4.1 Short range order analysis

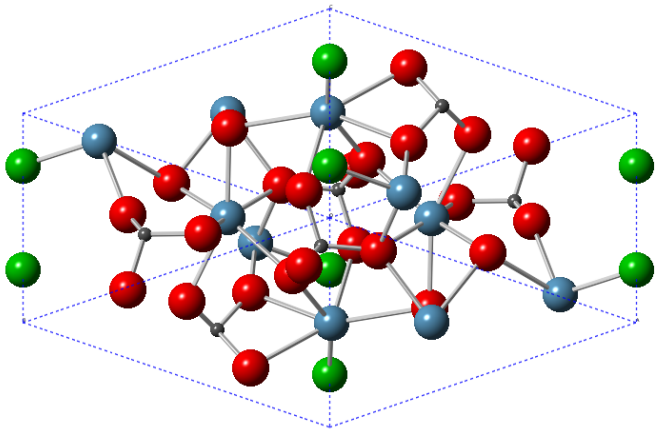

FIGURE 6.1: FAp unit cell generated by crystal maker. Atoms differentiated as follow, oxygen (red), calcium (blue), phosphorous (grey), and fluorine (green).

In previous studies, we have found that the crystallites synthesised at 70°C over a 7 day period have a similar orientation and morphology to hydrothermally produced apatite coatings with proven bio-ative properties. In our case, NMR analyses has revealed that our samples are composed of carbonated fluorapatite, CO_3FAp, Fluoridated-hydroxyapatite, FHA, and calcium fluoride, CaF_2. Analysis by DMFIT has also revealed that this synthesis method produces five distinct chemical environments represented by the ppm peak values. Two of which are carbonate groups, two are apatite and one is CaF_2. The carbonate groups will have formed within the apatite groups, and it is hard to differentiate between FHA and FAp, thus for simplicity we decided to fit the PDF data using a standard FAp structure using PDFfit2.

In this subsection, coatings produced at 70°C were analysed over a seven day period. Analysis at the nano-scale was conducted with SEM, EDX along with image analysis, whereas atomic analysis was carried out by PDF. PDF analysis of the first five days, obtained from Fourier transforming the diffraction data with GUDRUNx is shown in Fig. 6.2. Overall, the peaks are representative of an apatite structure, however, there are some indications towards a DCPD structure being formed. Peak 1, seen in region (a), stays fairly constant at 1.60 Å but appears to broaden at day 5, possibly composed of two peaks. Peak 1 is consistent with the structure of DCPD bonds H–H or P–O. Region (b), broad peak at day 1 appears to reduce to one peak on day 2 but then separate into two distinct peaks. This shows the breaking of a bond, (central peak: 3.13

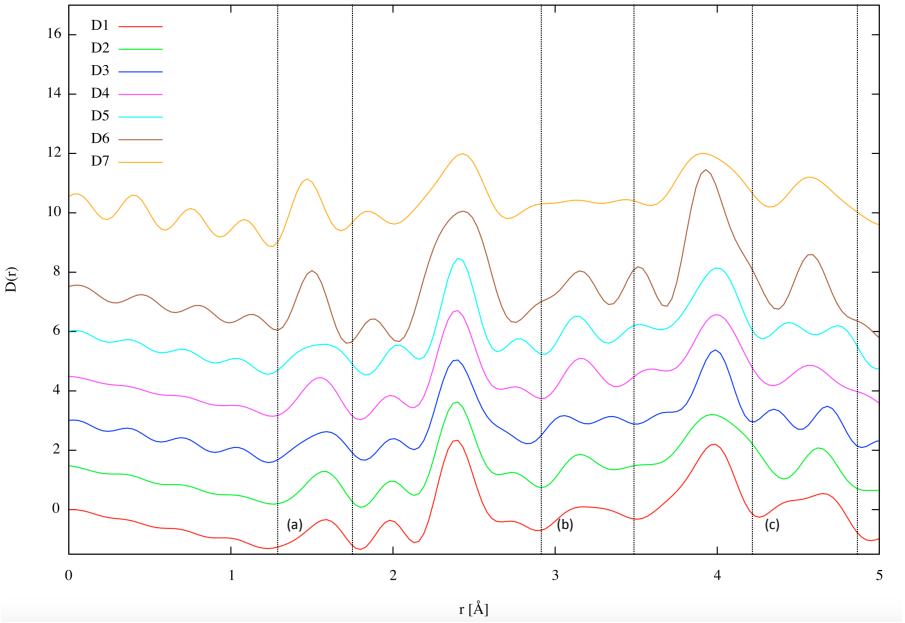

FIGURE 6.2: Pair distribution function of powders formed at 24 hour time points over seven days and incubated at 70°C.

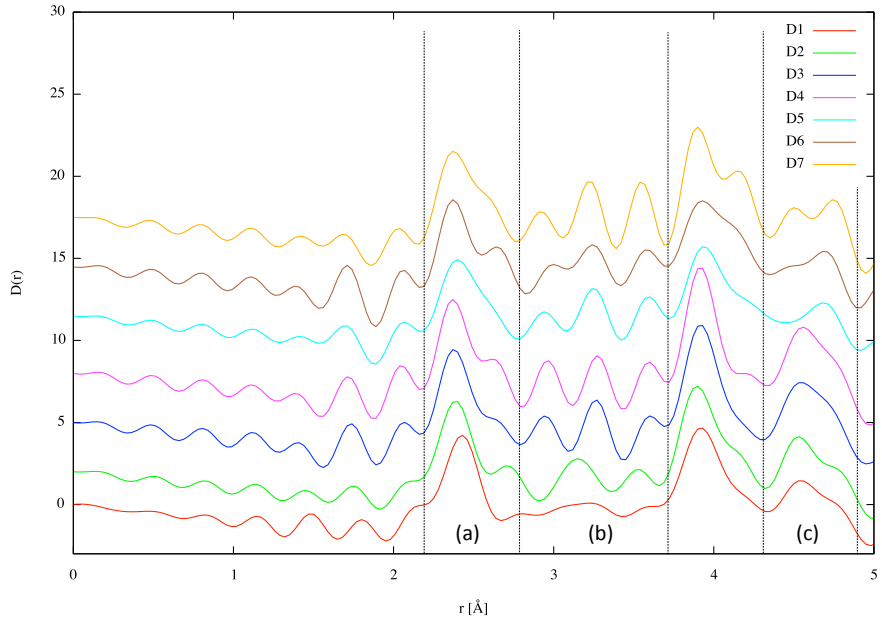

FIGURE 6.3: Pair distribution function of powders formed at 24 hour time points over seven days and incubated at 21°C.

Å) consistent with the following bonding: O–P or P–H and the formation of two new bonds; (left peak: 3.03 Å) O–O or O–H; (right peak: 3:33 Å) O–O or O–P; Region (c) shows transitions from two peaks to one peak throughout the 6 days. For the two peaks: (left peak: 4.42 Å) O–Ca or O–H, (right peak: 4.68 Å) P–P or O–H, where the former

and latter bonds correspond to apatite and DCPD bonds respectively. The single peak: 4.61 Å corresponds to either the H–Ca or O–H bonds which correspond only to DCPD.

Comparisons of bond length was made using a peak distance analysis through the Crystal Maker program. In the previous discussion on Fig. 6.2., we saw some evidence of DCPD structure when analysing the short range order. It is true that we have seen no evidence of DCPD from our XRD analysis. However, as previously stated, we would not be able to see amorphous phases of CaP-salts using the conventional XRD method. Amorphous calcium phosphates are often considered as an individual $CaPO_4$ compound with a variable chemical composition which. In reality ACP is just an amorphous state of order of other CaP-salts, thus, it could be possible that each of the CaP-salts might have their own ACP counterparts. [202]. The greater part of ACP has the Ca/P ratio close to 1.5, amorphous TCP (ATCP) are common in literature where as amorphous versions of other CaPs are rare, but have already been mentioned. An amorphous phase detected during a slow dehydration at slow heating rates of brushite (DCPD) and its transformation to monetite (DCPA). This amorphous phase could be defined as a highly disordered monetite with some free water trapped in the structure. ACPs prepared at pH 10.5 showed a molar ratio close to 1.5, suggesting a TCP composition, other research reported a ratio ranging from 1.35 to 1.38 suggesting a OCP-like stoichiometry, while ACPs with Ca/P < 1.0 are currently unknown [201]. Thus it could be argued that we are observing evidence of "amorphous-DCPD". This might be in contradiction with the lack of a Ca/P values of 1.00, but it may also be true that EDX analysis could not distinguish the true value of this structure due to the interference of other more prominent phases in the area. Again, samples containing 72.0 % monetite and 28.0 % apatite yielded Ca/P ratio values 1.4 [212]. It is known that DCPD is a precursor to apatite, OCP and β–TCP, thus it could be expected that DCPD is being formed at an amorphous level, and is then formed into apatite.

PDF data derived from seven day incubations at 21°C, Fig. 6.3, has also been split up into three sections, (a), (b) and (c). We can see that the first two days show the greatest changes in peak position, whereas, from day three onwards, the changes appear to become more subtle. In these days, it is the intensity that reveals the greatest difference between the days. In region (a), we can see that there is a, Ca–O, pair at around (2.43 Å), which remains fairly consistent throughout the seven days. Relative to this peak is another pair, Ca–O, which shifts from 2.70 Å to 2.67 Å when we move from day 1 to 2. In day 3, this pair seem to have vanished, and a new pair, O–O, can be seen at 2.67 Å. In region (b), we can see a similar trend whereby there are three bonding pairs in day 1, Ca–P, O–O and CaP at 3.09 Å, 3.21 Å, and 3.57 Å, respectively. By day 2, only two bonding pairs can be seen in this region, P–O and O–O at 3.15 Å and 3.51 Å, respectively. Finally, form day 3 onwards, a new group of peaks can be found at 2.94

Å, 3.27 Å, and 3.60 Å, which correspond to pairs O–O, Ca–F, and F-P, respectively. Clearly, there are many more changes in the atomic structure in these first 3 days, than there are for the duration of the seven days. This is in contrast to what we can see in the samples that were produced at 70°C, where we can see a continual breaking and reformation of bonds on a daily basis. In region (c) day 1, we can see a peak at 4.53 Å with a shoulder onset from 4.74 Å. These positions could indicate a F–O and a Ca–O peak, respectively. These peaks persist on until day 5 where a single O–O peak can be found at 4.68 Å, which again is present at day 6, however, in this case a the peak is accompanied by a Ca–O peak at 4.47 Å. Finally, on day 7 we can see that two very clear peaks are present, one at 4.50 Å and another at 4.74 Å. These correspond to Ca–O and Ca–F, respectively. Along with previous SEM and XRD studies of samples produced at 21°C.

We did expect some differences in the PDF when comparing those derived from 21°C, and 70°C due to the face that the SEM results Fig. 5.16 and Fig. 5.7 showed that the products formed over the seven days not only formed different morphologies but also followed different transitional progressions. Furthermore, EDX analysis showed clearly that the Ca/P ratio of the apatite materials were different in both cases, see Fig. 5.9 and Fig. 5.19. In the case of those formed at 21°C, the Ca/P ratio covered a greater spread between 1.38 and 1.73 throughout the seven days, where as a majority of the results found in samples incubated at 70°C show values closer to 1.48 most consistent with carbonated-apatite. As we know, the structure and the kinetics of crystal growth will be affected by substitutional species, not to mention the effect that temperature will play. What was a surprise was the existence of peaks that did not fall into the range of either of the previously identified compounds. i.e. an apatite based phase of a calcium phosphate one. Instead, some of the bonding pairs found could only have been the result of peaks from DCPD which did not show up in any of the previous XRD patterns. Comparisons of the peak values of the bonding pairs found within all of the other calcium phosphate phases showed that there was no other phase that could match these peak values. Thus, it was considered weather these peaks were the result of amorphous structures that showed some characteristics of DCPD within its short range order.

Fig. 6.4 and Fig. 6.5 show typical fitting up to $r = 5$ Å and 10 Å, respectively. Both illustrate a fairly reasonable fit up to 10 Å was achieved when using PDFfit2 on experimental data. As we know, PDFfit2 uses a small box model for refinement. Thus, this fitting is representative of changes at the level of the unit cell. Here we are able to show an example of how experimental data has been fitted using the PDFfit2 refinement method.

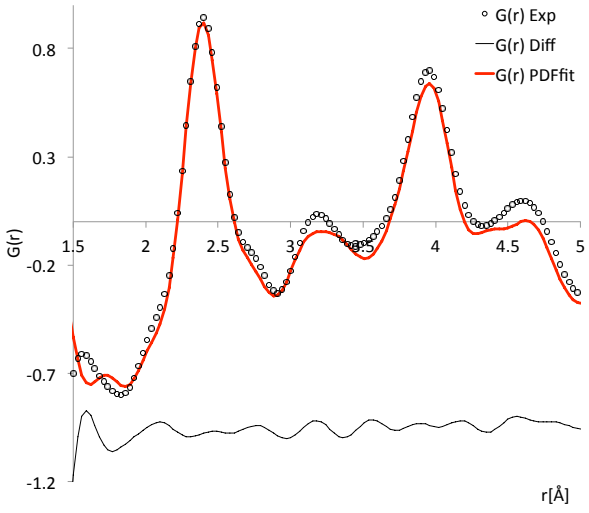

FIGURE 6.4: Example of PDFfit2 fitting performed on s typical G(r) of 70°C sample. Data (circle), refinement (red line), and difference (black line).

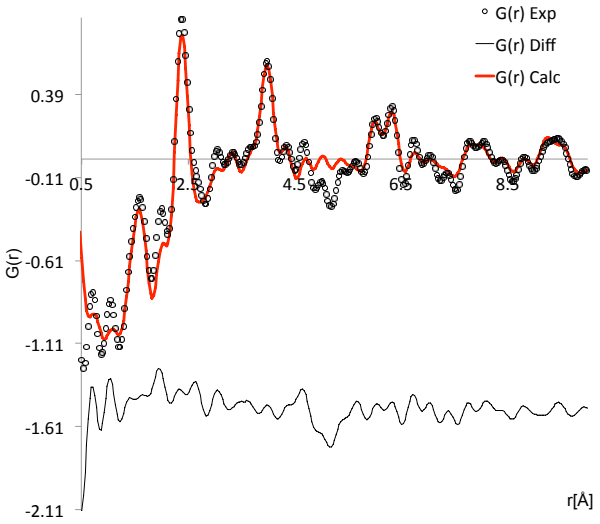

FIGURE 6.5: Example of PDFfit2 fitting performed on s typical G(r) of 70°C sample. Data (circle), refinement (red line), and difference (black line).

6.4.2 GULP models used to compare against PDF

After identifying the structure of the materials produces via the use of PDF we then wanted to validate the use of exsisting apatite potential models. In this way, I could find out if the potential models that I intended to use for MD simulation best represented the actual system being used chemically. For this, we employed the use of simulation software such as the general lattice utility programme (GULP)[7] and DLPOLY. GULP

[7]GULP is a program for performing a variety of types of simulation on 3D periodic solids, gas phase clusters and isolated defects in a bulk material. In particular GULP is designed to handle both molecular solids and ionic materials through the use of the shell model.

was used to help us to check that the interatomic potential that we were using were accurate. This was later used in DLPOLY to generate a 4-dimensional simulation to represent the experimental system.

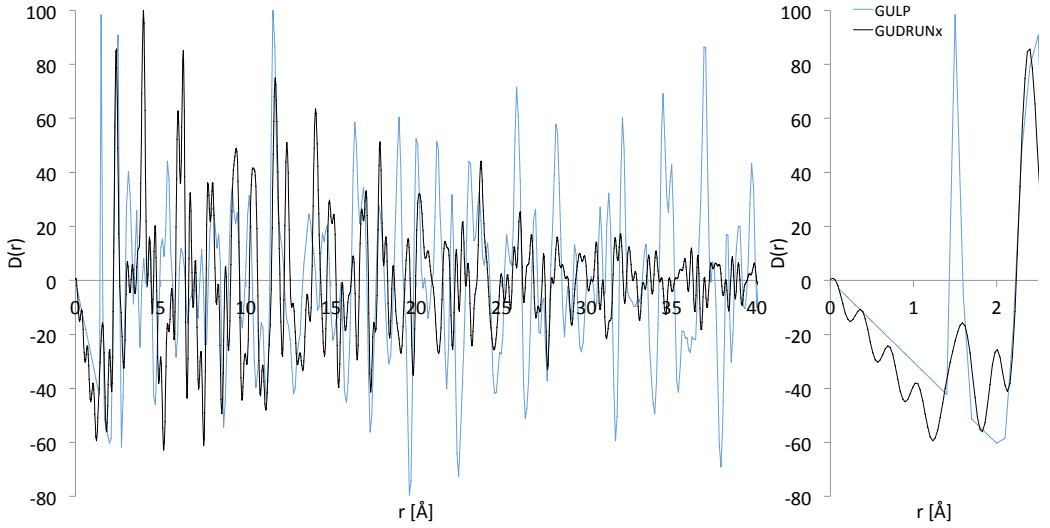

FIGURE 6.6: Comparison between GULP and a typical GUDRUNx generated pair distribution functions. As can be seen, right, noise can be seen in the experimental GUDRUNx derived data, most importantly a peak at 1.89 Å.

GULP generated PDF data was compared to a typical experimentally derived PDF data set, illustrated by Fig. 6.6. Apart from noise, the peak position for both data sets are consistent up to large r. The intensity of the phonon based GULP simulation however maintains a strong peak intensity at large r whereas our synthesised material shows a drop off with increasing r value, likely due to a scaling factor.

The atomic structure is represented in Fig. 6.7, here represented as a 3-dimensional output to see the changes in atomic bonds throughout the days. Structural refinement of PDF data using PDFfit2 methods allowed for the extraction of bond-angles, Table 6.2 and bond-lengths, Table 6.3, which revealed that crystal remodelling continued throughout the seven days. As we can see in Fig. 6.7, there are many changes in the atomic structure of the apatite crystals throughout the seven days. From day 1 to day 2, we can clearly see that a bond is formed between the phosphorous, oxygen and calcium atoms that were not previously there in Fig. 6.7(D1). In the transition from day 1 to day 2, Fig. 6.7(D2) we can see the formation of O–P–O bonds in place of the void. On day 3, Fig. 6.7(D3), we can see the formation of P_2O_3 tetrahedra that seems to have formed transiently as it only appears at this time point.

Again, at day 4, Fig. 6.7(D4), we can see that the O–O bonds between the O–Ca and the O-P–O bonds that formed on day 3 have been broken, which persists in day 5,

TABLE 6.2: Atomic bond (°) angle changes derived from experimental data refined with PDFfit2, and represented in Fig. 6.7.

Bond	D1	D2	D3	D4	D5	D6	D7
O–Ca(2)–F	158.78	153.38	159.59	107.46	108.18	106.69	109.85
O–Ca(2)–O	81.11	71.98	84.10	154.56	72.95	67.22	71.71
O–Ca(1)–O	90.75	111.68	90.75	70.79	76.34	63.63	67.22
Ca(1)–O–P	128.14	97.29	128.14	125.09	127.06	103.89	127.34
F–Ca(2)–O	78.51	84.73	78.51	107.46	108.18	106.69	109.85
O–Ca(1)–O	104.21	149.74	140.77	125.37	96.69	125.72	77.41
O–Ca(1)–O	62.87	85.39	90.75	73.75	120.13	73.81	71.71
O–Ca(2)–O	69.46	57.12	62.87	104.47	53.31	67.22	73.809

TABLE 6.3: Atomic bond length changes derived from experimental data refined with PDFfit2, and represented in Fig. 6.7.

Bond	D1	D2	D3	D4	D5	D6	D7
P–O (1)	1.4717	1.5763	1.4717	—	1.6263	1.6162	1.5088
P–O (2)	—	1.7027	1.7189	1.6343	1.7751	1.6718	1.6517
P–O (3)	1.7364	—	1.7364	—	2.0128	1.6883	2.9727
O–O (1)	2.2709	2.4032	2.2709	1.9788	2.4920	2.3132	2.2311
O–O (2)	2.3692	2.4740	2.3692	2.4542	2.6617	2.3766	2.5280
O–O (3)	2.3809	2.7305	2.3808	2.4811	2.7693	2.4690	2.7099
O–O (4)	2.5315	2.8347	2.5315	2.7598	2.7737	2.7197	2.8739
O–O (5)	2.9045	2.8965	—	2.8868	2.8193	2.8189	—
O–O (6)	2.9979	2.9788	2.9979	2.9501	2.9863	2.8410	—
O–O (6)	—	—	—	—	—	2.8905	—
O–O (6)	—	—	—	—	—	2.9971	—
O–Ca (1)	2.3856	2.3399	2.3661	2.3121	2.2434	2.1940	2.2905
O–Ca (2)	2.4269	2.4531	2.3856	2.3590	2.3196	2.3349	2.3388
O–Ca (3)	2.6726	2.5005	2.4801	2.3824	2.3893	2.4068	2.3596
O–Ca (4)	2.7708	2.8202	2.5513	2.5340	2.4160	2.4842	2.4758
O–Ca (5)	—	—	2.6633	2.5567	2.4840	2.6429	2.5109
O–Ca (6)	—	—	2.7708	2.7296	2.5749	2.7186	2.5974
O–Ca (7)	—	—	—	—	2.8966	—	2.7984
Ca–F (1)	2.4691	2.2389	2.4691	2.3483	—	2.4148	2.3195
Ca–F (2)	—	—	2.5013	—	—	—	—
Ca–Ca (1)	2.8106	—	2.8106	—	—	—	—
Ca–P (1)	—	2.8995	—	—	2.9331	—	—
O–F (1)	—	—	—	2.8809	2.9336	—	—

Fig. 6.7(D5). Also, at this time point we can see the loss of a P–O bond from the PO_3 tetrahedra.

Days 4 and 5 also show remodelling of the crystal at the atomic scale. Here, most of the changes are due to the forming of bonds and the breaking of other bonds. On the contrary, 6 and 7 Fig. 6.7(D6 and D7), show quite similar structures when viewed from the naked eye. This shows that by day 6 the crystallisation is near completion and from

here the major changes are seen more in the changes in bond angle and length rather than the reformation of bonds.

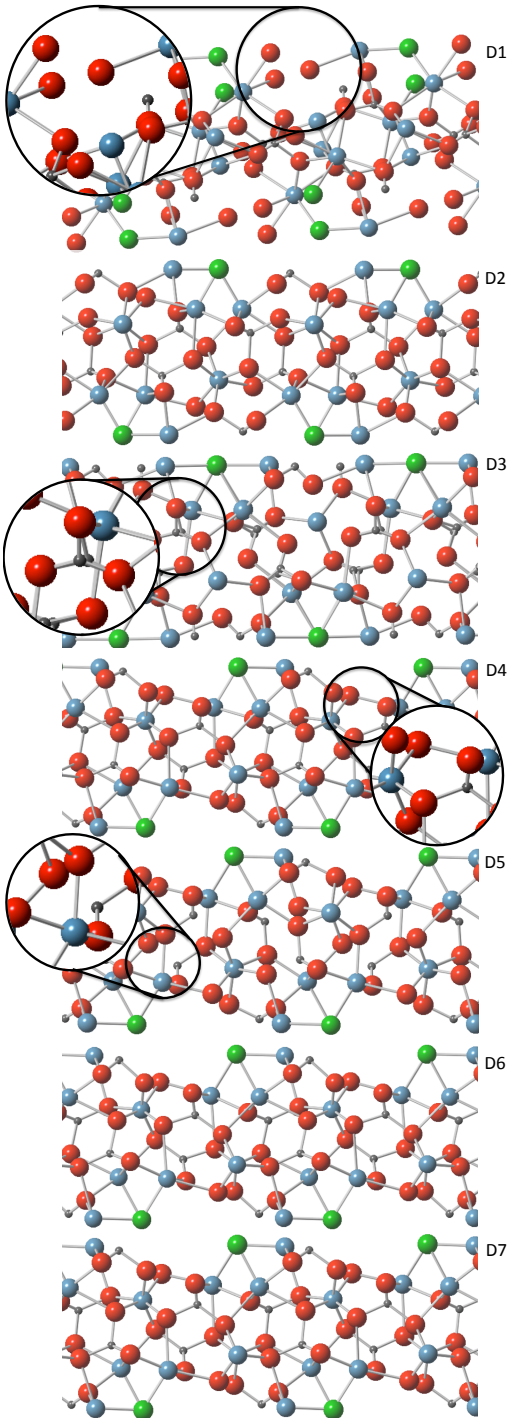

FIGURE 6.7: Fractional coordinates of structures derived from PDFfit2 refinement of data from samples incubated at 70°C, Fig. 6.2.

As the level of disorder in the system increases, it is expected that there will be an increase in variation of bond lengths for any particular bonding pair. Table 6.3, shows the bonds that were derived from the crystallographic structure files generated from

PDFfit2 analysis. Only three of these "bonds" represent real bonds within the system, Ca–F, O–Ca, and P–O. All others represent pair distributions between atoms, which has also been included for a greater understanding. Over all, there is an increase in the number of bond lengths per pair of atoms with an increase in time. There is also an increase in the lengths of these bonds as time increases, most notably seen in P–O, O–O, and O–Ca. In the case of O–O, we can see that from D3 to D7, we can see a greater variation in the number of bond lengths between 2.6 – 3.0 Å, increasing as 1, 3, 5, and 5, for D3, D4, D5, D6, and D7, respectively. At D2, we can see a large variation in lengths that does not follow the trend, possibly owing to more rapid phase transitions. D6, shows the greatest variation with 8 distinct atoms pair lengths. In the case of O–Ca, the variation in the bond lengths also increase after D3. There are many changes in bond length throughout the seven days showing a continual remodelling up until the final day. Most notably, we can see that in terms of the distribution of bond lengths, D6 and D7 are actually quite different from each other, with D6 containing 18 distinct lengths where as D7 only has 15. Furthermore, D7 has a much smaller variation in the distances between O–O, showing a smaller amount of disorder in this region. In previous studies, SEM analysis has revealed interconnections with a curvy-linear morphology between rod-like crystallites at day 6 that were not found at day 7. It suggested the presence of a distinct phase, perhaps a layer of ACP that had formed on top of lower layer, or a dissolution of the previous layer in an atomic remodelling process. This result may hint towards a greater amount of disorder at D6 than in other time points.

With regard to the bond lengths and the atomic bond angles derived from PDFfit2 analysis, we did not expect to see such a variation in the number of bond lengths for any particular bonding pair, Table 6.3. Previous structurally based work with XRD and visual based work with SEM suggested that for the greater duration of the seven day synthesis, the products being formed were crystalline in nature. As such, one would expect a greater regularity in the bonding lengths. Similarly, there were also a range of bonding angles that were found to differ for each other from day to day.

6.4.2.1 Analysis of Phase Transitions at Early Time Points

After taking results at 24 hr intervals we wanted to see what was happening in the early stages of incubation. For this a freeze drying technique was used to capture what ever products were formed and to prevent them from transitioning into another state. This time readings were taken over an 11 min period with roughly 2-3 mins between samples. Fig. 6.8, illustrates the transition from ACP. At time point 4 mins, a broad peak is found from 20–40° (2θ) with it's maximum is found at 30.116622° (2θ). When compared to the maximum X-ray count number, time points 4 mins and 11 mins have a maximum

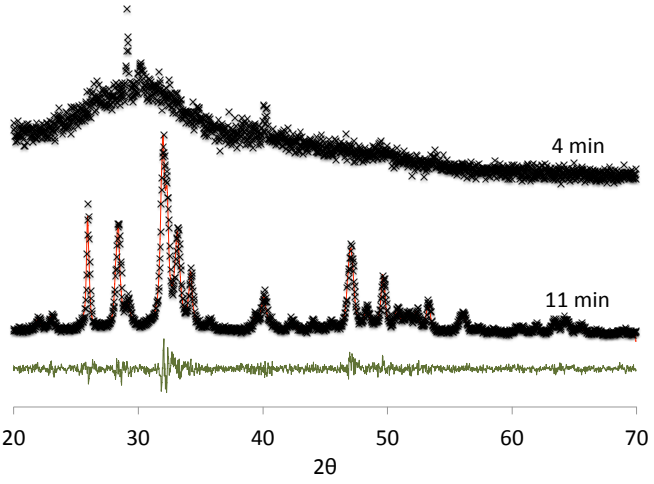

FIGURE 6.8: Normalised Cu-source X-ray diffractograms, of freeze dried precipitate collected at time points 4 mins and 11 mins (day 6) were refined by Rietveld refinement. X (observed), red (calculated), green (observed–calculated).

count of 424 and 1266, respectively. That is to say that the maximum found on the broad peak is 33.5% the size of the more crystallised pattern. Which was an indication found by Eanes in 1965 to distinguish between the amorphous phase and that of a very small crystallite that appears to give a broad amorphous like XRD pattern [222]. Thus, we can see here that we have found evidence of an amorphous phase formation.

As seen in previous work, the precipitate produced at day 6 is compared to ensure that the freeze drying process did not alter the products formed. A sample at day 6 was analysed using XRD. The resulting particle size and abundance was compared to non-freeze dryed samples from previous work. composed of apatite and CaF_2. However, unlike in previous experiments in which freeze drying was not used, the weight percent was found to be 64.28 w% and 35.72 w%, for apatite and CaF_2. Moreover, the average particle size was 206.57 Å, and 232.41 Å in that same order.

In order to further corroborate the findings of ACP, Ag-source XRD data was used to analyse the sample from 2 mins. Fig. 6.9 shows the difference between the Pair distribution function of samples retrieved after only 2 mins of incubation and those formed after 24 and 48 hours. Clearly, we can see that the sample is amorphous due to the reduction in intense peaks after about 4 Å. In other words, this samples maintains short range order but not long range order. At the same time, we can clearly see that this sample shares very similar peaks with those of the clearly defined crystalline samples of day 1 (24 hr) and 2 (48 hr) which were incubated at 70°C, as previously shown in Fig. 6.2. This is the first evidence that this chemical route takes on an amorphous calcium phosphate stage.

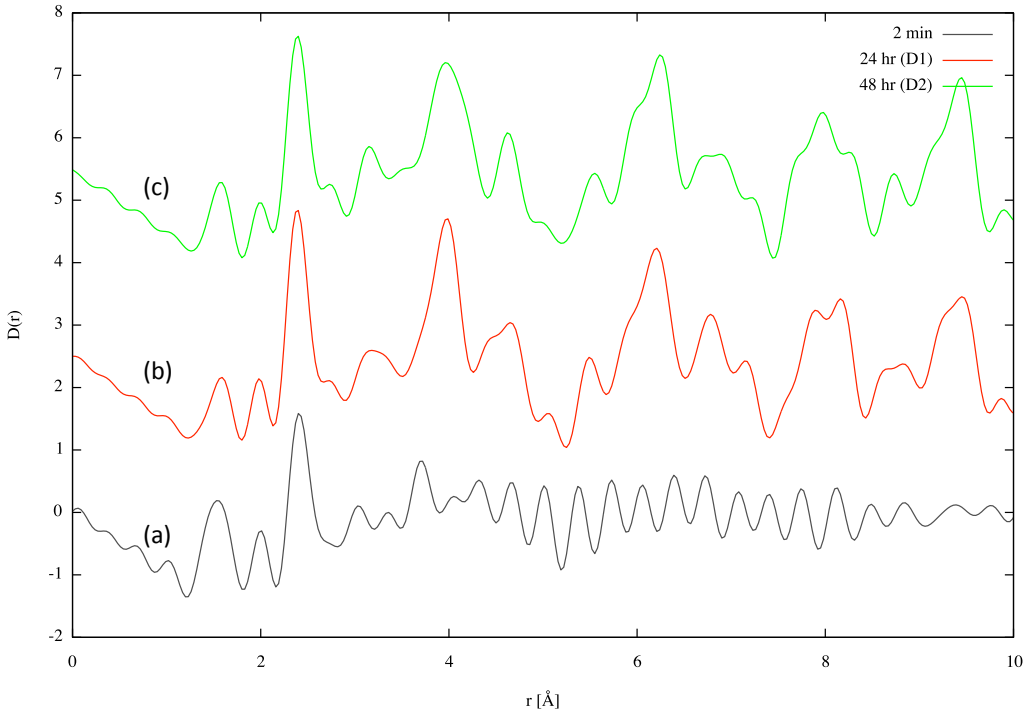

FIGURE 6.9: Pair distribution function of powders formed from 2 mins to 48 hours. Produced with GUDRUNx

As can be seen in Fig. 6.9(a), the amorphous calcium phosphate stage shares at least two peaks in common with its crystalline counter parts (b) and (c). Namely, these would be the first and third most prominent peaks from the left at 1.53 Å (P–O), and 2.40 Å (Ca–O). Both of these peaks are similar to that of bond lengths found in apatite. Further to this, peaks at positions 3.03 Å (O–O), 4.02 Å (Ca-Ca), and 4.29 Å (O-Ca) are all consistent with the bond lengths found in apatite. As can be seen at high r, there is a lot of noise within this data set for which the Lorch function was unable to remove, we can also find a peak at 1.98 Å that can not here be accounted for. A peak found at 3.36 Å could not be connected to a bond length in either HAp or FAp but could be found in DCPD with a H-H bond. Finally, a peak at 3.69 Å could be found in both FAp and DCPD but not in HAp. There was no evidence of any bonds associated with F, which may suggest that the incorporation of F^- ions occurs more closer to the crystallisation stage of development.

6.4.3 Molecular dynamics model experimentation and development

It was decided that the development of the MD simulation would be directed to wards representing the set-up of the actual system. However, each aspect of the system (the

surface, the solution and the amorphous structure) had to be designed and checked separately.

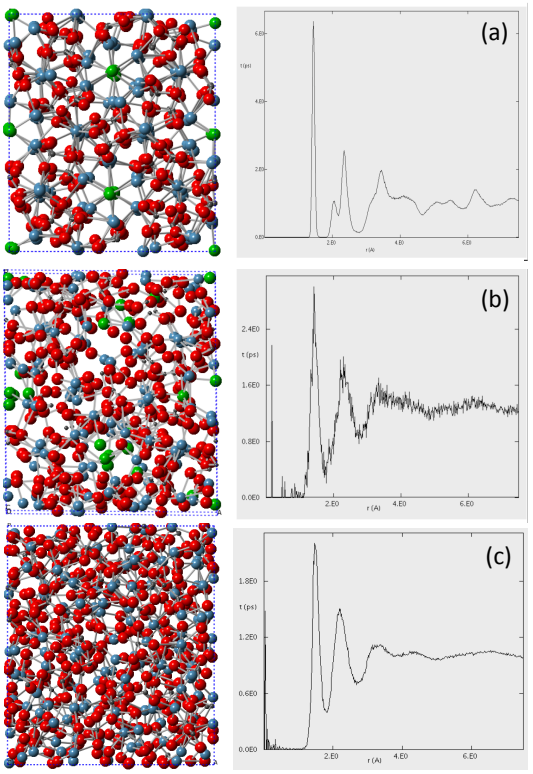

FIGURE 6.10: Comparison between disordered FAp and crystalline FAp structure simulated using DLPOLY 4. (right) MD simulated structure, (middle) G(r) of simulated structure, and (right) GUDRUNx derived G(r) = $\sum g(r)$.

Each stage of the simulation was developed separately. Fig. 6.10, shows the development of the disordered system used in this study. Fig. 6.10(a), shows the structure of FAp, simulated through the use of interatomic potentials. Its simulated distribution function was compared to that of the GUDRUNx derived PDF. As can be seen, peak positions are consistent between the simulated and experimentally derived D(**r**). Following this, disorder was added into the FAp simulation to generate an FAp simulation with a disordered configuration, Fig. 6.10(b). This was done by increasing the simulation temperature to above the melting point of fluroapatite (1200 °C), and then using the melted structure as the basis for future simulation. Again its distribution function shows similarities with that of the ACP samples previously found. Finally, Fig. 6.10(c), shows the generation of a disordered β-TCP. β-TCP was chosen due to its compositional ratio. β-TCP has a composition of $Ca_9(PO_4)_6$, which is consistent with the composition of the Posner cluster, having a composition of -$(Ca_3(PO_4)_2)_n$-. As can be seen, its simulated PDF is also similar to that of the experimentally derived D(**r**) for ACP.

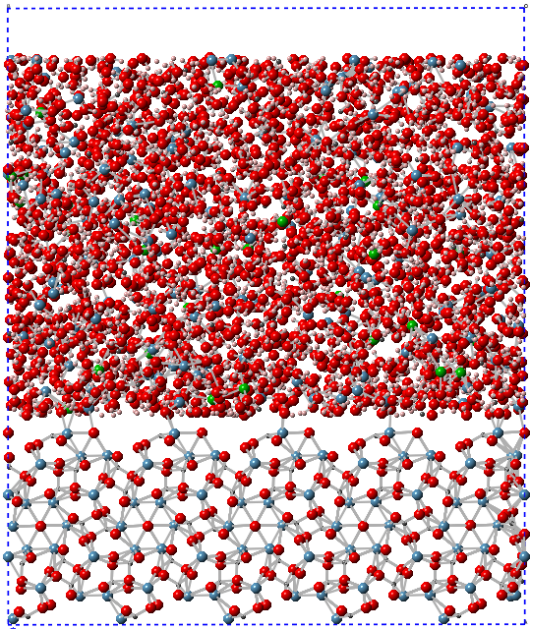

FIGURE 6.11: Starting configuration for DLPOLY molecular dynamics simulation.

Following from this, we were able to set-up a system which included the formation of ACP and further interaction with the surface by combining the three separate MD simulations, the diffusion of ions in solution, the stable apatite surface, and the disordered ACP. As can be seen in Fig. 6.11, a surface of crystalline hydroxyapatite has been generated to simulate the surface of the apatite substrate that has been used within the chemical synthesis experiments. The water used is based on the simple point charge (SPC) model[8]. and has the same concentration of ions required for the formation of FAp. For each part of the simulation, i.e. the surface, the ions and the SPC model of water, the force fields were tested individually and then again when each component was combined to see if the force fields would work in the combined model. The simulation was run such that 5 ns worth of steps occurred and the formation of the ACP could be observed. The resulting structures were then extracted and a PDF was generated from its configuration. This configuration was later compared to that of the experimentally derived PDF seen for ACP, as seen in Fig. 6.9. the system was allowed to run further to permit the formation of a crystalline structure, with the expectation that the presence of the crystalline hydroxyapatite surface would encourage the ACP to progress to FAp.

Fig. 6.12(a), show the formation of a calcium phosphate molecule in solution. This molecule has no crystalline structure and as such has been considered to be 'disordered calcium phosphate'. In Fig. 6.12(b) shows an enlarged view of the disordered calcium phosphate formed in solution. Fig. 6.13(a), shows what happens to the ions when they

[8]the SPC model, assumes an ideal tetrahedral shape (HOH angle of 109.47°C) instead of the observed angle of 104.5°C

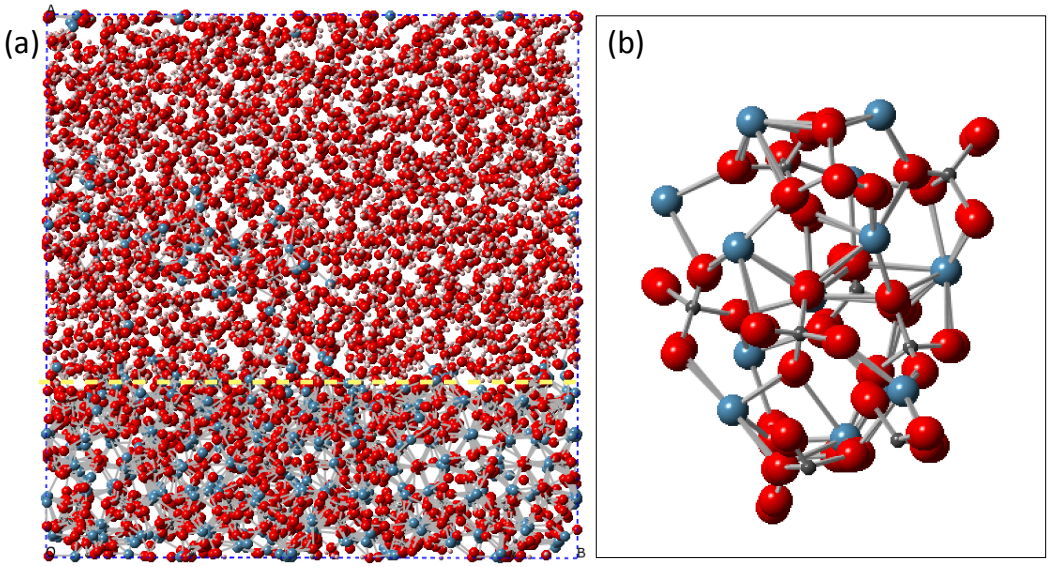

FIGURE 6.12: Molecular dynamics simulation formation of disordered calcium phosphate in solution, (a) full system, and (b) disordered calcium phosphate formed in simulation. Yellow line showing clearly the boundary between the apatite surface and the solution.

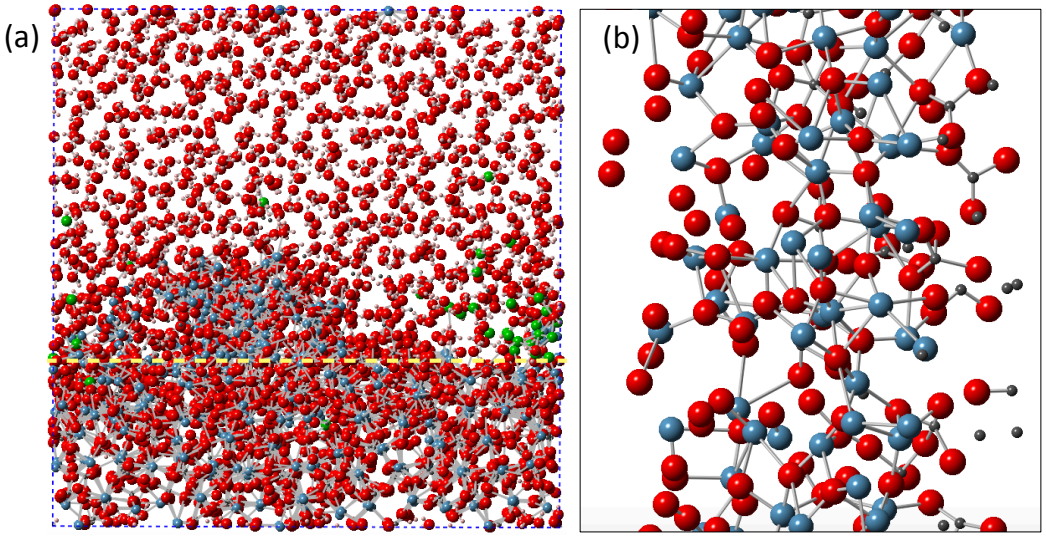

FIGURE 6.13: Molecular dynamics simulation of crystallisation at surface, (a) full system, and (b) 'crystallisation' formed on the surface. Yellow line showing clearly the boundary behind the apatite surface and the solution.

are close enough to the apatite surface. Due to time constraints, it was not possible to run the system from the initial diffused ion state to one where a large enough number of ions were found at the surface. In many cases the random walk persisted throughout the entirety of the simulation, meaning that most of the ions stayed within the few angstroms of their original position. To account for this, we altered the system such that the ions would be evenly distributed but also closer to the side in which the surface

was set. In this case, we were able to see that after a short time the ions quickly formed bonds with the surface of the crystalline surface. The molecule, Fig. 6.13(b), appeared to have a some what repeating structure, but it did not resemble that of either apatite or DCPD.

6.5 Summary

In summary, we are able to gain a perspective on the processes involved during the seven days of incubation. After 2–4 mins ACP has formed with bonds that largely resemble apatite, as seen in XRD and PDF data. However, one peak present could not be accounted for by apatite but instead DCPD. This is the first indication that there are competing phases in the early stages of formation. After 11 mins, the transition to a crystallised apatite phase has occurred. However, as can be seen in the seven day trials, there is a continued reformation at the atomic scale throughout the seven days. During this seven day period, there is strong evidence for apatite bonds at every day yet there are transitions between bonds that are related to that of DCPD. Since we do not see any evidence for DCPD in the XRD data it is possible that just as we see ACP with apatite-like bond lengths in the early stages, we could be seeing ACP with DCPD like bond-lengths at later stages. However, in this case we also have a large presence of crystalline apatite which shows up in both the XRD and the PDF. After analysing the bond distribution and bond lengths that are derived from the fitted PDF data we can see that there is an increase in the number of bond lengths and continual changes in the bond angle throughout the seven day period. This shows that the level of disorder in the system remains present throughout the synthesis period even though we have clear crystalline features in the XRD and the PDF data. This is another hint towards the continued presence of ACP throughout the synthesis route.

6.5.1 Main findings

We found that:

- Samples at 70°C show evidence of bond formation breaking and lengthening on a daily basis. Whereas, 21°C samples show consistent bonds over 5 days in region (b), region (c) also shows a more gradual change in bond formation. 21°C peaks persist over many days but change length.
- Overall, the peaks are representative of an apatite structure but with some indications towards a DCPD structure being formed. Peaks 1.60 Å(representing H –

H or P – O) and 4.42 Å(representing O – Ca or O – H) are only possible in DCPD and not apatite.

- Changes in atomic bond length and angles throughout the seven day incubation of 70°C samples revealed that crystal remodelling continued throughout the duration of the incubation.

- The increasing level of bond lengths in the system suggests a level of disorder that is not present in a purely crystalline structure.

- XRD scans between 0 – 11 mins revealed that at 4 mins and amorphous-like XRD peak could be seen. Having a maximum at 30.116622° (2θ) that was 33.5% the size of the crystalline apatite pattern. This was confirmed to be amorphous via Pair Distribution Function analysis that showed prominent peaks at 1.53 Å, and 2.40 Å, both of which can be found in crystalline samples but no bonding pairs beyond this.

- A successful Molecular Dynamics system including a stable apatite substrate surface and an ion filled solution. Generating both in solution and on the surface ACP formation.

Chapter 7

Conclusions, Future work, applications and development of the field

3-4 years ago we did not know the exact temperature that produced aligned rod-like apatite coatings with a precipitation method at temperatures under 100°C. In this study we have found two temperatures in which we can observe this phenomena.

One of the biggest problems that we had to over come was the identification of ACP as part of this system. This required the use of a make shift freeze drying method which involved both an instantaneous freezing with super cooled liquid nitrogen and then later freeze drying over 3 days. Due to the set-up of our labs this meant that samples had to be prepared in one locations and then nitrogen frozen in another. In turn this added some time constraints to the experiment that mean that the smallest time interval we could measure was 2 mins. Adding to this, the frozen storage capsules had a limited storage space which meant that running repeats for each time point on the same day was not possible. Even so, it was possible to isolate an amorphous band at 4 mins but none there after. The transition from a purely ACP phase to a more crystalline phase happens so quickly in this system that it can be very easy to miss.

At this stage, this innovation is still in its infancy. Even though it resembles the nano structure of nano-apatite coatings that have been formed via another route that itself had been proven to show biological response. We have not here studied the effect of our material on that of any biological systems either in vitro or in vivo (be it animal or human). However, due to its morphological similarities, and its chemical composition being similar to that of organic apatite it is safe to say that this material shows promise

in the area of implant coating. Not only could this material be used in dental implants, but it can also find use in total joint replacements which included knee, hip, elbow etc. The potential for a faster healing time could see its use in areas where people have higher risk of implant failure. Some examples of these are those with poor bone quality, heavy smokers, heavy drinkers, diabetics all fall into this category.

For the academic world, the development of the MD system for ACP formation can lead to further discoveries in the kinetics of these two systems. Here, we have proven that each stage nucleation to ACP and crystallisation at the surface level are possible. However, to provide a more accurate view of the real system we would need to further develop this simulation to be able to transition from phase to phase. The system so far will serve as a starting point for the next researcher who is interested in understanding the physics of these or similar systems.

The time restrictions on a PhD program means that there are still some open questions. One of the first this that we had to decide upon was whether to study the evolution of the systems of both the temperatures 21°C and 70°. Due to the nature and complexity of the MD simulations we had to choose only one. 70°C was considered more desirable due to the properties being closer to that which we were aiming for with regards to implant coating applications. However, due to the dramatic differences in the synthesis route between both temperatures, a comparative study would provide greater clues to the underlying physics that cause these system to diverge. In this study, the activation energy and energy barriers required during the phase transition would be of interest. However, to simulate a phase transition within an MD simulation that runs over a few nano-seconds is quite difficult. In this study, we attempted to encourage nucleation to occur in the presence of a crystalline surface. Even though we were able to isolate each stage into parts and show that it is indeed possible to achieve some level of crystallisation at the surface we were not able to run one continuous system from ions to ACP to crystalline phases (perhaps DCPD or FAp). Truly this was a complex system. As part of our experimentation, we also explored the effect of a ZnO pre-coating on the substrates. It was also decided that we would not include findings based on a the effects of ZnO rods. Some samples that were coated with ZnO, which has a habit similar to that of the apatite nano-rods that we intend to form. Where the ZnO coatings were performed by Prof. Steve Dunn from the School of Engineering and Materials Science. Furthermore, theses rods are within the length scale that we with to replicate. These ZnO nano-rods had a width of width 123.9 ± 8.7 nm. Apatite Crystals that were precipitated on top of ZnO nano-rods, regime, appear to have produced very promising results of ordered apatite nano crystals with a rod width of 126.0 ± 8.7 nm. This is possibly due to the similar unit cell, both having a hexagonal space group which encourages epitaxial growth. Furthermore the size of the ZnO nano rods generate a surface with the size

requirements desired for the formation of apatite nano-rods. However, further study into the composition using NMR or XRD was not followed in this section primarily because the focus on this study was directed towards the formation of ordered surfaces at 21°C and 70°.

The primary aim of this research was to develop a bioactive surface of densely packed rod-like apatite crystal, aligned along the c-axis and of size range 25 – 100 nm wide and 100 nm to 100 μm long. It would also have to achieve a surface coverage of 95% Vol and have a stoichometry of Ca/P ratio = 1.67. Following this, an application of diffraction and simulation based techniques were to be used to gain a deeper knowledge of the mechanism by which synthesis progressed. A range of nano structures were produced as part of this research but formed branches that deviated away from the core aims of this research. However, these findings could also prove to yield some future interest in other areas. Nano-rod slabs showed some level of temperature dependent structural changes that were similar to some of the findings seeing on the 21°C and 70°C. It is possible that a greater look into this section could also provide interesting information. Adding to this, another branch that was not explored was the surfaces formed on the EHA substrates at 37°C. At first glance, the structure has multiple levels of hierarchy, and forms a 'interwoven mesh' of nano rods. Along with both the 21°C and 70°C samples, it would be interesting to conduct biological testing to see how these nano-coatings compare to their hydrothermal counterparts in terms of cell response. The level of adhesion, cell abundance and bone formation could be tested in vitro while animal trials could also help to see how well these surface treatment stand up to a more bio-chemical environment.

Greater comparison of the differences between 21°C and 70°C at the molecular level through the use of molecular dynamics and PDF analysis could yield more understanding of the processes at play and the differences within this work. Here, more focus was given to the development of the molecular dynamics simulation for that of 70°C, while the synthesis pathway of 21°C, while clearly distinct from that of coatings formed at 70°C was not developed further due to time restraints. The Reverse Monte Carlo Method could prove to be the more useful tool in the refinement of the Pair Distribution Functions of the syntheses materials than PDFfit. PDFfit2, uses a 'small box' model to refine the data. This means that this method is extremely good for crystalline materials which have long range order, however, in the case of an amorphous counterpart this technique is no-longer a viable option. In this case, the unique feature of the Reverse Monte Carlo Method is better suited, as it is able to use a larger number of atoms and is able to alter each atom individually, until a goodness-of-fit is achieved. This method would be better suited to model the small changes in the system based on a atomic based as apposed to a unit cell based approach.

There are a number of future improvements that could be made in order to further develop the concerns of this research. The first is to gain a better understanding of the crystallite size and the relationship with the surface gap size. Analysis of the size of crystallites at earlier time points may reveal a closer relationship between the surface gap size and the crystallite size that is here not scene. Secondly, to better understand the synthesis route, time study can be conducted throughout the full duration of the synthesis.

Chapter 8

Appendix

.1 Fitting

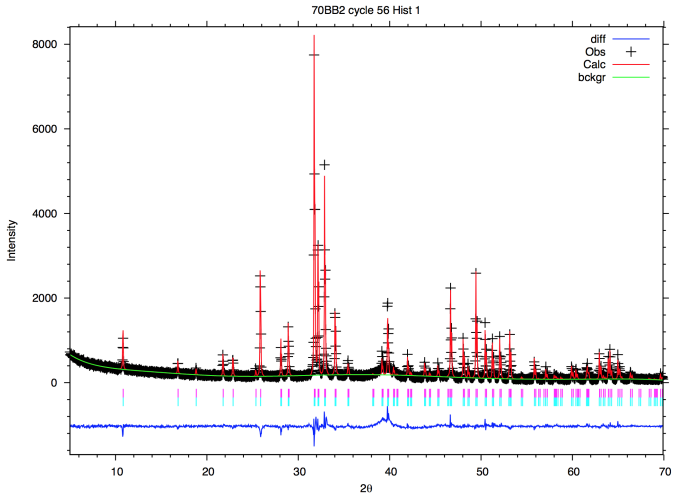

FIGURE 1: XRD fitting of CaF_2 and FAp phases using GSAS (EXPgui).

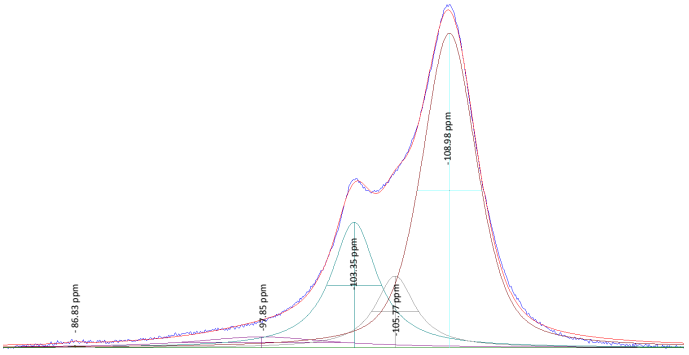

FIGURE 2: NMR data deconvoluted using DMFIT method. Clearly showing the five peaks that are identified and how small the first two peaks are in comparison to the other three.

.2 NRM deconvolution

.2.1 Unbuffered NMR samples

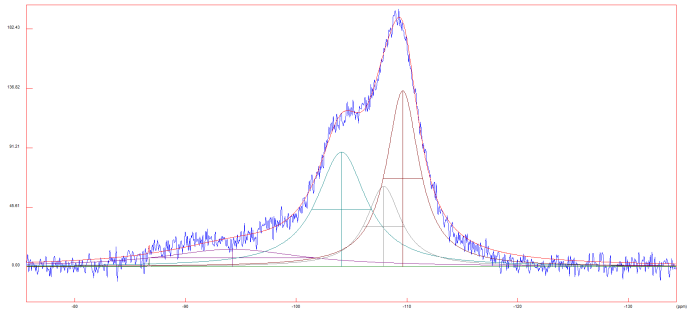

FIGURE 3: NMR data deconvoluted using DMFIT method. Clearly showing deconvoluted peaks for unbuffered samples incubated at 5°C.

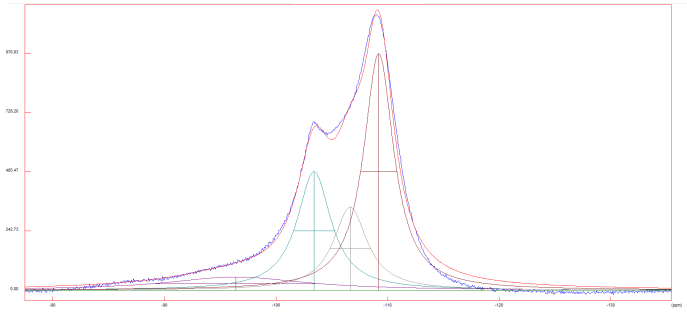

FIGURE 4: NMR data deconvoluted using DMFIT method. Clearly showing deconvoluted peaks for unbuffered samples incubated at 21°C.

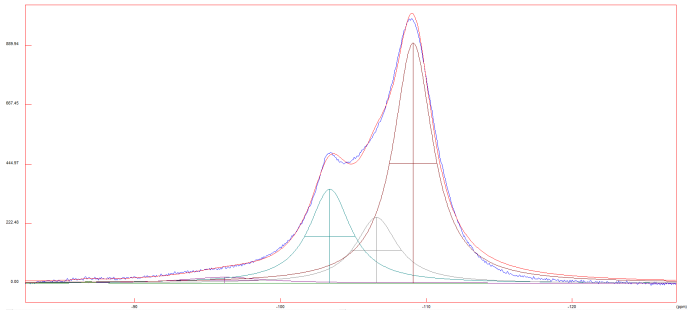

FIGURE 5: NMR data deconvoluted using DMFIT method. Clearly showing deconvoluted peaks for unbuffered samples incubated at 37°C.

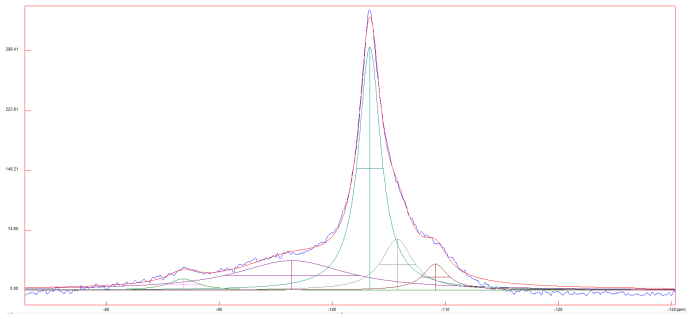

FIGURE 6: NMR data deconvoluted using DMFIT method. Clearly showing deconvoluted peaks for unbuffered samples incubated at 54°C.

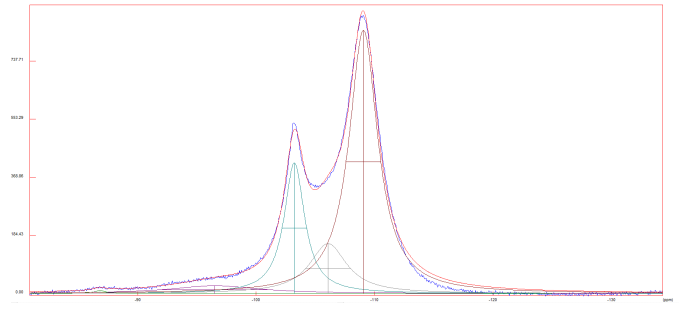

FIGURE 7: NMR data deconvoluted using DMFIT method. Clearly showing deconvoluted peaks for unbuffered samples incubated at 70°C.

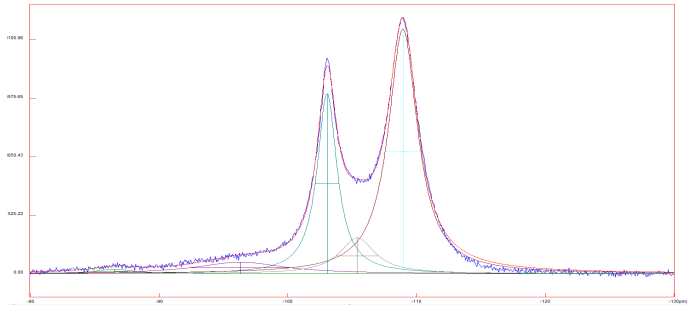

FIGURE 8: NMR data deconvoluted using DMFIT method. Clearly showing deconvoluted peaks for unbuffered samples incubated at 90°C.

.2.2 Buffered NMR samples

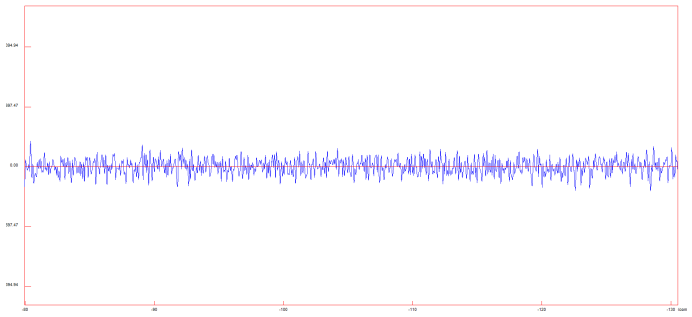

FIGURE 9: NMR data deconvoluted using DMFIT method. Clearly showing deconvoluted peaks for buffered samples incubated at 5°C.

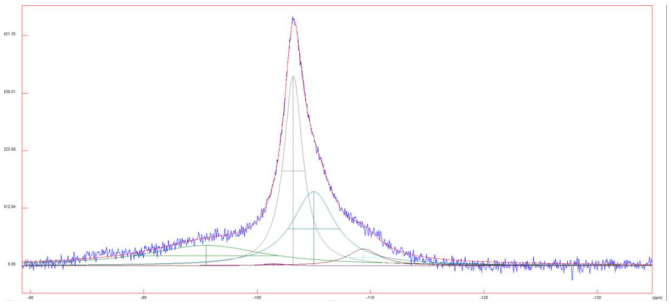

FIGURE 10: NMR data deconvoluted using DMFIT method. Clearly showing deconvoluted peaks for buffered samples incubated at 21°C.

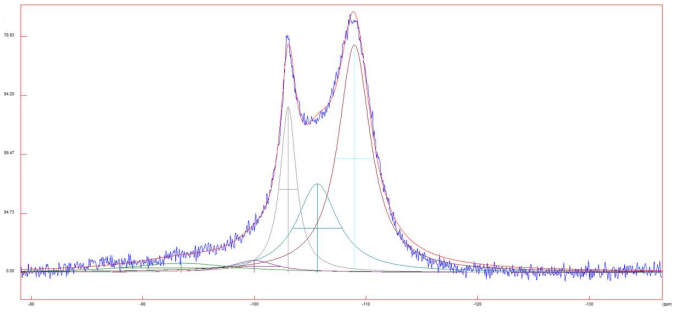

FIGURE 11: NMR data deconvoluted using DMFIT method. Clearly showing deconvoluted peaks for buffered samples incubated at 37°C.

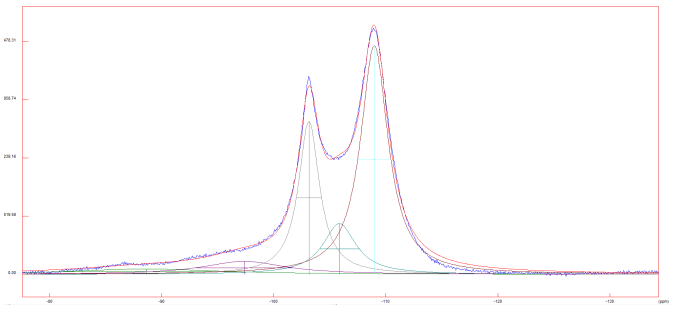

FIGURE 12: NMR data deconvoluted using DMFIT method. Clearly showing deconvoluted peaks for buffered samples incubated at 54°C.

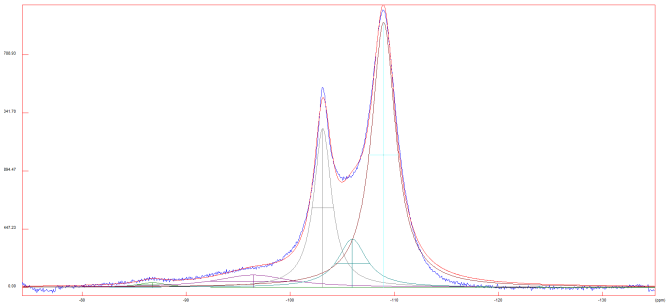

FIGURE 13: NMR data deconvoluted using DMFIT method. Clearly showing deconvoluted peaks for buffered samples incubated at 70°C.

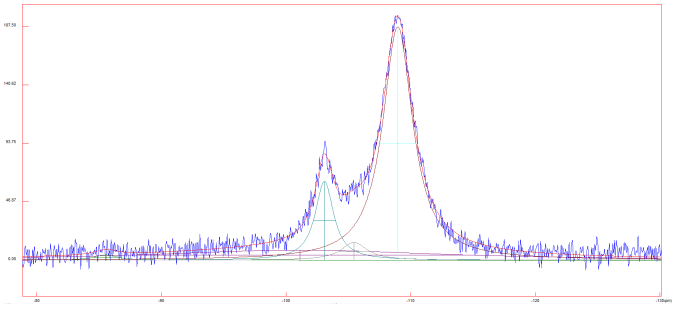

FIGURE 14: NMR data deconvoluted using DMFIT method. Clearly showing deconvoluted peaks for buffered samples incubated at 90°C.

.2.3 NMR deconvolution 21°C

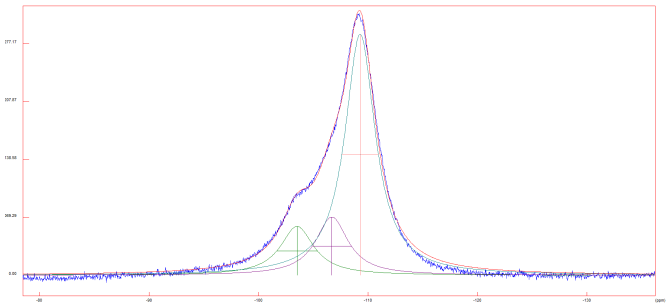

FIGURE 15: NMR data deconvoluted using DMFIT method. Clearly showing deconvoluted peaks for unbuffered samples incubated at 21°C for day 1.

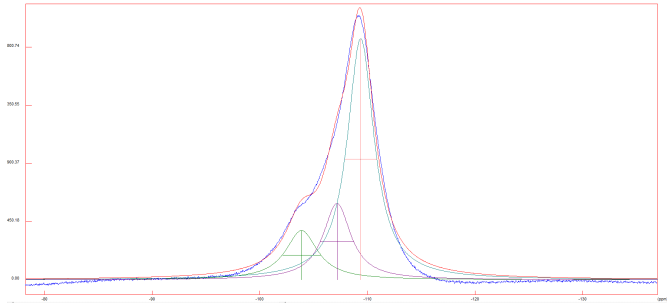

FIGURE 16: NMR data deconvoluted using DMFIT method. Clearly showing deconvoluted peaks for unbuffered samples incubated at 21°C for day 2.

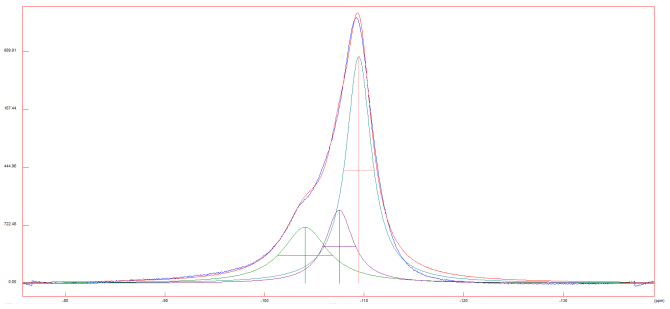

FIGURE 17: NMR data deconvoluted using DMFIT method. Clearly showing deconvoluted peaks for unbuffered samples incubated at 21°C for day 3.

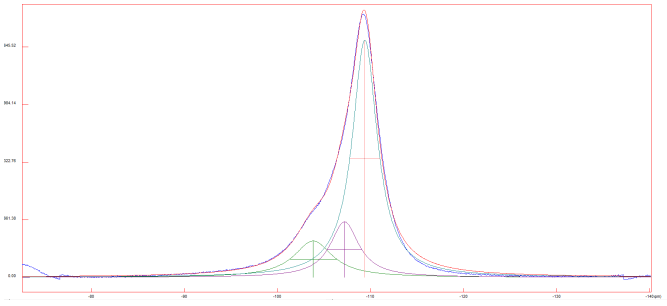

FIGURE 18: NMR data deconvoluted using DMFIT method. Clearly showing deconvoluted peaks for unbuffered samples incubated at 21°C for day 4.

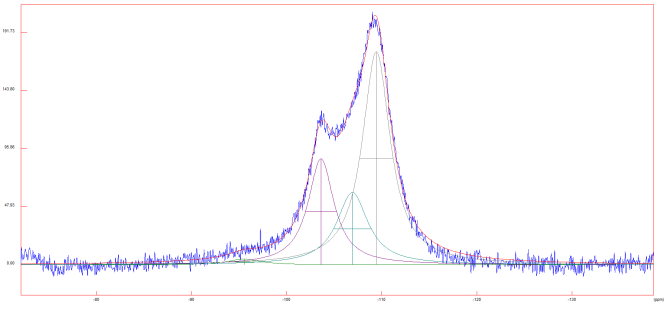

FIGURE 19: NMR data deconvoluted using DMFIT method. Clearly showing deconvoluted peaks for unbuffered samples incubated at 21°C fo day 5.

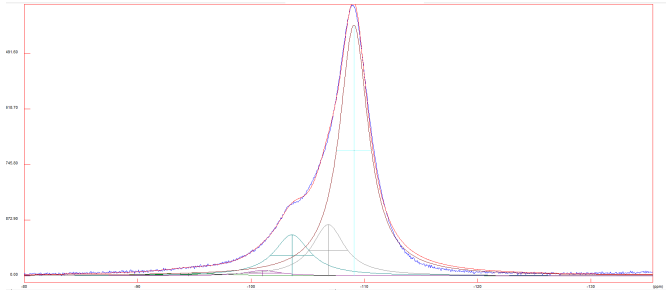

FIGURE 20: NMR data deconvoluted using DMFIT method. Clearly showing deconvoluted peaks for unbuffered samples incubated at 21°C for day 6.

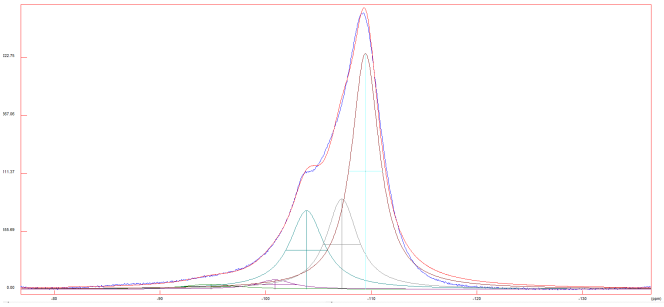

FIGURE 21: NMR data deconvoluted using DMFIT method. Clearly showing deconvoluted peaks for unbuffered samples incubated at 21°C for day 7.

.2.4 NMR deconvolution 70°C

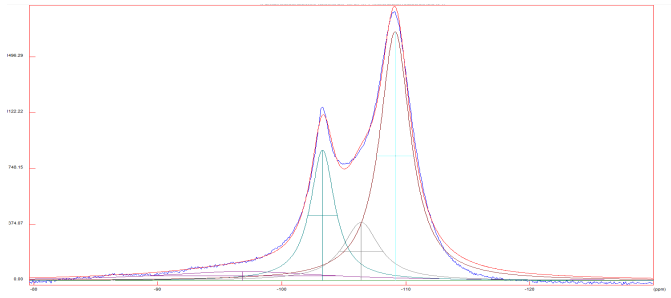

FIGURE 22: NMR data deconvoluted using DMFIT method. Clearly showing deconvoluted peaks for unbuffered samples incubated at 70°C for day 1.

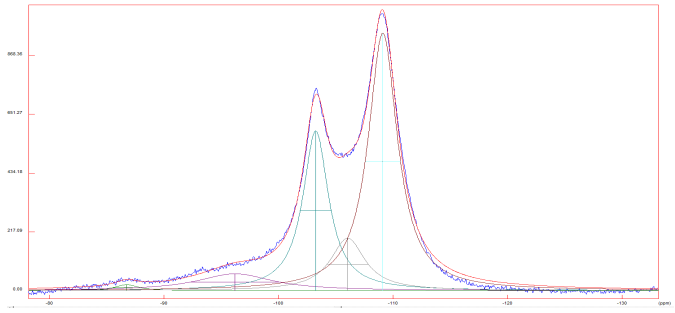

FIGURE 23: NMR data deconvoluted using DMFIT method. Clearly showing deconvoluted peaks for unbuffered samples incubated at 70°C for day 2.

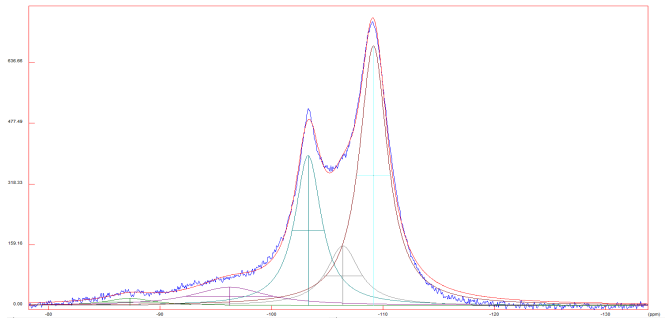

FIGURE 24: NMR data deconvoluted using DMFIT method. Clearly showing deconvoluted peaks for unbuffered samples incubated at 70°C for day 3.

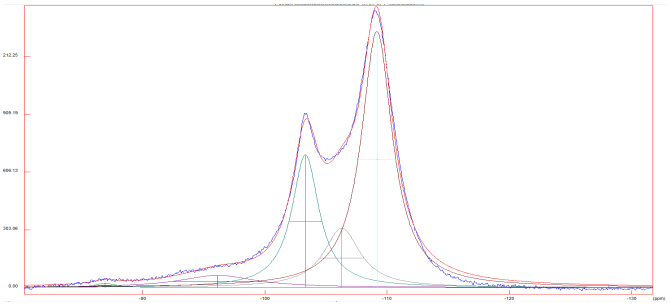

FIGURE 25: NMR data deconvoluted using DMFIT method. Clearly showing deconvoluted peaks for unbuffered samples incubated at 70°C for day 4.

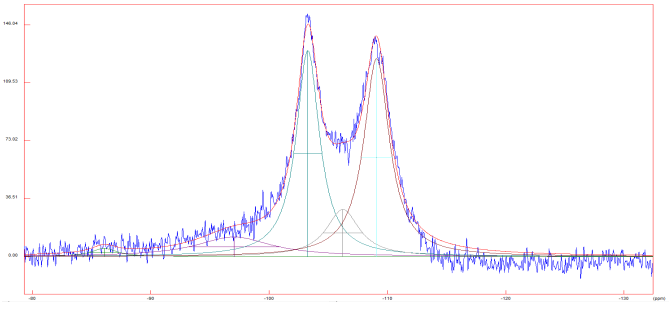

FIGURE 26: NMR data deconvoluted using DMFIT method. Clearly showing deconvoluted peaks for unbuffered samples incubated at 70°C fo day 5.

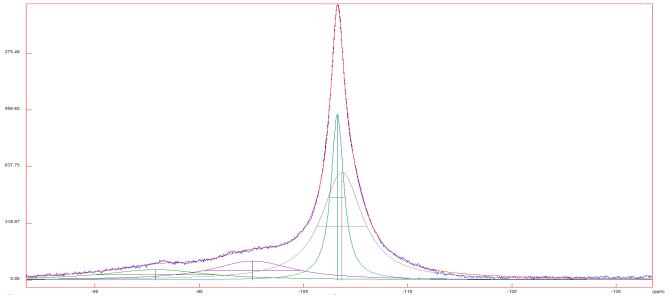

FIGURE 27: NMR data deconvoluted using DMFIT method. Clearly showing deconvoluted peaks for unbuffered samples incubated at 70°C for day 6.

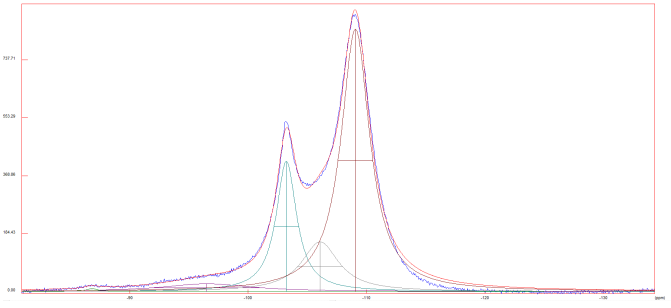

FIGURE 28: NMR data deconvoluted using DMFIT method. Clearly showing deconvoluted peaks for unbuffered samples incubated at 70°C for day 7.

.2.5 NMR deconvolution 70°C between day 6 and 7

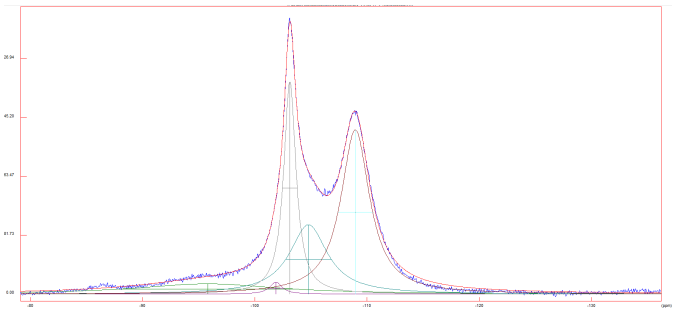

FIGURE 29: NMR data deconvoluted using DMFIT method. Clearly showing deconvoluted peaks for unbuffered samples incubated at 70°C for day 6.1.

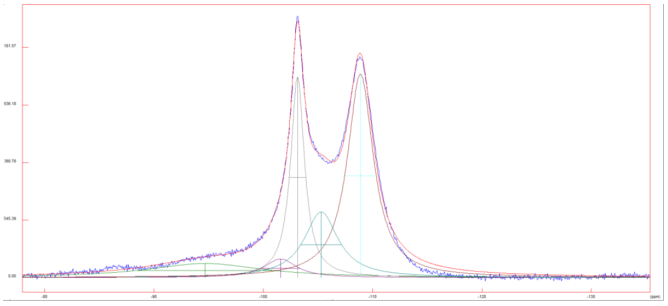

FIGURE 30: NMR data deconvoluted using DMFIT method. Clearly showing deconvoluted peaks for unbuffered samples incubated at 70°C for day 6.2.

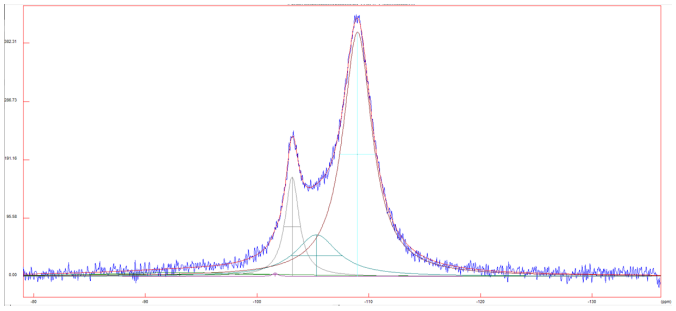

FIGURE 31: NMR data deconvoluted using DMFIT method. Clearly showing deconvoluted peaks for unbuffered samples incubated at 70°C for day 6.3.

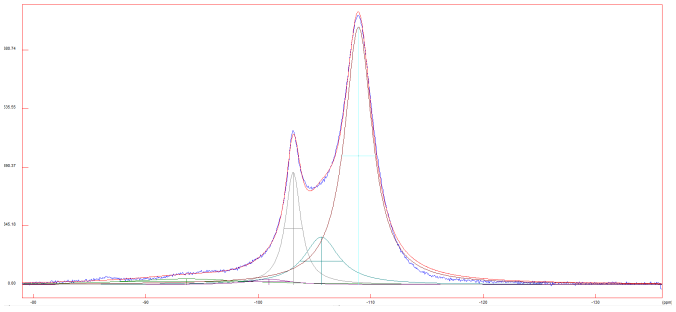

FIGURE 32: NMR data deconvoluted using DMFIT method. Clearly showing deconvoluted peaks for unbuffered samples incubated at 70°C for day 6.4.

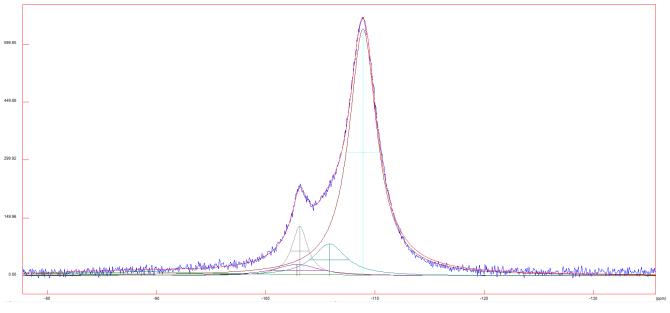

FIGURE 33: NMR data deconvoluted using DMFIT method. Clearly showing deconvoluted peaks for unbuffered samples incubated at 70°C fo day 6.5.

.3 Rietveld Refinement of cu-source data

[1]

.3.1 Rietveld Refinement of unbuffered

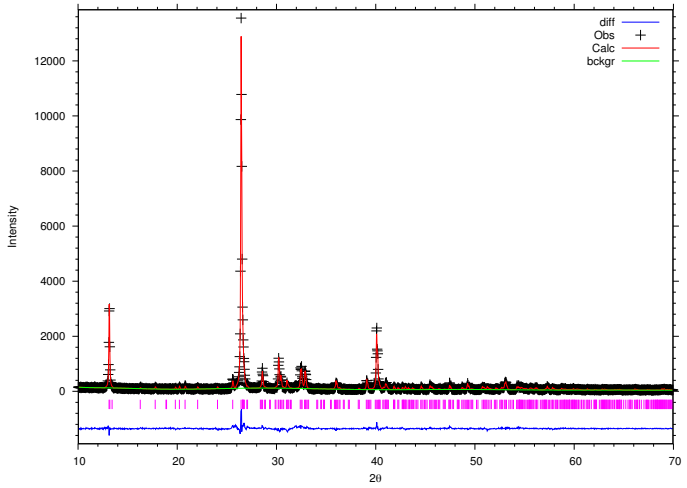

FIGURE 34: XRD using Rietveld refinement GSAS method. Clearly showing fitting of two phases to experimentally derived XRD peaks for unbuffered incubated at 5°C.

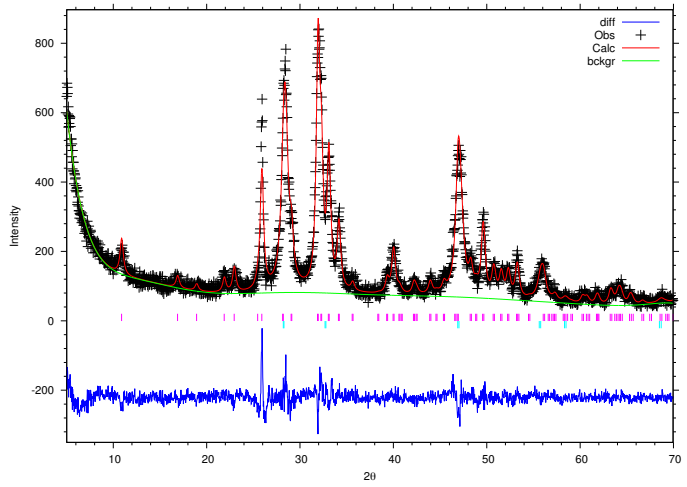

FIGURE 35: XRD using Rietveld refinement GSAS method. Clearly showing fitting of two phases to experimentally derived XRD peaks for unbuffered incubated at 21°C.

[1] XRD data was added following amendments phase. GSAS I., was no longer operational, as such old data files had to be loaded into GSAS 2. This meant that both powpref and genles had to be run again in order to generate the fitting. The problem with this is that in some cases, especially those which require intensive March Dollase corrections became less refined. As there was no longer any time to correct these issues but are here presented.

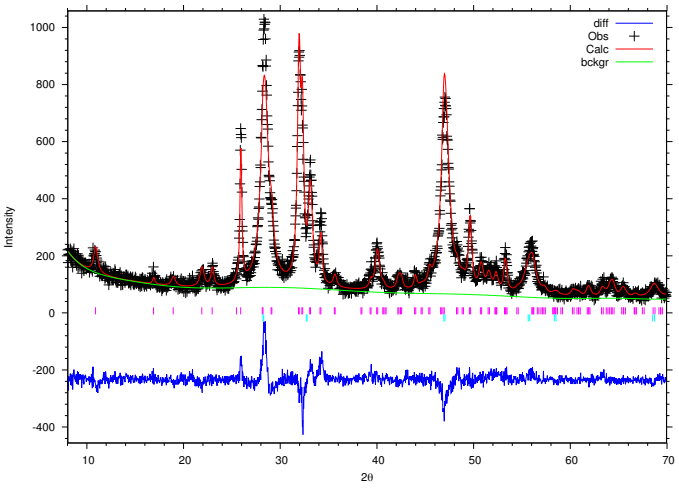

FIGURE 36: XRD using Rietveld refinement GSAS method. Clearly showing fitting of two phases to experimentally derived XRD peaks for unbuffered incubated at 37°C.

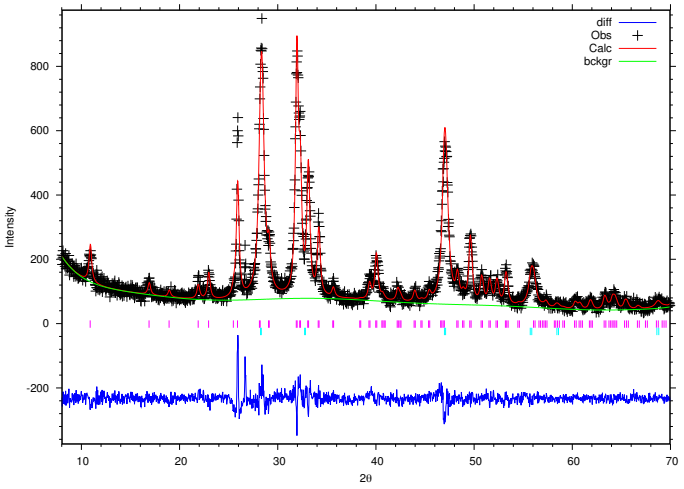

FIGURE 37: XRD using Rietveld refinement GSAS method. Clearly showing fitting of two phases to experimentally derived XRD peaks for unbuffered incubated at 54°C.

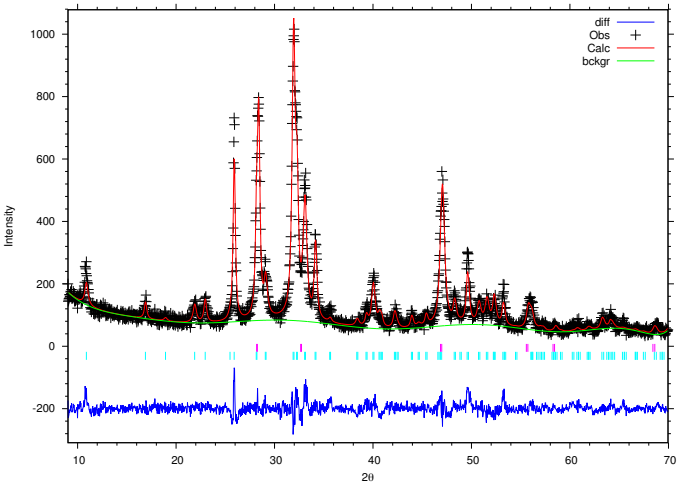

FIGURE 38: XRD using Rietveld refinement GSAS method. Clearly showing fitting of two phases to experimentally derived XRD peaks for unbuffered incubated at 70°C.

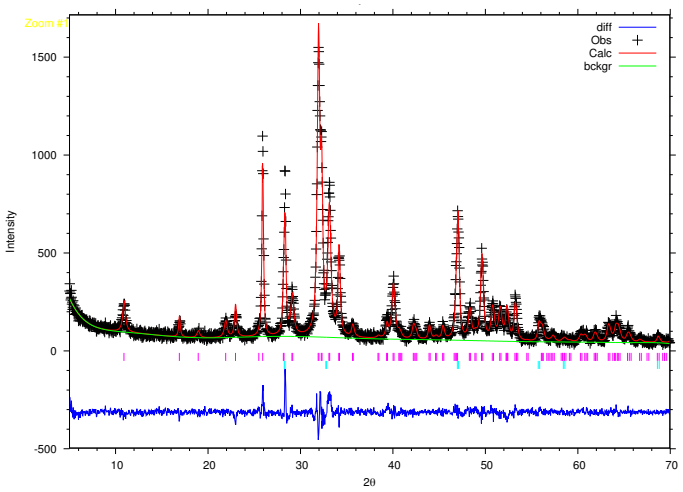

FIGURE 39: XRD using Rietveld refinement GSAS method. Clearly showing fitting of two phases to experimentally derived XRD peaks for unbuffered incubated at 90°C.

.3.2 Rietveld Refinement of buffered

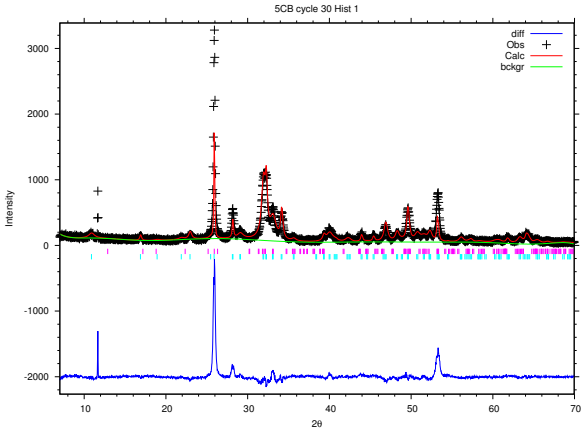

FIGURE 40: XRD using Rietveld refinement GSAS method. Clearly showing fitting of two phases to experimentally derived XRD peaks for buffered incubated at 5°C.

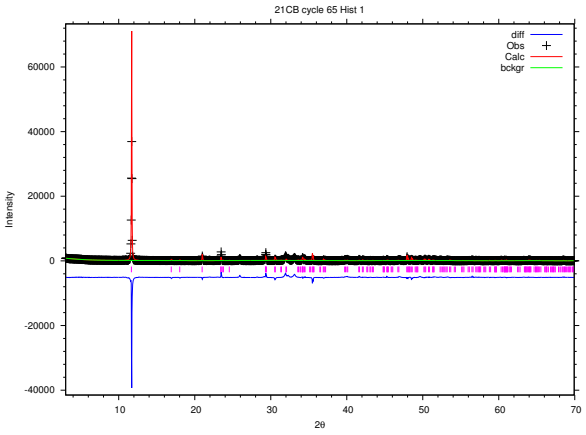

FIGURE 41: XRD using Rietveld refinement GSAS method. Clearly showing fitting of two phases to experimentally derived XRD peaks for buffered incubated at 21°C.

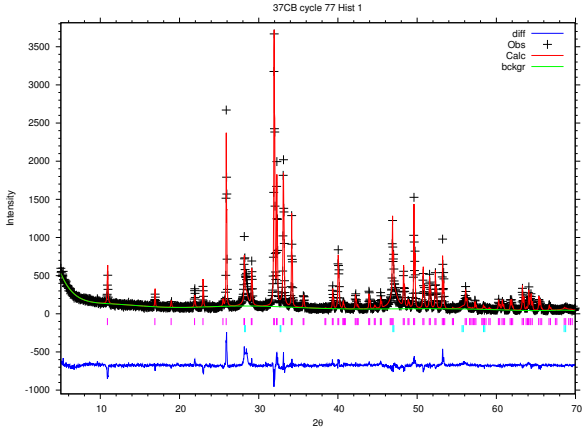

FIGURE 42: XRD using Rietveld refinement GSAS method. Clearly showing fitting of two phases to experimentally derived XRD peaks for buffered incubated at 37°C.

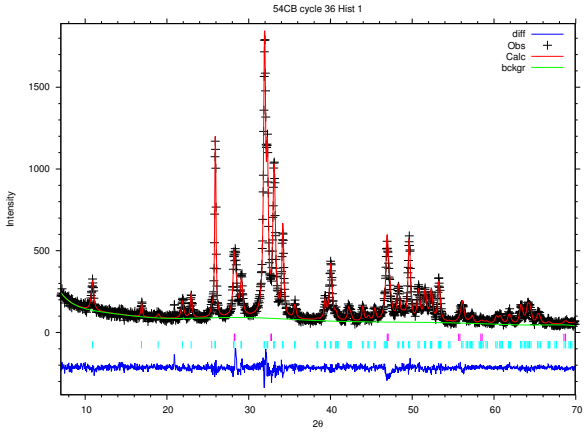

FIGURE 43: XRD using Rietveld refinement GSAS method. Clearly showing fitting of two phases to experimentally derived XRD peaks for buffered incubated at 54°C.

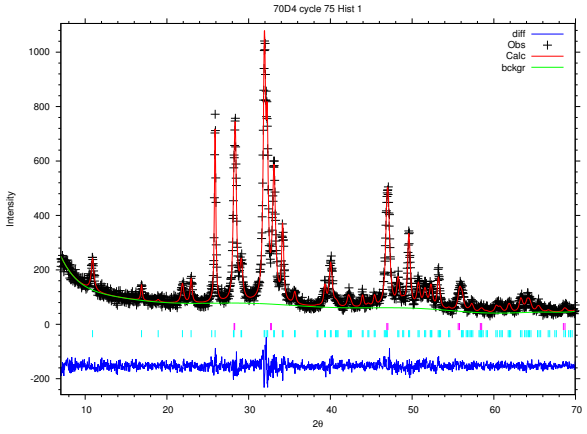

FIGURE 44: XRD using Rietveld refinement GSAS method. Clearly showing fitting of two phases to experimentally derived XRD peaks for buffered incubated at 70°C.

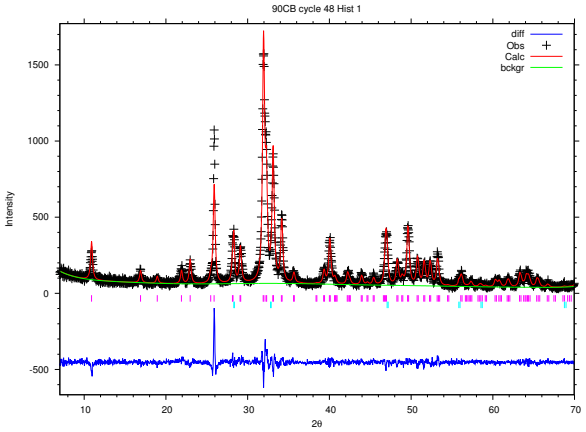

FIGURE 45: XRD using Rietveld refinement GSAS method. Clearly showing fitting of two phases to experimentally derived XRD peaks for unbuffered incubated at 90°C.

.3.3 XRD GSAS fitting 21°C

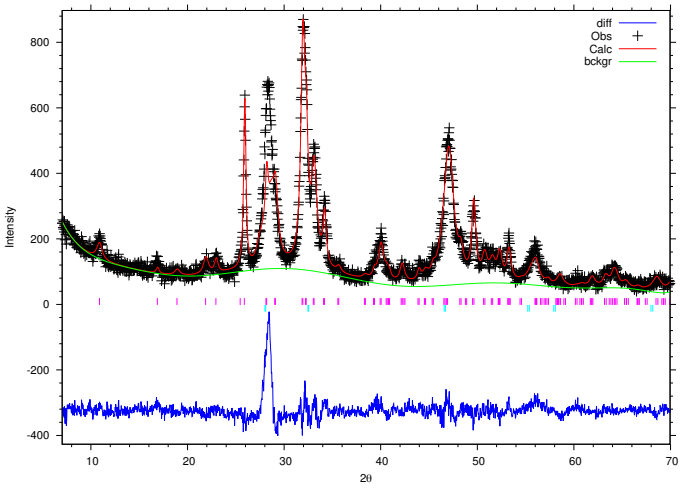

FIGURE 46: XRD using Rietveld refinement GSAS method. Clearly showing fitting of two phases to experimentally derived XRD peaks for unbuffered samples incubated at 21°C for day 1. Phase 1 shown in pink (apatite), phase 2 shown in blue (Calcium fluoride), and difference graphs shown below in dark blue.

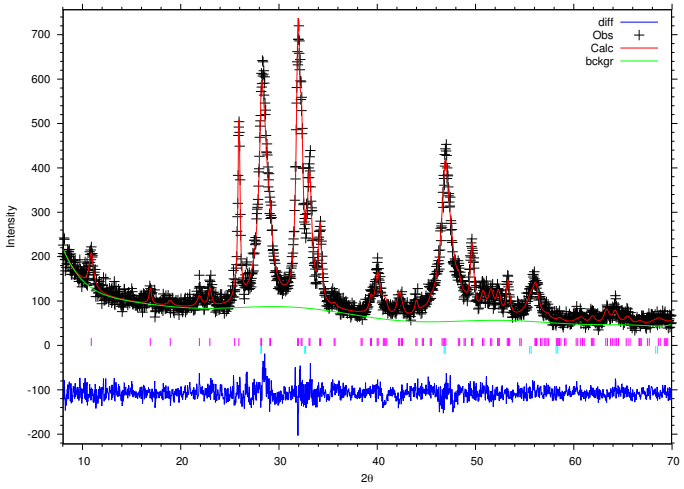

FIGURE 47: XRD using Rietveld refinement GSAS method. Clearly showing fitting of two phases to experimentally derived XRD peaks for unbuffered samples incubated at 21°C for day 2. Phase 1 shown in pink (apatite), phase 2 shown in blue (Calcium fluoride), and difference graphs shown below in dark blue.

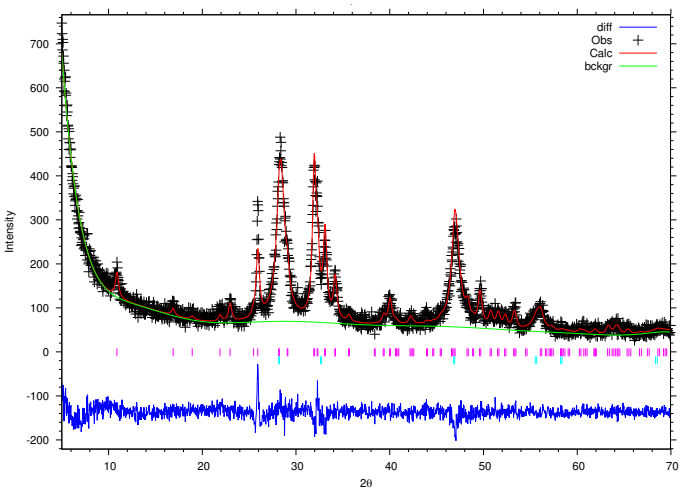

FIGURE 48: XRD using Rietveld refinement GSAS method. Clearly showing fitting of two phases to experimentally derived XRD peaks for unbuffered samples incubated at 21°C for day 3. Phase 1 shown in pink (apatite), phase 2 shown in blue (Calcium fluoride), and difference graphs shown below in dark blue.

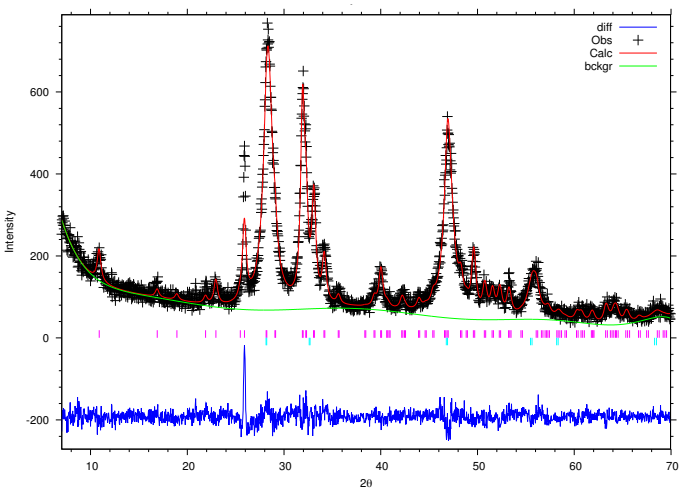

FIGURE 49: XRD using Rietveld refinement GSAS method. Clearly showing fitting of two phases to experimentally derived XRD peaks for unbuffered samples incubated at 21°C for day 4. Phase 1 shown in pink (apatite), phase 2 shown in blue (Calcium fluoride), and difference graphs shown below in dark blue.

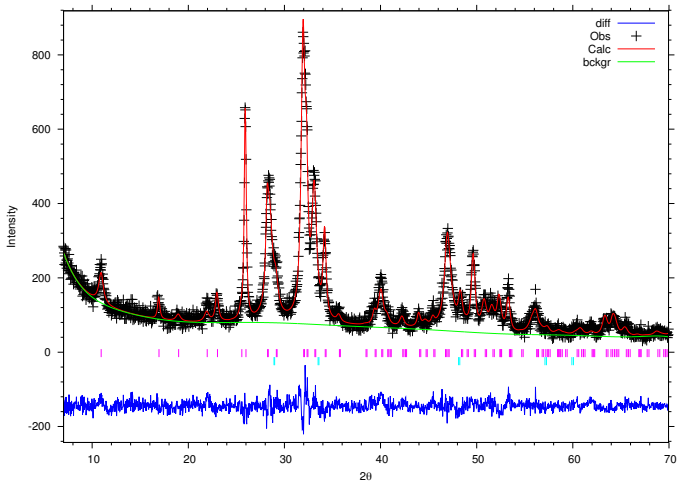

FIGURE 50: XRD using Rietveld refinement GSAS method. Clearly showing fitting of two phases to experimentally derived XRD peaks for unbuffered samples incubated at 21°C for day 5. Phase 1 shown in pink (apatite), phase 2 shown in blue (Calcium fluoride), and difference graphs shown below in dark blue.

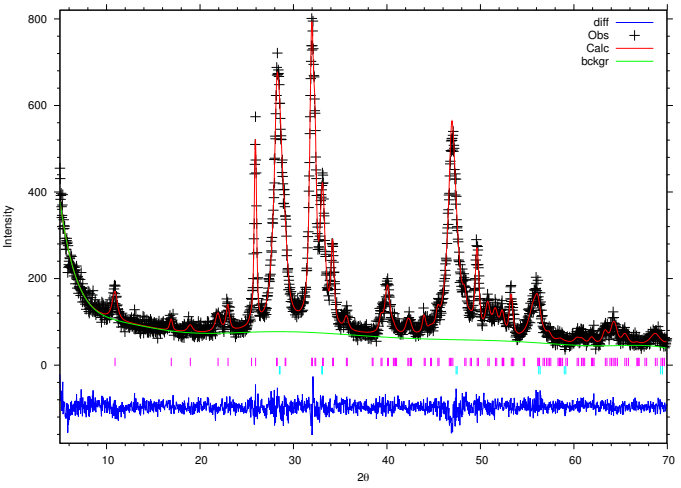

FIGURE 51: XRD using Rietveld refinement GSAS method. Clearly showing fitting of two phases to experimentally derived XRD peaks for unbuffered samples incubated at 21°C for day 6. Phase 1 shown in pink (apatite), phase 2 shown in blue (Calcium fluoride), and difference graphs shown below in dark blue.

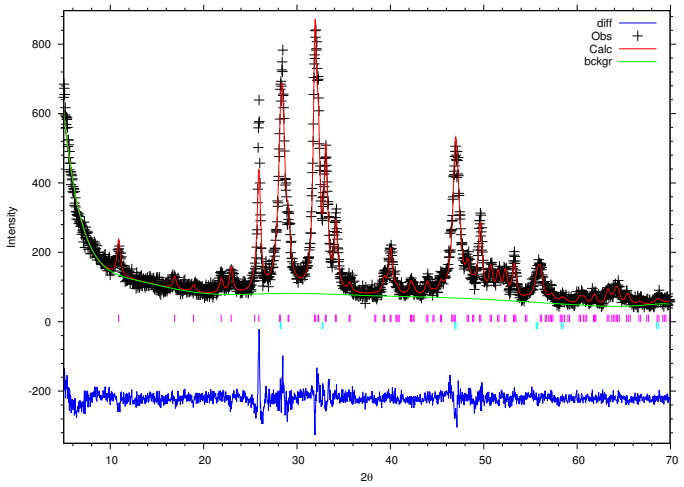

FIGURE 52: XRD using Rietveld refinement GSAS method. Clearly showing fitting of two phases to experimentally derived XRD peaks for unbuffered samples incubated at 21°C for day 7. Phase 1 shown in pink (apatite), phase 2 shown in blue (Calcium fluoride), and difference graphs shown below in dark blue.

.3.4 XRD GSAS fitting 70°C

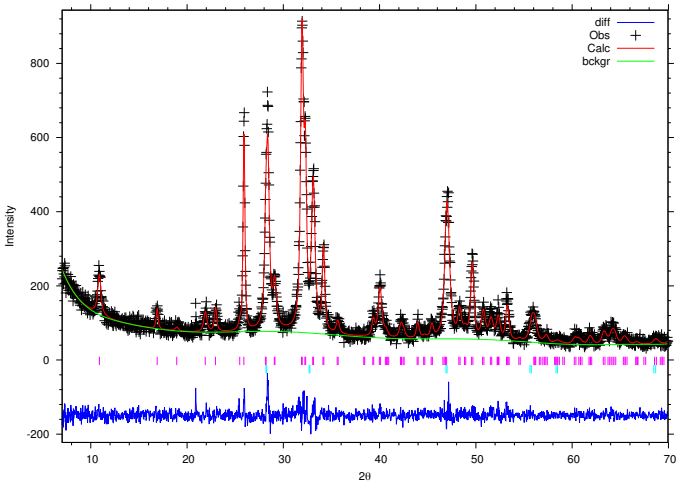

FIGURE 53: XRD using Rietveld refinement GSAS method. Clearly showing fitting of two phases to experimentally derived XRD peaks for unbuffered samples incubated at 70°C for day 2. Phase 1 shown in pink (apatite), phase 2 shown in blue (Calcium fluoride), and difference graphs shown below in dark blue.

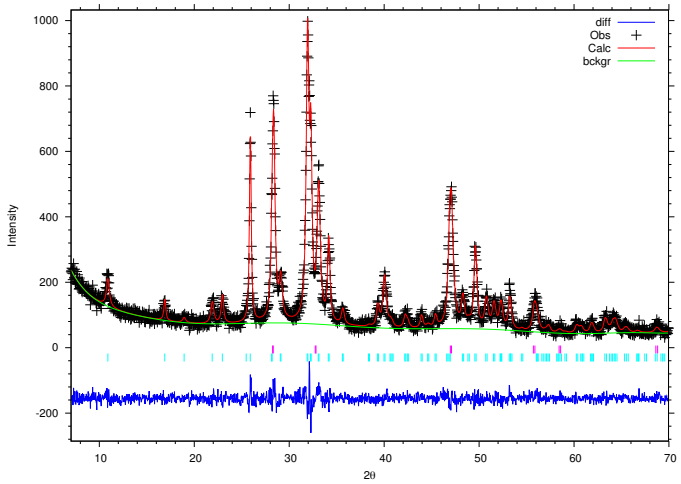

FIGURE 54: XRD using Rietveld refinement GSAS method. Clearly showing fitting of two phases to experimentally derived XRD peaks for unbuffered samples incubated at 70°C for day 3. Phase 1 shown in pink (apatite), phase 2 shown in blue (Calcium fluoride), and difference graphs shown below in dark blue.

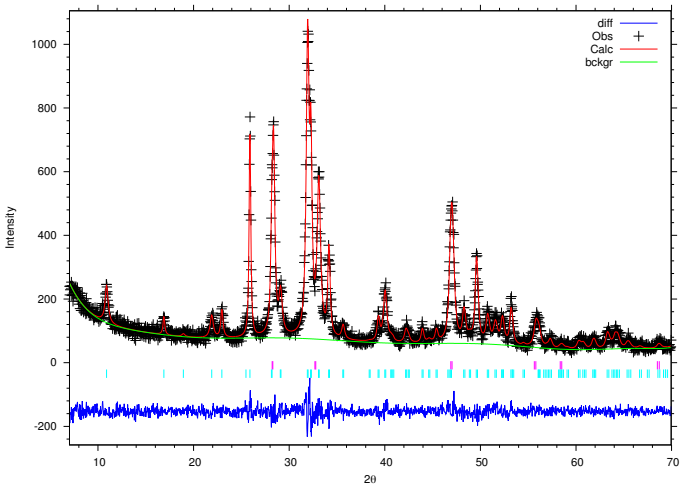

FIGURE 55: XRD using Rietveld refinement GSAS method. Clearly showing fitting of two phases to experimentally derived XRD peaks for unbuffered samples incubated at 70°C for day 4. Phase 1 shown in pink (apatite), phase 2 shown in blue (Calcium fluoride), and difference graphs shown below in dark blue.

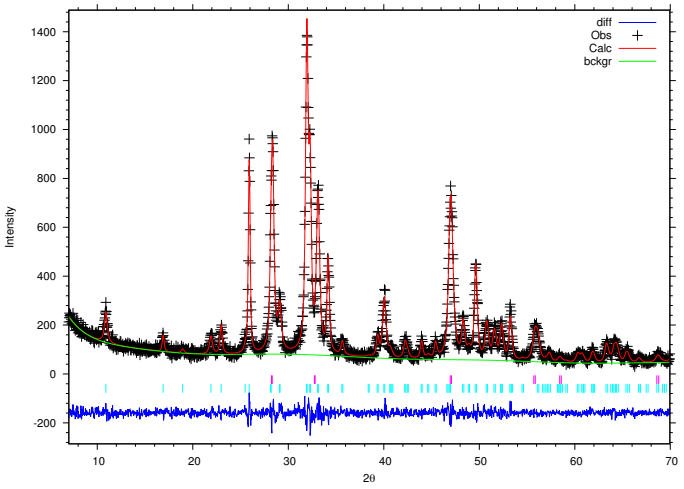

FIGURE 56: XRD using Rietveld refinement GSAS method. Clearly showing fitting of two phases to experimentally derived XRD peaks for unbuffered samples incubated at 70°C for day 5. Phase 1 shown in pink (apatite), phase 2 shown in blue (Calcium fluoride), and difference graphs shown below in dark blue.

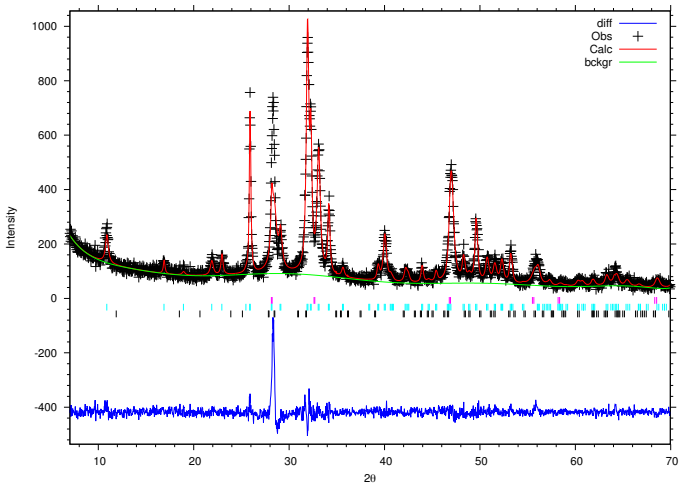

FIGURE 57: XRD using Rietveld refinement GSAS method. Clearly showing fitting of two phases to experimentally derived XRD peaks for unbuffered samples incubated at 70°C for day 6. Phase 1 shown in pink (apatite), phase 2 shown in blue (Calcium fluoride), and difference graphs shown below in dark blue.

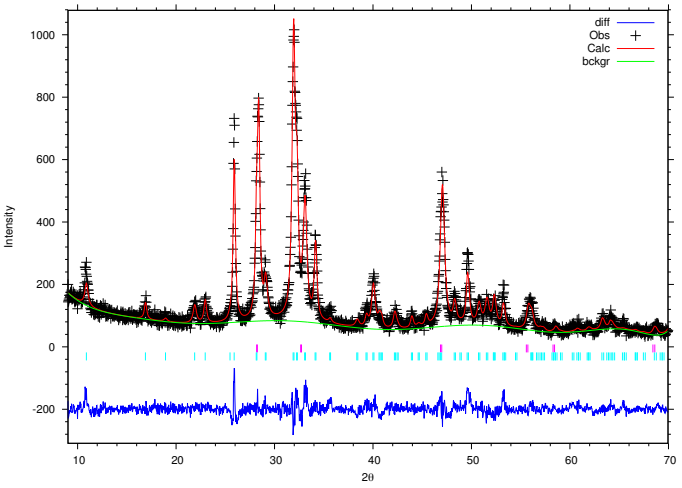

FIGURE 58: XRD using Rietveld refinement GSAS method. Clearly showing fitting of two phases to experimentally derived XRD peaks for unbuffered samples incubated at 70°C for day 7. Phase 1 shown in pink (apatite), phase 2 shown in blue (Calcium fluoride), and difference graphs shown below in dark blue.

List of Figures

1.1 SEM image of plasma sprayed coatings. Showing rodlike apatite crystallites with a misaligned (or disordered micro-scale) orientation, taken from [37] 4

1.2 3-dimensional reconstruction of the implant-tissue interface and 1D concentration profiles. (a) Atom probe microscopy image displaying the direct contact between Ca of the bone mineral and Ti of the coating surface. (b) 1D concentration profiles of Ti, Carbon (C), Calcium (Ca) and Phosphorus (P) from the coating and across the interface into the bone tissue, obtained from the reconstruction in (a), taken from [48]. 6

1.3 Increasing number of articles published on apatite coatings each year, for the last 10 years. Showing the increased interest and importance of that the scientific community have placed on this field. 7

1.4 Histological examination of bone growth chamber implanted into the lateral metaphysis of the distal femur of dog for 8 weeks. Osteoblast cells (orange), Ti implant (black). Showing the improvement of bone ingrowth with the application of a nano-apatite coating. Taken from [41]. 9

1.5 SEM of synthesised ordered (A) and disordered (B) FAp crystal surfaces. Cell density on ordered and disordered FAp surfaces (right). The attached cell numbers on the ordered FAp surfaces were significantly higher than that on the disordered surfaces (*** $p < 0.001$, see figure). Showing that the cell behaviour of the bone forming cells can be further enhanced by controlling the orientation of the crystals at the nano-scale. Taken from [73] In that paper ordered and disordered are the terms used in their research, but here we refer to this as aligned and misaligned to differentiate from crystalline structure. 9

1.6 Cell density (light grey), on etched SS surfaces, and aligned and misaligned FAp surfaces. (SS and aligned, $p < 0.01$). Quantitative analysis of the optical band density of osteocalcin expression (dark grey), by the ratio of OCN/GAPDH using ImageJ program (NIH). Samples; stainless steel (SS), misaligned, aligned and control. Samples studied after 7 days of osseointegration for 7 weeks are accompanied by OI. Showing that Aligned nano-rods show a good trade off between the number of cells produced and the amount of osteocalcin produced when compared to non-coated and misaligned coatings. Adapted from [74]. 10

1.7 Articles released for different methods for apatite production. Out of all methods, the precipitation method is currently the most popular method for research. Typically owed to its low energy of production requirements when compared to its contemporaries. [76] 12

2.1 Vertical symmetry elements of the space group $P6_3/m$. The dashed lines indicate the apatite unit cells with the c-axis out of the plane of the diagram. There are also horizontal mirror planes at $z = \frac{1}{3}$ and $\frac{3}{4}$, and numerous centres of symmetry. [84] 17
2.2 Depicting a view looking down the hydroxyl column of calcium hydroxyapatite. Here we see the arrangement of the Ca I, Ca II, the P atoms and the OH group which could be substituted by F, or Cl. [87]. 18
2.3 Diagram of the arrangement of calcium and hydroxyl ions in calcium hydroxyapatite. This schematic shows the relationship between the hexagonal cell described (in previous figure) and the hexagonal crystallographic unit cell, which is shown in heavier lines The hydroxyl column, calcium II triangles a, b, and c-axis directions are shown [87, 97]. 19
2.4 Solubility isotherms of CaP phases in a system $Ca(OH)^{2-}$ $H_3PO_4^-$ H_2O at 37 °C calculated with the program RAMESES. Showing the connection between pH of solution and the Ca concentration with that of phase transition between the calcium phosphate phases. Taken from [112]. . . . 24

3.1 X-ray spectrum of molybdenum as a function of applied voltage (schematic). Line widths not to scale [118]. 31
3.2 X-ray spectrum of molybdenum as a function of applied voltage (schematic). Spectrum of Mo at 35 kV (schematic). Line widths not to scale [118]. . . 32
3.3 Electronic transitions in an atom (schematic) emission processes indicated by arrows [118] 34
3.4 Atomic energy levels (schematic). Excitation and emission processes indicated by arrows. The insert at top shows the fine structure of the L state [118]. 35
3.5 Comparison of the spectra of copper radiation (a) before and (b) after passage through a nickel filter (schematic). The dashed line is the mass absorbance coefficient of nickel. 36
3.6 The conventional unit cells of the 14 Bravis lattices, with the lattice points represented by spheres. The primitive trigonal lattice is the same as the hexagonal lattice[118]. 39
3.7 Miller indices of lattice planes. The distance d is the plane spacing [118]. . 40
3.8 illustration of Bragg's law for crystal diffraction. A reflection will occur if $n\lambda = 2d\sin\theta$. 40
3.9 Primary layout of a neutron or X-ray diffractometer. 42
3.10 Sideways divergence of either the incident or scattered beam can be controlled using Soller slits (shown in the right-hand photograph above) inserted in the X-ray beam path. These consist of a set of fine parallel foils which prevent angular divergence of the beam out of the $\theta/2\theta$ plane. This gives a less asymmetric and narrower peak shape, especially at low scattering angles. 44
3.11 Example of the change in resolution with the change in Q, PDF around the nearest neighbour peaks of $ZnSe_{0.5}$ $Te_{0.5}$. The solid line corresponds to terminating at $Q_{max} = 40$ Å^{-1} clearly showing the two bond lengths Zn-Se and Zn-Te which differ by $\Delta r = 0.14$ Å. The dotted line shows the PDF obtained from the same data terminated at $Q_{\max} = 17$ Å^{-1}. In this case the peak split is smeared out, taken from [148]. 57

3.12 PDF comparison of the same material with different short range order, (a) shows a random distribution of vacancies and (b) preferred ordering in x and y directions. Panel (c) shows the corresponding PDFs for the random distribution (filled circles) and the short-range ordered distribution (solid line). The difference is shown below. Taken from [148]. 58
3.13 PDF, G(r), of $ZnSe_{1-x}Te_x$. Clearly showing two regions in which atom pair peaks show changes with a change in composition. Taken from [148]. 60
3.14 Normalized height PDF of $La_{1-x}Ca_xMnO_3$ at r = 2.75 Å vs. temperature for various conditions of x. (a) $x = 0.25$, (b) $x = 0.21$ and (c) $x = 0.12$. Insets show the resistivity vs. temperature for the same samples. The arrows indicate the MI transition temperature in both the insets an main panel. Taken from [148]. 61
3.15 Graphic representation of (a) atoms within a material, (b) representing bonding pairs as existing on a circumference a distance r_i from the origin, each bonding pair is represented by a series of Dirac delta functions, (c) integration from $r = 0$ to $r = \infty$, (d) Spherical averaging for 3D modelling. 62
3.16 Example pair distribution function, $g(r)$, for supercooled liquid nickel shown in 1-dimensional (top) and 2-dimensional (bottom) representations. Derived from data shown in [153, 154]. 63
3.17 Molecular dynamics simulation of (a) aggregates after 5 ns: (b) detail of one of the Posner-like clusters formed with formula $Ca_9(PO_4)_6$. Colour key Ca: light blue, P: green, O: red, atoms not forming Posner's clusters: grey. Taken from [166]. 68

4.1 SEM of substrate surfaces, (a) HAp, (b) Ti, (c) etched-HAp, and (d) etched-Ti, before incubation. Inserts showing a higher magnification of the same material. Scale bars for (a), (c) and (d) were 10 μm, in both, the inserts were 2 μm. For (b) the scale bar is 3 μm. 80
4.2 DECTAKX 1000 x 1000 μm map scans showing, (a) Ti, and (b) ETi surfaces. Positive and negative values indicate surface hight with respect to colour, red - elevated above mid point, blue - below base level. 81
4.3 DECTAKX 1000 x 1000 μm map scans showing, (a) Ti, and (b) ETi surfaces. Positive and negative values indicate surface hight with respect to colour, red - elevated above mid point, blue - below base level. Distinct ridge seen could be a grain boundary, however, the DECTAKX optical resolution does not permit the indication of such surface features. 81
4.4 SEM images of typical precipitates formed of unbuffered samples, magnification $80,000\times$. 82
4.5 SEM images of typical precipitates formed of buffered samples, magnification $80,000\times$. 82
4.6 SEM comparison of NRS morphology formed on ETi in buffered solution and incubated at 5°C, 21°C, 37°C and 54°C. Images shown below are magnifications of pictures above. Scale bar (between internal white bars); top row: 100 μm, 1mm, 100 μm, 20 μm; bottom row: 5 μm, 1 μm, 10 μm, 1 μm. 83

4.7 Catalogue of morphologies found to date, Scale bars as follows: (a) 300 μm; (b) 3 μm; (c) 2 μm; (d) 1 μm; (e) 2 μm; (f) 2 μm; (g) 1 μm; (h) 5 μm; (i) 1 μm; (j) 1 μm ; (k) 1 μm; (l) 5 μm; (m) 20 μm; (n) 100 μm; (o) 20 μm; (p) 1 μm; (q) 20 μm; (r) 1 μm; (s) 10 μm; (t) 10 μm; (u) 1 μm; (v) 5μm. 84
4.8 Morphologies found when incubated on (a) titanium, (b) etched-titanium, (c) HAp, (d) etched-HAp substrates while using unbuffered solution. NB: Connections between points are a function of the plotting software and do not represent a relationship between data points. 86
4.9 FTIR comparison of precipitate derived from unbuffered solution at different temperatures 88
4.10 XRD comparison of precipitate derived from unbuffered solution at different temperatures 89
4.11 NMR analysis of precipitated CaP nano crystals formed via wet chemical method in unbuffered solution. 89
4.12 Morphologies found when incubated on (a) titanium, (b) etched-titanium, (c) HAp, (d) etched-HAp substrates while using buffered solution. NB: Connections between points are a function of the plotting software and do not represent a relationship between data points. 92
4.13 Comparison of FTIR spectra from precipitate derived from buffered solution at different temperatures. 93
4.14 Comparison of XRD diffractograms from precipitate derived from buffered solution at different temperatures. 94
4.15 NMR analysis of precipitated CaP nano crystals formed via wet chemical method in buffered solution. 94
4.16 SEM images of pre-coated Ti samples before 7 day incubation. Scale bars for (a),(d), (e), and (g) are 1 μm; (b), (c), (f), and (h) are 2 μm. 97
4.17 SEM images of pre-coated Ti samples after 7 day incubation. Scale bars for (a), (b), (c), (e), (f), and (g) are 2μm, (d) 5 μm, and (h) 3 μm. 97

5.1 SEM showing the surface morphology of mineral that has been precipitated on Ti surfaces at (a) 21 °C, and (b) 70 °C, scale 1 μm. SEM of ordered apatite on HA surfaces. Incubated at , (c) 21 °C, showing a regular hexagonal cross-section with width range from 276–341 nm, and (d) 70 °C, showing an irregular hexagonal cross-section, scale 6.6 μm. (e) Uncoated 20% porous HAp substrate 113
5.2 ImageJ analyse of 21°C and 70°C compared with desired biomineral dimensions. As can be seen, there are a range of cross-sectional sizes in crystals formed at 70^oC where as the range in cross-section is much smaller in those formed at 21°C. 114
5.3 XRD of powders formed at 24 hour time points over seven days and incubated at 70°C. 115
5.4 FTIR of powders formed at 24 hour time points over seven days and incubated at 70°C. 116
5.5 NMR of powders formed at 24 hour time points over seven days and incubated at 70°C. 116
5.6 a-axis unit cell parameter plotted against time. 117

5.7 SEM of 20% HA substrate incubated at 70°C for seven days. Days 0 to 5 (a) to (f) scale bar: 2 μ m, day 6 (g) and 7 (h) and 8 (i) have scale bars 10 μm and 1 μm respectively. 118
5.8 Analysis of hexagonal crystal width, measured from furthest most corners. The width range is as follows: day 1 (290–163 nm), day 2 (1,109–305 nm), day 3 (527–366 nm), day 4 (489–275 nm), day 5 (594–257 nm), day 6 (287–73 nm), and day 7 (329–76 nm). Average crystal s size (Ave.size) derived from Rietveld refinement, an uncertaintly of 0.69 was calculated. 119
5.9 EDX analysis from atomic %, Ca/P ratio of disordered crystals incubated over seven days. Calculated uncertainty of 0.01 is not visible on figure. Interconnected misslaligined, see Fig. 5.7(g) 119
5.10 SEM of nano crystals grown on 20% porous HAp. (a) day 4, (b) day 5, and (c) day 6. Scale, 4μ m, 2μ m and 5μ m, respectively. 121
5.11 ^{19}F MAS NMR of time points between day 6 and 7 with 70°C samples. . 121
5.12 XRD of powders formed at 24 hour time points over seven days and incubated at 21°C. 122
5.13 FTIR of powders formed at 24 hour time points over seven days and incubated at 21 °C. 124
5.14 NMR of powders formed at 24 hour time points over seven days and incubated at 21 °C. 124
5.15 a axis unit cell parameter plotted against time for samples incubated at 21°C. 126
5.16 SEM of mineral formed on HAp substrates at 24 hour time points over seven days and incubated at 21°C. Days 0 to 6 (a) to (f) scale bar: 2 μ m, day 6 (g) scale bar 5 μm, day 7 (h) has Scale bar of 1 μm (insert 40 μm) and day 8 (i) has a scale bars of 2 μm. 127
5.17 SEM of mineral formed on HAp substrates on day 1 and incubated at 21°C, as seen in Fig. 5.16. Scale bar 10 μm. 128
5.18 Size analysis of morphologies seen at 24 hour time points over seven days and incubated at 21°C. Average apatite particle size (AAPS) and average CaF_2 particle size (ACPS). 128
5.19 EDX, Ca/P ratios of powders formed at 24 hour time points over seven days and incubated at 21°C. $\sigma = 0.01$ 129

6.1 FAp unit cell generated by crystal maker. Atoms differentiated as follow, oxygen (red), calcium (blue), phosphorous (grey), and fluorine (green). . . 148
6.2 Pair distribution function of powders formed at 24 hour time points over seven days and incubated at 70°C. 149
6.3 Pair distribution function of powders formed at 24 hour time points over seven days and incubated at 21°C. 149
6.4 Example of PDFfit2 fitting performed on s typical G(r) of 70°C sample. Data (circle), refinement (red line), and difference (black line). 152
6.5 Example of PDFfit2 fitting performed on s typical G(r) of 70°C sample. Data (circle), refinement (red line), and difference (black line). 152
6.6 Comparison between GULP and a typical GUDRUNx generated pair distribution functions. As can be seen, right, noise can be seen in the experimental GUDRUNx derived data, most importantly a peak at 1.89 Å. 153

6.7 Fractional coordinates of structures derived from PDFfit2 refinement of data from samples incubated at 70°C, Fig. 6.2. 155
6.8 Normalised Cu-source X-ray diffractograms, of freeze dried precipitate collected at time points 4 mins and 11 mins (day 6) were refined by Rietveld refinement. X (observed), red (calculated), green (observed–calculated). 157
6.9 Pair distribution function of powders formed from 2 mins to 48 hours. Produced with GUDRUNx 158
6.10 Comparison between disordered FAp and crystalline FAp structure simulated using DLPOLY 4. (right) MD simulated structure, (middle) G(r) of simulated structure, and (right) GUDRUNx derived G(r) = $\sum g(r)$. . . 159
6.11 Starting configuration for DLPOLY molecular dynamics simulation. . . . 160
6.12 Molecular dynamics simulation formation of disordered calcium phosphate in solution, (a) full system, and (b) disordered calcium phosphate formed in simulation. Yellow line showing clearly the boundary between the apatite surface and the solution. 161
6.13 Molecular dynamics simulation of crystallisation at surface, (a) full system, and (b) 'crystallisation' formed on the surface. Yellow line showing clearly the boundary behind the apatite surface and the solution. 161

1 XRD fitting of CaF_2 and FAp phases using GSAS (EXPgui). 168
2 NMR data deconvoluted using DMFIT method. Clearly showing the five peaks that are identified and how small the first two peaks are in comparison to the other three. 168
3 NMR data deconvoluted using DMFIT method. Clearly showing deconvoluted peaks for unbuffered samples incubated at 5°C. 169
4 NMR data deconvoluted using DMFIT method. Clearly showing deconvoluted peaks for unbuffered samples incubated at 21°C. 169
5 NMR data deconvoluted using DMFIT method. Clearly showing deconvoluted peaks for unbuffered samples incubated at 37°C. 169
6 NMR data deconvoluted using DMFIT method. Clearly showing deconvoluted peaks for unbuffered samples incubated at 54°C. 170
7 NMR data deconvoluted using DMFIT method. Clearly showing deconvoluted peaks for unbuffered samples incubated at 70°C. 170
8 NMR data deconvoluted using DMFIT method. Clearly showing deconvoluted peaks for unbuffered samples incubated at 90°C. 170
9 NMR data deconvoluted using DMFIT method. Clearly showing deconvoluted peaks for buffered samples incubated at 5°C. 171
10 NMR data deconvoluted using DMFIT method. Clearly showing deconvoluted peaks for buffered samples incubated at 21°C. 171
11 NMR data deconvoluted using DMFIT method. Clearly showing deconvoluted peaks for buffered samples incubated at 37°C. 171
12 NMR data deconvoluted using DMFIT method. Clearly showing deconvoluted peaks for buffered samples incubated at 54°C. 172
13 NMR data deconvoluted using DMFIT method. Clearly showing deconvoluted peaks for buffered samples incubated at 70°C. 172
14 NMR data deconvoluted using DMFIT method. Clearly showing deconvoluted peaks for buffered samples incubated at 90°C. 172

15 NMR data deconvoluted using DMFIT method. Clearly showing deconvoluted peaks for unbuffered samples incubated at 21°C for day 1. 173
16 NMR data deconvoluted using DMFIT method. Clearly showing deconvoluted peaks for unbuffered samples incubated at 21°C for day 2. 173
17 NMR data deconvoluted using DMFIT method. Clearly showing deconvoluted peaks for unbuffered samples incubated at 21°C for day 3. 174
18 NMR data deconvoluted using DMFIT method. Clearly showing deconvoluted peaks for unbuffered samples incubated at 21°C for day 4. 174
19 NMR data deconvoluted using DMFIT method. Clearly showing deconvoluted peaks for unbuffered samples incubated at 21°C fo day 5. 174
20 NMR data deconvoluted using DMFIT method. Clearly showing deconvoluted peaks for unbuffered samples incubated at 21°C for day 6. 175
21 NMR data deconvoluted using DMFIT method. Clearly showing deconvoluted peaks for unbuffered samples incubated at 21°C for day 7. 175
22 NMR data deconvoluted using DMFIT method. Clearly showing deconvoluted peaks for unbuffered samples incubated at 70°C for day 1. 176
23 NMR data deconvoluted using DMFIT method. Clearly showing deconvoluted peaks for unbuffered samples incubated at 70°C for day 2. 176
24 NMR data deconvoluted using DMFIT method. Clearly showing deconvoluted peaks for unbuffered samples incubated at 70°C for day 3. 177
25 NMR data deconvoluted using DMFIT method. Clearly showing deconvoluted peaks for unbuffered samples incubated at 70°C for day 4. 177
26 NMR data deconvoluted using DMFIT method. Clearly showing deconvoluted peaks for unbuffered samples incubated at 70°C fo day 5. 177
27 NMR data deconvoluted using DMFIT method. Clearly showing deconvoluted peaks for unbuffered samples incubated at 70°C for day 6. 178
28 NMR data deconvoluted using DMFIT method. Clearly showing deconvoluted peaks for unbuffered samples incubated at 70°C for day 7. 178
29 NMR data deconvoluted using DMFIT method. Clearly showing deconvoluted peaks for unbuffered samples incubated at 70°C for day 6.1. . . . 179
30 NMR data deconvoluted using DMFIT method. Clearly showing deconvoluted peaks for unbuffered samples incubated at 70°C for day 6.2. . . . 179
31 NMR data deconvoluted using DMFIT method. Clearly showing deconvoluted peaks for unbuffered samples incubated at 70°C for day 6.3. . . . 180
32 NMR data deconvoluted using DMFIT method. Clearly showing deconvoluted peaks for unbuffered samples incubated at 70°C for day 6.4. . . . 180
33 NMR data deconvoluted using DMFIT method. Clearly showing deconvoluted peaks for unbuffered samples incubated at 70°C fo day 6.5. . . . 180
34 XRD using Rietveld refinement GSAS method. Clearly showing fitting of two phases to experimentally derived XRD peaks for unbuffered incubated at 5°C. 181
35 XRD using Rietveld refinement GSAS method. Clearly showing fitting of two phases to experimentally derived XRD peaks for unbuffered incubated at 21°C. 181
36 XRD using Rietveld refinement GSAS method. Clearly showing fitting of two phases to experimentally derived XRD peaks for unbuffered incubated at 37°C. 182

37 XRD using Rietveld refinement GSAS method. Clearly showing fitting of two phases to experimentally derived XRD peaks for unbuffered incubated at 54°C. . . . 182
38 XRD using Rietveld refinement GSAS method. Clearly showing fitting of two phases to experimentally derived XRD peaks for unbuffered incubated at 70°C. . . . 182
39 XRD using Rietveld refinement GSAS method. Clearly showing fitting of two phases to experimentally derived XRD peaks for unbuffered incubated at 90°C. . . . 183
40 XRD using Rietveld refinement GSAS method. Clearly showing fitting of two phases to experimentally derived XRD peaks for buffered incubated at 5°C. . . . 184
41 XRD using Rietveld refinement GSAS method. Clearly showing fitting of two phases to experimentally derived XRD peaks for buffered incubated at 21°C. . . . 184
42 XRD using Rietveld refinement GSAS method. Clearly showing fitting of two phases to experimentally derived XRD peaks for buffered incubated at 37°C. . . . 185
43 XRD using Rietveld refinement GSAS method. Clearly showing fitting of two phases to experimentally derived XRD peaks for buffered incubated at 54°C. . . . 185
44 XRD using Rietveld refinement GSAS method. Clearly showing fitting of two phases to experimentally derived XRD peaks for buffered incubated at 70°C. . . . 185
45 XRD using Rietveld refinement GSAS method. Clearly showing fitting of two phases to experimentally derived XRD peaks for unbuffered incubated at 90°C. . . . 186
46 XRD using Rietveld refinement GSAS method. Clearly showing fitting of two phases to experimentally derived XRD peaks for unbuffered samples incubated at 21°C for day 1. Phase 1 shown in pink (apatite), phase 2 shown in blue (Calcium fluoride), and difference graphs shown below in dark blue. . . . 187
47 XRD using Rietveld refinement GSAS method. Clearly showing fitting of two phases to experimentally derived XRD peaks for unbuffered samples incubated at 21°C for day 2. Phase 1 shown in pink (apatite), phase 2 shown in blue (Calcium fluoride), and difference graphs shown below in dark blue. . . . 187
48 XRD using Rietveld refinement GSAS method. Clearly showing fitting of two phases to experimentally derived XRD peaks for unbuffered samples incubated at 21°C for day 3. Phase 1 shown in pink (apatite), phase 2 shown in blue (Calcium fluoride), and difference graphs shown below in dark blue. . . . 188
49 XRD using Rietveld refinement GSAS method. Clearly showing fitting of two phases to experimentally derived XRD peaks for unbuffered samples incubated at 21°C for day 4. Phase 1 shown in pink (apatite), phase 2 shown in blue (Calcium fluoride), and difference graphs shown below in dark blue. . . . 188

50 XRD using Rietveld refinement GSAS method. Clearly showing fitting of two phases to experimentally derived XRD peaks for unbuffered samples incubated at 21°C for day 5. Phase 1 shown in pink (apatite), phase 2 shown in blue (Calcium fluoride), and difference graphs shown below in dark blue. . . . 189
51 XRD using Rietveld refinement GSAS method. Clearly showing fitting of two phases to experimentally derived XRD peaks for unbuffered samples incubated at 21°C for day 6. Phase 1 shown in pink (apatite), phase 2 shown in blue (Calcium fluoride), and difference graphs shown below in dark blue. . . . 189
52 XRD using Rietveld refinement GSAS method. Clearly showing fitting of two phases to experimentally derived XRD peaks for unbuffered samples incubated at 21°C for day 7. Phase 1 shown in pink (apatite), phase 2 shown in blue (Calcium fluoride), and difference graphs shown below in dark blue. . . . 189
53 XRD using Rietveld refinement GSAS method. Clearly showing fitting of two phases to experimentally derived XRD peaks for unbuffered samples incubated at 70°C for day 2. Phase 1 shown in pink (apatite), phase 2 shown in blue (Calcium fluoride), and difference graphs shown below in dark blue. . . . 190
54 XRD using Rietveld refinement GSAS method. Clearly showing fitting of two phases to experimentally derived XRD peaks for unbuffered samples incubated at 70°C for day 3. Phase 1 shown in pink (apatite), phase 2 shown in blue (Calcium fluoride), and difference graphs shown below in dark blue. . . . 190
55 XRD using Rietveld refinement GSAS method. Clearly showing fitting of two phases to experimentally derived XRD peaks for unbuffered samples incubated at 70°C for day 4. Phase 1 shown in pink (apatite), phase 2 shown in blue (Calcium fluoride), and difference graphs shown below in dark blue. . . . 191
56 XRD using Rietveld refinement GSAS method. Clearly showing fitting of two phases to experimentally derived XRD peaks for unbuffered samples incubated at 70°C for day 5. Phase 1 shown in pink (apatite), phase 2 shown in blue (Calcium fluoride), and difference graphs shown below in dark blue. . . . 191
57 XRD using Rietveld refinement GSAS method. Clearly showing fitting of two phases to experimentally derived XRD peaks for unbuffered samples incubated at 70°C for day 6. Phase 1 shown in pink (apatite), phase 2 shown in blue (Calcium fluoride), and difference graphs shown below in dark blue. . . . 192
58 XRD using Rietveld refinement GSAS method. Clearly showing fitting of two phases to experimentally derived XRD peaks for unbuffered samples incubated at 70°C for day 7. Phase 1 shown in pink (apatite), phase 2 shown in blue (Calcium fluoride), and difference graphs shown below in dark blue. . . . 192

List of Tables

2.1 Main calcium phosphate (CaP) salts. Taken from [76, 110] 22
2.2 Standard thermodynamic quantities and calculated solubility product constants of caps at 298.15 K (25 °C) 23

3.1 The seven lattice types as defined by symmetry constraints [131]. 38
3.2 Atomic composition of kapton tube. 45

4.1 Profilometry scans performed of substrates. 80
4.2 Rietveld refinement results for unbuffered samples incubated at the six temperatures. APS = average particle size. 87
4.3 Deconvolution of NMR data performed by DMFIT. Showing percentage abundance of each chemical shift value identified for unbuffered samples derived at each temperature. Average ppm values are here given. Unidentified contaminant (UC). 88
4.4 Rietveld refinement results for buffered samples incubated at the six temperatures. APS = average particle size. DCPD and apatite samples were refined with space group Cc and $P6_3/m$, respectively. 91
4.5 Deconvolution of NMR data performed by DMFIT. Showing percentage abundance of each chemical shift value identified for buffered samples derived at each temperature. Average ppm values are here given. Unidentified contaminant (UC). 92

5.1 Rietveld refinement results for samples incubated at 70 °C, and refined against FAp unit cell. $a = b$, and $\alpha = \beta = 90°$, $\gamma = 120°$ for all values, indicating a hexagonal unit cell. APS = average particle size. 115
5.2 Deconvolution of NMR data performed by DMFIT. Showing percentage abundance of each chemical shift value identified at 70°C. Average ppm values are here given. An unknown contaminant (UC) has been included for completeness. Uncertainty on ppm, $\sigma = \pm 0.03$. 118
5.3 Deconvolution of NMR data performed by DMFIT. Showing percentage abundance of each chemical shift value identified for 5 time points 6.1, 6.2, 6.3, 6.4, 6.5, between day 6 and 7 at 70°C. Average ppm values are here given. An unknown contaminant (UC) has been included for completeness. Uncertainty on ppm, $\sigma = \pm 0.03$. 122
5.4 Rietveld refinement results for samples incubated at 21 °C, and refined against FAp unit cell. $a = b$, and $\alpha = \beta = 90°$, $\gamma = 120°$ for all values, indicating a hexagonal unit cell. APS = average particle size. 123

5.5 Deconvolution of 21 °C NMR data performed by DMFIT. Showing percentage abundance of each chemical shift value identified. An unknown contaminant (UC) has been included for completeness. Average ppm values are here given. 125

6.1 Parameters for the inter-atomic potentials used in this study. Note, O_po has been used to differentiate oxygen that is found as part of the phosphate group from those O that are found else where in the apatite lattice. 147
6.2 Atomic bond (°) angle changes derived from experimental data refined with PDFfit2, and represented in Fig. 6.7. 154
6.3 Atomic bond length changes derived from experimental data refined with PDFfit2, and represented in Fig. 6.7. 154

Bibliography

[1] Sangeetha Raghavendra, Marjorie C Wood, and Thomas D Taylor. Early wound healing around endosseous implants: a review of the literature. *International Journal of Oral & Maxillofacial Implants*, 20(3), 2005.

[2] Slactive the surface with success built in. Straumann, 2005, last accessed 06-05-2016. https://www.straumann.com/content/dam/internet/straumann_xy/resources/clinical-reviews/SLActive%20Scientific%20summary%202006.pdf. Last accessed 6-5-2016.

[3] Neil Meredith. Assessment of implant stability as a prognostic determinant. *International Journal of Prosthodontics*, 11(5), 1998.

[4] Bertil Friberg, Lars Sennerby, Kerstin Gröndahl, Christina Bergström, Thomas Bäck, and Ulf Lekholm. On cutting torque measurements during implant placement: A 3-year clinical prospective study. *Clinical implant dentistry and related research*, 1(2):75–83, 1999.

[5] Vladimir Kokovic, Miroslav Vasovic, and Ebadullah Shafi. Assessment of primary implant stability of self-tapping implants using the resonance frequency analysis. *The Saudi Journal for Dental Research*, 5(1):35–39, 2014.

[6] A Wennerberg, T Albrektsson, and B Andersson. An animal study of cp titanium screws with different surface topographies. *Journal of Materials Science: Materials in Medicine*, 6(5):302–309, 1995.

[7] Per Åstrand, Hartmut Feldmann, Bo Engquist, Simon Dahlgren, Eva Engquist, and Kerstin Gröndahl. Marginal bone reaction to oral implants: a prospective comparative study of astra tech and brånemark system implants. *Clinical oral implants research*, 13(1):30–37, 2002.

[8] Daniel Steenberghe, Greet Mars, Marc Quirynen, Reinhilde Jacobs, and Ignace Naert. A prospective split-mouth comparative study of two screw-shaped self-tapping pure titanium implant systems. *Clinical oral implants research*, 11(3): 202–209, 2000.

[9] JM Martınez González, F Garcıa Sabán, J Ferrándiz Bernal, JC Gonzalo Lafuente, J Cano Sánchez, and C Barona Dorado. Removal torque and physico-chemical characteristics of dental implants etched with hydrofluoric and nitric acid. an experimental study in beagle dogs. *Med Oral Patol Oral Cir Bucal*, 11:E281–5, 2006.

[10] M Wong, J Eulenberger, R Schenk, and E Hunziker. Effect of surface topology on the osseointegration of implant materials in trabecular bone. *Journal of Biomedical Materials Research Part A*, 29(12):1567–1575, 1995.

[11] Sung-Am Cho and Kyung-Tae Park. The removal torque of titanium screw inserted in rabbit tibia treated by dual acid etching. *Biomaterials*, 24(20):3611–3617, 2003.

[12] Giovanna Orsini, Bartolomeo Assenza, Antonio Scarano, Maurizio Piattelli, and Adriano Piattelli. Surface analysis of machined versus sandblasted and acid-etched titanium implants. *International Journal of Oral & Maxillofacial Implants*, 15(6), 2000.

[13] Carlo Galli, Stefano Guizzardi, Giovanni Passeri, Desiree' Martini, Anna Tinti, Giovanni Mauro, and Guido Maria Macaluso. Comparison of human mandibular osteoblasts grown on two commercially available titanium implant surfaces. *Journal of periodontology*, 76(3):364–372, 2005.

[14] DL Cochran, RK Schenk, A Lussi, FL Higginbottom, and D Buser. Bone response to unloaded and loaded titanium implants with a sandblasted and acid-etched surface: a histometric study in the canine mandible. *Journal of biomedical materials research*, 40(1):1–11, 1998.

[15] Stefano Sivolella, Eriberto Bressan, Luiz A Salata, Zoraya A Urrutia, Niklaus P Lang, and Daniele Botticelli. Osteogenesis at implants without primary bone contact–an experimental study in dogs. *Clinical oral implants research*, 23(5): 542–549, 2012.

[16] S Anil, PS Anand, H Alghamdi, and JA Jansen. Dental implant surface enhancement and osseointegration. In *Implant dentistry-A rapidly evolving practice*. InTech, 2011.

[17] Charles A Babbush, John N Kent, and Dale J Misiek. Titanium plasma-sprayed (tps) screw implants for the reconstruction of the edentulous mandible. *Journal of Oral and Maxillofacial Surgery*, 44(4):274–282, 1986.

[18] Despina D Deligianni, N Katsala, S Ladas, D Sotiropoulou, J Amedee, and YF Missirlis. Effect of surface roughness of the titanium alloy ti–6al–4v on human bone marrow cell response and on protein adsorption. *Biomaterials*, 22(11):1241–1251, 2001.

[19] JY Martin, Z Schwartz, TW Hummert, DM Schraub, J Simpson, J Lankford, DD Dean, DL Cochran, and BD Boyan. Effect of titanium surface roughness on proliferation, differentiation, and protein synthesis of human osteoblast-like cells (mg63). *Journal of Biomedical Materials Research Part A*, 29(3):389–401, 1995.

[20] D Buser, RK Schenk, S Steinemann, JP Fiorellini, CH Fox, and H Stich. Influence of surface characteristics on bone integration of titanium implants. a histomorphometric study in miniature pigs. *Journal of Biomedical Materials Research Part A*, 25(7):889–902, 1991.

[21] Zimmer Dental. Tapered screw-vent implant system, performance thousands count on, case after case, Last accessed 19-9-16 (2008). URL http://www.zimmerdental.com/pdf/im_tsvimpsysbro7457.pdf.

[22] JD Bobyn, GJ Stackpool, SA Hacking, M Tanzer, and JJ Krygier. Characteristics of bone ingrowth and interface mechanics of a new porous tantalum biomaterial. *Bone & Joint Journal*, 81(5):907–914, 1999.

[23] Zimmer Dental. Trabecular metal material: Designed to enhance secondary stability through bone ingrowth, Last accessed 19-9-16 (2014). URL http://www.zimmerdental.com/pdf/tm_materialdentimpbrochure5986.pdf.

[24] Neil Meredith. Assessment of implant stability as a prognostic determinant. *International Journal of Prosthodontics*, 11(5), 1998.

[25] R Adell, U Lekholm, B Rockler, and PI Brånemark. Osseointegrated titanium fixtures in the treatment of edentulousness: A 15-year follow up study. *Int J Oral Surg*, 10(387):80077–4, 1981.

[26] Naichuan Su, Li Yue, Yunmao Liao, Wenjia Liu, Hai Zhang, Xin Li, Hang Wang, and Jiefei Shen. The effect of various sandblasting conditions on surface changes of dental zirconia and shear bond strength between zirconia core and indirect composite resin. *The journal of advanced prosthodontics*, 7(3):214–223, 2015.

[27] CM Piao, JE Lee, JY Koak, SK Kim, IC Rhyu, CH Han, Y Herr, and SJ Heo. Marginal bone loss around three different implant systems: radiographic evaluation after 1 year. *Journal of oral rehabilitation*, 36(10):748–754, 2009.

[28] Emanuel A Bratu, Moshik Tandlich, and Lior Shapira. A rough surface implant neck with microthreads reduces the amount of marginal bone loss: a prospective clinical study. *Clinical oral implants research*, 20(8):827–832, 2009.

[29] Wenju Wu and George H Nancollas. Kinetics of nucleation and crystal growth of hydroxyapatite and fluorapatite on titanium oxide surfaces. *Colloids and Surfaces B: Biointerfaces*, 10(2):87–94, 1997.

[30] Hassan Serhan, Michael Slivka, Todd Albert, and S.Daniel Kwak. Is galvanic corrosion between titanium alloy and stainless steel spinal implants a clinical concern? *The Spine Journal*, 4(4):379–387, 2004. ISSN 1529-9430. doi: http://dx.doi.org/10.1016/j.spinee.2003.12.004. URL http://www.sciencedirect.com/science/article/pii/S1529943003005801.

[31] John B Brunski. In vivo bone response to biomechanical loading at the bone/dental-implant interface. *Advances in dental research*, 13(1):99–119, 1999.

[32] Lawrence D Dorr, Roy Bloebaum, Janson Emmanual, and Russell Meldrum. Histologic, biochemical, and ion analysis of tissue and fluids retrieved during total hip arthroplasty. *Clinical orthopaedics and related research*, 261:82–95, 1990.

[33] Limin Sun, Christopher C Berndt, Karlis A Gross, and Ahmet Kucuk. Material fundamentals and clinical performance of plasma-sprayed hydroxyapatite coatings: a review. *Journal of Biomedical Materials Research Part A*, 58(5):570–592, 2001.

[34] SR Radin and P Ducheyne. Plasma spraying induced changes of calcium phosphate ceramic characteristics and the effect onin vitro stability. *Journal of materials science: Materials in medicine*, 3(1):33–42, 1992.

[35] Paul A Clark, Anthony Rodriguez, D Rick Sumner, Mohammad A Hussain, and Jeremy J Mao. Modulation of bone ingrowth of rabbit femur titanium implants by in vivo axial micromechanical loading. *Journal of applied physiology*, 98(5):1922–1929, 2005.

[36] YZ Yang, JM Tian, JT Tian, ZQ Chen, XJ Deng, and DH Zhang. Preparation of graded porous titanium coatings on titanium implant materials by plasma spraying. *Journal of Biomedical Materials Research Part A*, 52(2):333–337, 2000.

[37] Bonemaster nano-crystalline ha coating technology design rationale. BIOMET, 2005, Last accessed 13-09-2017. http://biometitaly.it/userfiles/files/Technologies/Bonemaster

[38] GB Schneider, H Perinpanayagam, M Clegg, R Zaharias, D Seabold, J Keller, and C Stanford. Implant surface roughness affects osteoblast gene expression. *Journal of dental research*, 82(5):372–376, 2003.

[39] Chang Yu-Liang, Daniel Lew, Joon B Park, and John C Keller. Biomechanical and morphometric analysis of hydroxyapatite-coated implants with varying crystallinity. *Journal of Oral and Maxillofacial Surgery*, 57(9):1096–1108, 1999.

[40] IMO Kangasniemi, CCPM Verheyen, EA Van der Velde, and K De Groot. In vivo tensile testing of fluorapatite and hydroxylapatite plasma-sprayed coatings. *Journal of Biomedical Materials Research Part A*, 28(5):563–572, 1994.

[41] Panjian Li. Biomimetic nano-apatite coating capable of promoting bone ingrowth. *Journal of Biomedical Materials Research Part A*, 66(1):79–85, 2003.

[42] Z Zyman, J Weng, X Liu, X Zhang, and Z Ma. Amorphous phase and morphological structure of hydroxyapatite plasma coatings. *Biomaterials*, 14(3):225–228, 1993.

[43] K De Groot. Ceramics of calcium phosphate, preparation and properties. *Bioceramlcs of calcium phosphate*, 1983.

[44] Karlis A Gross and Christopher C Berndt. Structural changes of plasma sprayed hydroxyapatite coatings during in-vitro testing. In *Characterization and Performance of Calcium Phosphate Coatings for Implants*. ASTM International, 1994.

[45] Suzanne H Maxian, Joseph P Zawadsky, and Michael G Dunn. Mechanical and histological evaluation of amorphous calcium phosphate and poorly crystallized hydroxyapatite coatings on titanium implants. *Journal of Biomedical Materials Research Part A*, 27(6):717–728, 1993.

[46] Joost Dick de Bruijn, YP Bovell, and CA Van Blitterswijk. Structural arrangements at the interface between plasma sprayed calcium phosphates and bone. *Biomaterials*, 15(7):543–550, 1994.

[47] Johan Karlsson, Gustav Sundell, Mattias Thuvander, and Martin Andersson. Atomically resolved tissue integration. *Nano Letters*, 14(8):4220–4223, 2014. doi: 10.1021/nl501564f. URL http://dx.doi.org/10.1021/nl501564f. PMID: 24989063.

[48] Johan Karlsson, Gustav Sundell, Mattias Thuvander, and Martin Andersson. Atomically resolved tissue integration. *Nano letters*, 14(8):4220–4223, 2014.

[49] JOSHUA J. JACOBS, JEREMY L. GILBERT, and ROBERT M. URBAN. Current concepts review–corrosion of metal orthopaedic implants*. *The Journal of Bone & Joint Surgery*, 80(2):268–82, 1998. ISSN 0021-9355. URL http://jbjs.org/content/80/2/268.

[50] J. Gallo, P. Kaminek, V. Ticha, P. Rihakova, and R. Ditmar. Particle disease. a comprehensive theory of periprosthetic osteolysis: A review. *Biomed. Papers*, 146 (2):21–28, 2002. ISSN 0021-9355.

[51] Karthikeyan Subramani and Waqar Ahmed. *Emerging nanotechnologies in dentistry: Processes, materials and applications*. William Andrew, 2011.

[52] Mamadou Diallo, Anita Street, Richard Sustich, Jeremiah Duncan, and Nora Savage. *Nanotechnology Applications for Clean Water: Solutions for Improving Water Quality*. William Andrew, 2009.

[53] DA Puleo and A Nanci. Understanding and controlling the bone–implant interface. *Biomaterials*, 20(23):2311–2321, 1999.

[54] Daniel Buser, Simone FM Janner, Julia-Gabriela Wittneben, Urs Brägger, Christoph A Ramseier, and Giovanni E Salvi. 10-year survival and success rates of 511 titanium implants with a sandblasted and acid-etched surface: A retrospective study in 303 partially edentulous patients. *Clinical implant dentistry and related research*, 14(6):839–851, 2012.

[55] Karthikeyan Subramani and Waqar Ahmed, editors. *Nanotechnology Applications for Clean Water: Solutions for Improving Water*. William Andrew;, 1st ed. edition, (Nov. 15 2011). 412 pages.

[56] Anita Street Mamadou Diallo, Richard Sustich, Jeremiah Duncan, and Nora Savage, editors. *Emerging Nanotechnologies in Dentistry: Processes, Materials and Applications (Micro and Nano Technologies*. William Andrew, 2nd ed. edition, 2014. 700 pages.

[57] Anna M. Sanna, Liene Molly, and Daniel van Steenberghe. Immediately loaded cad-cam manufactured fixed complete dentures using flapless implant placement procedures: A cohort study of consecutive patients. *The Journal of Prosthetic Dentistry*, 97(6):331–339, 2007. ISSN 0022-3913. doi: http://dx.doi.org/10.1016/S0022-3913(07)60021-3. URL http://www.sciencedirect.com/science/article/pii/S0022391307600213.

[58] Simonis, Pierre, Dufour, Thomas, Tenenbaum, and Henri. Long-term implant survival and success: a 10 -16-year follow-up of non-submerged dental implants. *Clinical Oral Implants Research*, 21(7):772–777, 2010. ISSN 1600-0501. doi: 10.1111/j.1600-0501.2010.01912.x. URL http://dx.doi.org/10.1111/j.1600-0501.2010.01912.x.

[59] Larry L Hench. Bioceramics: from concept to clinic. *Journal of the american ceramic society*, 74(7):1487–1510, 1991.

[60] Guaracilei Maciel Vidigal, Mario Groisman, Luiz Henrique Gregório, and Gloria de Almeida Soares. Osseointegration of titanium alloy and ha-coated implants in healthy and ovariectomized animals: a histomorphometric study. *Clinical oral implants research*, 20(11):1272–1277, 2009.

[61] D Buser, N Broggini, M Wieland, RK Schenk, AJ Denzer, DL Cochran, B Hoffmann, A Lussi, and SG Steinemann. Enhanced bone apposition to a chemically modified sla titanium surface. *Journal of dental research*, 83(7):529–533, 2004.

[62] Wenju Wu and George H Nancollas. Kinetics of nucleation and crystal growth of hydroxyapatite and fluorapatite on titanium oxide surfaces. *Colloids and Surfaces B: Biointerfaces*, 10(2):87–94, 1997.

[63] Hassan Serhan, Michael Slivka, Todd Albert, and S Daniel Kwak. Is galvanic corrosion between titanium alloy and stainless steel spinal implants a clinical concern? *The Spine Journal*, 4(4):379–387, 2004.

[64] Lawrence D Dorr, Roy Bloebaum, Janson Emmanual, and Russell Meldrum. Histologic, biochemical, and ion analysis of tissue and fluids retrieved during total hip arthroplasty. *Clinical orthopaedics and related research*, 261:82–95, 1990.

[65] Joshua J Jacobs, Jeremy L Gilbert, and Robert M Urban. Corrosion of metal orthopaedic implants. *JBJS*, 80(2):268–282, 1998.

[66] Jiří Gallo, Petr Kamínek, Vlastislava Tichá, Petra Řiháková, Ditmar Rudolf, et al. Particle disease. a comprehensive theory of periprosthetic osteolysis: a review. *Biomedical papers*, 146(2):21–28, 2002.

[67] Kyung Mi Woo, Victor J Chen, and Peter X Ma. Nano-fibrous scaffolding architecture selectively enhances protein adsorption contributing to cell attachment. *Journal of biomedical materials research Part A*, 67(2):531–537, 2003.

[68] Hae-Won Kim, Hyoun-Ee Kim, and Jonathan C Knowles. Fluor-hydroxyapatite sol–gel coating on titanium substrate for hard tissue implants. *Biomaterials*, 25 (17):3351–3358, 2004.

[69] IMO Kangasniemi, CCPM Verheyen, EA Van der Velde, and K De Groot. In vivo tensile testing of fluorapatite and hydroxylapatite plasma-sprayed coatings. *Journal of biomedical materials research*, 28(5):563–572, 1994.

[70] J Liu, TC Jin, S Chang, A Czajka-Jakubowska, and BH Clarkson. Adhesion and growth of dental pulp stem cells on enamel-like fluorapatite surfaces. *Journal of Biomedical Materials Research Part A*, 96(3):528–534, 2011.

[71] HFTZ Chen, Zhiyong Tang, Jun Liu, Kai Sun, S-R Chang, Mathilde C Peters, John F Mansfield, Agata Czajka-Jakubowska, and Brian H Clarkson. Acellular synthesis of a human enamel-like microstructure. *Advanced Materials*, 18(14): 1846–1851, 2006.

[72] Emil Roduner. Size matters: why nanomaterials are different. *Chemical Society Reviews*, 35(7):583–592, 2006.

[73] J Liu, TC Jin, S Chang, A Czajka-Jakubowska, and BH Clarkson. Adhesion and growth of dental pulp stem cells on enamel-like fluorapatite surfaces. *Journal of Biomedical Materials Research Part A*, 96(3):528–534, 2011.

[74] Jun Liu, Taocong Jin, Syweren Chang, Agata Czajka-Jakubowska, Zhaocheng Zhang, Jacques E Nör, and Brian H Clarkson. The effect of novel fluorapatite surfaces on osteoblast-like cell adhesion, growth, and mineralization. *Tissue Engineering Part A*, 16(9):2977–2986, 2010.

[75] Jun Liu, Taocong Jin, Syweren Chang, Agata Czajka-Jakubowska, Zhaocheng Zhang, Jacques E Nör, and Brian H Clarkson. The effect of novel fluorapatite surfaces on osteoblast-like cell adhesion, growth, and mineralization. *Tissue Engineering Part A*, 16(9):2977–2986, 2010.

[76] Mehdi Sadat-Shojai, Mohammad-Taghi Khorasani, Ehsan Dinpanah-Khoshdargi, and Ahmad Jamshidi. Synthesis methods for nanosized hydroxyapatite with diverse structures. *Acta biomaterialia*, 9(8):7591–7621, 2013.

[77] Eric Formo, Pedro HC Camargo, Byungkwon Lim, Majiong Jiang, and Younan Xia. Functionalization of zro2 nanofibers with pt nanostructures: The effect of surface roughness on nucleation mechanism and morphology control. *Chemical Physics Letters*, 476(1-3):56–61, 2009.

[78] Xiaobo Chen, Alireza Nouri, Yuncang Li, Jianguo Lin, Peter D Hodgson, and Cui'e Wen. Effect of surface roughness of ti, zr, and tizr on apatite precipitation from simulated body fluid. *Biotechnology and bioengineering*, 101(2):378–387, 2008.

[79] MU Nylen, ED Eanes, and K-Å Omnell. Crystal growth in rat enamel. *The Journal of cell biology*, 18(1):109–123, 1963.

[80] NC Blumenthal, AS Posner, and JM Holmes. Effect of preparation conditions on the properties and transformation of amorphous calcium phosphate. *Materials Research Bulletin*, 7(11):1181–1189, 1972.

[81] Stephen Mann. *Biomineralization: principles and concepts in bioinorganic materials chemistry*, volume 5. Oxford University Press on Demand, 2001.

[82] RA Young and WE Brown. Structures of biological minerals. In *Biological mineralization and demineralization*, pages 101–141. Springer, 1982.

[83] JC Elliott. The problems of the composition and structure of the mineral components of the hard tissues. *Clinical orthopaedics and related research*, 93:313–345, 1973.

[84] CA Beevers and DB McIntyre. The atomic stucture of fluor-apatite and its relation to that of tooth and bone material. *The Mineralogical magazine*, 27(194):254–257, 1946.

[85] C Michael B Henderson, AMT Bell, JM Charnock, Kevin S Knight, Richard F Wendlandt, David A Plant, and Wendy J Harrison. Synchrotron x-ray absorption spectroscopy and x-ray powder diffraction studies of the structure of johnbaumite [ca10 (aso4) 6 (oh, f) 2] and synthetic pb-, sr-and ba-arsenate apatites and some comments on the crystal chemistry of the apatite structure type in general. *Mineralogical Magazine*, 73(3):433–455, 2009.

[86] Racquel Zapanta LeGeros. *Page/About the Author/Contents/Preface/Acknowledgements*. Karger Publishers, 1991.

[87] Colin Robinson, RC Shore, SJ Brookes, S Strafford, SR Wood, and J Kirkham. The chemistry of enamel caries. *Critical Reviews in Oral Biology & Medicine*, 11 (4):481–495, 2000.

[88] Patricia M Dove, James J De Yoreo, and Steve Weiner. *Biomineralization*. Mineralogical Society of America, 2003.

[89] Edmund Baeuerlein. *Biomineralization: Progress in biology, molecular biology and application*. John Wiley & Sons, 2004.

[90] RM Wilson, JC Elliott, and SEP Dowker. Rietveld refinement of the crystallographic structure of human dental enamel apatites. *American mineralogist*, 84(9): 1406–1414, 1999.

[91] MV Colaco, RC Barroso, IM Porto, RF Gerlach, FN Costa, D Braz, R Droppa, and FB de Sousa. Synchrotron x-ray diffraction characterization of healthy and fluorotic human dental enamel. *Radiation Physics and Chemistry*, 81(10):1578–1585, 2012.

[92] JC Elliott. Monoclinic space group of hydroxyapatite. *Nature*, 230(11):72–72, 1971.

[93] J C_ Elliott, PE Mackie, and RA Young. Monoclinic hydroxyapatite. *Science*, 180 (4090):1055–1057, 1973.

[94] AS Posner, Alvin Perloff, and AF Diorio. Refinement of the hydroxyapatite structure. *Acta Crystallographica*, 11(4):308–309, 1958.

[95] K Sudarsanan, PE Mackie, and RA Young. Comparison of synthetic and mineral fluorapatite, ca5 (po4) 3f, in crystallographic detail. *Materials Research Bulletin*, 7(11):1331–1337, 1972.

[96] Me I Kay, RA Young, and AS Posner. Crystal structure of hydroxyapatite. *Nature*, 204:1050, 1964.

[97] T Ichijo, Y Yamashita, and T Terashima. Observations on the structural features and characteristics of biological apatite crystals. 2. observation on the ultrastructure of human enamel crystals. *The Bulletin of Tokyo Medical and Dental University*, 39(4):71–80, 1992.

[98] G MacLennan and CA Beevers. The crystal structure of monocalcium phosphate monohydrate, ca (h2po4) 2. h2o. *Acta Crystallographica*, 9(2):187–190, 1956.

[99] DW t JONES and DWJ Cruickshank. The crystal structures of two calcium orthophosphates: Cahpo4 and ca (h2po4) 2· h2o. *Zeitschrift für Kristallographie-Crystalline Materials*, 116(1-6):101–125, 1961.

[100] B Dickens, E Prince, LW Schroeder, and WE Brown. Ca (h2po4) 2, a crystal structure containing unusual hydrogen bonding. *Acta Crystallographica Section B: Structural Crystallography and Crystal Chemistry*, 29(10):2057–2070, 1973.

[101] DW Jones and JAS Smith. 268. the structure of brushite, cahpo 4, 2h 2 o. *Journal of the Chemical Society (Resumed)*, pages 1414–1420, 1962.

[102] CA Beevers. The crystal structure of dicalcium phosphate dihydrate, cahpo4. 2h2o. *Acta Crystallographica*, 11(4):273–277, 1958.

[103] JG Rabatin, RH Gale, and AE Newkirk. The mechanism and kinetics of the dehydration of calcium hydrogen phosphate dihydrate. *The Journal of Physical Chemistry*, 64(4):491–493, 1960.

[104] MICHELE Catti, GIOVANNI Ferraris, and SA Mason. Low-temperature ordering of hydrogen atoms in cahpo4 (monetite): X-ray and neutron diffraction study at 145 k. *Acta Crystallographica Section B: Structural Crystallography and Crystal Chemistry*, 36(2):254–259, 1980.

[105] Tadashi Kawai, Seishi Echigo, Keiko Matsui, Yuji Tanuma, Tetsu Takahashi, Osamu Suzuki, and Shinji Kamakura. First clinical application of octacalcium phosphate collagen composite in human bone defect. *Tissue Engineering Part A*, 20 (7-8):1336–1341, 2014.

[106] M Mathew, LW Schroeder, B Dickens, and WE Brown. The crystal structure of α-ca3 (po4) 2. *Acta Crystallographica Section B: Structural Crystallography and Crystal Chemistry*, 33(5):1325–1333, 1977.

[107] AL Mackay. A preliminary examination of the structure of α-ca3 (po4) 2. *Acta Crystallographica*, 6(8-9):743–744, 1953.

[108] B Dickens, LW Schroeder, and WE Brown. Crystallographic studies of the role of mg as a stabilizing impurity in β-ca3 (po4) 2. the crystal structure of pure β-ca3 (po4) 2. *Journal of Solid State Chemistry*, 10(3):232–248, 1974.

[109] Stephen Mann, editor. *Structure and Chemistry of the Apatites and Other Calcium Orthophosphates*. Oxford University Press, illustrated, reprint. edition, (2001). 198 pages.

[110] Charles YC Pak, Edward D Eanes, and Belle Ruskin. Spontaneous precipitation of brushite in urine: evidence that brushite is the nidus of renal stones originating as calcium phosphate. *Proceedings of the National Academy of Sciences*, 68(7): 1456–1460, 1971.

[111] Haifeng Chen, Kai Sun, Zhiyong Tang, Robert V Law, John F Mansfield, Agata Czajka-Jakubowska, and Brian H Clarkson. Synthesis of fluorapatite nanorods and nanowires by direct precipitation from solution. *Crystal growth & design*, 6 (6):1504–1508, 2006.

[112] James Cornelis Elliott. *Structure and chemistry of the apatites and other calcium orthophosphates*, volume 18. Elsevier, 2013.

[113] ED Eanes and JL Meyer. The maturation of crystalline calcium phosphates in aqueous suspensions at physiologic ph. *Calcified tissue research*, 23(1):259–269, 1977.

[114] Jørgen Christoffersen, Margaret R Christoffersen, Wiktor Kibalczyc, and Flemming A Andersen. A contribution to the understanding of the formation of calcium phosphates. *Journal of crystal growth*, 94(3):767–777, 1989.

[115] MR Christoffersen, J Christoffersen, and W Kibalczyc. Apparent solubilities of two amorphous calcium phosphates and of octacalcium phosphate in the temperature range 30–42 °c. *Journal of Crystal Growth*, 106(2-3):349–354, 1990.

[116] Yu-Ju Wu, Yao-Hung Tseng, and Jerry CC Chan. Morphology control of fluorapatite crystallites by citrate ions. *Crystal Growth & Design*, 10(10):4240–4242, 2010.

[117] Vault Dweller. 1.3 vats 1.4 companions 2 plot 2.1 setting 2.2 story.

[118] Bernard Dennis Cullity and John W Weymouth. Elements of x-ray diffraction. *American Journal of Physics*, 25(6):394–395, 1957.

[119] Johann Kepler. *Strena, seu de NiVe sexangula*. 1966.

[120] Alexey Stakhov. *The mathematics of harmony: from Euclid to contemporary mathematics and computer science*, volume 22. World Scientific, 2009.

[121] Edward Harrington Lockwood and Robert Hugh Macmillan. *Geometric symmetry*. CUP Archive, 1978.

[122] Peter Engel. *Geometric crystallography: an axiomatic introduction to crystallography*. Springer Science & Business Media, 2012.

[123] Manijeh Razeghi. *Fundamentals of solid state engineering*. Springer Science & Business Media, 2009.

[124] André Authier. *Early days of X-ray crystallography*. OUP Oxford, 2013.

[125] Christopher Hammond and Christopher Hammond. *Basics of crystallography and diffraction*, volume 214. Oxford, 2001.

[126] Nicolaus Steno. 1669: De solido intra solidum naturaliter contento dissertationis prodromus. *Florence, 78p*, 1916.

[127] Herbert Percy Whitlock. *René Just Haüy and His Influence*. University of the State of New York, 1919.

[128] René-Just Haüy. *Essai d'une theorie sur la structure des crystaux, appliquee a plusieurs genres de substances crystallisees; par M. l'abbe Hauy.*. chez Gogue & Nee de La Rochelle, libraires, quai des Augustins, pres le pont Saint-Michel, 1784.

[129] Henk Kubbinga. a tribute to max von laue. *Europhysics News*, 43(6):20–23, 2012.

[130] Patrick J McNally. Techniques: 3d imaging of crystal defects. *Nature*, 496(7443): 37–38, 2013.

[131] Martin T Dove. *Structure and dynamics: an atomic view of materials*, volume 1. Oxford University Press, 2003.

[132] Auguste Bravais and Léonce Élie de Beaumont. *Etudes cristallographiques: Mémoire sur les systèmes formés par des points distribués régulièrement sur un plan ou dans l'espace*. Gauthiers-Villars, 1866.

[133] W Friedrich, P Knipping, and Mvon Laue. Sitzungsber. math. phys. kl. k. *Bayer. Akad. Wiss. München*, pages 303–322, 1912.

[134] William Hallowes Miller. *A treatise on crystallography*. For J. & JJ Deighton, 1839.

[135] Bob B He. *Two-dimensional X-ray diffraction*. John Wiley & Sons, 2011.

[136] William Henry Bragg and William Lawrence Bragg. The reflection of x-rays by crystals. *Proceedings of the Royal Society of London. Series A, Containing Papers of a Mathematical and Physical Character*, 88(605):428–438, 1913.

[137] AW Hull. A new method of chemical analysis. *Journal of the American Chemical Society*, 41(8):1168–1175, 1919.

[138] G Caglioti, A t Paoletti, and FP Ricci. Choice of collimators for a crystal spectrometer for neutron diffraction. *Nuclear Instruments*, 3(4):223–228, 1958.

[139] Alan Hewat, WI David, and L van Eijck. Hugo rietveld (1932–2016). *Journal of Applied Crystallography*, 49(4):1394–1395, 2016.

[140] HaM Rietveld. A profile refinement method for nuclear and magnetic structures. *Journal of applied Crystallography*, 2(2):65–71, 1969.

[141] J Cockcroft. R-factors, Last accessed 17-04-18 (1997 - 2006). URL http://pd.chem.ucl.ac.uk/pdnn/refine1/rfacs.htm.

[142] Ramachandran Saravanan and M Prema Rani. *Metal and Alloy Bonding-An Experimental Analysis: Charge Density in Metals and Alloys*. Springer Science & Business Media, 2011.

[143] WA Dollase. Correction of intensities for preferred orientation in powder diffractometry: application of the march model. *Journal of Applied Crystallography*, 19 (4):267–272, 1986.

[144] H-J Bunge. *Texture analysis in materials science: mathematical methods*. Elsevier, 2013.

[145] Alan K Soper and Emma R Barney. Extracting the pair distribution function from white-beam x-ray total scattering data. *Journal of Applied Crystallography*, 44(4): 714–726, 2011.

[146] Takeshi Egami and Simon JL Billinge. *Underneath the Bragg peaks: structural analysis of complex materials*, volume 16. Elsevier, 2003.

[147] Matthew G Tucker, David A Keen, Martin T Dove, Andrew L Goodwin, and Qun Hui. Rmcprofile: reverse monte carlo for polycrystalline materials. *Journal of Physics: Condensed Matter*, 19(33):335218, 2007.

[148] Th Proffen, SJL Billinge, T Egami, and D Louca. Structural analysis of complex materials using the atomic pair distribution function?a practical guide. *Zeitschrift für Kristallographie-Crystalline Materials*, 218(2):132–143, 2003.

[149] DA Keen, MG Tucker, and MT Dove. Reverse monte carlo modelling of crystalline disorder. *Journal of Physics: Condensed Matter*, 17(5):S15, 2005.

[150] PF Peterson, M Gutmann, Th Proffen, and SJL Billinge. Pdfgetn: a user-friendly program to extract the total scattering structure factor and the pair distribution function from neutron powder diffraction data. *Journal of Applied Crystallography*, 33(4):1192–1192, 2000.

[151] Peter F Peterson, Th Proffen, I-K Jeong, Simon JL Billinge, K-S Choi, Mercouri G Kanatzidis, and Paolo G Radaelli. Local atomic strain in znse 1- x te x from high real-space resolution neutron pair distribution function measurements. *Physical Review B*, 63(16):165211, 2001.

[152] John G Kirkwood. Order and disorder in liquid solutions. *Journal of Physical Chemistry*, 43(1):97–107, 1939.

[153] T Schenk, D Holland-Moritz, V Simonet, R Bellissent, and DM Herlach. Icosahedral short-range order in deeply undercooled metallic melts. *Physical review letters*, 89(7):075507, 2002.

[154] GW Lee, AK Gangopadhyay, KF Kelton, RW Hyers, TJ Rathz, JR Rogers, and DS Robinson. Difference in icosahedral short-range order in early and late transition metal liquids. *Physical review letters*, 93(3):037802, 2004.

[155] David A Keen. A comparison of various commonly used correlation functions for describing total scattering. *Journal of Applied Crystallography*, 34(2):172–177, 2001.

[156] IE Fermi, P Pasta, S Ulam, and M Tsingou. Studies of the nonlinear problems. Technical report, Los Alamos Scientific Lab., N. Mex., 1955.

[157] Berni J Alder and T? E Wainwright. Studies in molecular dynamics. i. general method. *The Journal of Chemical Physics*, 31(2):459–466, 1959.

[158] A Rahman. Correlations in the motion of atoms in liquid argon. *Physical Review*, 136(2A):A405, 1964.

[159] William Smith and Ilian Todorov Todorov. A short description of dl_poly. *Molecular Simulation*, 32(12-13):935–943, 2006.

[160] Sherina Peroos, Zhimei Du, and Nora Henriette de Leeuw. A computer modelling study of the uptake, structure and distribution of carbonate defects in hydroxyapatite. *Biomaterials*, 27(9):2150–2161, 2006.

[161] MJJM Van Kemenade and PL De Bruyn. A kinetic study of precipitation from supersaturated calcium phosphate solutions. *Journal of Colloid and Interface Science*, 118(2):564–585, 1987.

[162] Shuqin Jiang, Haihua Pan, Yan Chen, Xurong Xu, and Ruikang Tang. Amorphous calcium phosphate phase-mediated crystal nucleation kinetics and pathway. *Faraday discussions*, 179:451–461, 2015.

[163] F Betts and AS Posner. An x-ray radial distribution study of amorphous calcium phosphate. *Materials Research Bulletin*, 9(3):353–360, 1974.

[164] Kazuo Onuma and Atsuo Ito. Cluster growth model for hydroxyapatite. *Chemistry of materials*, 10(11):3346–3351, 1998.

[165] Ayako Oyane, Kazuo Onuma, Tadashi Kokubo, and Atsuo Ito. Clustering of calcium phosphate in the system cacl2- h3po4- kcl- h2o. *The Journal of Physical Chemistry B*, 103(39):8230–8235, 1999.

[166] Giulia Mancardi, Carlos Ernesto Hernandez Tamargo, Devis Di Tommaso, and Nora H de Leeuw. Detection of posner's clusters during calcium phosphate nucleation: a molecular dynamics study. *Journal of Materials Chemistry B*, 5(35): 7274–7284, 2017.

[167] Richard I Ainsworth, Devis Di Tommaso, Jamieson K Christie, and Nora H de Leeuw. Polarizable force field development and molecular dynamics study of phosphate-based glasses. *The Journal of chemical physics*, 137(23):234502, 2012.

[168] Harald A Posch, William G Hoover, and Franz J Vesely. Canonical dynamics of the nosé oscillator: Stability, order, and chaos. *Physical review A*, 33(6):4253, 1986.

[169] Jiri Kolafa and John W Perram. Cutoff errors in the ewald summation formulae for point charge systems. *Molecular Simulation*, 9(5):351–368, 1992.

[170] TR Bothe. Reaction of bone to multiple metallic implants. *Sur Gynecol Obst*, 71 (6):598–602, 1940.

[171] Charles A Homsy. Bio-compatibility in selection of materials for implantation. *Journal of Biomedical Materials Research Part A*, 4(3):341–356, 1970.

[172] T Albrektsson, G Zarb, P Worthington, and AR Eriksson. The long-term efficacy of currently used dental implants: a review and proposed criteria of success. *Int J Oral Maxillofac Implants*, 1(1):11–25, 1986.

[173] Stephen D Cook, John F Kay, Kevin A Thomas, and Michael Jarcho. Interface mechanics and histology of titanium and hydroxylapatite-coated titanium for dental implant applications. *International Journal of Oral & Maxillofacial Implants*, 2(1), 1987.

[174] Michael S Block, Israel M Finger, Mark G Fontenot, and John N Kent. Loaded hydroxylapatite-coated and grit-blasted titanium implants in dogs. *International Journal of Oral & Maxillofacial Implants*, 4(3), 1989.

[175] JA Lewandowski and CM Johnson. Structural failure of osseointegrated implants at the time of restoration. a clinical report. *The Journal of prosthetic dentistry*, 62(2):127–129, 1989.

[176] Gianni L Maistrelli, Nizar Mahomed, Victor Fornasier, Luca Antonelli, Yue Li, and Allan Binnington. Functional osseointegration of hydroxyapatite-coated implants in a weight-bearing canine model. *The Journal of arthroplasty*, 8(5):549–554, 1993.

[177] GH Nancollas and BE Tucker. Dissolution kinetics characterization of hydroxyapatite coatings on dental implants. *Journal of Oral Implantology*, 20:221–221, 1994.

[178] Fumitaka Takeshita, Haruhiko Kuroki, Akemi Yamasaki, and Tsuneo Suetsugu. Histopathologic observation of seven removed endosseous dental implants. *International Journal of Oral & Maxillofacial Implants*, 10(3), 1995.

[179] Joo L Ong and Daniel CN Chan. Hydroxyapatite and their use as coatings in dental implants: a review. *Critical Reviews? in Biomedical Engineering*, 28(5&6), 2000.

[180] Nikolaus Aebli, Jörg Krebs, Hermann Stich, Peter Schawalder, Mark Walton, Daryl Schwenke, Heiko Gruner, Beat Gasser, and Jean-Claude Theis. In vivo comparison of the osseointegration of vacuum plasma sprayed titanium-and hydroxyapatite-coated implants. *Journal of Biomedical Materials Research Part A*, 66(2):356–363, 2003.

[181] A Nanci, JD Wuest, L Peru, P Brunet, V Sharma, S Zalzal, and MD McKee. Chemical modification of titanium surfaces for covalent attachment of biological molecules. *Journal of Biomedical Materials Research Part A*, 40(2):324–335, 1998.

[182] Yanjie Zhang and Jinjun Lu. A simple method to tailor spherical nanocrystal hydroxyapatite at low temperature. *Journal of Nanoparticle Research*, 9(4):589–594, 2007.

[183] MP Binitha and PP Pradyumnan. Dielectric property studies of biologically compatible brushite single crystals used as bone graft substitute. *Journal of Biomaterials and Nanobiotechnology*, 4(02):119, 2013.

[184] Theodore R Bott. Aspects of crystallization fouling. *Experimental thermal and fluid science*, 14(4):356–360, 1997.

[185] Jie Weng, Qing Liu, JGC Wolke, Xingdong Zhang, and K De Groot. Formation and characteristics of the apatite layer on plasma-sprayed hydroxyapatite coatings in simulated body fluid. *Biomaterials*, 18(15):1027–1035, 1997.

[186] Hyun-Min Kim, Fumiaki Miyaji, Tadashi Kokubo, and Takashi Nakamura. Preparation of bioactive ti and its alloys via simple chemical surface treatment. *Journal of Biomedical Materials Research Part A*, 32(3):409–417, 1996.

[187] Seiji Ban and Jiro Hasegawa. Morphological regulation and crystal growth of hydrothermal-electrochemically deposited apatite. *Biomaterials*, 23(14):2965–2972, 2002.

[188] D Turnbull. Kinetics of heterogeneous nucleation. *The Journal of Chemical Physics*, 18(2):198–203, 1950.

[189] Levente Vitos, AV Ruban, Hans Lomholt Skriver, and J Kollar. The surface energy of metals. *Surface Science*, 411(1):186–202, 1998.

[190] GB Schneider, H Perinpanayagam, M Clegg, R Zaharias, D Seabold, J Keller, and Clark Stanford. Implant surface roughness affects osteoblast gene expression. *Journal of dental research*, 82(5):372–376, 2003.

[191] Bertil Friberg, Lars Sennerby, Kerstin Gröndahl, Christina Bergström, Thomas Bäck, and Ulf Lekholm. On cutting torque measurements during implant placement: A 3-year clinical prospective study. *Clinical implant dentistry and related research*, 1(2):75–83, 1999.

[192] S Anil, H Alghamdi, JA Jansen, and PS Anand. *Dental implant surface enhancement and osseointegration*. InTech Open Access Publisher, 2011.

[193] EOR Beake, MT Dove, AE Phillips, DA Keen, MG Tucker, AL Goodwin, TD Bennett, and AK Cheetham. Flexibility of zeolitic imidazolate framework structures studied by neutron total scattering and the reverse monte carlo method. *Journal of Physics: Condensed Matter*, 25(39):395403, 2013.

[194] Donald S Young, Bruce S Sachais, and Leigh C Jefferies. *The rietveld method*. Citeseer, 1993.

[195] AC Larson and RB Von Dreele. Gsas general structure analysis system, report laur 86-748. *Los Alamos National Laboratory, Los Alamos, NM*, 1986.

[196] Dominique Massiot, Franck Fayon, Mickael Capron, Ian King, Stéphanie Le Calvé, Bruno Alonso, Jean-Olivier Durand, Bruno Bujoli, Zhehong Gan, and Gina Hoatson. Modelling one-and two-dimensional solid-state nmr spectra. *Magnetic Resonance in Chemistry*, 40(1):70–76, 2002.

[197] CB Baddiel and EE Berry. Spectra structure correlations in hydroxy and fluorapatite. *Spectrochimica Acta*, 22(8):1407–1416, 1966.

[198] Hassen Bachouâ, Masseoud Othmani, Yannick Coppel, Nabil Fatteh, Mongi Debbabi, and Béchir Badraoui. Structural and thermal investigations of a tunisian natural phosphate rock. *J Mater Environ Sci*, 5(4):1152–1159, 2014.

[199] Haohao Yi, Etienne Balan, Christel Gervais, Loïc Ségalen, Damien Roche, Alain Person, Franck Fayon, Guillaume Morin, and Florence Babonneau. Probing atomic scale transformation of fossil dental enamel using fourier transform infrared and nuclear magnetic resonance spectroscopy: A case study from the tugen hills (rift gregory, kenya). *Acta biomaterialia*, 10(9):3952–3958, 2014.

[200] Yajie Gao, Natalia Karpukhina, and Robert V Law. Phase segregation in hydroxyfluorapatite solid solution at high temperatures studied by combined xrd/solid state nmr. *RSC Advances*, 6(105):103782–103790, 2016.

[201] Sergey V Dorozhkin. Amorphous calcium orthophosphates: nature, chemistry and biomedical applications. *Int. J. Mater. Chem*, 2(1):19–46, 2012.

[202] Sergey V Dorozhkin. Calcium orthophosphates (capo4): occurrence and properties. *Progress in Biomaterials*, 5(1):9–70, 2016.

[203] HFTZ Chen, Zhiyong Tang, Jun Liu, Kai Sun, S-R Chang, Mathilde C Peters, John F Mansfield, Agata Czajka-Jakubowska, and Brian H Clarkson. Acellular synthesis of a human enamel-like microstructure. *Advanced Materials*, 18(14): 1846–1851, 2006.

[204] Yanjie Zhang and Jinjun Lu. A simple method to tailor spherical nanocrystal hydroxyapatite at low temperature. *Journal of Nanoparticle Research*, 9(4):589–594, 2007.

[205] S Raynaud, E Champion, D Bernache-Assollant, and P Thomas. Calcium phosphate apatites with variable ca/p atomic ratio i. synthesis, characterisation and thermal stability of powders. *Biomaterials*, 23(4):1065–1072, 2002.

[206] J. C. Elliot, editor. *Structure and Chemistry of the Apatites and Other Calcium Orthophosphates*. Elsevier Science B.V., 1st ed. edition, (Jan. 1 1994). 404 pages.

[207] Jens-Hilmar Bradt, Michael Mertig, Angelika Teresiak, and Wolfgang Pompe. Biomimetic mineralization of collagen by combined fibril assembly and calcium phosphate formation. *Chemistry of Materials*, 11(10):2694–2701, 1999.

[208] Mayumi Iijima. Formation of octacalcium phosphate in vitro. In *Octacalcium phosphate*, volume 18, pages 17–49. Karger Publishers, 2001.

[209] F Barrere, P Layrolle, CA Van Blitterswijk, and K De Groot. Biomimetic calcium phosphate coatings on ti6al4v: a crystal growth study of octacalcium phosphate and inhibition by mg 2+ and hco 3-. *Bone*, 25(2):107S–111S, 1999.

[210] Philip James Thomas Reardon, Albertus Denny Handoko, Lin Li, Jie Huang, and Junwang Tang. Dimensionally and compositionally controlled growth of calcium phosphate nanowires for bone tissue regeneration. *Journal of Materials Chemistry B*, 1(44):6170–6176, 2013.

[211] Larry L Hench. Bioceramics: from concept to clinic. *Journal of the American Ceramic Society*, 74(7):1487–1510, 1991.

[212] Philip James Thomas Reardon, Albertus Denny Handoko, Lin Li, Jie Huang, and Junwang Tang. Dimensionally and compositionally controlled growth of calcium phosphate nanowires for bone tissue regeneration. *Journal of Materials Chemistry B*, 1(44):6170–6176, 2013.

[213] S Mandal and S Mayadevi. Adsorption of fluoride ions by zn–al layered double hydroxides. *Applied Clay Science*, 40(1-4):54–62, 2008.

[214] Racquel Zapanta LeGeros. *Crystallographic studies of the carbonate substitution in the apatite structure*. PhD thesis, N. Y. U., Graduate School., 1967.

[215] RZ LeGeros, OR Trautz, JP LeGeros, and E Klein. Carbonate substitution in apatite structure (1). In *Bulletin de la Societe Chimique de France*, page 1712. EDITIONS SCIENTIFIQUES MEDICALES ELSEVIER 23 RUE LINOIS, 75724 PARIS CEDEX 15, FRANCE, 1968.

[216] Rory M Wilson, James C Elliott, Stephanie EP Dowker, and Ron I Smith. Rietveld structure refinement of precipitated carbonate apatite using neutron diffraction data. *Biomaterials*, 25(11):2205–2213, 2004.

[217] Ch Rey, JL Miquel, L Facchini, AP Legrand, and MJ Glimcher. Hydroxyl groups in bone mineral. *Bone*, 16(5):583–586, 1995.

[218] C-K Loong, C Rey, LT Kuhn, C Combes, Y Wu, S-H Chen, and MJ Glimcher. Evidence of hydroxyl-ion deficiency in bone apatites: an inelastic neutron-scattering study. *Bone*, 26(6):599–602, 2000.

[219] MG Taylor, SF Parker, and PCH Mitchell. A study by high energy transfer inelastic neutron scattering spectroscopy of the mineral fraction of ox femur bone. *Journal of molecular structure*, 651:123–126, 2003.

[220] Gyunggoo Cho, Yaotang Wu, and Jerome L Ackerman. Detection of hydroxyl ions in bone mineral by solid-state nmr spectroscopy. *Science*, 300(5622):1123–1127, 2003.

[221] RZ LeGeros, OR Trautz, E Klein, and JP LeGeros. Two types of carbonate substitution in the apatite structure. *Experientia*, 25(1):5–7, 1969.

[222] ED Eanes, IH Gillessen, and AS Posner. Intermediate states in the precipitation of hydroxyapatite. *Nature*, 208(5008):365–367, 1965.

[223] Arthur Bienenstock and Aaron S Posner. Calculation of the x-ray intensities from arrays of small crystallites of hydroxyapatite. *Archives of Biochemistry and Biophysics*, 124:604–607, 1968.

[224] Aaron S Posner and Foster Betts. Synthetic amorphous calcium phosphate and its relation to bone mineral structure. *Accounts of Chemical Research*, 8(8):273–281, 1975.

[225] Matthew G Tucker, Martin T Dove, and David A Keen. Total scattering and reverse monte carlo modelling of disordered crystalline materials. *From semiconductors to proteins: beyond the average structure/Fundam. Mater. Res. Ser./. New York: Kluwer Academic–Plenum*, pages 85–103, 2002.

[226] Chengde Huang and AN Cormack. The structure of sodium silicate glass. *The Journal of chemical physics*, 93(11):8180–8186, 1990.

[227] Adrian C Wright. Neutron scattering from vitreous silica. v. the structure of vitreous silica: What have we learned from 60 years of diffraction studies? *Journal of non-crystalline solids*, 179:84–115, 1994.

[228] Callum A Young and Andrew L Goodwin. Applications of pair distribution function methods to contemporary problems in materials chemistry. *Journal of Materials Chemistry*, 21(18):6464–6476, 2011.

[229] Kostya Trachenko, Martin T Dove, and Ekhard KH Salje. Structural changes in zircon under α-decay irradiation. *Physical Review B*, 65(18):180102, 2002.

[230] Kostya Trachenko, Martin T Dove, Emilio Artacho, Ilian T Todorov, and W Smith. Atomistic simulations of resistance to amorphization by radiation damage. *Physical Review B*, 73(17):174207, 2006.

[231] Ilian T Todorov, John A Purton, Neil L Allan, and Martin T Dove. Simulation of radiation damage in gadolinium pyrochlores. *Journal of Physics: Condensed Matter*, 18(7):2217, 2006.

[232] Donald Mkhonto and Nora H de Leeuw. A computer modelling study of the effect of water on the surface structure and morphology of fluorapatite: introducing a ca 10 (po 4) 6 f 2 potential model. *Journal of Materials Chemistry*, 12(9):2633–2642, 2002.

[233] NH De Leeuw. Density functional theory calculations of local ordering of hydroxy groups and fluoride ions in hydroxyapatite. *Physical Chemistry Chemical Physics*, 4(15):3865–3871, 2002.

[234] Nora H de Leeuw. A computer modelling study of the uptake and segregation of fluoride ions at the hydrated hydroxyapatite (0001) surface: introducing a ca 10 (po 4) 6 (oh) 2 potential model. *Physical Chemistry Chemical Physics*, 6(8): 1860–1866, 2004.

[235] Muthuramalingam Prakash, Thibault Lemaire, Devis Di Tommaso, Nora de Leeuw, Marius Lewerenz, Matthieu Caruel, and Salah Naili. Transport properties of water molecules confined between hydroxyapaptite surfaces: A molecular dynamics simulation approach. *Applied Surface Science*, 418:296–301, 2017.

[236] N Almora Barrios. *A computational investigation of the interaction of the collagen molecule with hydroxyapatite*. PhD thesis, UCL (University College London), 2010.

[237] E Hayek and W Stadlmann. Darstellung von reinem hydroxylapatit für adsorptionszwecke. *Angewandte Chemie*, 67(12):327–327, 1955.

[238] Eliane Schutte, Grace Lee Picciolo, and David S Kaplan. *Tissue engineered medical products (TEMPs)*. ASTM [American Society for Testing and Materials], 2004.

[239] Marina Sansiñena, María Victoria Santos, Noemi Zaritzky, and Jorge Chirife. Comparison of heat transfer in liquid and slush nitrogen by numerical simulation of cooling rates for french straws used for sperm cryopreservation. *Theriogenology*, 77(8):1717–1721, 2012.

[240] Julian D Gale and Andrew L Rohl. The general utility lattice program (gulp). *Molecular Simulation*, 29(5):291–341, 2003.

[241] WT Lee, MT Dove, and EKH Salje. Surface relaxations in hydroxyapatite. *Journal of Physics: Condensed Matter*, 12(48):9829, 2000.

[242] Jeremy Andrew Lesl Rabone and NH De Leeuw. Interatomic potential models for natural apatite crystals: incorporating strontium and the lanthanides. *Journal of computational chemistry*, 27(2):253–266, 2006.

[243] JAL Rabone, Andrew Carter, AJ Hurford, and Nora Henriette de Leeuw. Modelling the formation of fission tracks in apatite minerals using molecular dynamics simulations. *Physics and Chemistry of Minerals*, 35(10):583–596, 2008.